UNIVERSITÀ DEGLI STUDI DI CATANIA

DIPARTIMENTO DI FISICA E ASTRONOMIA

DOTTORATO DI RICERCA IN FISICA

GABRIELE COCI

PROBING THE QUARK-GLUON PLASMA PROPERTIES THROUGH HEAVY QUARKS' DYNAMICS: TRANSPORT COEFFICIENTS AND ELLIPTIC FLOW

Tesi di Dottorato

P.h.D. Coordinator:
Chiar.mo Prof. Vincenzo Bellini

Tutor:
Chiar.mo Prof. Vincenzo Greco
Dott. Salvatore Plumari

Ciclo XXXI 2015/2018

CONTENTS

ABSTRACT

Quantum Chromodynamics (QCD) is the non-abelian gauge field theory that within the Standard Model describes the strong interaction between quarks and gluons. QCD exhibits two main properties: color confinement and asymptotic freedom. The former implies that in ordinary matter quarks and gluons are bounded within colorless hadrons. The latter is related to the decrease of the QCD strength coupling with increasing characteristic energy of the process. Asymptotic freedom implies that under extreme conditions of high temperature and density the interaction affecting quarks and gluons is so weakly that they are released from the bounding state to form a deconfined phase of matter known as the Quark-Gluon Plasma (QGP). Numerical solutions of QCD equations on lattice (lQCD) predict that such transition is properly a *crossover* at almost zero baryon density and with a critical temperature $T_c = 155\,MeV$. The study of nuclear matter under extreme conditions is the main program of the experiments at the Relativistic Heavy Ion Collider (RHIC) and Large Hadron Collider (LHC) where ultrarelativistic Heavy-Ion Collisions (uHICs) are conducted to create an almost baryon free QGP with initial $T \approx 3T_c$. In this scenario Heavy Quarks (HQs), mainly charm and bottom, play a unique role. Due to their large masses HQs are created at initial stage of HICs by hard perturbative QCD scattering processes. Moreover, their thermalization time is comparable with the QGP lifetime. Hence HQs can probe the entire evolution of the *fireball* carrying more information about their initial properties. The most important observables in the HQ sector are the nuclear modification factor R_{AA} and the elliptic flow v_2. The challenge of each theoretical framework is to provide a simultaneous description of these two observables that have been measured both at RHIC and LHC energies.

In this thesis we study the HQ dynamics within the QGP by means of a relativistic Boltzmann transport approach. In this framework we treat non-perturbative QCD effects by prescription of a Quasi-Particle Model (QPM) in which light quarks and gluons of the bulk are dressed with effective masses and the T dependence of the strength coupling is fitted to lQCD thermodynamics. In the first part of this thesis we discuss about HQ transport coefficients by performing simulations in static QCD medium. We compare our extracted *drag* and *diffusion* coefficients with results obtained through a MonteCarlo integration. Afterwards we investigate charm suppression and compare the results among various theoretical models. In the second part we focus on the dynamical evolution of HQs within the QGP by carrying out simulations of realistic HICs. We observe that within our QPM interaction, which implies a T-dependent drag coefficient almost constant near T_c, we are able to describe simultaneously the R_{AA} and v_2 of D mesons both at RHIC and LHC energies. In order to compare with the experimental measurements we couple the final HQ spectra to a hybrid coalescence plus fragmentation hadronization model which is suitable to describe the large magnitude of the observed baryon-to-meson ratio $\Lambda_c/D^0 \sim 1$. In the same framework we provide our predictions for B meson R_{AA} and v_2 and compare our results with the available experimental data. A goal of this work is to include the effect of enhanced Λ_c production in HICs on the nuclear modification factor of D mesons. Finally, we present our estimate of the HQ spatial diffusion coefficient $D_s(T)$ within our Boltzmann approach. We show that our phenomenological predictions of D_s for charm quark are in agreement with lQCD expectations, meaning that through the study of HQ thermalization we can probe the QCD interaction within the present uncertainties of lQCD. We point out also that the possibility to calculate transport coefficients at the bottom mass scale allows to reduce uncertainties coming from the adopted transport model and to bring the estimate of D_s closer to the quenched lQCD.

Abstract in lingua italiana

La Cromodinamica Quantistica (QCD) è la teoria di gauge non-abeliana che nell'ambito del Modello Standard descrive l'interazione forte fra quark e gluoni. La QCD possiede due proprietà principali: il confinamento e la libertà asintotica. A causa del confinamento quark e gluoni nella materia ordinaria non possono esistere isolati, ma formano stati legati privi di colore noti come adroni. La libertà asintotica si riferisce al fatto che la costante di accoppiamento della QCD diminuisce all'aumentare dell'energia del processo fisico. Essa implica anche che in condizioni estreme di alta temperatura o densità quark e gluoni interagiscono così debolmente da essere rilasciati dagli adroni e formare un nuovo stato di materia chiamato Quark-Gluon Plasma (QGP). Calcoli numerici basati sulla soluzione della QCD su reticolo (lQCD) hanno mostrato che questa transizione di fase è in realtà un *crossover* che si verifica ad una temperatura critica $T_c = 155\, MeV$. Lo studio della materia nucleare in condizioni estreme è oggetto principale degli esperimenti al Relativistic Heavy-Ion Collider (RHIC) e al Large Hadron Collider (LHC) dove si effettuano collisioni di ioni pesanti (HICs) ad energie ultrarelativisitche per creare il QGP a potenziale barionico $\mu_B \sim 0$ e con una temperatura iniziale di circa $T \approx 3T_c$. In questo scenario i quark pesanti (HQs), charm e bottom, hanno un ruolo unico. Infatti, a causa della loro massa elevata, essi vengono creati da processi "hard" negli stati iniziali di HICs e inoltre il loro tempo di termalizzazione è confrontabile con la vita media del QGP. Perciò i HQs si propagano lungo l'intera fase evolutiva della *fireball* preservando molte informazioni sulle loro proprietà dinamiche. Le più importanti osservabili sono il fattore di modificazione nucleare R_{AA} e il flusso ellittico v_2. I modelli teorici mirano a fornire una descrizione simultanea delle due osservabili misurate sia a RHIC che a LHC. In questa tesi descriviamo la dinamica dei HQs all'interno del QGP per mezzo di un approccio del trasporto relativistico di Boltzmann. Includiamo gli effetti non-perturbativi della QCD attraverso un modello a Quasi-Particelle (QPM) in cui quark leggeri e gluoni sono rivestiti con una massa termica e la dipendenza da T della costante di accoppiamento è fittata sulla termodinamica di lQCD. Nella prima parte ci concentriamo sullo studio dei coefficienti del trasporto dei HQs effettuando simulazioni in un mezzo statico. Quindi confrontiamo i risultati estratti per i coefficienti di *drag* e *diffusion* con dei calcoli ottenuti attraverso un'integrazione Montecarlo e studiamo la soppressione dei quark charm facendo un confronto fra vari modelli teorici. Nella seconda parte discutiamo l'evoluzione dinamica dei HQs nel QGP in simulazioni HICs realistiche. Osserviamo che con l'interazione QPM, che determina un coefficiente di *drag* costante vicino a T_c, descriviamo simultaneamente R_{AA} e v_2 dei mesoni D alle energie di RHIC e di LHC. Per confrontarci con le misure sperimentali accoppiamo gli spettri finali dei HQs con un meccanismo di adronizzazione basato su un modello ibrido di frammentazione e coalescenza con cui spieghiamo anche il rapporto elevato barioni-mesoni in HICs. Con lo stesso approccio del trasporto riportiamo le nostre predizioni per R_{AA} e v_2 dei mesoni B. Una novità di questo lavoro è rappresentata dall'impatto della produzione elevata di barioni Λ_c in HICs sul fattore di modificazione nucleare dei mesoni D. Infine presentiamo le nostre stime sul coefficiente di diffusione spaziale $D_s(T)$ dei quark charm mostrando che esse sono in accordo con i valori calcolati in lQCD. Ciò dimostra che entro le incertezze di lQCD è possibile esplorare le proprietà dell'interazione di QCD attraverso la termalizzazione dei HQs. Mostriamo inoltre che lo studio del D_s alla scala di massa del quark bottom riduce le incertezze che derivano dai modelli del trasporto utilizzati e garantisce un maggiore accordo con l'approssimazione statica di lQCD.

INTRODUCTION

In the Standard Model of fundamental forces the current theory that describes the strong interaction among particles is Quantum Chromodynamics (QCD). The elementary constituents of QCD are represented by quarks and gluons which carry a “color” charge through which their dynamics is delineated in terms of a quantum field Yang-Mills theory. The two main features of QCD are color confinement and asymptotic freedom. The first one implies that in ordinary nuclear matter quarks and gluons cannot exist as free particles, rather they are bounded within a length scale $d \sim 1\, fm$ inside colorless hadron states which mainly divide into mesons and baryons. The second one is related to the decrease of the interaction strength at small distance, i.e. with the increasing energy scale of the processes. Therefore, asymptotic freedom allows to treat such processes within a perturbative QCD (pQCD) framework and it implies also that under extreme conditions of high temperature and density the strong interaction is sufficiently weak that quarks and gluons are released from the bounding hadrons and become the degrees of freedom of a new state of matter, known as the Quark-Gluon Plasma (QGP). With the advent of high speed and powerful computers the study of strong interacting systems has been carried out by solving the QCD equations numerically on a lattice. In particular, lattice QCD (lQCD) calculations show that nuclear matter experiences a *crossover*, rather than a sharp phase transition, at a critical temperature $T_c \approx 155\, MeV$. Most recent analysis indicate that at $T > T_c$

the system is characterized by a high degree of non-perturbative effects estimated by a non-vanishing trace anomaly $(\epsilon - 3P)/T^4$ jointly with chiral symmetry restoration $< q\bar{q} >= 0$ as expected within the deconfined QGP phase. In the standard cosmological scenario it is believed that the QGP has filled the early hot Universe for the first $10 - 20\,\mu s$ after the Big Bang with almost zero baryon chemical potential $\mu_B \sim 0$ and down to a temperature value $T \approx 150\,MeV \simeq 10^{12}\,K$, then the system has undergone to hadronization to form protons and neutrons. On the contrary a transition from hadronic state to a quark phase with finite baryon density and almost $T \sim 0$ can occur inside the center of compact stellar objects, such as neutron stars, where the matter density in the core reaches values $\rho_m \geq 3 - 8 \cdot 10^{17}\,Kg/m^3$, i.e. several times larger than the ordinary nuclear matter $\rho_0 = 0.16\,fm^{-3}$. The study of nuclear matter under extreme conditions is pursued by performing Heavy-Ion Collisions (HICs) at ultrarelativistic energies (above $\sim 10\,GeV$ per nucleon). The experiments conducted at the Relativistic Heavy Ion Collider (RHIC) at Brookhaven National Laboratory (BNL) with beam energy up to $200\,AGeV$ have given clear evidence of the QGP formation through the measurements of collective flow and suppression of high transverse momentum (p_T) hadrons. Such indications have been confirmed by the experimental measurements at CERN Large Hadron Collider (LHC) where heavy nuclei are smashed up with energies up to $5.5\,ATeV$ and thus it is possible to scratch the QCD phase diagram in the region of $\mu_B \sim 0$ and $T \approx 3T_c$. Moreover, new interesting phenomena arising at initial stage of HICs have been discovered that can be analyzed by looking at the possible formation of QGP drops in small system reactions (such as pp, pA collisions) and through the beam energy scanning of the critical end-point.

In this scenario Heavy Quarks (HQs), mainly charm and bottom, play a fundamental role which arises from two specific properties. The first one is that they have masses much higher than the perturbative scale of QCD, i.e. $M_{HQ} \gg \Lambda_{QCD} = 0.2\,GeV$. From the point of view of particle physics this implies that HQs are created by hard binary collisions at initial stage of HICs with a formation time $\tau_f \sim 1/2M_{HQ} \leq 0.1\,fm$ and production cross sections that can be calculated within pQCD-like schemes at Next-to-Leading Order

(NLO). The second one is typical of plasma physics and corresponds to the condition $M_{HQ} \gg T$. This ensures that the probability to pop out a charm-anticharm or bottom-antibottom pair from thermal excitation of the vacuum is negligible. Therefore, HQs are witness of the entire phase space evolution of the *fireball* and eventually carry out more information of their initial properties, because their thermalization time is comparable with the lifetime of the QGP, i.e. $\tau_{th}(HQ) \sim \tau_{QGP} \gg \tau_f$. Two key observables for studying the impact of HQ dynamics on QGP physics are the nuclear modification factor $R_{AA}(p_T)$ which measures the suppression of high p_T spectra of Heavy-Flavor (HF) hadrons in nucleus-nucleus collisions compared to the proton-proton collisions and the elliptic flow $v_2(p_T) = \langle\cos(2\phi)\rangle$ which provides an estimate of anisotropies with respect to the azimuthal angle ϕ in momentum space. The challenge of each theoretical model is to provide a simultaneous description of R_{AA} and v_2 which have been widely measured (at least for D mesons) both at RHIC and LHC energies. However, difficulties may arise that are mostly due to the complex correlations among these two observables that can be related to the dependence of HQ interaction on the medium evolution and to the impact of the hadronization mechanism.

In this thesis we discuss about a relativistic transport approach to study the dynamical properties of HQs and the role of coalescence and fragmentation processes with the aim to give a correct solution of the the $R_{AA} - v_2$ "puzzle" and to explore the hot QCD matter properties by examining charm and bottom thermalization. This thesis is organized as follows.

In Chapter 1 we will describe in a nutshell the construction of QCD as a gauge field theory and we will come at its most relevant properties which are asymptotic freedom and color confinement. We will also overview global symmetries of the QCD Lagrangian in order to discuss about the chiral symmetry breaking and dynamical mass generation for light quarks in the Nambu Jona-Lasinio (NJL) model which shares some properties of QCD theory. Finally we will summarize all the main features of strongly interacting systems to build up the QCD phase diagram where the transition from hadron gas to deconfined QGP is reported along the temperature-baryon chemical potential space region which has been traversed by the evolving Universe at dawn of time and it is partially accessible by HICs nowadays.

In Chapter 2 we will discuss about the physics of ultrarelativistic HICs which we divide into two parts. In the first one we will look at the initial stages of HICs that can be modeled by geometrical Glauber or effective QCD-like theories. Then we will describe how the formed hot QGP expands as a nearly perfect fluid, i.e. with small value of shear viscosity to entropy density η/s, and cools down until the free partons hadronize by fragmentation or coalescence at $T \sim T_c$ to produce the final particles which in the end are measured by the experimental detectors. In the second part we will focus on the role of Heavy Quarks (HQs) production within the QGP. In particular, we will discuss about the calculation of the HQ cross sections in high energy reactions distinguishing between elementary pp collisions and HICs. We will mention about the propagation of HQs in the early and pre-equilibrium stages of the *fireball* evolution based on a recent work which is suitable for studying HQ suppression and anysotropic flow both in pA and in AA collisions. We will treat extensively the hadronization mechanism of HQs by describing a hybrid fragmentation plus coalescence model that we will couple at the final stage of their evolution through the QGP to obtain the final p_T spectra of the corresponding HF mesons and baryons. Finally, we will introduce the definitions of nuclear modification factor R_{AA} and elliptic flow v_2. We will briefly overview the most recent measurements of these two observables both at RHIC and LHC and we will focus on the state-of-art in the HF sector through a direct comparison with light hadrons.

In Chapter 3 we will review the formulation of classical kinetic theory by deriving the relativistic Boltzmann-Vlasov equation which describes the dynamical evolution of interacting plasmas and we will also give a brief introduction to transport equations in quantum theory both in the non-relativistic and in the relativistic case employing the Wigner formalism and using as an example the QCD-like sigma model. After that, we will discuss about the main properties of our 3+1 dimensional transport cascade approach which is based on the implementation of the Relativistic Boltzmann Equation (RBE) for describing both *bulk* matter, i.e. gluons and light quarks (u, d, s), and HQ dynamics in the QGP. We will show how to account for non-perturbative interaction within the QCD medium by prescription of a Quasi-Particle Model (QPM) where the T-dependence of the strength coupling $g(T)$ is fitted to reproduce lQCD thermodynamics. We will mention also how we can constraint the dissipative effects by tuning the collision integral to a fixed value of $\eta/s(T)$ in order to gauge our transport approach for the QGP evolution to the viscous hydrodynamical scheme. We will briefly remind also how to derive the Fokker-Planck equation to describe the propagation of HQs through the hot QCD plasma within a Brownian motion approximation. In particular, we will concentrate on the role of transport coefficients, mainly *drag* and *diffusion*, which encode the main properties of the interaction and for this reason they are fundamental ingredients which allow to probe the QGP features through HQ thermalization. In the last part of the chapter we will focus on the test particle method and the stochastic algorithm that we employ to solve numerically the RBE both for the *bulk* partons and for the HQs and to examine two-particle collisions in accordance with Lorentz covariance and causality.

In Chapter 4 we will focus on the calculation of *drag* and *diffusion* coefficients for HQs in a pQCD scheme or in our QPM through the implementation of a multidimensional Monte-Carlo integration code. We will use these results to make a comparison with the same coefficients extracted from the Boltzmann framework that we set up to carry out numerical simulations in static medium (“box”) at fixed temperature. Then we will present a comparison among various transport models for charm quark dynamics developed by different theoretical groups (Catania, Duke, Berkeley-Wuhan, Nantes, Frankfurt, Texas A&M) to reduce the uncertainties in the estimated *drag* coefficient.

In Chapter 5 we will present our Relativistic Boltzmann approach properly set up to perform simulations of realistic HICs at the energy of RHIC and LHC. In the case of HQs we will couple our transport model self-consistently to our hybrid fragmentation plus coalescence mechanism to obtain the final HF hadrons nuclear modification factor $R_{AA}(p_T)$ and elliptic flow $v_2(p_T)$. We will compare our results for D mesons with the available experimental data and we will provide our predictions for B mesons. In this framework we will address also the role of coalescence to reproduce the p_T dependence of the baryon-to-meson ratios at the level of charm quarks that has been measured both at RHIC and LHC energies and whose magnitude indicates the scenario of a strong Λ_c enhancement. We will discuss the impact of Λ_c production on the D meson suppression factor $R_{AA}(p_T)$, showing that the tracking of such effect leads to a significant improvement of our results towards the experimental data and represents a novelty for the evolution of this observable. Finally, we will look at charm and bottom thermalization by estimating the spatial diffusion coefficient $2\pi T D_s(T)$ extracted from our Boltzmann approach with QPM interaction tuned to fit the measured R_{AA} and v_2 simultaneously and we will compare our results with lQCD and other phenomenological expectations.

This thesis ends up with the Conclusions where we will make a summary of the most relevant points on the physics of HQs and delineate future works that demonstrate their unique role for probing the features of the QGP.

CHAPTER 1

QUANTUM CHROMODYNAMICS IN A NUTSHELL

1.1 QCD as a gauge field theory

In the Standard Model of particle physics *Quantum Chromodynamics* (QCD) describes the strong interaction between quarks and gluons, which are the basic constituents of hadrons, i.e. mesons and baryons, among which are protons and neutrons eventually bounded into the wide range of nuclei. In the Quantum Field Theory (QFT) paradigm QCD is a Yang-Mills theory constructed on the $SU(N_c)$ Lie group. Therefore for a rapid issue of its basic properties, we start writing a Dirac-like Lagrangian density in Minkowski space

$$\mathcal{L}_D = \sum_f \bar{q}_\alpha^{(f)}(x)\left(i\gamma^\mu\partial_\mu - m_f\right)q_\alpha^{(f)}(x) \tag{1.1}$$

In this Lagrangian the spinor field $q_\alpha^{(f)}$ represents a quark having mass m_f in one of the N_f possible flavors and we consider also an internal degree of freedom, named *color*, denoted with the lower index α running from 1 to N_c. Quarks possess also spin degrees of freedom, but we do not explicitly indicate in Eq. (1.1) in order to streamline the notation[1]. If we look at the possible symmetries of the theory, we easily discover a global symmetry, i.e. not depending on the space coordinates x, due to the invariant form of $\mathcal{L}_D$ with respect to any rotation of the quark fields in the color internal space. The general operator U which represents mathematically this transformation and acting on the various components $q_\alpha^{(f)}(x)$, belongs to the $SU(N_c)$ and quark fields build its fundamental representation. In Yang-Mills theories the symmetry group $SU(N_c)$ is called *gauge group* and any of its element U performs a gauge transformation. In particular, for QCD the gauge group is $SU(3)$ where $N_c = 3$ are the quark colors. Each element of $SU(N_c)$ can be written in the form $U = \exp(-i\theta^a T^a)$ where θ^a are x-independent parameters of the gauge transformation and T^a are traceless hermitian matrices, the $(N_c^2 - 1)$ generators of the $SU(N_c)$ Lie group. The group generators T^a close a Lie algebra which is independent on the group representation and it is represented by the following commutation relation

$$\left[T^a, T^b\right] = i f^{abc} T^c \tag{1.2}$$

The f^{abc} parameters are the so-called *structure constants* of the gauge group. They are anti-symmetric quantities for index permutation and they also fulfill the Jacobi identity

$$f^{abc} f^{cdf} + f^{acf} f^{cdb} = f^{acd} f^{bcf} \tag{1.3}$$

Instead, the matrix form of the generators T^a depends on the specific group representation which in turn is given by the field on which the gauge transformation U acts [2]. When the Lie group generators commute with each other, that means from Eq. (1.2) all f^{abc} have zero value, the Lie group is called

---

[1] Through the course of this thesis we adopt Einstein notation by which a sum over Lorentz and other repeated indices is implied.

[2] In the fundamental representation of QCD gauge group $SU(3)$ the Lie generators which fulfill the commutator relation Eq. (1.2) are the 3×3 Gell-Mann matrices $(T^a)_{\alpha\beta} = (\lambda^a/2)_{jk}$: j and k run from 1 to 3 corresponding to the three pictorial values Red-Green-Blue (RGB) for quark colors. There exists also an adjoint representation of $SU(3)$ where the the relation $(T^a)_{bc} = -i f^{abc}$ links directly the matrix form of the generators to the structure constants and the value of all indices a, b and c equals the number of 8 generators of $SU(3)$.

Abelian. On the other hand, if the generators T^a do not commute, the Lie group is non-Abelian. This seems just a mathematical variance, however it has a remarkable consequence on the physical. We have already said that the gauge group corresponding to QCD is $SU(3)$, which is a non-Abelian Lie group. *Quantum Electrodynamics* (QED), the corresponding Yang-Mills theory describing the electromagnetic force in QFT, is based on a symmetry for the $U(1)$ gauge group, which is instead an Abelian one. Such difference makes QCD a much more complex theory compared to QED and one can physically observe it in all the problems regarding the strong interacting systems, some of which we will discuss in this thesis. For detail discussion of Lie groups and Yang-Mills theories in QFT one can refer to a wide list of books, some with introductory approach [1] [2] [3] and others more advanced [4] [5]. We will now go further on the construction of the QCD Lagrangian referring specifically to [6]. The gauge principle states that from a physical perspective the global symmetry of $\mathcal{L}_D$ has to be promoted as a local symmetry, which means that the in the operator U the parameters θ^a acquire a coordinate dependence. We can write an infinitesimal gauge transformation of the quark fields by expanding the exponential form of U at first order

$$q_\alpha^{(f)}(x) \rightarrow q_\alpha^{(f)}(x) - i\theta^a(x)\,(T^a)_{\alpha\beta}\,q_\beta^{(f)}(x) \tag{1.4}$$

Substituting the transformed field Eq. (1.4) in the Lagrangian Eq. (1.1) an extra term of the form $\bar{q}_\alpha^{(f)}(x)\gamma^\mu(T^a)_{\alpha\beta}q_\beta^{(f)}\partial_\mu\theta^a(x)$ will prevent our theory to be locally gauge invariant already at initial stage. The minimal application of the gauge principle is simply pursued by replacing the normal space derivative ∂_μ appearing in Eq. (1.1) with the so called *covariant derivative* which clearly has to be defined in the following way

$$(D_\mu)_{\alpha\beta} = \delta_{\alpha\beta}\,\partial_\mu - ig\,T^a_{\alpha\beta}A^a_\mu(x) \tag{1.5}$$

Therefore, we move from the Dirac-like Lagrangian Eq. (1.1) to the gauge invariant expression

$$\mathcal{L}_F = \sum_f \bar{q}^{(f)}_\alpha(x)\left(i\gamma^\mu D_\mu(x)_{\alpha\beta} - m_f\,\delta_{\alpha\beta}\right) q^{(f)}_\beta(x) \tag{1.6}$$

In this expression we are introducing new degrees of freedom through the eight four-vector fields $A^a_\mu(x)$, known as *gauge fields*. In QCD these fields represent vector bosons with spin 1 which are endowed with color charge and couples to the fermionic current $J^{a,\mu}(x) = \bar{q}^{(f)}(x)\gamma^\mu T^a q^{(f)}(x)$ with the intensity of strong interaction given by the QCD *coupling constant* g. The elementary particles corresponding to the gauge fields are the gluons and the way how the gluon fields $A^a_\mu(x)$ transform by color rotation is derivable by imposing the local gauge invariance of the Lagrangian $\mathcal{L}_F$ Eq.(1.6). Hence, we have

$$T^a A^a_\mu(x) \to U(x)(T^a A^a_\mu(x))U^+(x) - \frac{i}{g}(\partial_\mu U(x))U^+(x) \tag{1.7}$$

If we apply the transformation rules for quark Eq. (1.4) and gluon Eq. (1.7) fields respectively, with simple algebraic steps we obtain that the product $D_\mu(x)\,q^{(f)}(x)$ is gauge rotated into $U(x)\left[D_\mu(x)\,q^{(f)}(x)\right]$, i.e. as the quark field alone $q^{(f)}(x) \to U(x)q^{(f)}(x)$, where color indices are omitted. Using this observation together with unitary of $SU(3)$ elements the covariance of the modified Dirac-like Lagrangian Eq. (1.6) by local gauge transformation is straightforward. Moreover, we may use this shortcut to calculate the transformation of $A^a_\mu(x)$ fields if we impose such rule to covariant object $D_\mu(x)\,q^{(f)}(x)$ and we isolate the terms connected only to the gauge fields. This method is equivalent to the previous one and leads to the following result

$$A^a_\mu(x) \to A^a_\mu(x) + f^{abc}\theta^b(x)A^c_\mu(x) - \frac{1}{g}\partial_\mu\theta^b(x) \tag{1.8}$$

This formula proves that gluons are really in the the adjoint representation of the gauge group and that color rotations mix gluon fields in a non-trivial fashion due to the non-Abelian feature of the theory. Finally, the complete QCD Lagrangian in Minkowski space is constructed adding to $\mathcal{L}_F$ a contribution describing the dynamics of the gluon fields

$$\mathcal{L}_{QCD} = \sum_f \bar{q}^{(f)}_\alpha(x)\left((i\gamma^\mu(D_\mu)_{\alpha\beta} - m_f\,\delta_{\alpha\beta}\right) q^f_\beta(x) - \frac{1}{4}F^a_{\mu\nu}(x)F^{a\,\mu\nu}(x) \qquad (1.9)$$

The object $F^a_{\mu\nu}(x)$ is called the *gluon strength tensor* and it is formally defined through the commutator of the covariant derivatives which we can be expanded into

$$\begin{aligned} T^a\,F^a_{\mu\nu}(x) &= \frac{i}{g}\left[D_\mu(x)\,,\,D_\nu(x)\right] \\ &= T^a\left[\partial_\mu A^a_\nu(x) - \partial_\nu A^a_\mu(x) + g f^{abc} A^b_\mu(x) A^c_\nu(x)\right] \qquad (1.10) \end{aligned}$$

If we substitute Eq. (1.10) into the last term of the QCD Lagrangian Eq.(1.9), the product $F^a_{\mu\nu}F^{a\,,\mu\nu}$ exhibits not only a kinetic part $(\partial_\mu A^a_\nu - \partial_\nu A^a_\mu)^2$, but carries also other two terms which involve the product of respectively three and four gluon fields: the former is proportional to g while the latter to g^2. From a physical point of view these terms describe the self-interaction between gluons which as quarks and anti-quarks carry a net color charge. As we will see, the gluon self-interaction terms are multiplied by the structure constant of $SU(3)$, therefore they arise singularly because the QCD gauge group is non-Abelian. In QED framework we would construct the full Lagrangian by starting with a local $U(1)$ covariant Dirac-like Lagrangian and adding the pure Electro-Magnetic field contribution, represented by the Maxwell tensor $F_{\mu\nu}(x) = \partial_\mu A_\nu(x) - \partial_\nu A_\mu(x)$, whose expression is visible in Eq. (1.10) if we put $f^{abc} = 0$ and replace g with the electric charge e: there would be also no color index and $T^a \rightarrow 1$, as trivial generator of $U(1)$. Then, we will arrive to the well known result that the QED gauge bosons, i.e. photons, do not carry electric charge and cannot self-interact[3]. We still need to determine the transformation rule for the strength field tensor $F^a_{\mu\nu}(x)$. Of course, if we want the whole $\mathcal{L}_{QCD}$ to be gauge invariant under local transformation of $SU(3)$ group, the product $F^a_{\mu\nu}F^{a\,,\mu\nu}$ appearing in Eq. (1.9) has to be gauge invariant. However, this does not automatically translate into a covariant condition for

---

[3] QED contemplates the possibility of light-light scattering, but this process is realized through fermionic boxes rather than direct photon-photon links in Feynman diagrams [7].

$F^a_{\mu\nu}(x)$ singularly [4]. We may apply a generic rotation $U(x)$ on the commutator defining the strength field and use the property of $T^a F^a_{\mu\nu}(x)$ to a tensor under gauge transformations

$$T^a F^a_{\mu\nu}(x) \rightarrow U(x) T^a F^a_{\mu\nu}(x) U^{+}(x) \tag{1.11}$$

or we may use the transformation law for the gauge field $A^a_\mu(x)$ given in Eq. (1.8) and treat each component $F^a_{\mu\nu}(x)$ as a composed object. Then, we obtain

$$F^a_{\mu\nu}(x) \rightarrow F^a_{\mu\nu}(x) + f^{abc}\theta^b(x) F^c_{\mu\nu}(x) \tag{1.12}$$

We have now introduced all the dynamical degrees of freedom for the gauge theory of strong interaction and supplied the corresponding fields with the correct transformation rules. We need just to collect all the relevant parts and write the QCD Lagrangian in its full-glory

$$\begin{aligned} \mathcal{L}_{QCD} &= \sum_f \left[\bar{q}^{(f)} \left(i\gamma^\mu \partial_\mu - m_f \right) q^{(f)} + g\, A^a_\mu \bar{q}^{(f)} \gamma^\mu T^a q^{(f)} \right] + \left(\partial_\mu A^a_\nu - \partial_\nu A^a_\mu \right)^2 \\ &- g\, f^{abc} \left(\partial_\mu A^a_\nu \right) A^{b,\mu} A^{c,\nu} - \frac{g^2}{4} f^{abc} f^{adf} A^b_\mu A^c_\nu A^{d,\mu} A^{f,\nu} \end{aligned} \tag{1.13}$$

where for clarity we have omitted both color and spin indices as well as explicit coordinate dependence of the fields. After the treatment of QCD as a classical $SU(3)$ Yang-Mills theory and the application of the gauge principle to construct the QCD Lagrangian Eq. (1.13), one usually proceeds further with quantization. In standard QFT the problem of setting up a perturbative expansion is addressed either using the LSZ reduction formula or introducing the elegant Feynman path integral formalism [3], which by the way shows up to be more powerful when dealing with gauge theories. Of course, we have to jump over this discussion and go directly to the Feynman rules of perturbative QCD (pQCD). These can be taken from different books [8] [3] [2] and are also listed in the Appendix A of this thesis.

---

[4] The strength tensor will possess this property if the gauge group is abelian, as happens again in QED for the Maxwell tensor.

1.2 Main features of QCD

In the previous section we built up the QCD Lagrangian and revealed the fundamental degrees of freedom in terms of quark and gluon fields, now we want to look at the main properties of QCD, in particular the most important which eventually govern the physics of strong interacting systems, such the Quark-Gluon Plasma on which this thesis is focused. In order to do that we will concentrate on the behavior of the QCD coupling constant, defined as $\alpha_s = g/4\pi$ which we have seen is the only free parameter, together with the quark masses m_f appearing in the QCD Lagrangian Eq. (1.13), and is the same both for quark-gluon and gluon-gluon interaction.

1.2.1 QCD running coupling and Asymptotic Freedom

When setting up perturbative expansion in QFT, quantum corrections already at Next-to-Leading Order present singularities which arise very often due to the divergence of the free momentum in Feynman loops in the large limit and for this reason they are called Ultra-Violet (UV) divergences. The topology of UV divergences is peculiar for each theory depending on the interaction terms of the Lagrangian, as well as their number. If a theory is characterized by a finite number of them, i.e. that UV divergences can hide in all possible Feynman diagrams at higher order but their topology comes from a finite number of diagrams at lower order, then the theory is said to be renormalizable and it can be candidate to become a physical theory. In pertubative QCD (pQCD) UV divergences are nested in the connected Feynman diagrams in which a loop expansion is brought both for the gluon and the quark propagators, as well as in the vertex function defining the physical interaction strength. In Fig.(1.1) we show a schematic list of them without going in the detail of calculation. As we can see from Fig. (1.1) gluon propagator is corrected by quantum fluctuations originated by fermionic loops and this results in a variation of the color charge of the order of α_s. This *screening effect* is equivalent to what happens in QED where the Electro-Magnetic field acting on a test charge is screened by a surrounding charged cloud which originates

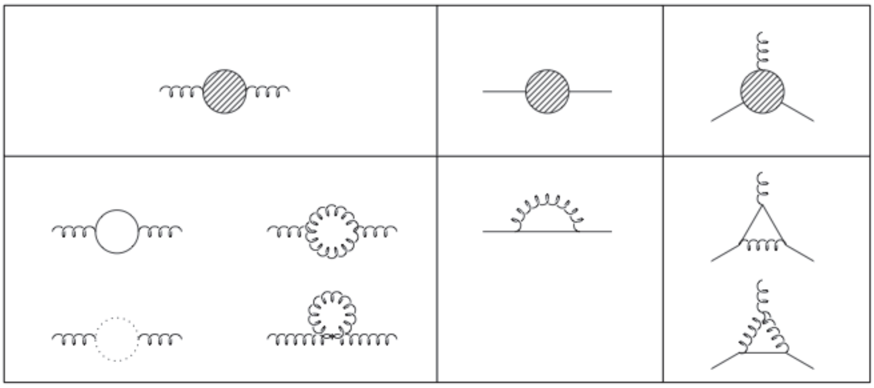

Figure 1.1: Bottom-left: Divergences in the gluon propagator arise from fermionic loop and gluon self interaction: apart from the couplinf constant and color factors the former diagram is equivalent to QED photon self energy, wile the latter belongs exclusively to QCD. Gluonic self interaction should account from the physical states of the gauge bosons, so ghost correction is introduced to reduce gluon loops at the physical ones. Bottom-center: The Divergence of quark propagator results in the fermionic self-energy in the same manner of QED. Bottom-right: Divergences of vertex function. Diagrams with filled blobs on the three upper boxes represent the correspondent full propagators or vertex function after resumming over a series of divergent diagrams.

from the continuous splitting of the photon into virtual fermion-antifermion pairs (*vacuum polarization*). However, in QCD there exists also an opposite *antiscreening effect* which comes out exclusively from the property of gluon to have a color charge and hence be able to self-interact through a three-vertex and four-vertex topology diagrams. In QFT there is a quite standard procedure to treat each divergence which arises order by order in the perturbative expansion. One usually ends up in formal steps where firstly the divergence is mathematically regularized introducing an explicit UV cut off Λ into the loop integral or in a more elegant fashion generalizing the space dimension d of integration[5]. Then, the singularity arising from taking the limit $\Lambda \to \infty$ or taking $d = 4-\epsilon$ and performing the limit $\epsilon \to 0$ is absorbed into bare parameters or perturbative counterterms through a procedure called renormalization

---

[5] In addition to be more elegant, dimensional regularization is useful in QFT gauge theories because it explicit preserves gauge invariance.

in order to get physical parameters which at the end have finite value and do not depend the regularization procedure.

In QCD the coupling constant α_s is modified when considering quantum corrections of the vertex function and also the contributions on the gluon propagator which arise from the multiple insertion of fermionic and gluonic loops. The analysis results into a strength interaction parameter $\alpha_s(Q^2)$ which is not a constant value anymore, rather it is a function of Q^2, which represents the transfer momentum, i.e. the energy scale, of a specific process. A fully pQCD calculation coupled to renormalization procedure leads to the following definition of such *running coupling constant*

$$\alpha_s(Q^2) = \frac{4\pi}{\left(11 - \frac{2}{3}N_f\right)\log\left(\frac{Q^2}{\Lambda^2_{QCD}}\right)} \tag{1.14}$$

We see from Eq. (1.14) that $\alpha_s(Q^2)$ is a monotonically decreasing as function of the Q^2 value. This means that at high energy QCD strength interaction becomes weaker [9], in contrast to what happens for example in QED, and this behavior is known as *asymptotic freedom*. Among the renormalizable quantum field theories in Minkowski space, only Yang-Mills ones, i.e. non-Abelian gauge theories, are asymptotically free and the proof of this statement represents a milestone result achieved in modern QFT [10] [11]. In Fig. (1.2) we present the state-of-the-art for the estimation of the value of α_s as function of transfer momentum Q up to the highest energies achieved in accelerator factories. Points are experimental measurements for particular processes involving QCD corrections [12] [13],while lines represent predictions from pQCD calculations employing Eq. (1.14) or slightly modified behavior of the running coupling. In Fig. (1.2) the world average value of α_s at the pole mass of Z^0 boson $M_Z = 91.18\,GeV$ as reported from Particle Data Group (PDG) [14]. In Eq.(1.14) Λ_{QCD} is the QCD scale parameter. When the transfer momentum or the energy regime of a system $Q^2 \gg \Lambda^2_{QCD}$, then $\alpha_s(Q^2)$ is rapidly decreasing and as a consequence the constituent quarks and gluons fall in an asymptotically free state suffering weakly interacting scattering processes whose calculations can be suitably treated in the framework

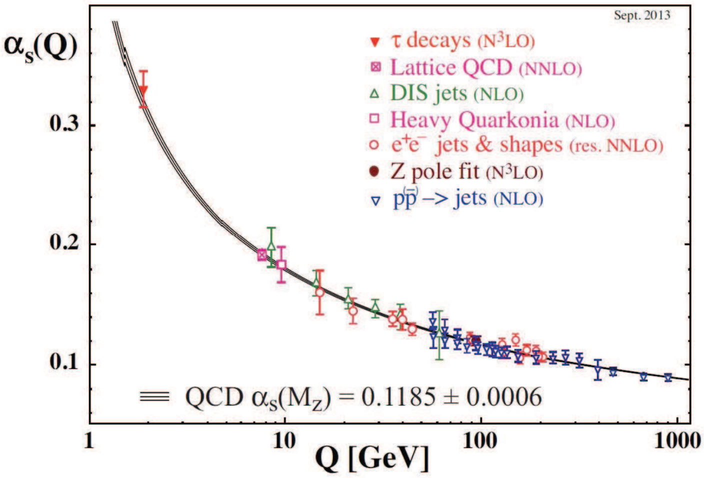

Figure 1.2: The behavior of $\alpha_s(Q^2)$ as function of transfer momentum Q^2 for different kind of experiments. The order of pQCD expansion of α_s for each set of measurements and theoretical predictions is indicated in brackets. The plot is adapted from Refs. [14].

of pQCD. On the contrary, when the energy scale approach the Λ_{QCD} value, then $\alpha_s \approx 1$ and strong interaction gets sufficient weight to lead quarks and gluons to interact in a non-perturbative fashion where of course pQCD breaks up. Theoretical models with quark flavor number $N_f = 3$ estimate a value of $\Lambda_{QCD} \approx 200\,MeV$ and in this regime a solution of the QCD field equations is realizable only in a discretized form, as firstly proposed by Wilson [15] and then become the paradigm of the so-called lattice QCD (lQCD) theories, which are tested by numerous experiments.

1.2.2 Wilson Action and Confinement

In ordinary matter there not exist particles with non-zero color charge, rather quarks and gluons are entrapped to form a wide range of colorless states called hadrons. This peculiar property of QCD is called *confinement*. Due to the fact that hadronic scale $d \sim 1\,fm$ corresponds to an energy of the order of $\Lambda_{QCD} \approx 200\,MeV$, we cannot treat confinement within the same pQCD framework we adopted to describe asymptotic freedom. In a pure gauge theory the non-perturbative nature of QCD vacuum leading to confinement force can be studied by looking at the expectation value of the Wilson loop [15]

$$\langle W(C)\rangle = \left\langle Tr\left[\mathcal{P}\left(e^{ig\oint_C dz_\mu A^\mu(x)}\right)\right]\right\rangle \tag{1.15}$$

In Eq.(1.15) the Wilson loop is defined as the trace of a path-ordered ($\mathcal{P}$) product of gluon links around a closed contour C and essentially measures the response of a gauge field to an external quark-like color source. The contour C can be simplified into a rectangle with time $\mathcal{T}$ and length R dimensions. Then if the time segment $\mathcal{T}$ is much larger than the distance R the Wilson loop is equivalent to the gauge field free energy $F_1(x)$ originating from a static quark-antiquark source and it can be expanded in the following potential form

$$\langle W(C)\rangle \underbrace{\approx}_{\mathcal{T}\gg R} e^{-V(R)\mathcal{T}} \approx \exp\left\{-\left(\frac{a}{R} + \sigma R + b + \ldots\right)\right\} \tag{1.16}$$

In particular, Eq.(1.16) is strictly valid if one considers heavy static color sources $Q\bar{Q}$ (quenched approximation). Moreover, one expects that for a large contour the potential is dominated by its linear term $V(R) \approx \sigma R$ resulting in an area law for the Wilson loop

$$\langle W(C)\rangle \approx e^{-\sigma R\mathcal{T}} \tag{1.17}$$

where $R\mathcal{T}$ is the area inside the rectangular contour C. With a non-zero value of the so called spatial string tension $\sigma \neq 0$ an estimate of the Wilson loop in quenched approximation would predict the existence of a strong-interacting linear confinement. In case of full QCD with N_f light quarks, the pop-up of virtual $q\bar{q}$ pairs breaks the heavy static string $Q\bar{Q} \to Q(\bar{q}q)\bar{Q}$ and the linear confining potential becomes flat. In non-perturbative numerical simulation where QCD equations are solved on a lattice grid [16] [17] one can still define a potential function of the source distance R and calculate

$$V(R) = \lim_{\mathcal{T}\to\infty}\left(\frac{\log\left(W(C(R,\mathcal{T}))\right)}{\mathcal{T}}\right) \tag{1.18}$$

Some results of these simulations are show in Fig.(1.3). On the left plot the free energy of a static (quenched) quark-antiquark pair at large distances approaches a constant value which depends on the temperature T of the surrounding medium, while at smaller distances it acquires a linear trend with some non-zero value of σ. The study of confinement force can be studied also through the analysis of bound states where a heavy quark HQ (charm or bottom)[6] is coupled to its corresponding anti-quark forming what is called a quarkonium state (charmonium or bottomium). In non-relativistic theory the energy spectrum of quarkonia can be treated by solving Schrödinger equation with a Cornell potential given by

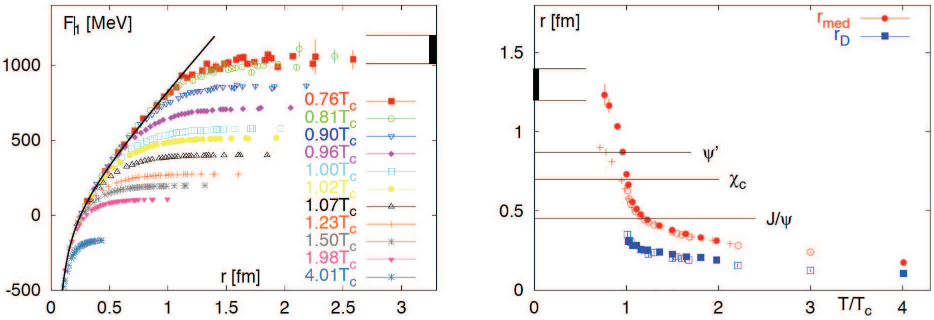

Figure 1.3: (left) The free energy $F_1(r)$ of static quark anti-quark source is calculated in lattice QCD from Refs.[17] and approaches at constant T-dependent value as the distance r between the two sources increases, meaning an interaction with the medium which dissolves the linear confinement. The solid line corresponds to the $T = 0$ case which is equivalent to a Cornell heavy quark potential Eq.(1.19). (right) The vanishing of the spatial string tension and similar deconfinement transition is expected when looking at the melting of charmonium states due to the formation of Debye color screening with decreasing radius r_D as the temperature T/T_c increases.

$$V_{HQ\bar{HQ}}(R) = -\frac{a}{R} + \sigma(R)R \tag{1.19}$$

The second term in Eq.(1.19) represents a linear confinement force and one can study the vanishing of such string tension $\sigma \to 0$ by looking at the melting of the quarkonium state inside a thermal medium with temperature T. This

---

[6] The large mass of top quark avoid the formation of bound states.

happens when the average radius r_{med} of the bound state becomes larger than the radius $r_D = 1/m_D = 1/gT$ of the Debye screening arising from the vacuum excitation of color charges as temperature increases, indicating a transition from hadronic states to free quark states at some critical temperature T_c. This is what is shown on the right plot of Fig.(1.3) for the case of charmonium spectrum.

1.3 Global Symmetries of QCD

We look now for other global symmetries QCD, i.e. other invariant properties of the Lagrangian Eq. (1.9) with respect to transformations whose parameters do not depend on a local space time position x.

1.3.1 Chiral Symmetry in a QCD 2-flavor model

Let us concentrate for a moment on the fermionic part of the QCD Lagrangian that we can read in Eq. (1.6) and consider two quark flavors $N_f = 2$, namely up and down with masses m_u and m_d respectively. We also compose the corresponding fields $u(x)$ and $d(x)$ into a column field ${}^t\boldsymbol{q}(x) = (u(x), d(x))$ which has the property of being an isospin doublet. Then, the Lagrangian $\mathcal{L}_F$ becomes

$$\mathcal{L}_2 = \bar{\boldsymbol{q}}(x)\left[i\gamma^\mu\left(\partial_\mu + igA^a_\mu(x)T^a\right) - M_{u,d}\right]\boldsymbol{q}(x) \tag{1.20}$$

where we ha define the mass matrix $M_{u,d} = diag\,(m_u, m_d)$. We introduce now the chiral projectors $P_L = (1-\gamma^5)/2$ and $P_R = (1+\gamma^5)/2$. If we apply them to the doublet field $\boldsymbol{q}(x)$ we get left-handed and right-handed quark fields which are. components in order to produce left-handed and right-handed quark fields which are eigenstates of the chirality operator γ^5 with eigenvalues -1 and $+1$ respectively

$$\boldsymbol{q_L}(x) = \frac{1}{2}\left(1-\gamma^5\right)\boldsymbol{q}(x) \qquad \boldsymbol{q_R}(x) = \frac{1}{2}\left(1+\gamma^5\right)\boldsymbol{q}(x) \tag{1.21}$$

which are still doublet fields with components $\boldsymbol{q_L}(x) = (u_L(x), d_L(x))$ and $\boldsymbol{q_R}(x) = (u_R(x), d_R(x))$. Then we can write the Lagrangian $\mathcal{L}_2$ in terms of the left-handed and right handed fields

$$\begin{aligned}\mathcal{L}_2 &= \bar{\boldsymbol{q}}_{\boldsymbol{L}}(x)\left[i\gamma^\mu\left(\partial_\mu + igA^a_\mu(x)T^a\right)\right]\boldsymbol{q}_{\boldsymbol{R}}(x) + \bar{\boldsymbol{q}}_{\boldsymbol{R}}(x)\left[i\gamma^\mu\left(\partial_\mu + igA^a_\mu(x)T^a\right)\right]\boldsymbol{q}_{\boldsymbol{R}}(x)\\ &+ \bar{\boldsymbol{q}}_{\boldsymbol{L}}(x)M_{u,d}\boldsymbol{q}_{\boldsymbol{R}}(x) + \bar{\boldsymbol{q}}_{\boldsymbol{R}}(x)M_{u,d}\boldsymbol{q}_{\boldsymbol{L}}(x) \qquad (1.22)\end{aligned}$$

What we observe is that in Eq. (1.22) that left- and right-handed components are mixed only through the mass term of $\mathcal{L}_2$. In the massless limit, i.e. $m_u\,, m_d \to 0$, we know that the free chiral quark eigenstates $\boldsymbol{q}_{\boldsymbol{L}}$, $\boldsymbol{q}_{\boldsymbol{R}}$, correspond also to eigenstates of the helicity operator which is defined as the projection of spin vector to the momentum direction $h = (\hat{\sigma}\cdot\vec{p})/|\vec{p}|$. One can check that q_L corresponds to helicity eigenstate with eigenvalue -1, while q_R is an helicity eigenstate with eigenvalue $+1$. For the corresponding antiquark fields the role of left-handed and right-handed components is inverted such that $\bar{q}_L$ has helicity $+1$, while $\bar{q}_R$ has helicity -1. The absence of the mass term in Eq. (1.22) leads to a Lagrangian which is invariant under the global $U(2)_L \times U(2)_R$ transformation

$$\boldsymbol{q}_{\boldsymbol{L}} \to e^{-i\sigma^j\theta^j_L}\boldsymbol{q}_{\boldsymbol{L}} \qquad \boldsymbol{q}_{\boldsymbol{R}} \to e^{-i\sigma^j\theta^j_R}\boldsymbol{q}_{\boldsymbol{R}} \qquad (1.23)$$

where the rotation angles $\theta^j_{L,R}$ ($j = 0, \ldots, N_f^2 - 1 = 3$) are space-time independent parameters and the matrices σ^j correspond to the generators of the symmetry group. By group composition we know that $U_{L,R}(2) = U_{R,L}(1) \times SU_{R,L}(2)$ and separate the $j = 0$ phase rotation with parameters θ^0_L and θ^0_R with generator $\sigma^0 = I_{2\times2}$, i.e. the identity matrix in the doublet isospin space. At quantum level we can construct the commutation relations between the remaining 3×3 conserved charges which are related to the global invariance with respect to $SU(2)_L \times SU(2)_R$

$$\left[Q^i_L, Q^j_L\right] = i\epsilon^{ijk}Q^k_L \qquad \left[Q^i_R, Q^j_R\right] = i\epsilon^{ijk}Q^k_R \qquad \left[Q^i_L, Q^j_R\right] = 0 \qquad (1.24)$$

We recognize that these conserved charges close two independent algebra of angular momentum group whose generators are the well-known Pauli matrices

$$\sigma^1 = \begin{bmatrix} 0 & 1 \\ 1 & 0 \end{bmatrix} \qquad \sigma^2 = \begin{bmatrix} 0 & -i \\ i & 0 \end{bmatrix} \qquad \sigma^3 = \begin{bmatrix} 1 & 0 \\ - & -1 \end{bmatrix} \tag{1.25}$$

The $U(2)_L \times U(2)_R$ is called *chiral symmetry*. If we look at the transformation properties of the doublet field $\boldsymbol{q}(x)$, we notice that the chiral symmetry includes a vector and an axial-vector transformation

$$U(1)_V \,:\, \boldsymbol{q}(x) \to e^{-i\alpha}\boldsymbol{q}(x) \qquad U(1)_A \,:\, \boldsymbol{q}(x) \to e^{-i\beta\gamma^5}\boldsymbol{q}(x) \tag{1.26}$$

In particular, the $U(1)_V$ transformation is realized when $\theta^0_R = \theta^0_L = \alpha$ and $\theta^j_{R,L} = 0$ ($j = 1, \ldots, N_f^2 - 1$) and it is related to the conservation of the *baryon number* $B = (N_u - N_{\bar{u}} + N_d - N_{\bar{d}})$, while the $U(1)_A$ transformation is the flavor-singlet axial rotation which is realized when $\theta^0_R = -\theta^0_L = \beta$ with $\theta^j_{R,L} = 0$ ($j = 1, \ldots, N_f^2 - 1$). The vectorial and axial nature of $U(1)_V$ and $U(1)_A$ symmetries are visible in behavior with respect to parity transformation of the conserved charges which are related to the currents calculated within the Noether's theorem [1]. Retaining the massive terms in the Lagrangian $\mathcal{L}_2$ we can calculate such currents

$$\begin{aligned} \partial_\mu J^\mu_V &= \partial_\mu \left(\bar{\boldsymbol{q}}(x)\gamma^\mu \boldsymbol{q}(x)\right) = 0 \\ \partial_\mu J^\mu_A &= \partial_\mu \left(\bar{\boldsymbol{q}}(x)\gamma^\mu\gamma^5 \boldsymbol{q}(x)\right) = 2i\boldsymbol{q}(x)M_{u,d}\gamma^5\boldsymbol{q}(x) \end{aligned} \tag{1.27}$$

Therefore, the $U_V(1)$ symmetry is preserved also in the massive case, i.e. baryon number is conserved in strong interacting systems, while the axial $U_A(1)$ is broken by the quark matrix. We mention here that in case of full QCD including also the gluon dynamics, the $U_A(1)$ would be broken also by a term $-(\alpha_s/2\pi)F^{a\mu\nu}\tilde{F}^a_{\mu\nu}$ where $\tilde{F}^a_{\mu\nu} = 1/2\epsilon_{\mu\nu\lambda\tau}F^{a\lambda\tau}$ is the dual field strength tensor. This breaking of $U_A(1)$ symmetry due to quantum effects is known as *axial anomaly*. Finally, the chiral symmetry group includes also the invariance of $\mathcal{L}_2$ with respect to a combined $SU(2)_V \times SU(2)_A$ group. The related Noether's current are respectively proper and axial vector in the flavor space and fulfills the following conditions

$$\begin{aligned} \partial_\mu J_V^{j,\mu} &= \partial_\mu \left(\bar{\boldsymbol{q}}(x)\gamma^\mu \frac{\sigma^j}{2} \boldsymbol{q}(x) \right) = i\bar{\boldsymbol{q}}(x) \left[M_{u,d}, \sigma^j \right] \boldsymbol{q}(x) \\ \partial_\mu J_{j,A}^\mu &= \partial_\mu \left(\bar{\boldsymbol{q}}(x)\gamma^\mu \gamma^5 \frac{\sigma^j}{2} \boldsymbol{q}(x) \right) = i\boldsymbol{q}(x) \left\{ M_{u,d}, \sigma^j \right\} \gamma^5 \boldsymbol{q}(x) \qquad (1.28) \end{aligned}$$

where $[\ldots]$, $\{\ldots\}$ indicate respectively commutator and anti-commutator of mass matrix with Pauli matrices with $j = 1, \ldots, N_f^2 - 1 = 3$. This means that both are exact symmetries in the limit of massless light quarks. More precisely $SU(2)_A$ breaks if m_u or m_d are different from zero, while $SU(2)_V$ endures even if m_u and m_d have non-zero but identical value. This is corresponds to an *isospin symmetry* of strong interaction in case $N_f = 2$, which is very slightly broken because $m_u \approx m_d$.

1.3.2 Dynamical chiral symmetry breaking and restoration

The inclusion a finite mass part in the Lagrangian $\mathcal{L}_2$ directly adds a term where the chirality eigenstates q_L and q_R are coupled in order to preserve parity invariance. Due to the fact that light quark masses are small, one expects that at ground state QCD realizes chiral symmetry with good approximation. However experimental observation on pion spectra showed a strong deviation from a chiral symmetric ground state. A solution of this problem was posed by Nambu and Jona-Lasinio who proved that a classical QCD Lagrangian like $\mathcal{L}_2$ with the chiral invariance property can lead to an effective theory of nucleons and mesons at non-zero density value of pion mass already at its vacuum state [18] [19]. In their famous NJL model with two flavor (u, d) and isospin symmetry $m_u = m_d = m$ the Lagrangian is

$$\mathcal{L}_{NJL} = \bar{\boldsymbol{q}} \left(-i] \gamma^\mu \partial_\mu + m I_{2\times 2} \right) \boldsymbol{q} - \frac{G_{NJL}^2}{2\Lambda_{NJL}^2} \left[(\bar{\boldsymbol{q}}\boldsymbol{q})^2 + \left(i\bar{\boldsymbol{q}}\vec{\sigma}\gamma^5 \boldsymbol{q} \right)^2 \right] \qquad (1.29)$$

with no gluon fields included and two couplings: the dimensionless G_{NJL} giving the intensity of attraction of the scalar quark anti-quark pair $\bar{\boldsymbol{q}}\boldsymbol{q}$ and the pseudo-scalar channel $i\bar{\boldsymbol{q}}\vec{\sigma}\gamma^5\boldsymbol{q}$ and the characteristic Λ_{NJL} which has dimension of inverse length and measure the deviation of $\bar{\boldsymbol{q}}\boldsymbol{q}$ interaction from being point-like. The Lagrangian in Eq.(1.29) has global $U_V(1) \times SU_L(2) \times SU_R(2)$ symmetry but breaks $U_A(1)$ for manifestly maintaining QCD axial anomaly. The mark for chiral symmetry restoration is a vanishing value for the scalar quark condensate defined as $\langle \bar{\boldsymbol{q}}\boldsymbol{q} \rangle$ which is realized in the limit $G_{NJL} \to 0$. Such mechanism can occur already at zero temperature and quark mass in the form of *Spontaneous Symmetry Breaking* (SSB). The consequence of a spontaneous breaking of a continuous symmetry is that new massless modes show up. The most important property of these modes, named as *Goldstone bosons*, is that they do not acquire a mass whatever the order of perturbative expansion. In case of chiral symmetry these Goldstone bosons were predicted to be the pions. Then pions can have a finite mass because chiral symmetry is just an approximate symmetry for QCD. The NJL model can be formulated within a low-energy effective field theory regarding G_{NJL} as a fixed parameter and obtaining a gap equation

$$\frac{G_c^2}{G_{NJL}^2} \simeq 1 - \frac{1}{2} (G\sigma)^2 \log\left(\frac{4}{(G\sigma)^2 e}\right) \tag{1.30}$$

where $G_c = \pi \sqrt{8/6}$ is the value of G_{NJL} at critical point and σ is an order parameter related to chiral condensate $\langle \bar{\boldsymbol{q}}\boldsymbol{q} \rangle$. The gap equation has solution

$$\bar{\sigma} \propto \sqrt{\frac{G_{NJL}^2 - G_c^2}{-\log\left(G_{NJL}^2 - G_c^2\right)}} \tag{1.31}$$

when G_{NJL} approaches G_c from below. Due the non-zero value of the chiral condensate $\langle \bar{\boldsymbol{q}}\boldsymbol{q} \rangle$ instead, quark masses acquire an extra effective mass of about $m \approx 300\, MeV$ which is called *constituent* or *dynamical* QCD mass connected to a non-zero value of the quark scalar density $\langle \bar{\boldsymbol{q}}\boldsymbol{q} \rangle$ at ground state. [20] In the chiral limit $m = 0$, a second order phase transition occurs at critical point and one obtains in particular

$$M_{u,d} = G_{NJL}\bar{\sigma} \qquad \left\langle \bar{u}u + \bar{d}d \right\rangle = -\frac{\Lambda_{NJL}^2}{G_{NJL}}\bar{\sigma} \tag{1.32}$$

In case $m \neq 0$ the second order transition is washed out and one obtains a smooth crossover. The behavior of the transition for various initial quark mass parameter m_q is presented in Fig.(1.4) where it is clearly visible the restoration of the chiral limit through the vanishing of the dynamical quark mass in the situation where $G < G_c$. In conclusion, chiral symmetry is exact only for

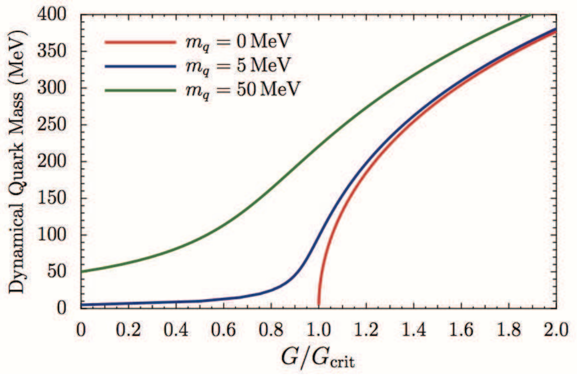

Figure 1.4: Dynamical light quark mass generation in the NJL model in chiral limit $m_q =$ or in non-zero light quark mass $m_q \neq 0$ (Ref. [21]).

the case of zero quark masses. Hence, one should find some evidence of an approximate chiral symmetry breaking and generation of dynamical masses only in the light quark sector (u, d and eventually s). On the other hand, such effect should not characterize the QCD feature at the level of heavy quarks (c, b, t) sector. In that case the generation of heavy quark masses should be considered only within the Higgs mechanism for spontaneous breaking of electroweak symmetry. This is summarized in Fig.(1.5) where total mass of all quark flavors included in the Standard Model is analyzed in terms of generation from Higgs field fluctuations and QCD vacuum dynamical symmetry breaking.

1.4 The QCD phase diagram

In the previous sections we discussed about confinement and asymptotic freedom as fundamental properties of QCD that should govern the evolution of any strong interacting system as function of energy scale. In particular,

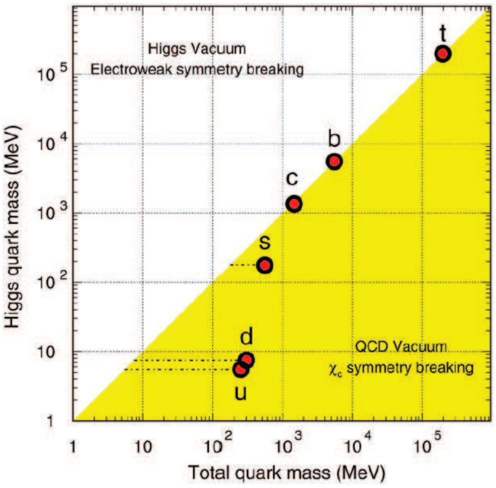

Figure 1.5: Quark mass generation: mass values of u, d and slightly s quarks fall in the domain of spontaneous chiral symmetry breaking, while all heavy quark masses seem to arise totally from Higgs mechanism. Picture is adapted from PDG 2004 Ref. [22]

we focused on the fact that at high energies, i.e. small distances, quarks and gluons enter in asymptotically free regime suffering weak interaction which can be described within a perturbative framework.On the other hand, non-perturbative approach based on the solution of QCD equations of static color sources on a space-time grid predict that the string tension of the linear confining potential vanishes when the source distance approaches to zero, or in the same way as density increases. These results lead to the idea that strong interacting QCD matter in condition of high temperature or density suffers a phase transition in which quarks and gluons are released from the bounding hadrons and become the real degrees of freedom of a new state matter. More specifically Lattice QCD (lQCD) calculations at zero baryon chemical potential $\mu_B = 0$ showed up that this phase transition is rather a *crossover* occurring at critical temperature $T_c \approx 155 - 175\, MeV$ where thermodynamic functions smoothly grow from the expected value of a pion gas to that of a gas composed of quarks and gluons [23]. Instead, the region of finite chemical potential μ_B was explored through phenomenological models, QCD-like effective field theories and later within lQCD simulations at finite density showing that actually strong interacting matter is characterized by a complex

QCD phase diagram which is sketched in Fig (1.6).

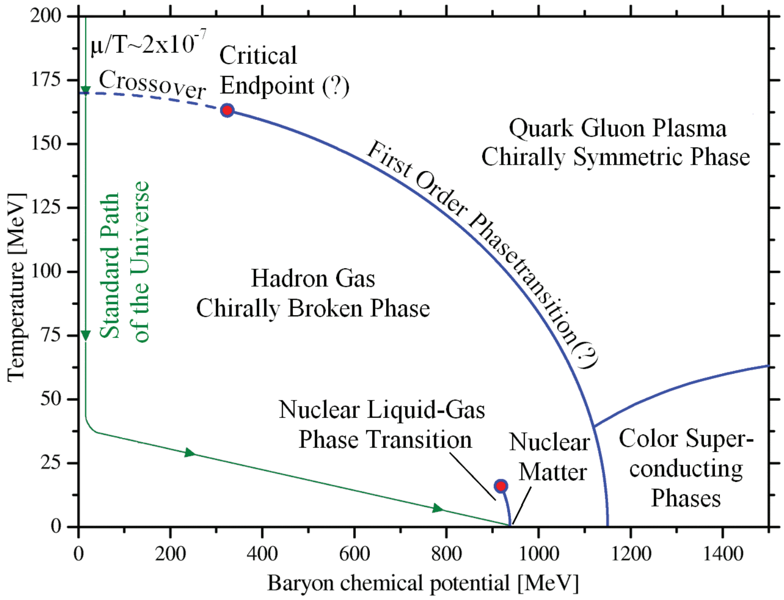

Figure 1.6: The QCD phase diagram from Ref .[24]. The baryon chemical potential μ_B or equivalently the nuclear matter density ρ (eventually normalized to the density of ordinary nuclei $\rho_0 = 0.16\, fm^{-3}$) is on the horizontal axis, while the temperature T of the strong interacting system at equilibrium is on the verical axis. The arrowed line represents the Standard Path of Universe Evolution ias reported in Ref. [25].

We summarize here the main structure of the QCD phase diagram:

I) The *nuclear liquid-gas* phase transition is represented by the short visible blue line emerging from the abscissa point $\mu_B \approx 920\, MeV$ ($T = 0$), which represents a nucleus at ground state, and ending up at a critical point located at $T \approx 7.5\, MeV$.

II) When temperature increase so far, many baryon and meson resonances are excited and the system falls in a state known as *Hadron Resonance Gas* (HRG) characterized by broken chiral symmetry.

III) For much higher temperatures deconfinement transition occurs and matter goes to so called the *Quark-Gluon Plasma* (QGP) phase where one expects also chiral symmetry to be restored.

IV) The green arrowed line starting from the upper left part of the diagram $T > 200\,MeV$, $\mu \approx 0$ and ending up in the ordinary nuclear matter point indicates the evolution of the Universe according to the Standard Cosmological Model. In this paradigm it is believed that a baryon-poor QGP filled up the hot primordial Universe about $12-20\,\mu s$ after the Big Bang. During its expansion the Universe cooled down passing through the HRG state and at ending up into the ordinary nuclear matter with roughly $T \approx 0$.

V) The crossover transition separating the HRG state from the QGP is represented with the blue dashed line. This is region of the phase diagram with high temperature and vanishing baryon chemical potential explored very well within lQCD framework. Recent lattice QCD calculations [26][27] supported by other effective QCD models allowed to fix a new value of critical temperature $T_c \approx 155\,MeV$ at $\mu_B = 0$ and could be also extended for the search of the *Critical End-Point* (CEP) which is expected to locate at moderate T an non-zero μ_B. Subsequently to the CEP ithe crossover changes eventually into a first order phase transition, which is represented by the solid blue line.

VI) Theoretical calculations based on QCD effective models predict that another phase transition should occur for cold but extremely dense nuclear matter. The main features of this phase transition are similar in some sense to the behavior of superconductors, leading to the so-called *Color Superconducting Phase*. The system should locate in a kind of color superconductor state which is separated from the QGP state by another first order phase transition. Experimentally it is very difficult, and currently not feasible, to probe this region because even at low energy collisions nuclear matter is compressed and heated. A chance to understand this region of phase diagram is by studying cosmological objects of the Universe, such as the compact neutron (or quark) stars and supernovae remnants.

CHAPTER 2

QUARK-GLUON PLASMA AND HEAVY QUARKS IN RELATIVISTIC HEAVY-ION COLLISIONS

Relativistic and Ultra-Relativistic Heavy-Ion Collisions (HICs) have been designed to run in the most powerful accelerators with the aim to study the properties of Quark-Gluon Plasma (QGP) and in general the strongly interacting nuclear matter under extreme hot and dense conditions. The area under experimental investigation is spread along the phase transition line from almost zero baryon density μ_B to values close to that of ordinary nuclear matter. This allows to cover a large portion of the QCD phase diagram as shown on the pictorial representation in Fig. (2.1). Inversely to what happened in Universe history, the evolution line of QCD matter in HICs starts from the point corresponding to the ordinary nuclear matter to suddenly jump just above the transition line. However, such phase of matter created at the initial stage HICs has not reached the equilibrium condition yet and thus it does not appear on the diagram. At later time the produced systems shows up at some position which depends on the total center-of-mass energy indicated by the invariant Mandelstam variable $\sqrt{s}$. In nucleus-nucleus collisions rather the total energy $\sqrt{s}$, the center-of-mass energy per nucleon (pair) $\sqrt{s_{NN}}$ is commonly used. By means of some phenomenological conjectures, the initial tempera-

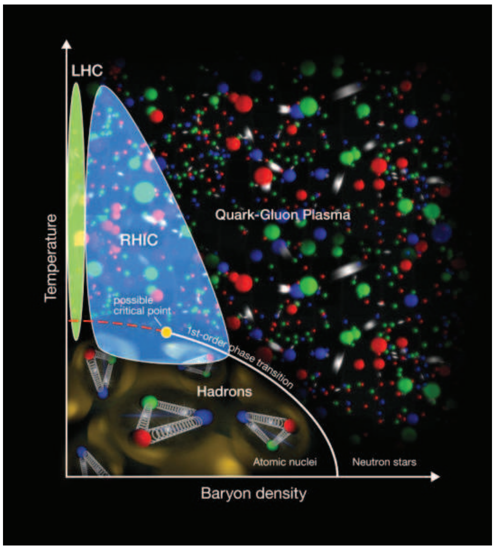

Figure 2.1: QCD phase diagram: Courtesy from Brookhaven National Laboratory.

ture T_0 of the thermalized fireball created in the central region of the collision can be related to $\sqrt{s_{NN}}$. Of course, the larger the collision energy the higher the value of T_0, while usually the baryon density μ_B decreases with $\sqrt{s_{NN}}$ due to the saturation of the nuclear stopping power. After that the QGP medium goes through a rapid evolution characterized by hydrodynamic expansion and cooling down to finally ends up when quarks and gluons merge back into the confined phase through a mechanism called *hadronization* happening at $T \approx T_c$. In the first part of this chapter we will present a brief description of these stages and discuss about a theoretically treatment of the QCD matter evolution in relationship with main QGP observables. In the second part instead we will introduce Heavy Quarks (HQs) produced in HICs focusing on some essential properties that makes them unique probes to investigate the QGP features. In Fig. (2.2) we quote a sketch of the time evolution of the QCD matter created in HICs correlated with a survey of the most important probes of the QGP, among which we include HQs.

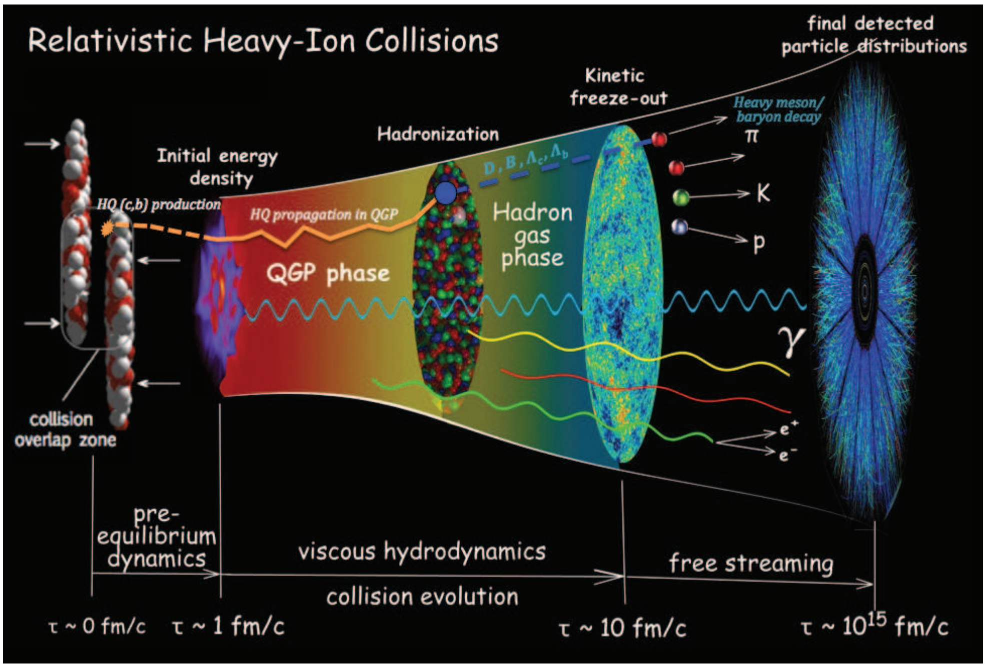

Figure 2.2: Evolution of QCD matter in HICs: adapted from Chu Shen sketch https://u.osu.edu/vishnu/author/shen-201-2/. In evidence, production of heavy quarks (charm and bottom) at initial stage of HICs: from propagation through the QGP to hadronization into heavy mesons and baryons.

2.1 Nucleus-Nucleus collisions from first experiments to RHIC and LHC program

Experiments on Heavy-Ion Collisions (HICs) started in Lawrence Berkeley National Laboratory (LBNL) at beginning of 70s with the construction of Bevatron-Bevalac, best known for the discovery of the anti-proton by E. Segre and O. Chamberlain in 1955, but where also nitrogen and uranium beams were accelerated for the first time at energies of about $1\,GeV$ per nucleon. A decade later the HICs program began also at Brookhaven National Laboratory (BNL) and at the European Organization for Nuclear Research (CERN). In 1986 the Alternating Gradient Synchrotron (AGS) at BNL and the Super Proton Synchrotron (SPS) at CERN could accelerate respectively ^{28}Si ions at $\sqrt{s_{NN}} = 14\,GeV$ per nucleon and ^{16}O at energies among $60 - 200\,AGeV$. With the energy density reached in the central collisions at AGS and SPS it was possible to observe shock waves propagating in compressed baryonic matter and study the nuclear Equation of State (EoS). However, such conditions could only slightly scratch the phase transition region, indicating that more powerful accelerating facilities were necessary in order to evidence the formation of a QGP phase along a sufficient time interval. In 1995 at the upgraded SPS ^{208}Pb ion beams started to run in circle with energy from $158\,AGeV$ to $200\,AGeV$, marking officially the beginning of ultra-Relativistic Heavy-Ion Collisions (uRHICs) era. On February 10 of 2000 the combined analysis of seven experiments at CERN SPS lead to the announcement of the observation of a created new state of matter [28] whose characteristics were consistent with the predicted QGP.

Still in 2000 experimental data were firstly collected at BNL Relativistic Heavy Ion Collider (RHIC) and measurements are conducted even today. In this facility fully stripped ^{198}Au ions are accelerated into two colliding tubes each one at beam energy of $E_b = 100\,AGeV$, resulting in total center-of mass energy of $\sqrt{s_{NN}} = 2E_b = 200\,GeV$ per nucleon. The evidence of the created QGP phase at uHICs was confirmed by RHIC experiments and the possibility to for a quantitative study of its properties was achieved through the analysis of new observables. Initially there were four experiments built-up at RHIC:

1) BRAHMS detector extended over a broad range of rapidity in order to identify particles, among which produced exited nuclei, during nuclear reactions at relativistic energies.

2) PHOBOS apparatus devoted to estimate initial quantities of the formed fireball, such as the temperature, size, and density, by measuring multiplicity, ratios and correlations among the various produced particles.

3) PHENIX the largest of the four experiments designed to investigate the properties of the QGP through ma measure of direct probes such as electrons, muons and photons.

4) STAR detector covers a large solid angle to measure the production of particular hadron species and to extract information about the transport

coefficients (viscosity) and chiral effects in the QGP through analysis of collective motions and correlations.

While PHOBOS and BRAHMS finished the data-taking respectively in 2005 and in 2006, PHENIX and STAR are still operating with renew setup. In particular, PHENIX is currently going through an upgrade process for becoming the sPHENIX detector devoted to explore the physics of the QGP at the Critical End Point (CEP) as main goal of the RHIC Beam Energy Scan program. STAR instead has been recently provided with a new tracking system constituted by a Time Projection Chamber (TPC) and a Vertex detector for measuring the major observables in the Heavy Quark sector with more efficiency.

In 2010 the era of Large Hadron Collider (LHC) began officially with first proton beams accelerated at $500\,GeV$ and soon pushed at highest energy scale ($7-14\,TeV$) ever achieved in an accelerating facility. LHC community joined quite immediately the HIC program with a run of lead ions accelerated at $5.5\,TeV$. This run took almost a month starting on 8 November 2010 and ending on 6 December 2010. A sufficiently amount of luminosity that brought the ALICE experiment to observe the behavior of nuclear matter under extreme conditions, similarly to what happened in the entire Universe at about $10-20\,\mu s$ after the Big Bang (see Fig. (2.1)). At this energies indeed the QGP is formed at very high temperature and with almost zero baryon chemical potential, a configuration of matter that has been predicted to exist in the primordial Universe. There are four main experiments built-up around the $27\,km$ forming the ring of superconducting beamline at LHC. The largest community of physicists joined the ATLAS and CMS collaborations whose scientific program is mainly focused on researches within the Standard Model of Particle Physics. ATLAS and CMS achieved the milestone result of observing Higgs boson with mass of about $126\,GeV$ [29] [30] and announced it in a jointly speech on 4 July 2012. The ALICE experiment instead is devoted essentially to the physics of Heavy-Ions and since 2010 collects data on $Pb-Pb$ collisions at $2.76\,TeV$ and since 2016 also on $Pb-Pb$ and $p-Pb$ at $5.02\,TeV$ for studying the properties of the QGP and evidence on its eventual creation in high energy small nuclear systems, such as $p-A$ collisions.

ALICE is a complex system of detectors, among which the inner tracker and the TPC are devoted to identify Heavy-Flavor hadron yields and collective flows. From this point of view, ATLAS and CMS have recently join the HICs program, the former focusing on jet physics while the latter measuring charm and beauty mesons at very high p_T. The last of the four large experiments is the LHCb collaboration where production of antimatter as well as study of CP symmetry violation in the beauty sector ($B^0\bar{B}^0$ meson mixing and $b\bar{b}$ cross section measure) are conducted. In conclusion we mention that at LHC the TOTEM (total cross section, elastic scattering and diffraction dissociation), MoEDAL (monopole and exotic particle) and LHCf (measurement of neutral π^0 meson production in order to understand ultra high energy cosmic rays) are currently taking data.

2.2 Models for initial states of HICs

2.2.1 The Glauber Model

The Glauber model is based on a semi-classical approach in which nucleus-nucleus collisions are treated as a superposition of multiple independent nucleon-nucleon interactions. In this model one adopts also the so-called eikonal approximation for which the nucleons are assumed to travel along straight lines and do not suffer deflection after the collisions. Such approximation holds quite effectively at very high energies. We provide a brief description of the Glauber model referring in particular to Ref. [31]. The collision between the projectile nucleus B with the target nucleus A is illustrated in Fig. (2.3) where in the standard description the beamline is along the z direction and the impact parameter $\vec{b}$ is directed along the x axis. The density of nucleons inside the target nucleus A is usually parametrized by a Woods-Saxon expression

$$\rho_A(r_p) = \frac{\rho_0}{1 + exp\left(\frac{r_p - R_A}{a}\right)} \quad , \quad \int d^3\vec{r}_p \rho_A(r_p) = A \tag{2.1}$$

where r_p is the position of the nucleon, R_A is the radius of the nucleus A, in particular $R_A = r_0 A^{1/3}$ given the atomic number A and the constant value

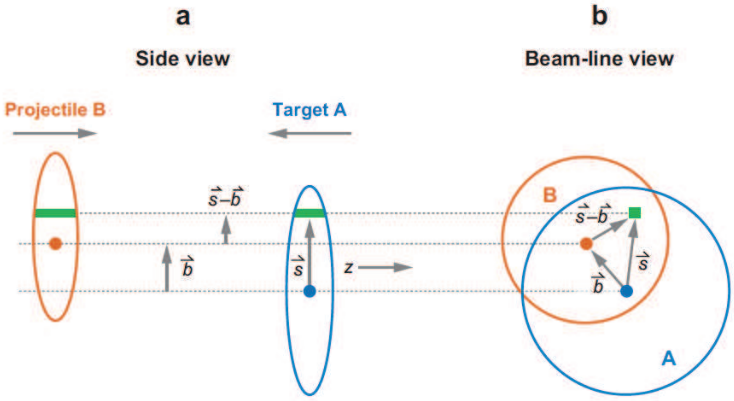

Figure 2.3: Illustration of high-energy nucleus-nucleus collision between projectile B and target A at given impact parameter $\vec{b}$: (a) transverse side view, (b) longitudinal beam view [31].

$r_0 \approx 1.2fm$, $\rho_0 \approx 0.16fm^{-3}$ is the density of nuclear matter at equilibirum and a is the surface thickness parameter. Similarly for the projectile nucleus B a Wood-Saxon density ρ_B is defined and finally both ρ_A and ρ_B are properly normalized to the total number of nucleons inside the corresponding nuclei, as explicitly shown in the second expression in Eq. (2.1) for nucleus A. At RHIC and LHC facilities symmetric collisions between gold Au and lead Pb nuclei are performed, meaning that in this framework one assumes the nuclei A and B to be the same. For Au nucleus we have $A = 197$, hence $R_{Au} = 6.38\,fm$ with parameter $a = 0.535\,fm$ while for Pb nucleus we have $A = 208$, so one gets $R_{Pb} = 6.68\,fm$ and value of $a = 0.546\,fm$. A collection Wood-Saxon parameters for various nuclei species is reported in Ref. [32]. The nuclear matter thickness function for nucleus A is defined through the projection of the density of nucleons ρ_A along the beam axis z

$$T_A(\vec{s}) = \int dz_A \, \rho_A \, (\vec{s}, z_A) \tag{2.2}$$

Then the overlap function [33] for collisions between nucleus A and nucleus B at given impact parameter $\vec{b}$ is constructed by folding T_A with the corre-

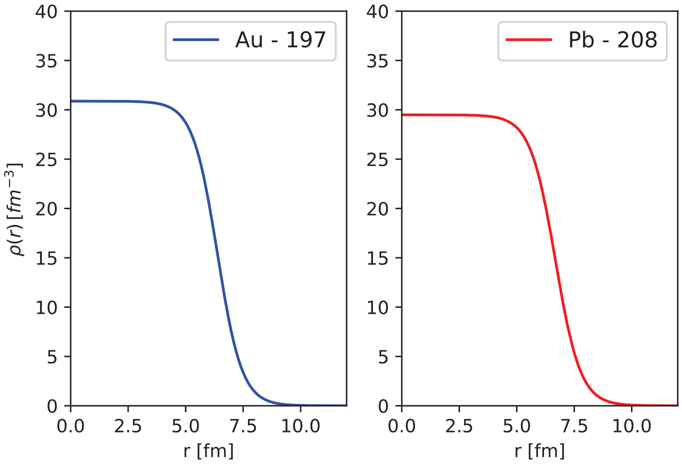

Figure 2.4: Wood-Saxon profile of density distribution of nucleons for $Au-197$ (left) and $Pb-208$ (right) nuclei. The parameter values are taken from Ref. [32]

sponding thickness function T_B for the nucleus B in the following manner

$$T_{AB}(\vec{b}) = \int d^2\vec{s}\,T_A(\vec{s})T_B(\vec{s}-\vec{b}) \tag{2.3}$$

in Eq. (2.3) the convolution with respect to the $\vec{s}$ variable is performed according to the sketch in Fig. (2.3) and also the following normalization condition is considered

$$\int d^2\vec{b}\,T_{AB}(\vec{b}) = AB \tag{2.4}$$

The overlap function T_{AB} is given in unit of an inverse area and can be interpreted as the effective overlap area for which a certain nucleon of the projectile B can interact with a nucleon of target A assuming that distance between the center of nuclei in transverse plane is equivalent to $\vec{b}$. Then it is possible to define the probability of having one single nucleon-nucleon interaction within an $A+B$ collision at impact parameter $\vec{b}$ as

$$p_{AB}(\vec{b}) = \sigma_{NN}^{in}\frac{T_{AB}(\vec{b})}{AB} \quad , \quad \int d^2\vec{b}\,p_{AB}(\vec{b}) = \sigma_{NN}^{in} \tag{2.5}$$

Assuming that binary nucleon-nucleon collisions are independent with each other, i.e. one nucleon from A after a collision with one nucleon of B maintains the same cross section σ^{in}_{NN} when it collides eventually with another nucleon inside B, then the probability that n inelastic nucleon-nucleon collisions within the $A + B$ reaction at impact parameter $\vec{b}$ occurs, follows a bynomial distribution

$$\begin{aligned} P(n|A, B, \vec{b}) &= \binom{AB}{n} p_{AB}(\vec{b})^n \left(1 - p_{AB}(\vec{b})\right)^{AB-n} \\ &= \frac{AB!}{(AB-n)!} \left(\sigma^{in}_{NN} \frac{T_{AB}(\vec{b})}{AB}\right)^n \left(1 - \sigma^{in}_{NN} \frac{T_{AB}(\vec{b})}{AB}\right)^{AB-n} \qquad (2.6) \end{aligned}$$

where in the second line we substituted the explicit formula for $p_{AB}(\vec{b})$ Eq. (2.5). In high energy HICs the inelastic nucleon-nucleon cross section σ^{in}_{NN} is identified with the inelastic cross section in proton-proton collisions σ^{in}_{pp}. A large amount of experimental data from the total proton-proton cross section in a wide range of center-of-mass energy is collected in the PDG database from which it is possible to extract the inelastic contribution. In particular, at the energies of RHIC ($\sqrt{s} = 200\,GeV$) and LHC ($\sqrt{s} = 7\,TeV$) proton-proton collisions the value σ^{in}_{pp} is equivalent respectively to about $40\,mb$ and $70\,mb$. Having a probability expression we can calculate the average number of binary nucleon-nucleon collisions $< n >$ and the variance δn^2 with respect to it, because they correspond respectively to the first and second momenta of the binomial distribution in Eq. (2.6). Hence, we obtain for the mean value

$$< n(A, B, \vec{b}) >= \sum_{n=0}^{AB} nP(n|A, B, \vec{b}) = \sigma^{in}_{NN} T_{AB}(\vec{b}) \qquad (2.7)$$

while for the variance we get

$$\delta n^2 =< n^2 > - < n >^2= \sigma^{in}_{NN} T_{AB}(\vec{b}) \left(1 - \frac{\sigma^{in}_{NN} T_{AB}(\vec{b})}{AB}\right) \qquad (2.8)$$

We also observe that, in the limit of large nuclei $AB \gg n$, binary nucleon-nucleon collisions become rare events and the bynomial distribution Eq. (2.5) can be approximated by a Poisson distribution which has single parameter corresponding precisely to the mean value Eq. (2.7)

$$P(n|A,B,\vec{b}) \approx \frac{< n(A,B,\vec{b}) >^n}{n!} e^{-<n(A,B,\vec{b})>} \tag{2.9}$$

The sum of the probability of inelastic nucleon-nucleon collisions over all possible outcomes (assuming at least one binary nucleon-nucleon collision $n = 1$ to occur within the $A + B$ reaction) results in a total probability for inelastic nucleus-nucleus collision whose integral in turn is normalized to the total inelastic cross section

$$\begin{aligned} P^{in}_{tot}(A,B,\vec{b}) &= 1 - \left(1 - \frac{\sigma^{in}_{NN} T_{AB}(\vec{b})}{AB}\right)^{AB} \approx 1 - e^{-\sigma^{in}_{NN} T_{AB}(\vec{b})} \\ \sigma^{in}_{AB} &= \int d^2\vec{b} P^{in}_{tot}(A,B,\vec{b}) \end{aligned} \tag{2.10}$$

where the approximated expression for P^{in}_{tot} is valid in the Poisson condition. Among the value of σ^{in}_{AB}, the Glauber model provides more importantly the estimates of the $N_{coll}(\vec{b})$ and $N_{part}(\vec{b})$ [33] [34]. The former is the mean number of binary nucleon-nucleon collisions, each one occurring with probability distribution $P(n|A,B,\vec{b})$, so we can immediately identify it with the first momentum of the probability distribution P^{in}_{tot}, i.e. the mean value $< n(A,B,\vec{b}) >$

$$N_{coll}(\vec{b}) =< n(A,B,\vec{b}) >= \int d^2\vec{s} \sigma^{in}_{NN} T_A(\vec{s}) T_B(\vec{s} - \vec{b}) \tag{2.11}$$

where in Eq. (2.11) we used the expressions for the overlap function in terms of the thickness functions Eq.(2.3). The latter represents the total number of nucleons which participate into the nucleus-nucleus collision and it is easy to prove taht in the Glauber Model this value can be written as

$$\begin{aligned} N_{part}(\vec{b}) = &\int d^2\vec{s}\,T_A(\vec{s})\left(1 - e^{-T_B(\vec{s})\sigma_{NN}^{in}}\right) \\ &+ \int d^2\vec{s}\,T_B(\vec{s}-\vec{b})\left(1 - e^{1-T_A(\vec{s})\sigma_{NN}^{in}}\right) \end{aligned} \tag{2.12}$$

We observe from Eq. (2.11) and (2.12) how such estimates scale correctly with the mass number of both nuclei, due to the geometrical nature of the Glauber model. The outputs of the Glauber model represented by N_{coll} and N_{part} are not measurable quantities, but their monotonic behavior as function of the impact parameter $\vec{b}$ can be used to trace back its value from the dependence of some experimental observables. In particular, the inclusive charged particle multiplicity N_{ch} strongly depends on the value of b: the smaller its value, more central is the collision between the nuclei resulting in a larger production of charged particles, i.e. higher N_{ch}. Then, it is possible to perform a subdivision of N_{ch} in terms of so-called *centrality classes* as depicted in Fig. (2.5) and map its measured value by means of the phenomenological distributions $N_{coll}(b)$ and $N_{part}(b)$ of the Glauber model. In conclusion, we mention that by means of the Glauber model it is possible to sample an initial distribution of particles inside the overlap region by calculating the integration kernel of Eq. (2.3) and not performing the integration which results in the discussed T_{AB} function. Then, applying Eq. (2.11) and Eq. (2.12) we can obtain the initial density profile of *hard* and *soft* partons which follow respectively the distributions of binary collisions and whole participant nucleons in the transverse plane and from which we can estimate the initial energy density (temperature) profile of the thermalized system (Chapter 4).

2.2.2 The Monte-Carlo Glauber Model

The geometrical approach for initial state of HICs introduced firstly by Glauber [35] and developed in Ref. [31] is also known as optical or standard Glauber model, because as we have seen in the previous paragraph the construction of the thickness function and resulting binary collisions and par-

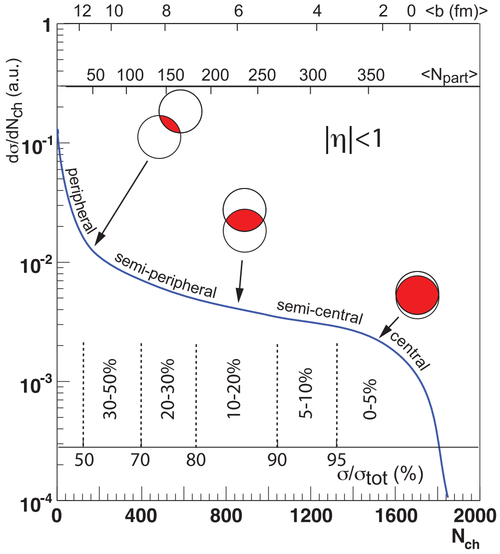

Figure 2.5: Centrality classes related to the average number of participant nucleons $< N_{part} >$ which is calculated from Glauber model Eq. (2.12). The experimental differential pseudo-rapidity distribution $d\sigma_{ch}/d\eta \sim \sigma_{in}^{pp} dN_{ch}/d\eta$ is shown as function measured of total number of charged particle N_{ch} at midrapidity $|\eta| < 1$. Plot is taken from Ref. [31].

ticipant nucleons is based on a derivation from a continuous density profile of the nucleons inside the nuclei. We remind also in this approach nucleons are assumed to move undeflected after collisions (eikonal limit), which is a valid approximation until the overlapping region is larger than the range of nuclear force. Hence, in the optical limit there is no need to provide a specific localization for each nucleon to get the estimates of N_{coll} and N_{part} as function of the impact parameter b. Moreover, the motion of nucleons is treated independently from the nucleus state and this is reflected in the fact that the overall nucleus-nucleus cross section σ_{AB}^{in} directly depends on the probability of a single nucleon-nucleon interaction as we can infer from Eq. (2.10).

Monte-Carlo calculations of the Glauber model, shortly named as MC Glauber, can be carried out through a stochastical sample of the nucleons inside overlapping region provided some specific functions for the density of nucleons inside the target and projectile nucleons are defined. Usually $\rho_A(r)$ and $\rho_B(r)$ follow gaussian or more widely a Wood-Saxon shape as we have seen in Eq.(2.1). In this case a proper normalization constant should be chosen in order to define the correct probability density distributions for the radial coordinate r. The azimuthal and polar angles of the nucleons instead can be extracted uniformly. Given the spatial coordinates for the nucleons in the overlap region, one can calculate the separation distance $\vec{s}$ for each pair nucleons, one belonging to the projectile nucleus B and the other to the target one A. and make a stochastic comparison with the inelastic cross section $\sqrt{\sigma_{NN}^{in}}$: a collision between the nucleons of the pair occurs for a given impact parameter $\vec{b}$ if their distance satisfy the condition $|\vec{s}| < \sqrt{\sigma_{NN}^{in}/\pi}$. Within the stochastic algorithm nucleons are assumed to move along straight lines and suffer no deviation from previous collisions (eikonal approaximation). Finally, this MC Glauber procedure is repeated iteratively by simulating many $A+B$ reactions and the knowledge of density profile in the overlapping region allows the calculate the average number of binary nucleon-nucleon collisions $< N_{coll} >$ and the average number of participants $< N_{part} >$ as function of the randomly given impact parameter $\vec{b}$. Consequently in a single Monte-Carlo event thickness functions of nuclei are not anymore smooth distributions, but rather they can be written as a sum of various random deltas

$$\hat{T}_A(\vec{s}) = \sum_{i=1}^{A} \delta^2\left(\vec{s} - \vec{r}_{\perp,i}^{A}\right) \quad , \quad \hat{T}_B(\vec{s}') = \sum_{i=1}^{B} \delta^2\left(\vec{s}' - \vec{r}_{\perp,i}^{B}\right) \tag{2.13}$$

where each $\vec{r}_{\perp,i}^{A(B)}$ is the position in the transverse plane to the beam axis z of each nucleon whose complete location in the coordinate space $\vec{r}_i = (z_i^{A,B}, \vec{r}_{\perp,i}^{A(B)})$ is sampled according to the density distribution $\rho_{A(B)}(r)$ of the owner nucleus. Analogously to what we have done for the optical Glauber model, we can define the overlap function in the following manner

$$
\begin{aligned}
\hat{T}_{AB}(\vec{b}) &= \int d^2\vec{s}\,T_A(\vec{s})T_B(\vec{s}+\vec{b}) \\
&= \int d^2\vec{s}\sum_{i=1}^{A}\delta^2\left(\vec{s}-\vec{s}_i^A\right)\sum_{j=1}^{B}\delta^2\left(\vec{s}+\vec{b}-\vec{s}_j^B\right) \\
&= \sum_{i=1}^{A}\sum_{j=1}^{B}\delta^2\left(\vec{s}_j^B-\vec{s}_i^A-\vec{b}\right) \qquad (2.14)
\end{aligned}
$$

Then the resulting function in Eq. (2.14) at some fixed impact parameter value $\vec{b}$ is specific for the space configuration of the nucleons in the colliding nuclei, $\left[A(\vec{s}_1^A,...,\vec{s}_A^A), B(\vec{s}_1^B,...,\vec{s}_B^B)\right]$ (MC event), and the the total number of binary collisions occurring at each MC event can be derived by simply multiplying the obtained overlap function Eq. (2.14) with the inelastic nucleon nucleon cross section σ_{NN}^{in}

$$
< n\left(\left[A(\vec{s}_1^A,...,\vec{s}_A^A), B(\vec{s}_1^B,...,\vec{s}_B^B)\right], \vec{b}\right) >= \sigma_{NN}^{in}\sum_{i=1}^{A}\sum_{j=1}^{B}\delta^2\left(\vec{s}_j^B-\vec{s}_i^A-\vec{b}\right) \qquad (2.15)
$$

In the end, the average number of binary collisions $N_{coll}(\vec{b})$ in the MC-Glauber model is the average over all sampled binary nucleon-nucleon scattering events Eq. (2.15) weighted with the related thickness functions (2.13) and integrated over all possible coordinates of the nucleons in the transverse plane $(\vec{s}_i^A, \vec{s}_j^B)$. This corresponds to the following expression

$$
\begin{aligned}
N_{coll}(\vec{b}) &= \left(\prod_{i=1}^{A}\int d^2\vec{s}_i^A\,\frac{\hat{T}_A(\vec{s}_i^A)}{A}\right)\left(\prod_{j=1}^{B}\int d^2\vec{s}_j^B\,\frac{\hat{T}_B(\vec{s}_j^B)}{B}\right)\sigma_{NN}^{in}\sum_{i=1}^{A}\sum_{j=1}^{B}\delta^2\left(\vec{s}_j^B-\vec{s}_i^A-\vec{b}\right) \\
&= \frac{\sigma_{NN}^{in}}{AB}\sum_{i=1}^{A}\sum_{j=1}^{B}\int d^2\vec{s}_i^A\,\hat{T}_A(\vec{s}_i^A)\hat{T}_B(\vec{s}_j^B)\delta^2\left(\vec{s}_j^B-\vec{s}_i^A-\vec{b}\right) = \sigma_{NN}^{in}\hat{T}_{AB}(\vec{b}) \qquad (2.16)
\end{aligned}
$$

Carrying out the multiple integrations and performing the sums over all the nucleons in the $A + B$ reaction, we arrive in the end at the same formula for $N_{coll}(\vec{b})$ we have derived for the optical Glauber model. However, the result is very different in substance, due to the intrinsic dependence of the overlap function $\hat{T}_{AB}(\vec{b})$ on the stochastic sample, which can be alternatively interpreted as a variation of the impact parameter itself b for each collision event. Hence, individual collisions between the two nuclei can be visualized as a discrete geometric overlap between the interacting nucleons and maintain the characteristic *fluctuations event-by-event* before they are obscured through an ensemble average. In Fig. (2.6) we present a 2D-illustration profile of a single $Au - Au$ collision event at RHIC energy $\sqrt{s_{NN}} = 200\, GeV$ for three different centrality classes. We show also also two orthogonal prospects of each event: the side view on the xz plane (left) and the beam's eye view on the yz plane (right) where the magnitude and direction of the impact parameter b is represented with a red line. The position of the nucleons inside the target and projectile nuclei is sampled according to the MC Glauber model available online (*https://github.com/MCGlauber/MCG*). Nucleons from the projectile nucleus B are represented as red spots among which the participants are colored in yellow, while nucleons from the target nucleus A are represented as blue spots with participants in violet. Similarly initial conditions from the MC Glauber model can be obtained for $Pb - Pb$ collisions at LHC energies $\sqrt{s_{NN}} = 2.76\, TeV$. We shown a single LHC event in Fig.(2.7) for three different values of centrality.

Finally, in Fig. (2.8) we present the extracted values for $< N_{part} >$ and $< N_{coll} >$ as function of impact parameter b obtained by running several simulations at RHIC $Au - Au@200\, AGeV$ and LHC $Pb - Pb@5.5\, ATeV$ energies within the MC Glauber model. The strong dependence of $< N_{part} >$ and $< N_{coll} >$ on the impact parameter value b is clearly visible in both cases and it plays a fundamental role in order to relate both quantities to some experimentally measurable observable with same monotonic behavior, such as charged particle multiplicity N_{ch}.

2.2.3 Electro-Magnetic Fields in HICs

In the classical picture of HICs the incoming nuclei are composed objects which propagate along the z axis at almost speed of light. In the center-of-mass (CM) frame of the two nuclei they appear as tiny *pancakes* of thickness

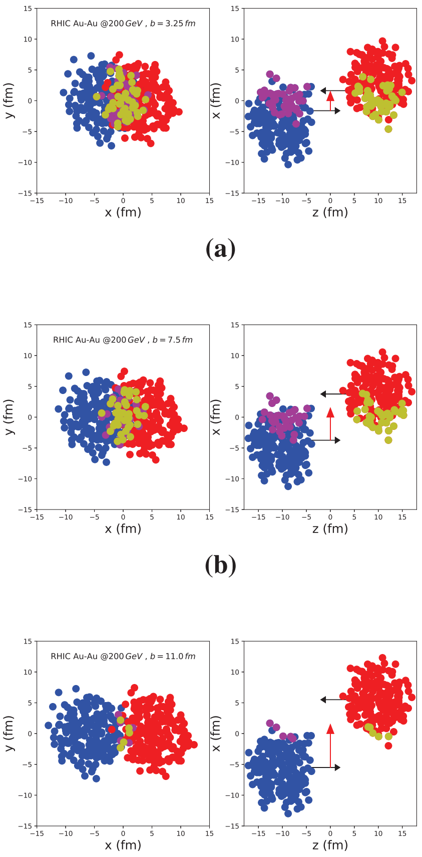

(a)

(b)

(c)

Figure 2.6: Ilustration plot of colliding gold nuclei $A = B = Au - 197$ at RHIC energy $\sqrt{s_{NN}} = 200\,GeV$ for three different centrality classes: (a) central collision $0 - 10\%$ with $b = 3.25\,fm$, (b) peripheral collision $10 - 40\%$ with $b = 7.5\,fm$, (c) most peripheral collision $10 - 80\%$ with $b = 11\,fm$.

$2R_A/\gamma_{CM}$ where R_A is the nuclear radius and γ_{CM} is the Lorentz factor which is given by

$$\gamma_{CM} = (1 - \beta^2)^{-\frac{1}{2}} = \left(1 - \frac{p_z^2}{E_{CM}}\right) \tag{2.17}$$

In Eq. (2.17) p_z is the momentum value along the beam axis, while E_{CM} is the energy of each nucleus in the CM frame. Lorentz contraction leads proton inside the nuclei to be squeezed along the longitudinal direction within a size Δz which depends on the collision energy (at $\sqrt{s} = 200\,AGeV$ $\Delta z \sim 1\,fm$). This brings to a de-localization of protons and neutrons inside the nuclear

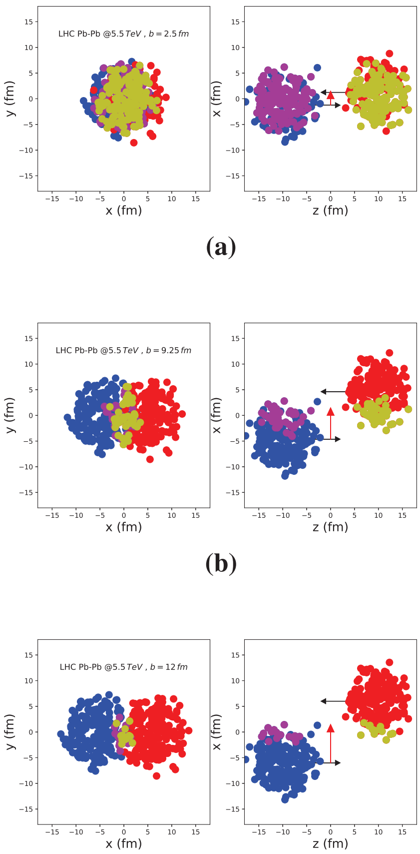

(a)

(b)

(c)

Figure 2.7: Ilustration plot of colliding lead nuclei $A = B = Pb-208$ at LHC energy $\sqrt{s_{NN}} = 2.76\,TeV$ for three different centrality classes: (a) central collision $0 - 10\%$ with $b = 3.25\,fm$, (b) peripheral collision $30 - 50\%$ with $b = 9.25\,fm$, (c) most peripheral collision $50 - 60\%$ with $b = 12\,fm$.

disks and increases their transparency to the stopping power. Consequently nucleons leave the central region of the reaction at almost speed of light and maintaining a frozen transverse position $\vec{x}_{\perp}$. In non-central collisions, with impact parameter $b \neq 0$ directed along the x axis, protons leaving the *fireball*, i.e. in the spectators region, with flying speed $\vec{\beta} = \beta\hat{z}$ are responsible for the creation of intense magnetic field $\vec{B}$, whose dominant component is parallel to the y direction as schematically represented in Fig. (2.9). The magnitude of such field can estimated by applying Biot-Savart law with in an initial value of $eB_y \approx 5m_\pi^2$ and $eB_y \approx 50m_\pi^2$ respectively at RHIC and LHC energies. In

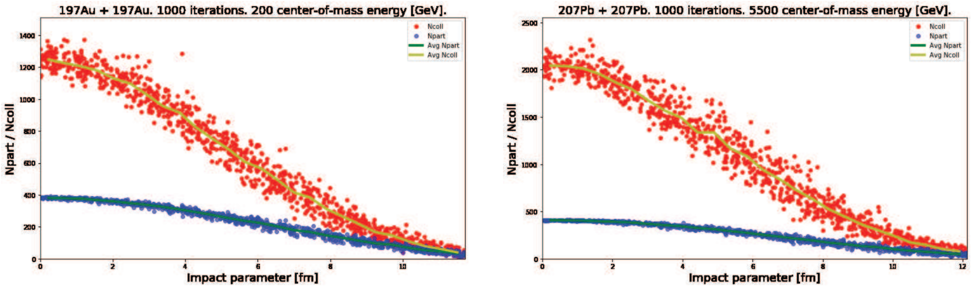

(a) **(b)**

Figure 2.8: Binary collisions $N_{part}(b)$ and participant nucleons $N_{part}(b)$ as function of impact parameter b for various simulations of RHIC $Au - Au$ collisions (left) and LHC $Pb - Pb$ collisions (right) performed within the MC Glauber model package available online (*https://github.com/MCGlauber/MCG*). Spots represent the extracted values for 1000 MC iterations, while lines are the resulting averages: green for $< N_{part}(b) >$ and yellow for $< N_{coll}(b) >$.

Standard Unit Measure this is equivalent of an order $B \sim 10^{19}\, Gauss$, meaning as the most intense field ever formed in the entire Universe, even larger than the one of magnetic stars. Spectator sources of this field leave the colliding region at almost speed of light, resulting in a magnetic field which is rapidly decreasing in time. However, it is believed that this enormous field can survive quite sufficiently to leave an imprint on the azimuthal distributions and correlations of produced particles, as well as induce a measurable charged and rapidity odd direct flow $v_1 \sim \langle p_x \rangle$ of heavy flavor hadrons due to short time of formation of heavy quarks [36]. In the following we will briefly introduce a realistic calculation of Electro-Magnetic (E.M.) fields in Heavy-Ion Collisions (HICs) [37] by focusing on the aspects that allow to construct a transport model for Heavy-Quarks (HQs) coupled to Maxwell fields that can address this problem and lead to the prediction collected in the result section of Chapter 5. It is important to mention also that the interplay of magnetic fields with quantum anomalies could lead to some phenomena, including chiral magnetic, quadrupole deformation and enhancement of anysotropic photons by magneto-sonoluminescence, that are very interesting especially in the light quark sector, but due to their complex and twined nature they have not been related to some measured observable yet and also foul up the E.M. drift through many opposite sources. On the other hand, due to their large masses (see Fig.(1.5)) are decoupled from this chiral effects and they can dynamical retain the initial E.M. kick leading to the possibility to enhance their corresponding v_1.

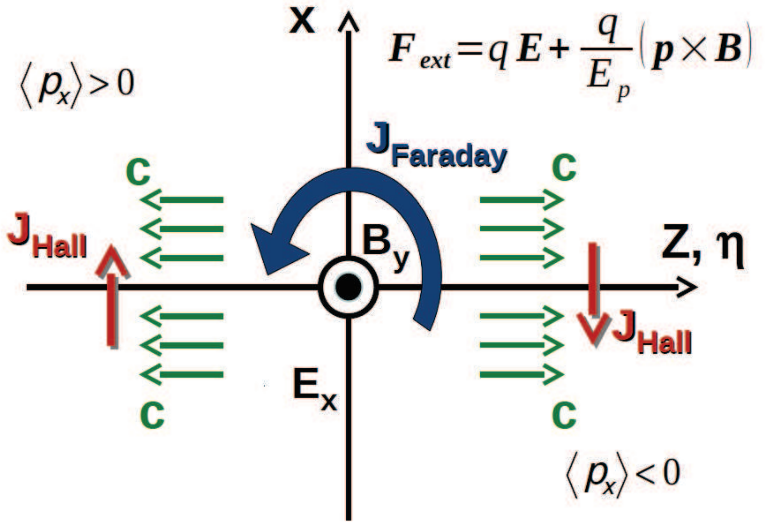

Figure 2.9: Sketch of the formation of charge and rapidity-odd finite directed flow $v_1 = \langle p_x \rangle \neq 0$ due to presence of E.M. fields at initial stages of HICs. Picture is taken from Ref. [37]

Referring to the scheme in Fig. (2.9) the produced E.M. fields act on the charged quark and anti-quarks forming the QGP matter mainly in a twofold manner. The first one originates from the time variation of $\vec{B}$ induces an electric field $\vec{E}$ with dominant component E_x by construction, which in turn results in a Faraday current opposite to the magnetic field variation and obtained by the Ohm's law

$$J_{Faraday} = \sigma_{el}\vec{E} \tag{2.18}$$

In Eq. (2.18) σ_{el} is the electric conductivity of expanding plasma which consequently should have a temperature dependence related to the various stages of HICs, from pre-equilibrated matter to hadronic phase transition with hydrodynamical phase-space evolution in between. However, models approximate σ_{el} of the QGP medium as constant function and choose a value in agreement QGP with the order of magnitude estimated by lattice QCD [38].

In particular, calculations are performed considering $\sigma_{el} = 0.023\, fm^{-1}$ at $T \sim 1.5 - 2T_c$. A detail extraction of electric conductivity from field correlators and Kubo formulas with a specific analysis on the QCD medium within a transport framework is described in Ref. [39] (see also [**?**]). Meanwhile, a second contribution to the Lorentz force $q\vec{v} \times \vec{B}$ acts on the moving particles with charges q and longitudinal velocity $\vec{v} \approx c\hat{z}$ akin to a classical Hall current $\vec{J}_{Hall}$ which lies perpendicularly to both $\vec{v}$ and $\vec{B}$ and it is also opposite in sign to $J_{Faraday}$. The net combination of these effects produces a drift of the charged particles in the xz plane leading to a finite value of $v_1 \propto \langle p_x \rangle$ which is an odd function of electric charge and rapidity. In particular from Fig (2.9), when the induced electric force is lower than the Hall effect, $J_{Faraday} < J_{Hall}$ the flow is negative $\langle p_x \rangle < 0$ for positive charges ($q > 0$) at forward (pseudo-)rapidity $\eta > 0$, while is positive for negative charges ($q < 0$). The result is opposite at backward (pseudo-)rapidity $\eta < 0$, due to the change of sign of particle velocity $\vec{v} \to -\vec{v}$.

We mentioned previously that the produced E.M. fields come from the whole contribution of protons inside the charged ions colliding at non-zero impact parameter $\vec{b}$. Hence, one has to start with the elementary magnetic and electric fields from a single point-like charge e located at frozen transverse direction $\vec{x}_\perp$ and propagating along the $+z(-z)$ direction with velocity β. In order to calculate these elementary fields in the conducting medium σ_{el} one needs to solve Maxwell equation

$$\begin{cases} \nabla \cdot \vec{E} & = \delta(z' - \beta t)\delta(\vec{x}'_\perp - \vec{x}_\perp) \\ \nabla \cdot \vec{B} & = 0 \\ \nabla \times \vec{E} & = -\partial_t \vec{B} \\ \nabla \times \vec{B} & = (\partial_t + \sigma_{el})\vec{E} + e\vec{\beta}\delta(z' - \beta t)\delta(\vec{x}'_\perp - \vec{x}_\perp) \end{cases} \tag{2.19}$$

The solutions of this system, which can be written in terms two wave equations one for the magnetic and the other for the electric field, is obtained by means of the Green function method [40] and are indicated respectively as $\vec{B}^+$, $\vec{E}^+$ for particles in the forward light-cone $t > z$ and as $\vec{B}^-$, $\vec{E}^-$ for particles in the backward light-cone $t > -z$. These elementary fields are function of an arbitrary space-time point $(t, \vec{x}_\perp, z)$, then one can obtain a simple analytic formula in the Milde framework by replacing t and z coordinates with the proper time the proper time $\tau = \sqrt{t^2 - z^2}$ and the spacetime rapidity $\eta = \tanh^{-1}(z/t)$. In particular, the main components of the electric and the magnetic fields are related to each other by the following expression

$$eE_x^+(\tau, \eta, x_\perp, \phi) = eB_y^+(\tau, \eta, x_\perp, \phi)\coth\left(Y_\beta - \eta\right) \tag{2.20}$$

where $\vec{x}_\perp = (x_\perp \cos\phi,\ x_\perp \sin\phi)$ and $Y_\beta = \tanh^{-1}(\beta)$ is the momentum rapidity of the forward source. For the specific expressions of eB_y^+ and eE_x^+ we refer to Ref. [37] and originally to Ref. [41]. One can also prove that these are actually the dominant components in any case when fluctuations in event-by-event non-central collisions are not included. Nonetheless, it has been proven that initial stage of HICs are characterized by sharp density profile which lead to large fluctuations that can be addressed for example within a MC Glauber discrete distribution. However, the generated components of the E.M. fields within an event-by-event analysis usually remain comparable and eventually smaller than $B_y^{(\pm)}$ and $E_x^{(\pm)}$, so they can be kept easily under control.

The whole contribution from the spectators is obtained by folding these elementary E.M. fields with the transverse density which takes the form

$$\rho_\pm(x_\perp,\ \phi) = \frac{3}{2\pi R_A}\sqrt{R_A^2 - \left(x_\perp^2 \pm b x_\perp \cos\phi + \frac{b^2}{4}\right)} \tag{2.21}$$

if one projects the probability distribution of protons in either the + or the − moving direction, assuming they are distributed uniformly inside the spherical nuclei of radius R_A, with the centers displaced by $x = \pm b/2$, $y = 0$. On the other hand, one has to perform explicit integration over the longitudinal direction, in case of a Wood-Saxon parametrization of the nuclear density distribution Eq.(2.1). Then, the resulting magnetic field generated by Z point-like spectator protons summing over forward (η) and backward ($-\eta$) rapidity is given by

$$eB_y = -Ze\int d\phi' dx'_\perp x'_\perp \left[\rho_-(x'_\perp,\phi')\vec{B}_s^+(\tau,\eta,x_\perp,\phi) + \rho_+(x'_\perp,\phi')\vec{B}_s^{\,+}(\tau,-\eta,x_\perp,\phi)\right] \tag{2.22}$$

with an analogous formula for the electric component eE_x. Participant protons lose some rapidity during collisions, so their contribution is smoothed out by some empirical distribution $f(Y_b)$ which makes the produced E.M. fields of secondary order compared to the spectator part at least in the initial stage. We display the time evolution of eB_y and eE_x at $\vec{x}_\perp = 0$ at respectively RHIC $Au-Au$ @200 $AGeV$ semi-peripheral collisions ($b = 7.5\,fm$) for $\eta = 0.5$ and at LHC $Pb-Pb$ @2.76 $ATeV$ peripheral collisions ($b = 9.25\,fm$) for $\eta = 1.0$ as derived from Ref. [36].

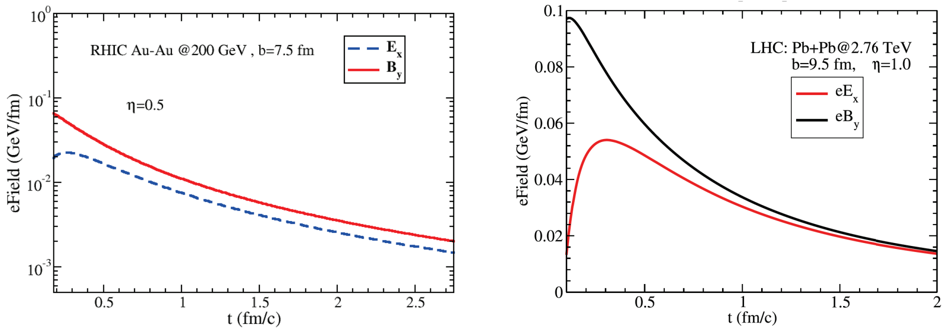

(a) **(b)**

Figure 2.10: Adapted from [36]. Time variation of E.M. fields eB_y and eE_x produced by spectator protons in HICs at RHIC (right) and LHC (left) events.

2.3 QGP phase at thermal equilibrium

The concept of thermalization of the fireball created in the central region of HICs was firstly introduced by Bjorken in his milestone work [42] where he related the initial time τ_0 and initial energy density ϵ_0 (or equivalently entropy density s_0) of his hydrodynamical scenario to some measurable observables. It is rather well known the formula where in case of free streaming expansion he derived an estimate of ϵ_0

$$\epsilon_{0,Bjorken} = \frac{1}{\pi R_A^2 \tau_0} \frac{dE_T}{dy}|_{y=0} \tag{2.23}$$

as function of the total transverse energy per unit of rapidity at mid-rapidity and extracted a value of $\tau_0 \approx 1\, fm$ by fitting the final particle multiplicity to the experimental data. Models for initial stages of HICs, like standard or MC Glauber as well as microscopic theories based on parton cascade and more recent color-string or Color Glass Condensate (CGC) model that we do not discuss in this thesis but we mention trough some references [43, 44, 45, 46], also attempt to provide an estimate of the initial time τ_0. Some studies have tried to estimate τ_0 applying relativistic transport theory based on Boltzmann equation but considering gluon distribution which is initially out of equilibrium and derived from CGC factorized form, like the Kharzeev-Levin-Nardi (KLN) model, known also as fKLN [47]. Similarly other approaches coupled the Boltzmann equation to a classical field description, i.e. Yang-Mills equations [48], and predicted that system thermalization occurs at shorter time compared to Bjorken's paradigm, obtaining a value of $\tau_0 \approx 0.6 - 0.8\, fm/c$. A precise value of initial time is not needed in the aim of this work, rather it is important for us to known that within different approaches there is strong evidence that the system has reached local thermalization at about $\tau_0 \approx 1\, fm$. At ultra-relativistic HICs conducted at RHIC and LHC facilities the observation of high multiplicity events is associated by Eq. (2.23) to the formation of a hot baryonic-free *fireball* with an initial energy density ϵ_0 which is larger than the critical value $\epsilon_c \sim 1\, GeV/fm^3$. Hence, it is expected that the system has crossed the transition line and founds in the QGP phase. In the case the thermalization condition is also established one it is possible to assign an initial temperature T_0 higher than the critical value $T_c \approx 155\, MeV$ expected by lQCD [49]. This temperature can be related to other thermodynamical quantities which together with Heisenberg relation $T_0\tau_0 \sim 1$ allow to state quite reasonably that in $Au-Au$ collisions at RHIC with $\sqrt{s_{NN}} = 200\, GeV$ the system has $T_0 \approx 2\, T_c$, while at LHC $Pb-Pb$ collisions $\sqrt{s_{NN}} = 2.76\, TeV$ the system has $T_0 \approx 3 - 4\, T_c$. Quarks and gluons produced within the central region are not free to escape, rather they scatter through elastic and inelastic collisions forming a hot and dense interacting *bulk*. Such microscopic processes are responsible to the development of pressure gradients which drive the macroscopical expansion and cooling of the QGP medium. The appropriate framework for describing the dynamical evolution of a complex system formed by many particles, whether it is in equilibrium or not, is *Relativistic Kinetic Theory*. In this section we want to provide the basic ideas of kinetic theory, getting from specific books [50] [51], and through which we can introduce another widespread approach for treating the QGP phase-space evolution. A detail discussion of relativistic kinetic theory with a focus on the derivation of our transport equations for *bulk* and heavy quarks dynamics will be the topic of the next chapter. The main concept of kinetic theory is the *distribution function* for a single particle of type-i, namely a gluon or a quark (anti-quark) $i = g, q(\bar{q})$, defined as $f_i(x, p)$ and which gives the probability of finding such kind of particle at general phase-space (x, p). It makes sense to introduce the distribution function if the system is formed by a large number of particles. Hence, by definition $f_i(x, p)\Delta^3\vec{x}\Delta^3\vec{p}$ is equivalent to the average number of particles which at certain time $t = x^0$ are located within the volume element $\Delta^3\vec{x}$ centered at $\vec{x}$ and whose momentum lies in the range $(\vec{p}, \vec{p} + \Delta^3\vec{p})$, while energy is obtained by relativistic dispersion relation $p^0 = E_p = \sqrt{p^2 + m_i^2}$, being m_i the mass of a particle of i species. Relativistic kinetic theory is based on the derivation of transport equations where starting from initial conditions $f_i(t = 0, \vec{x}, \vec{p}) = f_i^0(\vec{x}, \vec{p})$ and accounting microscopic processes and interaction forces it is possible calculate the general solution $f_i(t, \vec{x}, \vec{p})$ for later time. However, taking respectively the first and second momenta of the distribution function $f_i(x, p)$ for each particle species one can construct the particle four-flow $J_i^\mu(x)$ and the energy-momentum tensor $T^{\mu\nu}(x)$ which are invariant macroscopic objects

$$J_i^\mu(x) \equiv \int \frac{d^4p}{(2\pi)^3}\delta(p^2 - m_i^2)p^\mu f_i(x, p) = \int \frac{d^3\vec{p}}{(2\pi)^3 E_p} p^\mu f_i(x, p) \qquad (2.24)$$

$$T_i^{\mu\nu}(x) \equiv \int \frac{d^4}{(2\pi)^3}\delta(p^2 - m_i^2)p^\mu p^\nu f_i(x, p) = \int \frac{d^3\vec{p}}{(2\pi)^3 E_p} p^\mu p^\nu f_i(x, p) \quad (2.25)$$

where we explicitly solved delta function to arrive to last expressions of Eq. (2.24) and Eq. (2.24). If $f_i(x, p)$ is a solution of the kinetic equations, $J^\mu_i(x)$ and $T^{\mu\nu}(x)$ fulfills respectively well known conservation laws for particle and energy-momentum conservation, which at the end represent the starting point for another successful framework for describing the QGP evolution, which is hydrodynamics. We will give now a short overview of the hydrodynamical paradigm and derive a part of the original Bjorken's scenario.

2.3.1 Ideal Hydrodynamics

Fluid dynamics is a continuum description based on the solution of macroscopic equations for baryon number and energy-momentum conservation laws which can be founded in the hypothesis that the system is in thermal equilibrium, at least locally, and which in the Lorentz covariant form are given by

$$\partial_\mu J^\mu_B(x) = 0 \tag{2.26}$$

$$\partial_\mu T^{\mu\nu}(x) = 0 \tag{2.27}$$

In Eq. (2.26) $T^{\mu\nu}$ and J_B are treated as classical continuum fields and their initial values are provided by some models, like for example Glauber or CGC. here we drop the index i by considering only one kind of particles, of course direct extension for a system formed by different particle species is simply realized by defining the energy-momentum tensor and current as the sum of all contributions $T^{\mu\nu} = \sum_i T^{\mu\nu}_i$ and $J^\mu_B = \sum_i B_i J^m_i$ where we account the baryon number $B_i = +(-)1/3$ for quarks (antiquarks) and $B_i = 0$ for gluons. As we have seen, in kinetic theory Eq. (2.24)-(2.25) these two quantities have a microscopic definition through the phase space distribution function $f(x, p)$. Instead, in hydrodynamics $T^{\mu\nu}$ and J^μ_B have to be expressed in terms of mascroscopic classical fields such as energy density $\epsilon(x)$, particle density $n(x)$, pressure $P(x)$, entropy density $s(x)$ temperature $T(x)$ and also chemical potential $\mu_B(x)$. Within this set of *thermodynamical functions* we can give a full description of the equilibrium state of the plasma. Moreover, because we deal with an expanding system, we need to introduce a relativistic flow velocity $u^\mu(x)$ consistently at each space-time point. The straightforward way to do that is to start from the Local Rest Frame (LRF) which corresponds to the coordinate system where locally the fluid is static. Then, in this frame the flow velocity reduces to the form $u^\mu_{LRF}(x) = (1, 0, 0, 0)$. This brings also to the following normalization

$$u_\mu u^\mu = 1 \tag{2.28}$$

valid in any inertial frame and Lorentz transformation with a fluid velocity $\vec{v}(x)$ applied on $u^\mu_{LRF}(x)$ gives us the general expression for the four-velocity

$$u_\mu = \gamma(x)\,(1,\ \vec{v}(x)) \tag{2.29}$$

with $\gamma(x) = 1/\sqrt{1 - v^2(x)}$. At local thermal equilibrium the distribution function gets the following exponential form

$$f_{eq}(x, p) = \frac{g}{2\pi}\left[exp\left(\frac{p^\mu u_\mu(x) - \mu_B(x)}{T(x)}\right) \pm 1\right]^{-1} \tag{2.30}$$

which corresponds to the covariant generalization of the Maxwell-Boltzmann function, known as Boltzmann-Jüttner distribution where g is the is the degeneracy factor due to spin, color and other internal degrees of freedom, while the ± corresponds to fermionic (+) and baryonic (-) statistics. Plugging Eq. (2.30) into the definition of the baryonic current Eq. (2.24) we obtain its expression in terms of the macroscopic fields. In particular, we have

$$J^\mu_B(x) = n(x)u_\mu(x) \tag{2.31}$$

where $n(x)$ is the particle baryon number density in the LRF of the system. The perfect fluid is characterized by conservation of entropy density for an observer which is locally comoving. This means also that local pressure $P(x)$ is isotropically the same in all directions and exerted by the fluid perpendicular to the container. The result is that in *ideal hydrodynamics* the energy momentum tensor in the LRF is diagonal and gets the form

$$T^{\mu\nu}_{LRF} = \begin{pmatrix} \epsilon(x) & 0 & 0 & 0 \\ 0 & P(x) & 0 & 0 \\ 0 & 0 & P(x) & 0 \\ 0 & 0 & & P(x) \end{pmatrix} \tag{2.32}$$

Then, Lorentz transformation to an inertial frame where a fluid element moves locally with flow velocity $u^{\mu}(x)$ given by Eq. (2.29) allows to derive the general formula of the energy-momentum tensor

$$T^{\mu\nu}(x) = [\epsilon(x) + P(x)]\, u^{\mu}(x)u^{\nu}(x) - P(x)\eta^{\mu\nu} \tag{2.33}$$

where $\eta^{\mu\nu}$ is the metric tensor for the Minkovski space. As we can see in Eq. (2.33) $T^{\mu\nu}(x)$ for an ideal fluid shows no dissipative term. The next step is to cast the obtained expressions for $J_B(x)$ Eq. (2.31) and $T^{\mu\nu}(x)$ Eq. (2.33) inside the conservation laws Eq. (2.26). These corresponds to a total of five equations, while we have to determine six thermodynamical variables: $\epsilon(x)$, $P(x)$, $n(x)$ and the three components of the flow velocity $v_x(x)$, $v_y(x)$ and $v_z(x)$.

In order to achieve a unique solution the hydrodynamical system has to be supplied with the so-called **Equation of State** (EoS) which is usually written as a relation between the energy density ϵ and the pressure P

$$P = \lambda\epsilon \tag{2.34}$$

assuming zero baryon chemical potential $\mu_B = 0$ which is a reasonable condition at ultra-relativistic HICs. Clearly, the specific expression for the numerical constant λ is directly connected to the properties of the QCD matter. Physically it has the meaning of the speed of sound $\lambda = c_s^2$ and for an ideal relativistic gas one can apply the black body radiation relation $c_s = 1/\sqrt{3} \rightarrow \lambda = 1/3$. However, the general derivation of a realistic QCD EoS $c_s = \sqrt{\partial P/\partial\epsilon}$ is a complex issue which at the same time has a large scale of interest, because it is a fundamental ingredient for the description of any strongly interacting system, from QGP to compact stars and cosmology for expanding Universe. A detail discussion about the status-of-art for the EoS within lattice QCD framework from pure gauge theory to quark extension at small non-zero chemical potential $\mu_B \neq 0$ is given in Ref. [23].

Once we have the EoS and initial conditions for $T^{\mu\nu}(x)$ and $J_B(x)$ hydrodynamical equations become a perfectly solvable system from which we can derive the space-time evolution of the thermodynamical variables for the expanding system. Instead of using directly the energy-momentum conservation given in its covariant form, we can extract a scalar equation by contracting Eq. (2.28) with flow velocity and using the normalization condition Eq. (2.28). Hence, by casting $T^{\mu\nu}(x)$ expression Eq. (2.33) in the contracted formula we get

$$\begin{aligned} &u_\nu \partial_\mu \left[(\epsilon(x) + P(x))\, u^\mu(x) u^\nu(x) - P(x)\eta^{\mu\nu} \right] \\ &\qquad = u^\mu \partial_\mu \epsilon + (\epsilon + P)\partial_\mu u^\mu = 0 \end{aligned} \tag{2.35}$$

Then, applying thermodynamic relations $\epsilon + P = T\,s + \mu_B\, n$ and using baryon number conservation Eq. (2.26), we arrive to the bright result

$$\partial_\mu (s(x)\, u^\mu) = 0 \tag{2.36}$$

which in terms of a defined four-vector $s^\mu(x) = s(x)u^\mu$, we can identify as the conservation of the entropy current $\partial_\mu s^\mu(x) = 0$ known also as *energy equation*. Equivalently the motion of the ideal fluid is an adiabatic and reversible process, something that we expect because it lacks of any dissipation force. To recover a total of five independent equations, next to the scalar condition Eq. (2.36) we have to combine other four equations which can obtained by projecting Eq.(2.28) along the transverse direction of the flow velocity

$$\begin{aligned} &(\eta_{\lambda\nu} - u_\lambda u_\nu)\partial_\mu \left[(\epsilon(x) + P(x))\, u^\mu(x) u^\nu(x) - P(x)\eta^{\mu\nu} \right] \\ &\qquad = -\partial_\lambda P + u_\lambda u^\mu \partial_\mu P + (\epsilon + P) u^\mu \partial_\mu u_\lambda = 0 \end{aligned} \tag{2.37}$$

This corresponds to the relativistic generalization of the *Euler equation* where the material derivative of the fluid velocity $(\partial/\partial t + \vec{v}\cdot\nabla)\,\vec{v}$ is related to pressure gradient ∇P.

Bjorken 's scenario

First hydrodynamical description of QGP was stated by Bjorken in Ref. [42] with the aim to examine the time evolution of the energy density and other thermodynamical variables for the hot and dense strong interacting system created at central region of HICs. Due to the fact that the quanta forming the *fireball* are created ensuing the reacting nuclei, they are affected by a strong expansion in the longitudinal beam direction. Hence, in first approximation one can assume to drop initially the transverse direction and apply ideal hydrodynamics to (1+1) dimensional system with coordinates z and t. Then, one introduces the Milne system for the forward lightcone $t > |z|$ where the coordinates are the proper time and the space-time rapidity which as we have seen in previous section are defined as

$$\tau = \sqrt{t^2 - z^2} \quad , \quad y = \frac{1}{2}\ln\frac{t+z}{t-z} \tag{2.38}$$

with the corresponding inverse transformations

$$t = \tau\cosh y \quad , \quad z = \tau\sinh y \tag{2.39}$$

Bjorken's model is constructed by making the following ansatz on the local velocity of the perfect fluid

$$u^{\mu}(x) = (t/\tau, 0, 0, z/\tau) = (\cosh y, 0, 0, \sinh y) \tag{2.40}$$

which is equivalent to the case where particles stream freely with velocity $v_z = z/t$ away from the origin along the z direction. Imposing such longitudinal boost-invariance or scaling flow on Euler equation Eq. (2.37) one obtains the following statement

$$\frac{\partial P(\tau, y)}{\partial y} = 0 \tag{2.41}$$

Therefore, pressure field and other thermodynamical variables do not depend on the space-time rapidity y, rather they are function only of the proper time τ, meaning they are constant along the hyperbola represented in Fig. (2.11) adapted from [33].

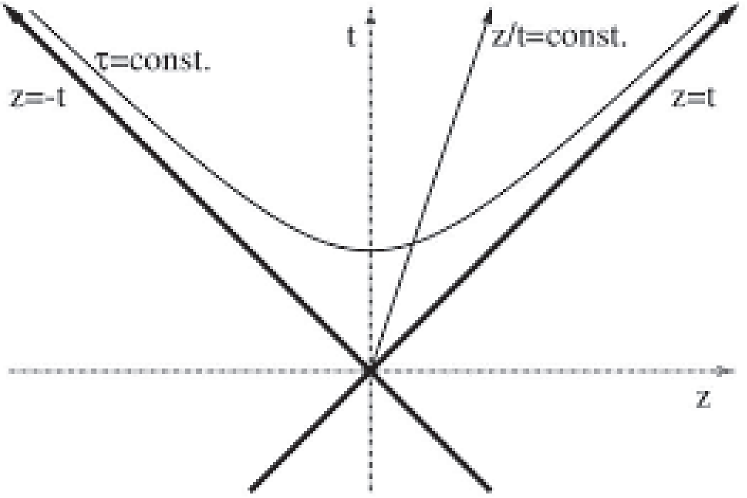

Figure 2.11: Fluid expansion within Bjorken's model: drawn hyperbola in the forward lightcone region $t \geq |z|$ corresponds to surface of constant $\tau = \sqrt{t^2 - z^2}$, while straight line from origin is the trajectory of free streaming with constant velocity $v_z = z/t$.

Entropy equation Eq. (2.36) reduces to the simple relation

$$s(\tau)\,\tau = s_0\tau_0 \tag{2.42}$$

with s_0 being the entropy density at initial proper time τ_0. That is precisely the isoentropic expansion of the relativistic ideal fluid. The corresponding energy equation which can be derived from Eq. (2.35) can be written as

$$\frac{d\epsilon}{d\tau} + \frac{\epsilon + P}{\tau} = 0 \tag{2.43}$$

Finally, one can solve this equation for a particular state of matter by imposing some EoS $P(\epsilon)$, for example Eq. (2.34) and derive the behavior for the thermodynamical variables within the scaling (1+1) ideal hydro framework

$$\begin{aligned} T(\tau) &= T_0\left(\frac{\tau_0}{\tau}\right)^{\lambda} \\ \epsilon(\tau) &= \epsilon_0\left(\frac{\tau_0}{\tau}\right)^{\lambda+1} \\ P(\tau) &= P_0\left(\frac{\tau_0}{\tau}\right)^{\lambda+1} \end{aligned} \tag{2.44}$$

together with Eq. (2.42) and thermodynamic relation $Ts = \epsilon + P$ with $\mu_B = 0$.

2.3.2 Viscous Hydrodynamics

Viscous corrections are introduced by including additional terms on the energy-momentum tensor, the baryon current and the entropy current which depends on the derivatives of the flow velocity $u^{\mu}(x)$ and the thermodynamical variables

$$T^{\mu\nu}(x) = T^{\mu\nu}_{ideal}(x) + \tau^{\mu\nu}(x) \tag{2.45}$$

$$J^{\mu}_{B}(x) = n(x)u^{\mu}(x) + \nu^{\mu}_{B} \tag{2.46}$$

$$s^{\mu}(x) = s(x)u^{\mu} + \sigma^{\mu} \tag{2.47}$$

where $T^{\mu\nu}_{ideal}$ stands for the energy-momentum tensor of the ideal fluid given in Eq. (2.33). Particle density n and energy density ϵ in the Local Rest Frame (LRF) as well as isotropic pressure P related to n and ϵ through specific EoS are defined in the same way as in Eq. (2.32)

$$n(x) = u_m J^{\mu}_{B}\,,\ \epsilon(x) = u_m T^{\mu\nu} u_n\,,\ P(x) = (\eta_{\mu\nu} - u_{\mu}u_{\nu})T^{\mu\nu}/3 \tag{2.48}$$

Then, one can derive viscous hydrodynamics equations from same conservation laws $\partial_{\mu}T^{\mu\nu} = 0$ and $\partial_{\mu}J^{\mu}_{B} = 0$ after proper definition of the fluid velocity which in the presence of dissipative corrections becomes more arbitrary [33] and coming to the following orthogonal constraints

$$u_{\mu}\tau^{\mu\nu} = 0 \quad , u_{\mu}\nu^{\mu}_{B} = 0 \tag{2.49}$$

Finally, one gets an explicit form and physical meaning of the viscous terms by making an expansion order-by-order on the derivatives of the fluid velocity. For this purpose, we follow a standard procedure by introducing a so-called projector tensor transverse to the flow velocity

$$\Delta_{\mu\nu} = \eta^{\mu\nu} - u^\mu u^\nu\,,\ u_\mu \Delta^{\mu\nu} = 0\,,\ \Delta^\mu_\mu = 0 \tag{2.50}$$

which we use to construct the covariant gradient $\nabla^\mu \equiv \Delta^{\mu\nu}\partial_\nu$. Then, at linear order the explicit form of $\tau^{\mu\nu}$ and ν^μ_B can be derived assuming they are functions only of first derivatives $\partial_\mu u_\nu$ and imposing the constraints in Eq. (2.49)

$$\nu^\mu_B = -\frac{m_B}{T}\sigma^\mu = \kappa\left(\frac{nT}{\epsilon + P}\right)^2 \left(\partial^\mu - u^\mu u\cdot\partial\right)\left(\frac{m_B}{T}\right) \tag{2.51}$$

$$\tau^{\mu\nu} = \pi^{\mu\nu} - \Pi\Delta^{\mu\nu} \tag{2.52}$$

where in the former equation μ_B is the baryon chemical potential, while the entropy equation is obtained from the scalar contraction $u_\mu \partial_\nu T^{\mu\nu} = 0$ analogously of the ideal hydrodynamics case

$$\partial_\mu s^\mu = \nu^\mu_B \left(\partial_\mu - u_\mu u\cdot\partial\right)\left(\frac{m_B}{T}\right) + \frac{1}{T}\tau^{\mu\nu}\left(\partial_\mu - u^\mu u\cdot\partial\right)u^\nu \tag{2.53}$$

with a last condition that the right hand side of Eq. (2.53) has to be non-negative because of the second law of thermodynamics generalized to relativistic systems: $\partial_\mu s^\mu \geq 0$. The coefficient $\kappa \geq 0$ denotes the fluid heat conduction which correspond to amount of energy dissipated without the particle flow. Focusing now on the latter equation, we observe that the dissipative term of the energy-momentum tensor $\tau^{\mu\nu}$ is divided in two parts which can be equivalently written as

$$\tau^{\mu\nu} = \eta\sigma^{\mu\nu} + \zeta\Delta^{\mu\nu}\left(\nabla\cdot u\right) \tag{2.54}$$

where we defined the traceless viscous stress tensor

$$\sigma^{\mu\nu} = \left[\partial^\mu u^\nu + \partial^\nu u^\mu - u\cdot\partial(u^\mu u^n)\right] - \frac{2}{3}\Delta^{\mu\nu}\left(\nabla\cdot u\right) \tag{2.55}$$

and enclosed the remaining volume effect on the trace part of the viscous tensor $\tau^{\mu\nu}$ in Eq. (2.54). In this equation the $\eta \geq 0$ and $\zeta \geq 0$ coefficients denote respectively the *shear viscosity* and the *bulk viscosity*. First order viscous hydrodynamics needs other four equations coupled to entropy Eq. (2.53) and EoS that we obtain by performing the following contraction

$$\Delta_{\rho\nu}\partial_{\mu}T^{\mu\nu} = 0 \tag{2.56}$$

from which we akin to the relativistic generalization of *Navier-Stokes equation* [50] which results as the first order viscous correction of *Euler equation* for dissipative fluid in the classical non-relativistic fluid dynamics. However, differently to this case, the introduction of linear order corrections into the entropy current violates causality, leading the solutions of Eq. (2.56) to propagate acausal information and making first order Navier-Stokes viscous hydrodynamics to be unconsistent with relativistic theory. Therefore, in order to account dissipative effects within a hydrodynamical description of QGP, it is necessary to go beyond the linear order. However, in this case there is no unique picture and one has to deal with the developing of many theories, starting for example from the Israel-Stewart method [52] and ending up with advanced moment approximation [53] for deriving fluid dynamics equations at truncated second order expansion with causality constraint. We mention here that this problem is related also to a very controversial question how hydrodynamics as a whole can be consistently derived from kinetic theory and how viscous corrections can be addressed in the form of deviation of single particle phase-space distribution from the equilibrium expression Eq. (2.30)

$$f(x,p) = f_{eq}(x,p) + \delta f(x,p) \tag{2.57}$$

Despite the aim of this work is far from the hydrodynamics vs kinetic theory quest, because we focus on the dynamics within the QGP of heavy quarks which are out of equilibrium for reasons that we will explain later, we will go back to part of this issue in the next chapter.

2.4 Hadronization and rescattering phase

Hydrodynamical simulations of the expanding system start at $\tau_0 \sim 0.6\, fm$ with $\epsilon_0 \sim 10 - 15\, GeV/fm^3$ for RHIC energies [54] and at $\tau_0 \sim 0.3\, fm$ with $\epsilon_0 \sim 25{-}40\, GeV/fm^3$ at LHC energies. The system spends a major time in the QGP phase with lifetime of about $\tau_{QGP} \sim 6 - 8\, fm$ and $\tau_{QGP} \sim 10 - 12\, fm$ respectively at RHIC and LHC, until the energy density drops down to the critical value $\epsilon_c \sim 1\, GeV/fm^3$ that happens also when cooling brings temperature close to the T_c value expected by lQCD. Then, the system undergoes to the confinement phase transition, more precisely a crossover becoming sharper first order phase transition at finite chemical potential (Chapter 1), during which quarks and gluons are bounded again in colorless states and finally the system emerges as a interacting gas of hadrons. Hydrodynamics gives a continuous fluid description of essentially massless quanta, but at the breaking-up it should turn into massive particles and in the meanwhile conserve both momentum and energy. A method for this mechanism was formulated by Cooper and Frye [55] [56] who derived an expression to get the invariant hadron spectrum from the single particle distribution of a relativistic gas. This is a very renowned result bearing the name of Cooper-Frye formula

$$E\frac{dN}{d^3\vec{p}} = \int_{\sigma_c} f(x,p) p^\mu d\sigma_\mu \tag{2.58}$$

where one imposes that at the freezout hypersurface σ_c the distribution function of the hadron gas $f(x,p)$ corresponds to that of a thermal system at equilibrium with local temperature $T(x)$ and also that the particle momentum is linked to the fluid velocity $\vec{v}(x)$ through the following $p^\mu = Eu^\mu$. Then, in Eq. (2.58) on can substitute $f(x,p) = f_{eq}(E(\vec{v}(x), T))$ and switch from hydrodynamics to a kinetic transport description of the hadronic phase. Beside the hydrodynamical breaking, the *hadronization* process itself appears as a complicated issue, because of the purely non-perturbative nature of QCD confinement, which is also worsen by the fact that in HICs hard partons hadronize surrounded by a strongly interacting medium, rather than what happens for elementary proton-proton collisions. Among the possible phenomenological models, a diffused microscopic description of the hadronization mechanism is based on the *fragmentation* and *coalescence* of quarks and gluons within the confinement length $d \sim 1\, fm$.

2.4.1 Fragmentation

Hadron production in lepton-lepton, lepton-proton and proton-proton collisions at energy $\sqrt{s}$ can be treated within a common framework which is based on the properties of QCD. In particular, given the momentum scale Q^2 of the specific process, one can separate the pQCD production of a leading parton c happening at high energy, i.e. small distance, from the subsequent conversion into the final hadronic state h, that belongs to low energy, i.e. high distance, non-perturbative QCD regime. This technique can be formally casted into the so-called factorization theorem [57]. Then, the semi-inclusive invariant cross section of hadron (h) production at mid-rapidity in pp collisions for example can be written in the following form

$$
\begin{aligned}
E_h \frac{d\sigma_{p+p\to h+X}}{d^2\vec{p}_{T,h}dy} = \sum_{ab\,,cd} \int dx_1 \int dx_2\, f_a^p(x_1, Q^2) f_b^p(x_2, Q^2) \\
\cdot E_c \frac{d\hat{\sigma}_{a+b\to c+d}}{d^2\vec{p}_{T,c}dy} \cdot D_{c\to h}\left(z,\, Q^2\right)
\end{aligned}
\tag{2.59}
$$

In Eq. (2.59) $f_i^p(x, Q^2)$ denotes the Parton Distribution Function (PDF) of i species inside the proton, while $d\hat{\sigma}_{a+b\to c+d}$ is the elementary pQCD cross section of leading c particle production from $a+b$ partonic scattering. Instead the $c \to h$ conversion is encoded in the so-called *Fragmentation Function* (FF) $D_{c\to h}(z, Q^2)$ defined as a dimensionless object which essentially gives the probability of the parton c with momentum $\vec{p}_c$ to hadronize by spraying multiple soft gluons into the final tagged hadron h which in the end carries a fraction $z = p_h/p_c \leq 1$ of the initial fragmenting parton [58] [59]. At LO pQCD level FFs do not depend on the specific value of Q^2 involved in the process, while it acquires such dependece already at NLO with consequent violation of scaling law and energy evolution according to the Dokshitzer-Gribov-Lipatov-Altarelli-Parisi (DGLAP) equations [60, 61, 62] similarly to what happens for the PDFs. Therefore, one can writes

$$Q^2\frac{\partial D_i(z,Q^2)}{\partial Q^2}=\sum_j\int_z^1 dx\frac{\alpha_s}{2\pi}P_{ji}(x,\alpha_s)\cdot D_j(x,Q^2) \tag{2.60}$$

where the splitting process of a parton of species j with corresponding FFs $D_j(x,Q^2)$ into a parton of species i with FFs $D_i(z,Q^2)$ in the end is considered through the function $P_{ji}(x,\alpha_s)$ which has also a perturbative expansion over $\alpha_s/2\pi$. FFs should satisfy also sum relations arising from total momentum conservation and hadron multiplicity. In particular

$$\sum_h\int_0^1 dz\,z\,D_{c\to h}(z,\,Q^2)=1\ ,\ \sum_c\int_0^1 dz\,[D_{c\to h}(z)+D_{\bar{c}\to h}(z)]=\frac{dN_h}{dy} \tag{2.61}$$

FFs are usually provided through parametrized expressions accounting for the universality of hadron production in elementary e^+e^-,ep and pp collisions and they are also differentiated for light quarks and heavy quarks. For the former we find interesting to mention KKP [63] and AKK parametrizations [64], while for the latter we will give a detail description in the appropriate section for describing the hadronization model for HQs. Finally, differences in the factorization formula Eq. (2.59) when moving to hadron production in nucleus-nucleus reactions due to the presence of initial bounded nucleon PDFs rather than free colliding proton ones ($f_i^p \to f_i^A$) will be addressed specifically for HQs but actually explained in a more general frame.

2.4.2 Coalescence

Since first observations of hadron production in HICs there was evidence of the fact that hadronization occurs differently compared to the vacuum fragmentation which we have described previously. This is due to presence of the medium, so quarks and antiquarks can merge with comoving partons of the reservoir, thus forming baryons and mesons with final momentum given by the sum of the combining partons, rather than keeping a fraction of the leading fragmenting one. The so-called covariant *coalescence* mechanism was firstly introduced to describe recombination for nucleons binding with each other into deuterons and light nuclei [65] and later on extended to quarks and antiquarks by treating the superposition of the partonic phase-space distribution functions to produce light hadron species at RHIC energy in a Wigner formalism [66, 67, 68, 69].

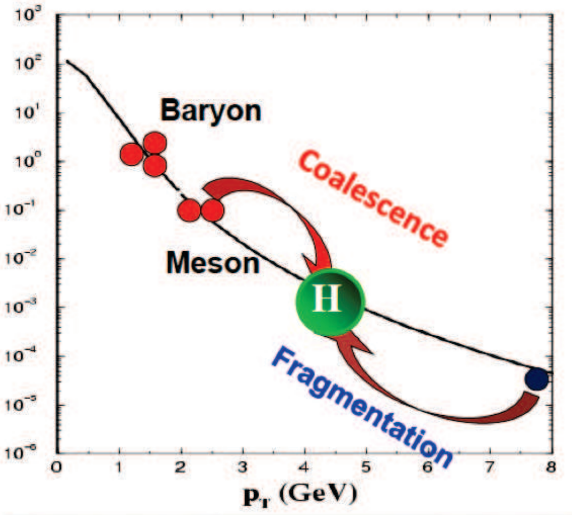

Figure 2.12: Competition among coalescence vs fragmentation on the formation of the final hadron p_T distributions. Sketch is adapted from Ref. [70, 71]

The idea is rather simple: two or three comoving partons in the QGP can combine with each other and produce a meson or a baryon with final transverse momentum which is higher than the original partons themselves. Therefore, the result is opposite with respect to the fragmentation of a high p_T parton where in that case the initial momentum is distributed among all the fragments. Moreover, in the recombination process the total momentum is conserved passing from the partonic species to the final hadronic state, while in fragmentation the initial p_T is not preserved by the produced hadron. The competition between the two hadronization mechanisms is depicted in Fig. (2.12) and it is subject of many studies. Since the probability to find two or three partons close in the phase-space decreases as function of the momentum, it is common opinion that coalescence becomes less important at high p_T and fragmentation starts to overcome until becoming the dominant hadronization mechanism at $p_T > 5\,GeV$. On the other hand, coalescence is preponderant at $p_T < 2\,GeV$ due to the high abundance of soft thermal partons. This condition may also change as function of the impact parameter. In particular, models agree in the opinion that recombination has a significant impact at central collisions, because the number of created partons is larger compared to peripheral collisions where thus fragmentation should become more relevant. The success of the coalescence scenario came up since the first application of this model for studying the produced light hadrons in the QGP [66] where it was found that it was not only possible to obtain a good agreement with the experimental data in terms of p_T spectra both at RHIC and LHC energy, but also to correctly predict the baryon-to-meson ratios in the light sector (p/π, $\bar{p}/\pi$, Λ/K) [72]. The recombination model is also useful for studying other observables of the QGP among which the collective flow is one of the most interesting. Indeed the strong flow enhancement of the transverse momentum spectra of hadrons at intermediate p_T can be addressed quite automatically within a coalescence approach which explains naturally also the quark number scaling in the observed azimuthal anysotropy [73] (see later in this Chapter). Above all this model has been rapidly developed to calculate the production heavy meson [74] and heavy baryon production at relativistic HICs aiming to describe the p_T dependence of charmed baryon-to-meson ratio for different energies and finding in agreement with the recent experimental measurements Λ_c/D^0 at RHIC and LHC, that makes also suitable for predictions of Λ_b/B^0 values. We will provide the theoretical skeleton of our coalescence model later on in this Chapter, while we will postpone the analysis of the results in the final chapter of this thesis. For both cases we will refer specifically to our work [75]. After hadronization the produced baryons and mesons continue to propagate and scatter either in an elastic or in a inelastic way. This phase of HICs is usually described by means of transport models for an interacting hadron gas and collisions among particles treated through effective theories. Within this framework inelastic collisions are responsible for the variation of the hadron species abundances and are the first to drop out leaving the system to evolve in the so-called *chemical freeze-out*. When also the probability of elastic collisions becomes negligible which is believed to occur at $T \approx 120\,MeV$, the *kinetic freeze-out* is reached, meaning that spectra do not change until hadrons are finally captured by the detectors.

2.5 Heavy Quarks in the QGP

This section in now devoted to the main research topic of this thesis which is the study of Heavy Quarks (HQs) production and dynamics in the QGP. Before discussing in detail the theoretical framework which we adopt to describe HQs propagation (see next Chapter), here we will concentrate on the main stages which characterize the evolution of HQs in the strong interacting matter, from initial production to hadronization mechanism and final Heavy-Flavor (HF) hadron detection. The aim is to demonstrate how HQs represent a powerful probe of the QGP features and among the other possible *hard probes* they maintain a kind of uniqueness. Historically such role has been considered already dawn to the exploration of the QCD phase diagram. Indeed, the dissolution of charmonium states (J/ψ) arising from Debye screening effect which we mentioned in Chapter 1 has been proposed as a clean signature of the existence of QGP phase [76]. Nowadays, more phenomena have been predicted to govern HQs interaction inside nuclear matter and to play a significant role for the description of the correlations of HQ observables, as summarized in very recent reviews [77] [78]. This opens a scenario where the study of QGP within the HQs sector become more challenging both from experimental and theoretical perspective, but also suitable for new progresses and discoveries.

2.5.1 HQ production and initial stage evolution

Heavy Quarks (HQs), mainly charm c, bottom b and top t quarks have respectively masses of about 1.3, 4.5 and 174 GeV. Being so massive the top quark have unique property that its mean lifetime ($t_{top} \sim 10^{-24}\, sec$) is smaller than the strong interaction time scale $\sim 1\, GeV^{-1}$. For this reason top quark decays directly in $t \rightarrow bW$ before creating any hadronic bound states. In such short lifetime top quark does emerge and decay before the deconfined phase sets in and thus it is not useful for carrying information within the plasma dynamics. It has proposed very recently the possibility to probe some QGP properties through indirect analysis of top product decays [79], but such preliminary studies are beyond the main purpose of this work. Hence, in discussing about HQs in QGP we refer exclusively to *c* and *b* flavors.

2.5.2 HQ production in *pp* collisions

Charm and bottom have masses larger than the QCD scale $M_{c,b} \gg \Lambda_{QCD}$. Therefore, they are produced in hard scattering processes whose cross sections at partonic level can be suitably calculated within a Leading-Order (LO) pQCD scheme. The resulting tree-level Feynman diagrams of these partonic processes are represented in Fig. 2.13 and the related cross sections ($\hat{\sigma}_{ij\to Q\bar{Q}}$) expressions were firstly derived in Ref. [80] and we collect the corresponding scattering matrices in the Appendix A. Partonic cross sections are employed as kernel within a pQCD factorization scheme to calculate HQ yields

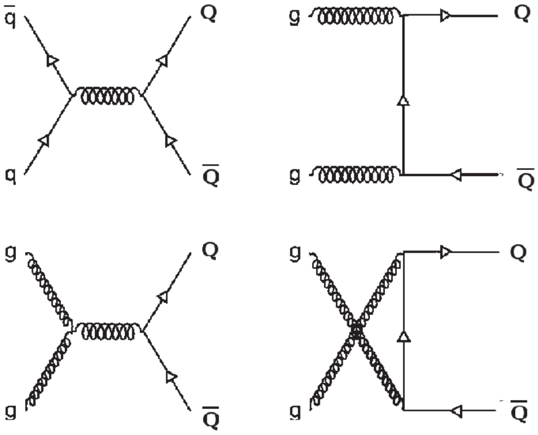

Figure 2.13: Associated production of HQs at LO pQCD level: starting from upper left the first diagram describes HQ production by quark-antiquark annihilation which in the high energy *pp* collisions conducted at RHIC and LHC facilities is overcome by the gluon-gluon fusion process which is represented by the last three diagrams in the picture.

in proton-proton (pp) collisions at center-of-mass energy $\sqrt{s}$

$$d\sigma^{pp}_{Q\bar{Q}}(\sqrt{s},\, p_T,\, M_{HQ}) = \sum_{i,j} \int dx_1 dx_2\, f_i^{(p)}(x_1, Q^2) f_j^{(p)}(x_2, Q^2) \times d\hat{\sigma}_{ij\to Q\bar{Q}}(x_1,\, x_2,\, p_T, Q^2) \tag{2.62}$$

In Eq. (2.62) $f_i^{(p)}(x_1, Q^2)$ are the Parton-Distribution Functions (PDFs) derived from phenomenological models and usually provided by parametrized expressions from analysis over many physics phenomena where universality law is assumed. Then the upper formula is coupled to an independent fragmentation function (FF) $D_{HQ}(z)$ which describes the non-perturbative transition of a HQ with transverse momentum p_T or total momentum p_{HQ} into a corresponding HF hadron with momentum $p_h = zp_{HQ}$ ($z < 1$). Detail expressions of the employed FFs will be presented in the hadronization paragraph. Hence, the cross section of heavy hadron (h_{HQ}) production in pp collisions is given by the following convolution

$$d\sigma^{pp}(h_{HQ}) = d\sigma^{pp}_{Q\bar{Q}} \otimes D_{HQ}(z) \tag{2.63}$$

with $d\sigma^{pp}_{Q\bar{Q}}$ defined in Eq. (2.62). The measured production yield of HF mesons at RHIC and LHC energies is already well reproduced within LO pQCD calculations. However, analytic extensions have been performed to provide a precise description of the inclusive heavy hadron production at Next-to-Leading-Order (NLO) and Next-to-Leading-Logarithm (NLL) pQCD accuracy by resummation of contributions of order $\alpha_s^n \log^k(p_{HQ}/M_{HQ})$. Models differ also in the choice of the renormalization scale μ_F and its relation to the energy scale Q^2 appearing explicitly in the PDFs and in the running coupling constant $\alpha_s(Q^2)$ inside the partonic cross section $d\hat{\sigma}_{ij\to Q\bar{Q}}$. In the Fixed-Flavor-Number Scheme (FFNS) [81, 82] a HQ is not considered as an active parton within the proton structure, so the sum over all the possible partonic pairs for charm production in Eq. (2.62) has to be performed only considering the three light quark flavors u, d, s with corresponding antiquarks and gluons g. The active flavor extends to $c, \bar{c}$ for bottom production because renormalization scale has to be taken larger than charm mass ($\mu_F > M_c$), even if for simplicity one usually neglects the terms containing M_c in the hard scattering cross sections. For this reason the FFNS scheme generally works in the low p_T region up to about $5M_{HQ}$. In order to extend the kinematical range of validity a better approach is the General Mass Variable Fixed Number Scheme (GV-VFNS) [83, 84] in which the number of active flavors is changed when μ_F crosses a transition scale fixed to the HQ mass. One of the most widespread approach that is valid in the entire kinematical range is the so-called Fixed Order Next Leading Logarithm (FONLL) [85, 86, 87] which is based on the idea to match the NLO cross sections evaluated by retaining HQ masses and tuning μ_F within the FFNS scheme to a massless NLO calculation performed within the Zero Mass (ZM)-VNFS scheme. This is equivalent to the previous GV-VFNS, but the fact that at high momenta M_{HQ} is discarded. We refer to [88] for a detail review. Experimental measurements of D and B production at both RHIC pp collisions at $\sqrt{s} = 200\,GeV$ and LHC pp collisions from $2.76\,TeV$ up to $14\,TeV$ are in agreement with the upper limits of the FONLL predictions. For this reason we will adopt FONLL central expectation values to derive charm and bottom initial spectra and perform convolution with appropriate FFs to derive heavy hadron spectra in pp collisions that we employ as a baseline for simulation in AA collisions and calculation of related observables (see Chapter 5). In conclusion the general fine working of these pQCD scheme and the most recent measurements from STAR, ALICE and CMS in pp collisions seem to confirm that both charm and bottom can be consistently treated as *heavy* particles being produced at hard scales and uncoupled to thermal excitation of the *bulk* matter, even if for charm quark there are still uncertainties in the low p_T regime. For bottom quarks instead direct measurements have been obtained presently only by LHC collaborations, while extrapolations at RHIC energies can be done through unfolding procedures on D and B decay products.

2.5.3 HQ production in HICs: Cold Nuclear Matter Effects

In nucleus-nucleus collisions the production of HQs at low momenta is influenced by various phenomena which originate from the presence of bound states of nucleons rather than having free protons in the colliding beams. These processes are overall denoted as Cold-Nuclear Matter Effects (CNMEs) in order to differentiate them from the follow-up modifications due to the HQ propagation and interaction within the QGP phase. However, trying to disentangle CNMEs from the whole effects resulting from the dynamical evolution of HQs in QCD matter is extremely hard and one way to study them is looking at small system scenarios, like for example nucleon-nucleus collisions in which a hot QGP medium should not be formed, or eventually be held in shorter lifetime compared to HICs [89]. From a theoretical perspective CNMEs are considered by modeling phenomenological nuclear Parton Distribution Functions (nPDFs) through the following expression

$$f_i^A\left(x,\, Q^2\right) = R_i^A\left(x,\, Q^2\right) f_i^p\left(x,\, Q^2\right) \tag{2.64}$$

$R_i^A(x,\, Q^2)$ are called the Nuclear Modification Functions of the free proton PDFs $f_i^p(x,\, Q^2)$ for all parton species and for HQ production in HICs they substitute the latter within the pQCD factorization formula Eq. (2.62). These functions are usually provided in parametrized form at the lowest energy scale corresponding to the charm quark mass $Q_0^2 = M_c^2 = 1.69\, GeV^2$ and baryon number together with momentum sum rules are imposed:

$$\int_{x_{min}}^{1} dx \left[f_{u_V}^A(x,\, Q_0^2) + f_{d_V}^A(x,\, Q_0^2)\right] = 3 \qquad \sum_{i=g,\, q,\, \bar{q}} \int_{x_{min}}^{1} dx f_i^A(x,\, Q_0^2) = 1 \tag{2.65}$$

where $x_{min} \rightarrow 0$ and on the left hand side of first expression of Eq. (2.65) the valence u and d quarks nPDFs are considered within an isospin symmetry. Then, the evolution of the nPDFs at higher scales $Q^2 > Q_0^2$ is obtained by solving the well known DGLAP equations within the same NLO pQCD renormalization scheme adopted for regular PDFs. Finally all possible cross sections for an extended set of phenomena are computed and analyzed in comparison with the experimental data, providing at the end an optimal parametrization fit for the calculation of the process of interest. In Fig. (2.14) we report the obtained Nuclear Modification Functions from the renowned EPS09 package [90] which we will couple to the FONLL pp HQ spectra to get initial charm and bottom p_T spectra for our simulations in AA collisions.

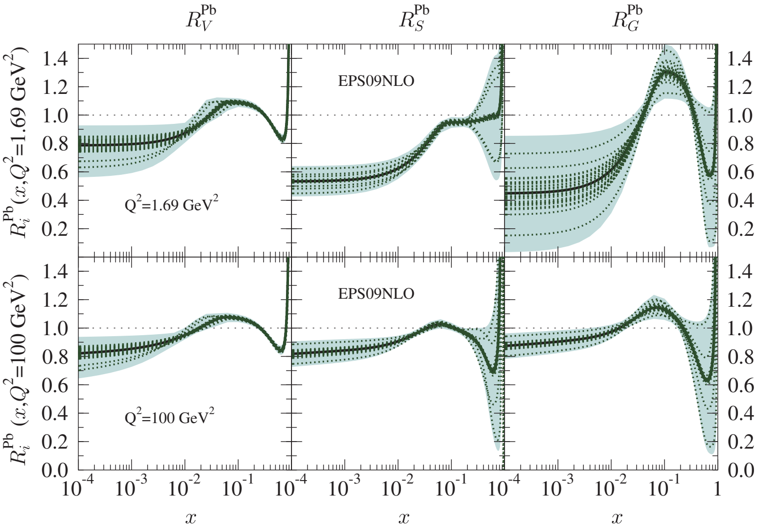

Figure 2.14: Nuclear Modification Functions $R_i^A(x)$ for valence quarks ($i = V$, left plots), see quarks ($i = S$, center plots) and gluons ($i = G$, right plots) in lead nuclei ($A = 297$) obtained from EPS09 package [90] and evaluated at $Q_0^2 = M_c^2$ scale (upper) and $Q^2 = 100\,GeV^2$ scale (lower).

2.5.4 HQ dynamics in pre-equilibrium phase

As we discussed previously in this Chapter, initial conditions of high energy pp, pA and AA collisions can be treated within the effective Color-Glass-Condensate (CGC) theory [43, 44, 45, 46] in which fast partons in the nuclei can be divided into large-x partons that serve as color sources of the radiating chromo-electric and chromo-magnetic fields and into small-x partons that are essentially the gluons in the hadron wavefunction, since the gluon PDF dominates at small x values. The collision between two color glass sheets leads to the formation of strong gluon fields in the forward light-cone region named as the Glasma system [91, 92, 93]. In the weak coupling regime the Glasma is constituted of longitudinal color-electric and color-magnetic fields $F^a_{\mu\nu}(x)$ which are characterized by large occupation number $A^a_\mu \simeq 1/g$. Hence they can be described by Classical Yang-Mills (CYM) theory with quantum fluctuations entering as corrections at higher order in the expansion over the coupling g. Theoretical studies based on the CGC model with dynamical evolution into CYM Glasma predict that this pre-equilibrium phase should form at about $\tau_{glasma} \simeq 0.1\, fm$ after the collision. Since HQs are produced in hard pQCD processes with characteristic formation time $\tau_f \simeq 1/2M_{HQ} \leq 0.1\, fm$ they can actually probe the Glasma phase in the background without disturbing its evolution because of their small number and their large mass which make HQs a negligible source of color currents. However, the investigation of HQ dynamics at initial or pre-equilibrium stages of HICs has been always tarnished compared to the standard description of their propagation within the hydro QGP phase. That is because the expected effect occurring in the initial phase may be washed out by the longer dynamics in the QGP in the case of AA collisions. The study of HQ dynamics in the Glasma phase started with simplified models that attempted to interpret it similarly to the evolution in the thermally equilibrated medium [94, 95]. In this paragraph we would like instead to focus on the development of a recent approach in which HQs, specifically charm quarks, propagate firstly in the Glasma modeled from a $SU(2)$ CYM theory and then at $\tau_0 \simeq 0.3 - 0.6\, fm$ their dynamics is shifted consistently to the standard description within the QGP. As discussed in Ref. [96], when charm quarks move under the effect of Lorentz force due to the interaction of their color charge with the evolving CYM fields of the Glasma $F^a_{\mu\nu}$, with index $a = 1, 2, 3$ and structure constants $f^{abc} = \epsilon^{abc}$ ($\epsilon^{123} = 1$), they follow precise equations of motion known as Wong equations [97]

$$\frac{dx_i}{dt} = \frac{p_i}{E} \tag{2.66}$$

$$E\frac{dp_i}{dt} = Q_a F^a_{i\nu} p^\nu \tag{2.67}$$

where $i = x, y, z$ and $E = \sqrt{p^2 + M_c^2}$ is the energy of the charm quark with momentum p. Moreover, this set of equations are coupled also to the evolution of the HQ color charge Q_a which is determined from the conservation law of gauge theory $\left[D_\mu, J^\mu\right] = 0$ that we can write explicitly as

$$E\frac{dQ_a}{dt} = -Q_c\epsilon^{cba}\boldsymbol{A}^b(x)\cdot\boldsymbol{p} \tag{2.68}$$

provided an initial charm color charge Q^a which is distributed randomly between (-1,1) for each component and where the fields $\boldsymbol{A}^b(x)$ with its conjugate momenta $\boldsymbol{E}^b(x)$ satisfying the $SU(2)$ CYM equations of motion [98] [99]

$$\frac{dA_i^b(x)}{dt} = E_i^b(x) \tag{2.69}$$

$$\frac{dE_i^b(x)}{dt} = \sum_j \partial_j F_{ji}^b(x) + \sum_{d,c,j} \epsilon^{bcd} A_j^c(x) F_{ji}^d(x) \tag{2.70}$$

These equations are consistently solved in a three dimensional space given some initial conditions from CGC model [43, 44, 45].

This approach has been firstly applied to describe the evolution of HQs in the initial stages of pA collisions and it has been found that the propagation of charm inside the Glasma lead to an average acceleration which can be interpreted as a *cathode tube effect* [98, 100]. Hence, the charm p_T spectrum is tilted in such a way that their yield is reduced below one at low p_T, while it is enhanced at intermediate p_T, in agreement with what has been experimentally measured at LHC pPb $\sqrt{s} = 5.02\,TeV$ collisions by ALICE [101] and LHCb [102] collaborations. The goal of this study was to offer a qualitative description of what is observed in pA collisions in order o give some alternative explanation regarding the standard use of CNMEs to the depletion of the charm spectrum at low p_T. In Ref. [96] the model has been extended for carrying out simulations for LHC $PbPb$ collisions at $\sqrt{s} = 5.02\,ATeV$. The main result was to show that HQ interaction with the glasma fields induces a dynamics that is opposite to the standard in medium scattering with thermal partons of the *bulk* (see Chapter 3). As a consequence there exists an anti-correlated behavior among the suppression factor and the collective flow of charm quarks which is then washed out during the propagation of HQs in the QGP. On the other hand the tilted effect on the charm p_T distribution leads to the necessity of a more interacting HQ evolution within the equilibrated plasma which results in a more effective coupling of HQs to the *bulk* anysotropies. We will not proceed further in discussing the HQ dynamics in the pre-equilibrium phase, just we point out that this novel study shows that HQs actually can keep memory of the initial dynamics, hence being sensitive to both initial E.M. fields [36] and vorticity effects, a prediction that appears to be confirmed by early experimental results both at RHIC [103] and LHC energies [104].s A chronological description about the propagation of HQs along the evolving *fireball* created at the center of HICs would lead us to discuss now about their dynamics and interaction within the thermal equilibrium phase, namely the QGP. However, since this represents the main topic of this thesis, we will postpone it to Chapter 3. There we will discuss about our transport approach to treat HQ energy loss and coupling with *bulk* anysotropies until the transition phase occurs and HQs fragment or recombine with light quarks of the medium to form the corresponding HF hadrons. We will address now about the description of such hadronization mechanisms.

2.5.5 Hadronization mechanisms for HQs

In the previous section we discussed about the general hadronization process by which partons are converted into corresponding hadrons. In particular, we focused on the idea that in medium hadronization at $T \sim T_c$ differs from that in vacuum, because instead of fragmenting into hadron sprays comoving partons in the QGP can combine in the phase-space and produce hadrons with final energy and momentum given by the sum of the two parton ones. Due to the fact that $M_{HQ} \gg T_c$, HQs can preserve their identity at hadronization both for recombination by picking-up a light quark of the bulk and for independent fragmentation. In this paragraph we present a detail analysis of a hybrid fragmentation plus coalescence model which we couple at the final stage of our HQ transport evolution to obtain the yield of heavy mesons and baryons with corresponding flow observables (see Chapter 5).

This model is described in Ref. [75] where it is applied for predictions of HF baryon-to-meson ratio which represent a genuine measure of the impact of hadronization by coalescence.

Coalescence for HQs

In the Wigner formalism [66, 67, 68, 69] the p_T-spectrum for Heavy-Flavor (HF) hadrons is given by the

$$\left(\frac{dN_{h(HQ)}}{d^2p_T dy}\right)_{coal.} = g_h \int \prod_{i=1}^{n} \frac{d^3p_i}{(2\pi)^3 E_i} p_i \cdot d\sigma_i \; f_{q_i}(x_i, p_i) \\ \times f_{h(HQ)}(x_1, ..., x_n; p_1, ..., p_n)\, \delta\left(p_T - \sum_{i=1}^{n} p_{T,i}\right) \qquad (2.71)$$

where $d\sigma_i$ denotes an element of a space-like hypersurface, $f_{q_i(\bar{q}_i)}(x_i, p_i)$ is the single quark (antiquark) phase-space distribution functions with spin $1/2$ and g_h is the statistical factor to form a colorless hadron. In particular, we use $g_h = 1/36$ for D and B mesons, while for Λ_c and Λ_b we fix $g_h = 1/108$. The number of multiple integrations is equivalent to $n = 2$ for mesons and to $n = 3$ for baryons. Finally $f_{h(HQ)}(x_1, ..., x_n; p_1, ..., p_n)$ is the Wigner function which describes the spatial and momentum distribution of quarks (antiquarks) inside the hadron and that can be related directly to its quantum wave function. In agreement with other models [105, 106] we adopt for $f_{h(HQ)}(x_1...x_n, p_1...p_n)$ a Gaussian shape in coordinate and momentum space. In particular, for mesons we use

$$f_M(x_1, x_2; p_1, p_2) = A_W \exp\left(-\frac{x_{r_1}^2}{\sigma_r^2} - p_{r_1}^2 \sigma_r^2\right) \qquad (2.72)$$

where x_{r_1} and p_{r_1} are the relative coordinate and momentum of the heavy-light quark (HQ-q) pair

$$x_{r_1} = x_1 - x_2 \quad , \quad p_{r_1} = \frac{m_q p_1 - M_{HQ} p_2}{m_q + M_{HQ}} \qquad (2.73)$$

while σ_r is a covariant width parameter that is linked to the size of the HF meson, i.e. to the root mean square charge radius, by the following formula

$$\left\langle r_M^2 \right\rangle_{ch} = \frac{3}{2} \frac{Q_{HQ} m_q^2 + Q_q M_{HQ}^2}{(m_q + M_{HQ})^2} \sigma_r^2 \tag{2.74}$$

In Eq.(2.72) A_W is a normalization constant that guarantees that in the limit $p \to 0$ all HQs hadronizes through recombination. Similarly we construct the Wigner function for baryons through a double Gaussian profile

$$\begin{aligned} f_B(x_1, x_2, x_3; p_1, p_2, p_3) = A_W \ \exp\left(-\frac{x_{r_1}^2}{\sigma_{r_1}^2} - p_{r_1}^2 \sigma_{r_1}^2 \right) \\ \times A_W \ \exp\left(-\frac{x_{r_2}^2}{\sigma_{r_2}^2} - p_{r_2}^2 \sigma_{r_2}^2 \right) \end{aligned} \tag{2.75}$$

In this case the coalescence mechanism is brought consecutively combining first two particles, regarding it is a light or heavy quark, and then collecting the third one with the resulting pair. Relative coordinates and momenta are so generalized as

$$x_{r_1} = x_1 - x_2 \quad , \quad p_{r_1} = \frac{m_2 p_1 - m_1 p_2}{m_1 + m_2} \tag{2.76}$$

for the first couple and

$$x_{r_2} = \frac{m_1 x_1 - m_2 x_2}{m_1 + m_2} - x_3 \quad , \quad p_{r_2} = \frac{m_3 (p_1 + p_2) - (m_1 + m_2) p_3}{m_1 + m_2 + m_3} \tag{2.77}$$

with the same normalization constant A_W in Eq.(2.75) and the two width parameters σ_{r_1} and σ_{r_2} related to the baryon root mean square charge radius

$$\begin{aligned} \left\langle r_B^2 \right\rangle_{ch} &= \frac{3}{2} \frac{Q_1 m_2^2 + Q_1 m_2^2}{(m_1 + m_2)^2} \sigma_{r_1}^2 \\ &+ \frac{3}{2} \frac{(Q_1 + Q_2) m_3^2 + Q_3 (m_1 + m_2)^2}{(m_1 + m_2 + m_3)^2} \sigma_{r_2}^2 \end{aligned} \tag{2.78}$$

The width parameters σ_r and $\sigma_{r_{1,2}}$ appearing respectively in the Wigner function for mesons Eq. (2.72) and baryons Eq. (2.75) depend on the hadron species and we calculated using the charge radius values taken from the quark model [107, 105]. The multi-dimensional integrals appearing in the coalescence spectrum are numerically evaluated by means of a Monte-Carlo test-particle method which has been firstly developed in Ref. [66] and it is described in detail in the Appendix of Ref. [75]. This method consists of introducing a large number of test partons distributed uniformly in momentum in the phase-space but associated probability $P_{q(i)}(P_{\bar{q}(i)})$ for the$i$ quark (antiquark) with corresponding transverse momentum p_T. Then this probability is normalized by requiring that the sum over the all parton probabilities equals to the total quark (antiquark) number

$$\sum_i P_q(i) = \frac{dN_q}{d^2p_T} \quad , \quad \sum_i P_{\bar{q}}(i) = \frac{dN_{\bar{q}}}{d^2p_T} \tag{2.79}$$

Within this test-particle method the coalescence formula Eq. (2.71) is mapped for HF mesons and baryons into the following expressions

$$\left(\frac{dN_M}{d^2p_T dy}\right)_{coal.} = g_M \sum_{i,j} P_q(i)P_{\bar{q}}(j)\, \delta(p_T - p_{i,T} - p_{j,T}) \\ \times f_M(x_i, x_j; p_i, p_j) \tag{2.80}$$

$$\left(\frac{dN_B}{d^2p_T dy}\right)_{coal.} = g_B \sum_{i\neq j\neq k} P)q(i)P_q(j)P_q(k)\delta^{(2)}(p_T - p_{i,T} - p_{j,T} - p_{k,T}) \\ \times f_B(x_i, x_j, x_k; p_i, p_j, p_k) \tag{2.81}$$

with Wigner functions f_M and f_B taken respectively from Eq. (2.72) and Eq. (2.75). In Fig. (2.15) we show the coalescence probability P_{coal} for charm and bottom quarks that is defined as the probability that a single HQ with transverse momentum p_T hadronize into a HF meson or baryon according to hadronization mechanism. We point out that for charm quarks a difference in P_{coal} passing from RHIC to LHC is visible in the high p_T tail, while for bottom quarks it is almost washed out due to the more hardness of the p_T distribution.

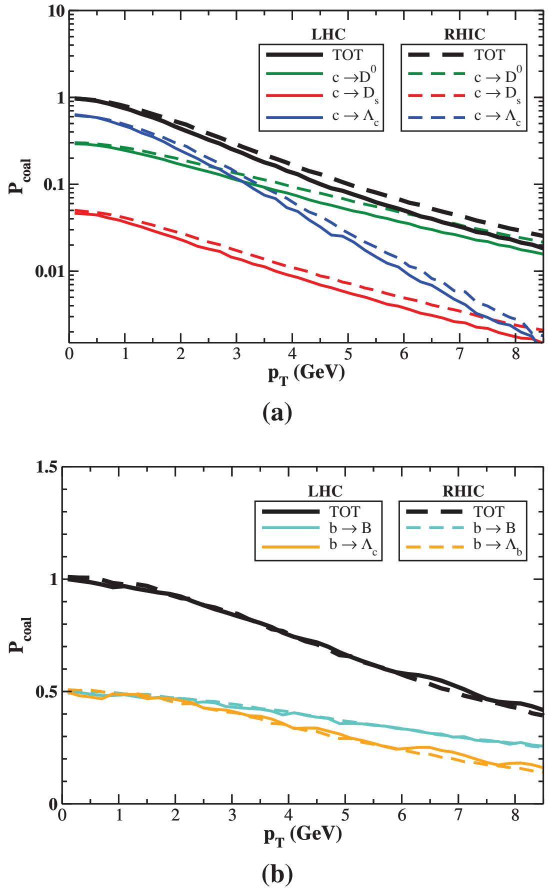

Figure 2.15: Coalescence probability P_{coal} for charm (upper) [75] and bottom (lower) as function of transverse momentum p_T. The various colors indicate the different hadron species, while black line represents the total probability that charm or bottom quarks hadronize by coalescence into all possible HF hadrons. The solid lines refer to LHC energies while dashed ones are for the RHIC case.

Fragmentation for HQs

After in medium evolution in the QGP phase, Heavy Quarks (HQs) which do not hadronize through recombination with light quarks of the bulk, convert to the corresponding Heavy-Flavor (HF) hadrons by fragmentation mechanism. From the coalescence probability $P_{coal}(p_T)$ we assign the fragmentation probability defined as $P_{fragm}(p_T) = 1 - P_{coal}(p_T)$ and compute the HF hadron

p_T spectrum in the following manner

$$\frac{dN_{h(HQ)}}{d^2p_T dy} = \int dz \left(\frac{dN_{HQ}}{d^2p_T dy}\right)_{fragm.} \frac{D(HQ \rightarrow h_{HQ})(z, Q^2)}{z^2} \tag{2.82}$$

In Eq.(2.82) the momentum spectrum of HQs which do not undergo to coalescence is indicated as $(dN_{HQ}/d^2p_T dy)_{fragm.}$ and it is convoluted with the fragmentation functions (FFs) $D(HQ \rightarrow h_{HQ})(z, Q^2)$, which give the probability of charm or bottom quark to fragment into a corresponding HF hadron carrying away a fraction $z = p_h/p_c$ of the total momentum of the leading HQ. Fragmentation process into a HF hadron is evaluated at momentum scale $Q^2 = (p_h/2z)^2$ and FFs are chosen within a universality class as in vacuum fragmentation mechanism with Q^2 evolution obtained through general DGLAP equations. In particular, for hadronization at HQ mass scale we employ Peterson FFs parametrization [108]

$$D(HQ \rightarrow h_{HQ})(z) = \frac{1}{z\left[1 - \frac{1}{z} - \frac{\epsilon_c}{1-z}\right]^2} = \frac{z(1-z)^2}{\left[(1-z)^2 + \epsilon_c z\right]^2} \tag{2.83}$$

which are characterized by a peaked shape at $z \rightarrow 1$ and so can feasible model the property of HQs to have a harder fragmentation with respect to light partons. In Fig. (2.16) we present Peterson FFs for charm and bottom quarks. As we will discuss in Chapter 5 the ϵ_c parameter is determined by tuning fragmentation from initial HQ spectra to reproduce the experimental HF mesons and baryons yields in pp collisions measured at RHIC and LHC.

Before introducing the main QGP observables in the HQ sector, in the next paragraph we will give a brief description of how the analysis of HQ interaction within the QCD medium can be treated by means of the non-perturbative lQCD approach (see Chapter 1).

2.5.6 Heavy quark diffusion in Lattice QCD

Transport properties of strongly interacting matter can be explored in lattice QCD (lQCD) by analyzing the current-current correlations. Given some

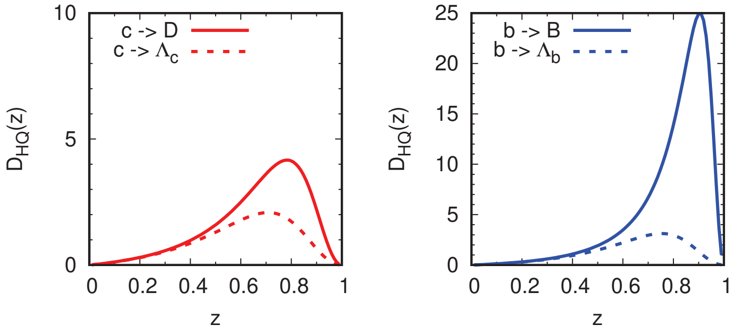

Figure 2.16: Peterson Fragmentation Functions (FFs) of charm (left) and bottom (right) quarks as function of hadron momentum fraction z. The parameter ϵ_c in Eq. (2.83) is tuned to fragmentation either into HF mesons (solid lines) or into HF baryons (dashed lines).

current $J(\tau, \vec{x})$ we can define the Eucildean space-time correlator [109]

$$G_J^{\alpha\beta}(\tau, \vec{x}) = \int d^3\vec{x}\, e^{i\vec{p}\vec{x}} < J^\alpha(\tau, \vec{x}) J^\beta(0, \vec{0}) >= \int \frac{d\omega}{2\pi} \rho_J^{\alpha\beta}(\omega, \vec{p}) K(\omega, \tau) \quad (2.84)$$

where in the last step of Eq. (2.84) we introduced the spectral representation of the euclidean space-time correlation functions. Spectral functions $\rho_J^{\alpha\beta}(\omega, \vec{p})$ are actually difficult objects to calculate but rather very important, because at high frequencies, i.e. large ω, they provide information about in-medium formation of bound states, like resonances and quarkonia, while for small values ω they give access to the response of the medium trough perturbations. This can be done in order to calculate electric conductivity σ_{el} in case the system is perturbed by an external external Electro-Magnetic (E.M.) field, or for example if we consider a HQ propagating in a thermodynamically equilibrated plasma whose properties are thus probed through the HQ interaction with the strong QCD fields. According to Kubo formulas in linear response theory, transport coefficients can be extracted from the spectral function in equilibrium thermodynamics by calculating its slope in the limit of vanishing energy. Hence, if we identify the fermionic current with the vector current of HQ fields $J^{\mu}_{V,HQ}(\tau,\vec{x}) = \bar{\psi}_{HQ}(\tau,\vec{x})\gamma^{\mu}\psi_{HQ}(\tau,\vec{x})$ the corresponding spectral function the vector channel is related to the diffusion coefficient D_s of HQs inside the QGP by the following expression [110]

$$D_s = \frac{1}{6\chi_2^{HQ}} \lim_{\omega\to 0} \lim_{p\to 0} \sum_{i=1}^{3} \frac{\rho^{ii}_{V,HQ}(\omega,\vec{p},T)}{\omega} \tag{2.85}$$

where χ_2^{HQ} is the HQ number susceptibility which is defined through the zeroth component of the temporal meson correlator in vector (V) channel. This is equivalent to the net charm number susceptibility calculated through an expansion of thermodynamic variables (P/T^4) in lQCD at small non-zero chemical potential [111]. The interest of calculating D_s in lattice QCD is motivated by the heavy quark energy loss puzzle [112, 113, 114]. Unexpectedly HQs are found to lose significant energy and meanwhile strongly couples to medium anysotropies. This results into measured observables which are not describable by pQCD scheme, rather they need the formulation of more complex non-perturbative interaction framework to be implemented within some transport approach. Then, it is possible to compare the obtained D_s from such phenomenological models to lQCD expectations of the same quantity with the aim to investigate directly the properties of the dynamical system interacting with the HQS with what QCD theory is indicating. That is actually a goal of this thesis, hence we will postpone a more quantitative discussion to the final Chapter.

2.6 QGP and HQ Observables

2.6.1 Nuclear Modification Factor

Particles with high transverse momentum p_T are produced at early-stages of HICs and propagate through the QGP phase loosing a significant amount of energy which is soon dissipated in the plasma. This phenomenon, commonly named as *jet quenching* of energetic partons [115], reflects into the suppression of hadron distributions at high p_T and is quantitatively estimated through the *nuclear modification factor* $R_{AA}(p_T)$ which is defined as follows

$$R_{AA}\,(b,p_T) = \frac{d^2N^{had}_{AA}/(d^2p_T\,d\eta)}{N_{coll}(b)\,d^2N^{had}_{pp}/(d^2p_T\,d\eta)} = \frac{d^2N^{had}_{AA}/(d^2p_T\,d\eta)}{T_{AA}(b)\,d^2\sigma^{had}_{pp}/(d^2p_T\,d\eta)} \tag{2.86}$$

Experimentally the R_{AA} corresponds to the ratio between hadron p_T spectra in nucleus-nucleus collisions and the same spectra measured in pp collisions, properly scaled by the number of binary nucleon-nucleon collisions calculated from the Glauber model (Eq. (2.11)). Equivalently the R_{AA} may be defined as the measured hadron yield in AA collisions at mid-rapidity divided by the production cross section of the same hadron species in pp collisions (Eq. (2.59)) scaled by the overlap function for the estimated centrality class (Eq. (2.3)). Hence, particles like photons which do not strongly interact with the system and instead leave the central region almost unaffected have by construction $R_{AA} \simeq 1$ as it is experimentally demonstrated by PHENIX data in Fig. (2.17) within the uncertainty bars. In the meantime this proves that the measured deviation of R_{AA} of π and η mesons from 1 at high p_T happens because of the scattering processes happening within the dense QCD plasma. There are many theoretical models which attempt to describe *jet quenching* in terms of opacity expansion performed at the beginning for static medium [116, 117] and later developed to included also the dynamical evolution of the medium [118, 119]. We refer to [120] for more details. First data on suppression of Heavy-Flavor (HF) hadrons were collected at RHIC experiments with the measurements of *non-photonic single electrons* $e^{\pm}$ coming from the combined decay of D and B mesons quenched distributions [122].

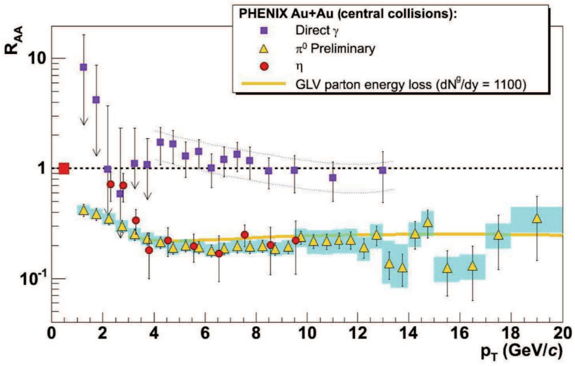

Figure 2.17: Picture from Ref. [121]: the nuclear modification factor of π^0 and η mesons at RHIC $AuAu$ central collisions at $\sqrt{s} = 200\,AGeV$ is compared to the measured R_{AA} of direct photons. PHENIX data are quite well reproduced within the parton *jet quenching* description through Gyulassy-Levai-Vitev (GLV) model [115].

Still at RHIC the upgrade of STAR detectors lead to direct measurement of R_{AA} of prompt D^0 in $AuAu$ collisions at $\sqrt{s} = 200\,GeV$ [123]. Both experimental results are shown in Fig. (2.18) adapted from the recent review [88]. During the drawing up of this thesis STAR collaboration announced a reanalysis of the measured D meson nuclear modification factor with consequent correction of the experimental data [124]. Compared to previous results the new data present significant suppression at low p_T with a discrepancy larger than their uncertainty bars, while they stay quite in agreement with the old ones at high p_T. With the beginning of the LHC era measurements of the nuclear modification factor were carried out both for charged and neutral light particles as well as for the HF hadrons where in this case the larger charm production cross section $\sigma_{c\bar{c}}(LHC) \approx 100 \cdot \sigma_{c\bar{c}}(RHIC)$ allowed for a sufficient statistics for D meson detection quite immediately. In Fig. (2.19) we report ALICE results for average D meson R_{AA} in a wide range of p_T measured at LHC $PbPb$ collisions at $\sqrt{s_{NN}} = 2.76\,TeV$ for central (left) and peripheral collisions (right) compared to some models where charm quarks lose energy either by only elastic collisions or where also energy loss by in medium gluon radiation is accounted. Nowadays, also data for D meson production at LHC most energetic HICs are available both from ALICE and also

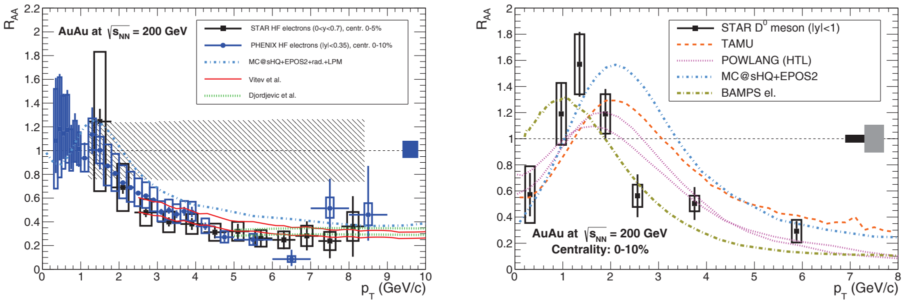

(a) **(b)**

Figure 2.18: Left: Suppression of single $e^{\pm}$ from HF decay measure at RHIC central collisions by PHENIX (black dots) and STAR (blue squares) collaborations compared to some jet quenching theoretical models (see [88] and references therein). The opaque region corresponds to the experimental normalization factor from experiments. Right: Measured R_{AA} of prompt D^0 meson from STAR at RHIC $AuAu$ central collisions at $\sqrt{s_{NN}} = 200\,GeV$ compared to transport approaches.

s

CMS collaborations [125] [126]. Let us focus on the problem arising from this experimental results. It was quite surprising to observe such significant suppression charm spectra with a value of the measured R_{AA} comparable with that for light hadrons. Such unexpected result is an indication that HQs propagate in a strongly interacting QGP and at least for charm quarks can achieve thermalization condition. This is the reason why preliminary models based on a pQCD interaction of HQs (see Ref. [127]) completely fails to reproduce the observed suppression with also a too large estimated thermalization time $\tau_{eq}(pQCD) \sim 15-20\,fm$ for charm quarks. Moreover the majority of theoretical models develop jet quenching kernel with a mass hierarchy condition, motivated for example by QED analogy of bremsstrahlung difference from electrons to muons whose, $\Delta E_{\mu} \simeq \Delta E_{e}(m_e/m_{\mu})^4$, or from QCD assumptions on color factors as firstly calculated in Ref. [128]. In the high p_T region where radiative energy loss is dominant, one should expect for the various partonic species such behavior $\Delta E_b < \Delta E_c < \Delta E_q \leq \Delta E_g$, the gluon being larger than the light quarks due to splitting contributions. However, this is not observed experimentally at least from the comparison of charm to charged suppression, while for a mass hierarchy condition between charm and bottom

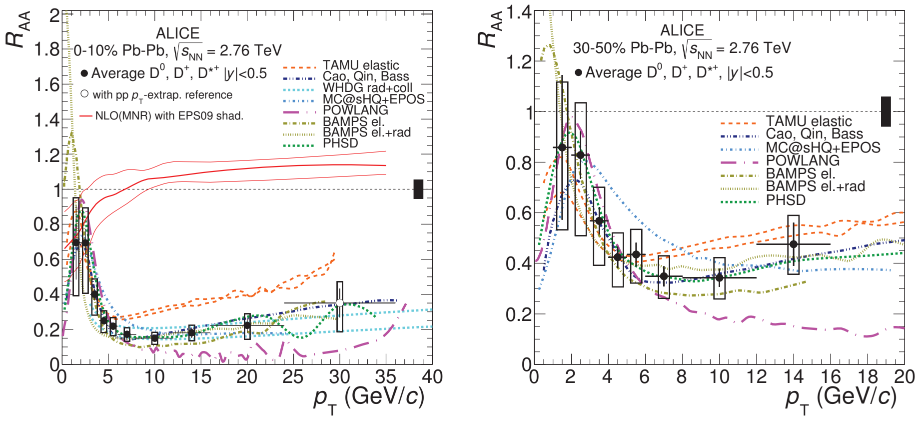

(a) **(b)**

Figure 2.19: Average D meson R_{AA} experimentally measured at LHC central collisions and compared to transport approaches. For central collisions (left) initial charm spectra in $PbPb$ accounts for CNMEs as pointed out by the red solid curves which come from the EPS09 parametrization [90]. For semi-peripheral collisions (right) shadowing is included within some models resulting in an integrated R_{AA} smaller than 1. Picture is adapted from Ref. [78]

a final conclusion cannot be established yet due to the large uncertainties in the available data form B mesons which at LHC lack of a significant amount of statistics, while at RHIC energies they can only be inferred by undirect unfolding extrapolations from D mesons measurements. That, of course, represents a very interesting puzzle which is also is conditioned by the fact of how interacting HQs then couple to the *bulk* anisotropies to the develop an observed large elliptic flow as we will soon discuss. We mention here that most part of this work is devoted to solve such puzzle and based on previous investigation which brought towards a solution of this problem we faced up with new unexpected phenomena which seem to us strongly correlated to the challenging of HQ observables. That relates for example to the inclusion of what hadronization of HQ tell us about the final produced HF mesons and baryons. We will focus on this discussion in Chapter 5.

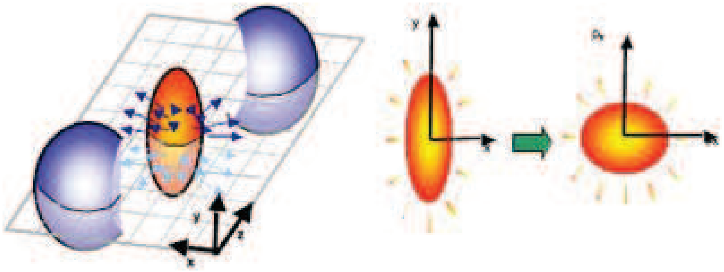

Figure 2.20: Schematic representation of collective flow formation. The Reaction Plane (RP) is identified by the impact parameter b and the longitudinal direction along the beam axis z.

2.6.2 Elliptic Flow

In non-central ($b \neq 0$) nucleus-nucleus collisions the overlapping region is characterized by a large anisotropy in coordinate space that can be quantified in terms of spatial eccentricity

$$\epsilon_x(b) = \frac{\langle y^2 - x^2 \rangle}{\langle y^2 + x^2 \rangle} \tag{2.87}$$

The initial value of such eccentricity can be calculated through Glauber Model or Color Glass Condensate [129] where x and y in Eq. (2.87) are the positions of the participating nucleons in the transverse plane, while the brackets denote an average over their number. In hydrodynamical description matter in this region is characterized by high density and temperature with pressure gradients that make it more compressed along the direction of impact parameter b with respect to the orthogonal direction in the transverse plane ($\partial_x P > \partial_y P$). Such pressure gradients generate collective flows which drive the expansion and cooling of the *fireball* to reach thermal equilibrium at estimated timescale of the order of 1 fm. A schematic illustration is given in Fig. (2.20). During this phase, the initial spatial deformation is converted by particle interaction to anysotropies in momentum space which experimentally can be analyzed in terms of Fourier expansion of the azimuthal momentum distribution of particles with respect to the Reaction Plane (RP). Hence, the invariant momentum distribution can be written as

$$E\frac{dN}{d^3\vec{p}}(b) = \frac{dN}{2\pi p_T dp_T dy} \cdot \left[1 + \sum_{n=1}^{\infty} v_n(b;\, p_T,\, y) \cos\left(n(\phi - \Phi_{RP})\right)\right] \tag{2.88}$$

where ϕ is the azimuthal angle of the particle and Φ_{RP} is the azimuthal angle of the reaction plane in the laboratory frame that is determined experimentally with sophisticated techniques [130, 131]. The magnitude of the anysotropic flows is encoded in the Fourier coefficients v_n in Eq. (2.88) which are defined with respect the angle of the reaction plane. In particular, if the evolution of the *fireball* starts from an initial almond shape as represented in Fig. (2.20), the largest harmonic flow is represented by the second coefficient of the density expansion which is known as *elliptic flow* and it is determined through the following formula

$$v_2(b;\, p_T,\, y) = \langle \cos\left(2\left(\phi - \Phi_{RP}\right)\right)\rangle = \left\langle \frac{p_x^2 - p_y^2}{p_x^2 + p_y^2} \right\rangle \tag{2.89}$$

Measurements of elliptic flow have been extensively conducted both at RHIC and LHC experiments. Since the angle of the reaction plane in Eq. (2.89) can not be directly measurable, the estimate of v_2 passed through the analysis of two and four-particle azimuthal correlations with the aim to suppress non-flow contributions generated by resonance decays and jets reconstruction [132]. In Fig. (2.21) experimental measurements of v_2 at RHIC $AuAu$ collisions at $\sqrt{s_{NN}} = 200\, GeV$ are compared with hydrodynamical calculations for different values of constant *shear viscosity* starting from perfect fluid simulations ($\eta/s = 10^{-4}$) and increasing the value of η/s with integer steps of the lowest bound conjecture $\eta/s = 1/4\pi$ that is computed through the correspondence of the Anti-de Sitter Conformal Field Theory (AdS/CFT) to a $SU(4)$ supersymmetric Yang-Mills theory [135]. Indeed since the expansion of the system and the build-up of collective motion depend on the velocity of sound $c_s = \sqrt{\partial P/\partial \epsilon}$, then elliptic flow is an observable that provides experimental information on the EoS of the expanding matter. In particular, if evolving matter is characterized by high density and large interaction cross

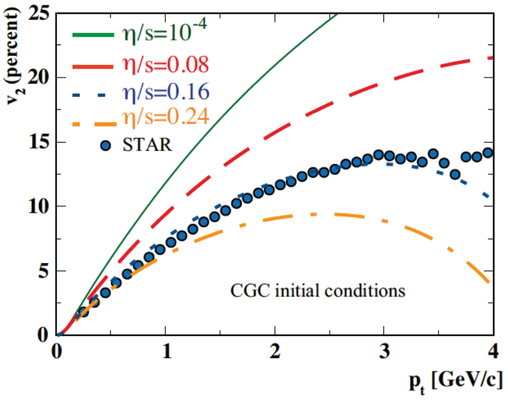

Figure 2.21: Measured elliptic flow for charged particles by STAR [133] as function of transverse momentum compared to viscous hydrodynamical calculations from [134].

section with reduced dissipative effects, i.e. low viscosity, is able to carry higher anysotropic correlations among particles, resulting in a large elliptic flow and indicating that system rapidly can reach thermalization. However, probing the EoS of QCD through the magnitude of the v_2 is affected by uncertainties in the initial spatial eccentricity as well as in the temperature dependence of the η/s coefficient. Another important property of the elliptic flow has been pointed out by measurements of correlations among charged particles at RHIC energy. In Fig. (2.22) we report experimental taken from PHOBOS [136] where the elliptic flow of identified mesons and baryons is plotted as function of transverse momentum divided by n_q which stands for the number of valence quarks within each hadron species ($n_q = 2$ fora mesons, $n_q = 3$ for baryons). One observes a scaling property which cannot be addressed within hydrodynamical description, while it finds a natural explanation in a coalescence hadronization model, which predicts that the v_2 of any hadronic species is related to the partonic flow of the recombining quarks in the following way

$$v_2^{had}(p_T) \simeq n_q v_2^q(p_T/n_q) \tag{2.90}$$

Such scaling property clearly indicates that collective flow is developed at the partonic level, hence it is a signature of the deconfined QGP phase. However,

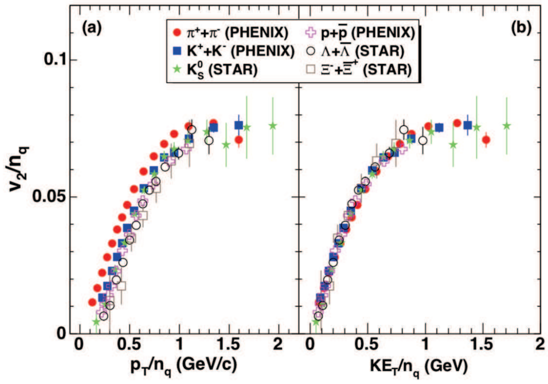

Figure 2.22: Picture from Ref. [136]: (a) scaled v_2/n_q as function of p_T/n_q where n_q is the number of constituent (recombined) quarks, no more large difference between baryon and meson v_2 is visible; (b) same v_2/n_q plotted as function of transverse kinetic energy $KE_T = m_T - m = \sqrt{p_T^2 + m^2} - m$, where also mass ordering is reabsorbed.

such results is spoiled since at RHIC energy a breaking of the scaling relation is already observed, that becomes stronger ($\approx$ 20 %) at LHC energy where hadronization by coalescence plays a secondary role.

The elliptic flow of charmed mesons and their decay products has been investigated for the first time at RHIC experiments, where PHENIX collected azimuthal anysotropic correlations for single non-photonic $e^{\pm}$ [122] while STAR recently achieved to measure the flow magnitude of prompt D^0 in minimum bias $AuAu$ collisions [137]. In both cases the observed v_2 value was large and almost comparable with the one of light hadrons, meaning that HQs are strongly coupled to the *bulk* anysotropies and indicating the possibility of HQS to reach thermalization at low p_T. The same trend was observed also at LHC $PbPb$ collisions at $\sqrt{s} = 2.76\,ATeV$ from ALICE detector, while at higher energy experimental results are available both from ALICE and CMS collaborations [138, 139] where also different techniques are employed to get rid of the dependence on the reaction plane and to measure the v_2 and higher flow harmonics v_n by means of event shape engineering [140]. These experimental results open a scenario where the observed high suppression of HQs is linked to their strong coupling with the *bulk* flow. This represents a challenge

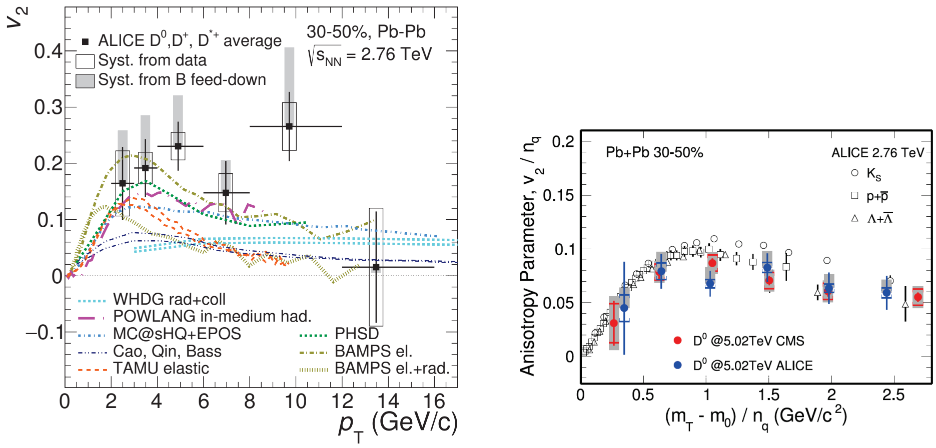

(a) **(b)**

Figure 2.23: **(a)** Average D meson $v_2(p_T)$ measured at LHC collisions $PbPb$ peripheral collisions at $\sqrt{s_{NN}} = 2.76\,TeV$ by ALICE and compared to some transport approaches. Picture is adapted from Ref. [78]. **(b)** Elliptic flow of prompt D^0 measurements from ALICE and CMS in $PbPb$ collisions at $\sqrt{s_{NN}} = 5.02\,TeV$ compared to the v_2 of identified charged hadrons at lower energy and represented as function of transverse mass scaled by the number of valence quarks. Picture is taken from [77].

for theoretical framework which attempt to describe HQ propagation in the QGP by means of pQCD driven interaction or in a non-perturbative fashion. Models which are able to reproduce the measured R_{AA} usually predicts too small v_2, while models which attempt to describe the observed v_2, generally they do despite a resulting too strong suppression. This puzzling problem has been addressed in different ways, among which the possibility to relate the correlation among these two observables to the dependence of HQ interaction on some physical properties of the medium. We will discuss in detail about this issue in Chapter 4.

CHAPTER 3

TRANSPORT THEORY AND HEAVY QUARK DYNAMICS IN QGP

3.1 Classical Relativistic Transport Theory

We introduced the concept of phase-space distribution function for a dynamical system constituted of many classical (relativistic) particles already in Chapter 2 when discussing about the QGP thermal phase before rapidly shift to formulation of hydrodynamics. Through the function $f(x, p)$ also called as Lorentz scalar phase density [141] we can define an appropriate probability in the phase space volume in the following way

$$dP(x, p) \equiv f(x, p) d^4x \, d^4p \tag{3.1}$$

In Eq. (3.1) $dP(x, p)$ denotes the probability of finding a particle in the space-time volume $d^4x = dt \, d^3\vec{x}$ centered at position $x = (t, \vec{x})$ and with four-momentum in the range $(p, p + d^4p)$. In case of a system formed by relativistic on-shell particles we take into account the dispersion relation which fixes the first component of the four-momentum p to the particle energy, i.e. $p^0 = E = \sqrt{|\vec{p}|^2 + m^2}$ where m is the particle mass. To construct a relativistic kinetic theory we need to derive an evolution equation for $f(x, p)$ in terms of the proper time τ of the system. In the case the system is a gas of non-interacting particles the uniqueness of Newton's equations in their relativistic generalization ensures that particle number remains constant within each phase-space volume whose size is also a constant integral of motion. Collecting both conditions and applying them directly on Eq. (3.1) we come up with the *Liouville's theorem* which states that the in the presence of only conservative forces the phase-space distribution function $f(x, p)$ is constant of motion

$$\frac{df(x,p)}{d\tau} = 0 \tag{3.2}$$

In order to work out with Liouville's statement we need to provide an explicit expression for the phase-density $f(x, p)$. In particular, with the meaning of single-particle distribution function $f(x, p)$ can be represented in terms of dynamical *test-particles*

$$f(x,p) = \sum_{i=1}^{N} \delta^{(4)}\left(x_i(\tau) - x\right) \delta^{(4)}\left(p_i(\tau) - p\right) \tag{3.3}$$

where in Eq. (3.3) each particle of the whole sample N is labelled by the index i and its motion trajectory in the space-time is indicated as $x_i(\tau)$ with four-momentum $p_(\tau)$. Then, substituting Eq. (3.3) in Eq. (3.2) and using definition of relativistic four-velocity $dx^\mu/d\tau = p^\mu/E$ and external or self-consistent internal four-force $F^m = dp^\mu/d\tau$ we obtain

$$\begin{aligned} \frac{df(x,p)}{d\tau} &= \sum_{i=1}^{N} \left\{ \frac{\partial x_i^\mu}{\partial\tau}\frac{\partial}{\partial x^\mu} + \frac{\partial p_i^\mu}{\partial\tau}\frac{\partial}{\partial p^\mu} \right\} \delta^{(4)}\left(x_i(\tau) - x\right) \delta^{(4)}\left(p_i(\tau) - p\right) \\ &= \left\{ \frac{p^\mu}{m}\frac{\partial}{\partial x^\mu} + F^\mu(x)\frac{\partial}{\partial p^\mu} \right\} f(x,p) = 0 \end{aligned} \tag{3.4}$$

which is known under the name of *Relativistic Vlasov Equation*. Generalization of transport theory should incorporate dissipative phenomena for the description of classical interacting gases. When we introduce scattering processes within the system, we have to consider Liouville's theorem as invalid because the number of particles within the phase-space volume is not constant anymore. This can be addressed by adding on the right hand side of Eq. (3.4) a *dissipative term* which accounts for the four-momentum variation through particle collisions

$$\left\{\frac{p^\mu}{m}\frac{\partial}{\partial x^\mu} + F^\mu(x)\frac{\partial}{\partial p^\mu}\right\} f(x,p) = C[f](x,p) \tag{3.5}$$

Eq. (3.5) is the well-known *Relativistic Boltzmann Equation* (RBE) and the interaction kernel $C[f](x,p)$ is called *collision integral*. In general $C[f](x,p)$ is a nonlinear functional of the density functions of each particle species k in the gas, being responsible of the coupling among the following equation of motions

$$\left\{\frac{p^\mu}{m}\frac{\partial}{\partial x^\mu} + F^\mu(x)\frac{\partial}{\partial p^\mu}\right\} f_k(x,p) = C[f_k, f_h, ...](x,p) \quad k,h = q,\bar{q},g \tag{3.6}$$

in the case for example we consider Boltzmann equations for an interacting plasma of quarks and gluons. Moreover, the collision integral includes all possible kind dissipative phenomena, usually divided into *elastic* and *inelastic* processes, while it could also account for two or higher particle correlations which are encoded within appropriate phase density distributions like for example $f_2(x_1,p_1;x_2,p_2)$ for the two-particle case. As a consequence the derivation of an explicit formula for $C[f](x,p)$ can be done only in advance of certain assumptions. In particular, we will make use of the relativistic equivalent statements [142]

1) The collision probability decreases as the number of particles involved in the reaction increases. Hence, we can expand the collision integral as a series on microscopic process and retaining for our work only the two-body scattering term.

$$C[f] = C_{22}[f] + C_{23}[f] + C_{32}[f] + \cdots \approx C_{22}[f] \tag{3.7}$$

This corresponds to the original assumption made by Boltzmann when he derived his own equation for non-relativistic dilute gases where he considered only elastic binary collisions between on-shell particles.

2) The distribution function $f(x, p)$ varies slowly on a time period which is comparable with the characteristic mean free path of the collision $\lambda_{mfp}|\nabla_x \log f(x, p)| \ll 1$. This means that within the duration of a scattering process we can consider $f(x, p)$ as a constant.

3) The particles' momenta and spatial coordinates are uncorrelated variables which means that in a uniform plasma the probability of finding two particles located at positions x_1 and x_2 having momenta respectively of p_1 and p_2 can be written as the product of the corresponding single-particle distribution functions

$$f_2(x_1, p_1; x_2, p_2) = f(x_1, p_1) \cdot f(x_2, p_2) \tag{3.8}$$

This statement is named as Boltzmann's *Stosszahlansatz* (molecular chaos) which implies also that the binary collision term $C_{22}[f](x, p)$ is proportional to the product of the phase densities of the two scattering particles $f(x, p)f(x, p')$.

3.2 Quantum Transport Theory

3.2.1 Non-Relativistic Wigner formalism

In the previous paragraph we have derived transport equations in classical kinetic theory provided a consistent definition of the density function $f(x, p)$. Now, considering some physical observable which is defined by a proper function $\mathscr{O}$ in the phase-space, its average value can be calculated through the following expression

$$\overline{\mathscr{O}} = \int dxdp\, \mathscr{O}(x, p) f(x, p) \tag{3.9}$$

involving the one-body density function $f(x, p)$. We may ask whether there exists in quantum mechanics a correspondence of the phase-space distribution function which yields to calculate the expectation value of the hermitian operator $\hat{O}$ related to the same physical observable in terms of a phase space integral similar to the classical form Eq. (3.9). One possible answer is provided by the formalism based on the Wigner function. In quantum theory the time evolution of a system can be described by formulating a hermitian *density matrix*

$$\hat{\rho} = \sum_i w_i \left|\psi_i\right\rangle \left\langle\psi_i\right| \tag{3.10}$$

where $\{\psi_i\}$ forms a complete orthonormal set and the real expansion coefficients are non-negative values $w_i \geq 0$ and fulfill the normalization condition $\sum_i w_i = 1$. The time evolution of the density $\hat{\rho}$, given the Hamiltonian operator $\hat{H}$ of the quantum mechanical system , can be derived through the Schrö equation for the state vectors

$$\left|\psi_i(t)\right\rangle = e^{-i\hat{H}t/\hbar} \left|\psi_i(0)\right\rangle \tag{3.11}$$

where we indicate explicitly the $\hbar$-dependence arising in the (unitary) time evolution operator. Then, plugging Eq. (3.11) in the $\hat{\rho}$ definition Eq. (3.10) we obtain straightforwardly

$$\frac{\partial\hat{\rho}(t)}{\partial t} = \frac{i}{\hbar}\left[\hat{\rho}(t), \hat{H}\right] \tag{3.12}$$

which differs from the usual equation for the time evolution of the operator $\hat{O}$ (in Heisenberg representation) by an additional minus sign on the right hand side. Consistently we can compute the expectation value of any observable as

$$\langle\hat{O}(t)\rangle = Tr\left[\hat{\rho}(t)\hat{O}\right] = \sum_i \left\langle\psi_i(t)\right| \hat{O} \left|\psi_i(t)\right\rangle \tag{3.13}$$

For any quantum mechanical operator $\hat{A}$ it is possible to define its Weyl transform [143]

$$\tilde{A}(x, p) = \int \frac{dy}{2\pi\hbar} e^{ipy/\hbar} \left\langle x_+\right| \hat{A} \left|x_-\right\rangle \tag{3.14}$$

where $x_\pm = x \pm y/2$ and which given another operator $\hat{B}$ leads to the following relation

$$Tr\left[\hat{A}\hat{B}\right] = \int dx dp\, \tilde{A}(x, p)\tilde{B}(x, p) \tag{3.15}$$

The Weyl transform of the density matrix $\hat{\rho}$ is known as *Wigner function*

$$W(x, p) = \int \frac{dy}{2\pi\hbar} e^{ipy/\hbar} \langle x_+ | \hat{\rho} | x_- \rangle = \int \frac{dy}{2\pi\hbar} e^{ipy/\hbar} \Psi(x_+) \Psi^*(x_-) \tag{3.16}$$

where in the last step we introduced the pair of wave functions $\Psi(x_+)\Psi^*(x_-)$ which has univocal expansion with respect to the orthonormal states entering in the definition of the $\hat{\rho}$ operator Eq. (3.10). Then, using Eq. (3.16) into the expectation value formula, it follows

$$\langle \hat{O}(t) \rangle = \int dx dp \, \tilde{O}(x, p) W(x, p) \tag{3.17}$$

which compared to Eq. (3.9) implies that the Wigner function in quantum theory plays in many aspects the same role that phase space density $f(x, p)$ has in classical statistical mechanics. The problem of quantum transport theory is encoded in the time evolution equation for the density matrix Eq. (3.12) and for the expectation values for the operators Eq (3.13) which through Ehrenfest's theorem obeys the laws of classical mechanics. Therefore, a quantum version of the Vlasov equation for the evolution of the Wigner function can be obtained by Weyl transforming these equations. In particular, starting from Eq. (3.12) with specific Hamiltonian $\hat{H} = \hat{p}^2/2m + \hat{U}$ and applying Wigner transformation, we get

$$\int \frac{dy}{2\pi\hbar} e^{ipy/\hbar} \langle x_+ | \left(\frac{\partial \hat{\rho}(t)}{\partial t} - \frac{i}{\hbar} [\hat{\rho}, \frac{\hat{p}^2}{2m} + \hat{U}] \right) | x_- \rangle = 0 \tag{3.18}$$

Then, after introducing coordinate and momentum unitary relations and performing some calculations we obtain what can be considered an equation of motion for the Wigner function

$$\frac{\partial W(x, p)}{\partial t} + \frac{p}{m} \frac{\partial W(x, p)}{\partial x} + \sum_{k=0} \frac{1}{(2k+1)!} \left(\frac{\hbar}{2} \right)^{2k} U(x) \left(\overleftarrow{\nabla}_x \cdot \overrightarrow{\nabla}_p \right)^{2k+1} W(x, p) = 0 \tag{3.19}$$

with gradients operator acting along the direction of the arrows. We have done no approximations so far, hence this result is exactly equivalent to the Schrödinger equation for the quantum wavefunction. At this point, if the gradient of the potential is not too strong, the summation over k index can be truncated at the first term. This implies that the $\hbar$-dependence does not appear explicitly, but still quantum dynamical effects are accounted within the Wigner function. Such truncation leads to the following result

$$\frac{\partial W(x,p)}{\partial t} + \frac{p}{m}\frac{\partial W(x,p)}{\partial x} + \nabla_x U(x)\cdot\nabla_p W(x,p) = 0 \tag{3.20}$$

which has the same form of the classical transport equation that can be derived from Eq. (3.4) in the non-relativistic limit

$$\left\{\frac{\partial}{\partial t} + \vec{v}\cdot\nabla_x + \boldsymbol{F}\cdot\nabla_p\right\} f(t,\vec{x},\vec{p}) = 0 \tag{3.21}$$

However, we notice that Eq. (3.20) remains exact in case of linear and quadratic (harmonic) potentials, since the original expression Eq. (3.19) contains only odd derivative of the potential.

3.2.2 Transport of Quantum Fields: The sigma model

In order to extend the Wigner formalism previously introduced to the relativistic quantum fields we employ as an example the $O(4)$ *linear* sigma model which among its various applications it undergoes a finite temperature second order phase transition through a spontaneous broken and restored symmetry phases which is very similar to the chiral properties of QCD [144, 145] (see Chapter 1). The Lagrangian density of the model is given by

$$\mathscr{L}_\sigma = \frac{1}{2}(\partial\boldsymbol{\phi}(x))^2 - \frac{1}{2}\mu^2\boldsymbol{\phi}^2(x) - \frac{\lambda}{4!}\boldsymbol{\phi}^4(x) \tag{3.22}$$

where $\boldsymbol{\phi}$ is a four-component scalar field parametrized as $\boldsymbol{\phi} = (\sigma, vec\pi)$ and the mass term is chosen with the wrong sign $\mu^2 < 0$, such that the potential $V(\boldsymbol{\phi}) = \frac{1}{2}\mu^2\boldsymbol{\phi}^2 + \frac{\lambda}{4!}\boldsymbol{\phi}^4$ is equivalent to the Mexican-hat form which leads the system to spontaneously brake symmetry already at three level. In particular, fluctuations of the $\sigma(x)$ field around the vacuum expectation value σ_0

obtained as a minimum of the potential

$$\frac{dV}{d\boldsymbol{\phi}} = \left(\mu^2 + \frac{\lambda}{3!}\boldsymbol{\phi}^2\right)\boldsymbol{\phi} \rightarrow \sigma_0 = \sqrt{-6\mu^2/\lambda} \tag{3.23}$$

causes the shifted field $\sigma \rightarrow \sigma - \sigma_0$ field to acquire a non-zero mass, while the pion fields $\vec{\pi}$ correspond to the three massless Goldstone modes each one related to a generator of the unbroken $O(3)$ symmetry. This is visible in the equation of motions of the corresponding Heisenberg operators

$$\begin{aligned}
&\partial^2\vec{\pi}(x) + m_\pi^2\vec{\pi}(x) + \frac{\lambda}{3!}|\vec{\pi}|^2\vec{\pi}(x) = 0 \\
&\partial^2\sigma(x) + m_\sigma^2\sigma(x) + \frac{\lambda}{2}\sigma_0\sigma^2(x) + \frac{\lambda}{3!}\sigma^3(x) = 0
\end{aligned} \tag{3.24}$$

with defined mass parameters

$$m_\pi^2 = \frac{\lambda}{3!}(\sigma^2 + 2\sigma_0\sigma) \quad , \quad m_\sigma^2 = \frac{\lambda}{3!}(|\vec{\pi}|^2 + 2\sigma_0^2) \tag{3.25}$$

where we can see that in the limit $\sigma \rightarrow 0$, we get $m_\pi \rightarrow 0$ and $m_\sigma^2 \rightarrow \lambda\sigma_0^2/3$. In order to solve the equation of motions of the field operators Eq. (3.24), we need to define a proper density matrix operator ρ and compute the expectation values, such as $\langle\sigma\rangle = Tr(\rho\sigma)$, which evolve consistently with the classical quantities. However, taking the expectation value of Eq. (3.24) determines a coupling among the general n-point correlation (Wightman) functions which generates a hierarchy of equations similar to the Bogoliubov-Born-Green-Kirkwood-Yvon (BBGKY) set [142] which couples the n-body distribution functions and truncated at first order with molecular chaos assumption on f_2 leads to classical kinetic Boltzmann theory. In QFT the simplest truncation of such hierarchy of Wightman function equations is realized through Hartree approximation which is realized by factorizing the higher order expectation values of fields into products of one- and two-point functions. Then, for example for the bracket $\langle ... \rangle$ of three sigma fields we have

$$\begin{aligned}\langle \sigma_1 \sigma_2 \sigma_3 \rangle &= \langle \sigma_1 \rangle \langle \sigma_2 \sigma_3 \rangle + \langle \sigma_2 \rangle \langle \sigma_1 \sigma_3 \rangle + \langle \sigma_3 \rangle \langle \sigma_1 \sigma_2 \rangle + \langle \sigma_1 \rangle \langle \sigma_2 \rangle \langle \sigma_3 \rangle \\ &= \overline{\sigma}_1 \langle \sigma_2 \sigma_3 \rangle + \overline{\sigma}_2 \langle \sigma_1 \sigma_3 \rangle + \overline{\sigma}_3 \langle \sigma_1 \sigma_2 \rangle + \overline{\sigma}_1 \overline{\sigma}_2 \overline{\sigma}_3 \end{aligned} \tag{3.26}$$

where the subscripts refer to different space-time points and in the last chain we interpret expectation values of the $\sigma(x)$ field shifted with respect the the mean field $\overline{\sigma}(x) = \langle \sigma(x) \rangle$. Similar equations holds for the Wightman functions of the pion fields for which we assume $\langle \vec{\pi}(x) \rangle = 0$. Within this procedure we can write down the dynamical equations for the mean field and the two-point correlation function

$$\begin{aligned}\left[\partial_1^2 + m_{\sigma_1}^2 + \frac{\lambda}{2} \left(\frac{\overline{\sigma}_1^2}{3} + \sigma_0 \overline{\sigma}_1 + \langle \sigma_1^2 \rangle \right) \right] \overline{\sigma}_1 + \frac{\lambda}{2} \sigma_0 \langle \sigma_1^2 \rangle &= 0 \\ \left[\partial_2^2 + m_{\sigma_2}^2 + \lambda \sigma_0 \overline{\sigma}_2 + \frac{\lambda}{2} \left(\overline{\sigma}_2^2 + \langle \sigma_2^2 \rangle \right) \right] \langle \sigma_1 \sigma_2 \rangle &= 0 \end{aligned} \tag{3.27}$$

In order to derive transport equations we define now a suitable Wigner operator as following [141]

$$W_{ab}(x, p) = \int \frac{d^4 y}{(2\pi\hbar)^4} e^{-ipy/\hbar} \langle : \hat{\mathbf{\Phi}}_a(x_+) \hat{\mathbf{\Phi}}_b(x_-) : \rangle \tag{3.28}$$

where with the capital $\hat{\mathbf{\Phi}}$ we indicate the four-component field $(\sigma, \vec{\pi})$ subtracted by the mean field $\overline{\sigma}(x)$, while the colons denote normal ordering to neglect the vacuum properties. The Wigner operator can be used straightforwardly to calculate the energy-momentum tensor $T^{\mu\nu}$ of the sigma $O(4)$-model and to write expectation values of the two-point correlation functions, such as

$$\langle \sigma^2(x) \rangle = \int d^4 p W_{\sigma\sigma}(x, p) \tag{3.29}$$

We can plug this relation directly in the second Eq. (3.27) to obtain

$$\left(\frac{\hbar^2}{4} \partial_x^2 - p^2 + i\hbar p_\mu \partial_x^\mu + \exp\left(-i \frac{\hbar}{2} \partial_x \partial_p \right) (m^*(x))^2 \right) W_{\sigma\sigma}(x, p) = 0 \tag{3.30}$$

where the x-derivative in the exponential acts on the quantity $(m^*(x))^2$ which is defined as following

$$(m^*(x))^2 = m_\sigma^2(x) + \lambda\sigma_0\overline{\sigma}(x) + \frac{\lambda}{2}\left(\overline{\sigma}^2(x) + \langle\sigma^2(x)\rangle\right) \tag{3.31}$$

We can handle this equation with its complex adjoint to derive the transport equation

$$\left[p\cdot\partial_x - \frac{1}{\hbar}\sin\!\left(\frac{\hbar}{2}\partial_x\cdot\partial_p\right)(m^*(x))^2\right]W_{\sigma\sigma}(x,p) = 0 \tag{3.32}$$

together with a generalized mass-shell condition

$$\left[p^2 - \frac{\hbar^2}{4}\cos\!\left(\frac{\hbar}{2}\partial_x\cdot\partial_p\right)(m^*(x))^2\right]W_{\sigma\sigma}(x,p) = 0 \tag{3.33}$$

Finally, we can perform a systematic semiclassical expansion in powers of $\hbar$ which at leading order results into a form of a Vlasov equation constrained with a mass-shell relation

$$\left[p\cdot\partial_x - \frac{1}{2}\partial_x\cdot\partial_p(m^*(x))^2\right]W_{\sigma\sigma}(x,p) = 0 \tag{3.34}$$

The Eq. (3.34) does not contain any collision term as we expect, since the Hartree approximation leads to an effective non-dissipative evolution of the quantum system [146]. On the other hand, difficulties arise because the effective mass $m^*(x)$ has to be calculated self-consistently by solving the dynamical equation for the mean field which involves integrals of the kind Eq. (3.29). Through relation between the Wigner function and the one-body phase space distribution $f(x,p) = W(x,p)/m^*(x)$ we obtain

$$\left(p_\mu\partial_x^\mu + m^*(x)\,\partial_x^\mu m^*(x)\,\partial_{p,\mu}\right)f(x,p) = 0 \tag{3.35}$$

which describes the evolution of $f(x,p)$ for particles under a $\lambda\phi^4$ interaction.

3.3 Boltzmann approach for QGP dynamics

A realistic description of the QGP evolution by means of transport approaches has to deal with two important issues. The first one is that Lattice QCD (lQCD) calculations predict that the energy density deviates from the Stefan-Boltzmann limit of a perfect gas by about $15 - 20\%$ resulting in a value of the interaction measures $\langle \Theta^{\mu}_{\mu} \rangle = \epsilon - 3P$ significantly different from zero [23]. In this scenario of course perturbative QCD treatment completely fails in reproducing lQCD expectations within the temperature range explored by HICs, while the agreement occurs at $T \geq 4 - 5T_c$. The second one is that by means of effective field theory based on a resummation over the soft gauge fields at the scale gT, the so-called Hard Thermal Loop (HTL) expansion [147], one is able to reproduce the trace anomaly down to $T \approx 2T_c$ already at next-to-leading order. What is important for our discussion is that the HTL approach motivates a QGP picture based on weakly interacting quasi-particle modes. A successful way to account the non-perturbative QCD effects at non-zero temperature which exhibit within the lQCD thermodynamical expectations is to encode part of these features within effective particle masses by prescription of a Quasi-Particle Model (QPM). In this section we provide a brief introduction of our Quasi-Particle Model (QPM) and its implementation within our Boltzmann transport framework for the description of dynamical evolution of the *bulk* matter above the critical temperature T_c. We stress here that even our focus is projected towards a transport approach for Heavy Quarks (HQs), a realistic evolution of the background medium is mandatory to achieve a correct description of HQs dynamics and their related observables.

3.3.1 Quasi-Particle Model for bulk interaction

The origin of quark and gluon masses can be explained as the energy contribution coming out from the particle correlations within the strongly interacting QCD medium [148]. If large part of the interaction can be absorbed into these effective masses, then we can treat the dynamical system as a gas formed by massive free quasi-particles and recast the dissipative effects within a Boltzmann-like collision kernel. In agreement with other approaches [149, 150, 151], we provide the expressions of these partonic masses according to their thermal pQCD evaluation at zero chemical potential which results for gluons and quarks respectively to the following temperature dependence

$$\begin{aligned} m_g^2(T) &= \frac{2N_c}{N_c^2-1}\, g^2(T)\, T^2 \\ m_q^2(T) &= \frac{1}{N_c}\, g^2(T)\, T^2 \end{aligned} \tag{3.36}$$

where $N_c = 3$ is the number of colors, $N_f = 3$ is the number of flavors and we consider the strength coupling g as general T-dependent function, rather than constraining it to the pQCD expectation which would not permit the match with lQCD thermodynamics. We refer briefly to the effective quasi-particle masses in Eq. (3.36) as QPM masses. In the end the model has to be completed by introducing a bag pressure contribution $B(T)$ which takes into account further non-perturbative effects like for example the formation of gluon condensate in a pure gauge theory [152]. Moreover, we consider a T-dependent bag contribution $B(T)$ in order to preserve thermodynamical consistency and preserve the entropy expression of an ideal gas $s(T) = \partial P/\partial T$ [148]. In this framework the pressure of the system is given by

$$P(m_g, m_u, m_d, m_s, T) = \sum_{i=u,d,s,g} \nu_i \int \frac{d^3\vec{p}}{(2\pi)^3} \frac{p^2}{3E_i(p)} f_i(E_i) - B(T) \tag{3.37}$$

where ν_i are the internal color and spin degrees of freedom, i.e. $\nu_g = 16$ for gluons and $\nu_q = 2 \times 6$ for quarks (plus antiquarks), $E_i(p) = \sqrt{p^2 + m_i^2}$ is the dispersion relation with QPM masses from Eq. (3.36) and $f_i(p) = \left[1 \pm \exp(E_i(p)/T)\right]^{-1}$ are the equilibrium Fermi (+) and Bose (-) distribution functions. Thermodynamic consistency is imposed by minimizing the pressure Eq. (3.37) with respect to the QPM masses at fixed temperature, i.e. $(\partial P/\partial m_i)_T = 0$, giving rise to the following set of equations for the bag pressure

$$\frac{\partial B}{\partial m_i} + \nu_i \int \frac{d^3\vec{p}}{(2\pi)^3} \frac{m_i}{E_i(p)} f_i(E_i) = 0 \tag{3.38}$$

which however are not independent, because the T-dependence of the partonic masses through the strength coupling $g(T)$ is constrained to the QPM expressions in Eq. (3.36). Finally, we derive the energy density from pressure by means of thermodynamics relationship $\epsilon(T) = T\,(\partial P/\partial T) - P(T)$, obtaining the following expression

$$\epsilon(T) = \sum_{i=u,d,s,g} \nu_i \int \frac{d^3\vec{p}}{(2\pi)^3} E_i(p) f_i(E_i) + B(m_i(T)) \tag{3.39}$$

In the model $B(T)$ and $\epsilon(T)$ are two unknown functions but they are not independent, because they are related through the thermodynamic consistency Eq. (3.39). Hence, we need to determine only one function and we choose to do so by fixing the energy density Eq. (3.39) to the expectations from lQCD, i.e. imposing

$$\epsilon_{QPM}(T) = \epsilon_{lQCD}(T) \tag{3.40}$$

We solve this condition by treating the strength coupling $g(T)$ as a free parameter and adopt for $T > T_c$ the following parametrization

$$g^2(T) = \frac{48\pi^2}{(11N_c - 2N_f)\,\text{In}\left[\lambda\left(\frac{T}{T_c} - \frac{T_s}{T_c}\right)\right]^2} \tag{3.41}$$

which is in agreement with other quasi-particle approaches [150, 153]. In Eq. (3.41) the parameter values are fitted to reproduce the lQCD energy density from Wuppertal-Budapest collaboration [154]. In particular, we obtain $\lambda = 2.6$ and $T_s/T_c = 0.57$ for critical temperature $T_c = 0.155\,GeV$. For a detail description of the derivation of the QPM strength coupling Eq. (3.41) and the subsequent derivation of the EoS tuned to the available expectations from the various lQCD collaborations we refer to [148].

In the picture below we present our results for the behavior of the strength coupling $g(T)$ and the resulting thermal masses Eq. (3.36) that from this moment on will constitute our QPM interaction to be included in our Boltzmann transport framework both for the bulk and heavy quark dynamics. We will address this issue in the next sections. We focus here on the fact that the inclusion of non-perturbative effects by means of QPM prescription leads to an enhancement of the strength coupling towards T_c that can be interpreted as the arising of a confining force which addresses also the increasing of the quasi-particle masses, while at higher temperatures the QPM interaction tends to the asymptotic pQCD behavior as we can see on the right hand side of Fig. (3.1) where we plot the defined coupling constant $\alpha_s = g^2/4\pi$ resulting the QPM fit Eq. (3.41) compared to the pQCD formula Eq.(1.14) in Chapter 1 where we used $Q^2 \sim (\pi T)^2$. For sake of completeness, other approaches encode the confinement remnants within a gluonic mean field procedure coupled to the same quasi-particle masses [152] and obtain a decreasing behavior of $m_g(T)$ as $T \rightarrow T_c$ in agreement with the melting expectation in a valence gluon model.

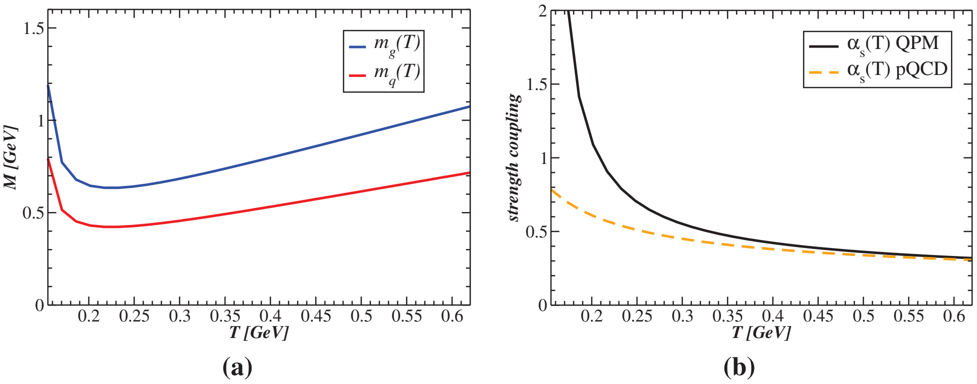

(a) **(b)**

Figure 3.1: The T-dependence behavior of effective thermal masses Eq. (3.36) for gluons (blue line) and quarks (black line) is plotted on the left plot, while the QCD strength coupling $\alpha_s = g^2/4\pi$ is shown on the right one. The QPM interaction represented by the solid black line of the right plot increases higher when $T \rightarrow T_c$ compared to the running pQCD formula represented by the orange dashed line. Both results are obtained by tuning the calculated QPM energy density Eq. (3.39) to lQCD expectations provided by Wuppertal-Budapest collaboration [154].

3.3.2 Transport approach for quasi-particles

In the previous paragraph we have introduced a Quasi-Particle Model (QPM) for describing the properties of a strongly interacting QGP at equilibrium in a wide range of temperatures and, in particular, we have shown that with the QPM microscopic description we can describe correctly the QCD thermodynamics in agreement with lQCD expectations. The goal is now to develop a kinetic theory for describing the dynamical evolution of the QPM distribution functions within a Boltzmann transport approach. In order to extend the quasi-particle picture to a non-equilibrium system we need to account for two considerations. The first one is that in the regime where local thermodynamic equilibrium is valid the dispersion relation for the quasi-particles becomes space-time dependent $E_i(p, x) = \sqrt{p^2 + m_i^2(x)}$ and the x dependence of the QPM masses Eq. (3.36) is given through the estimated temperature $T(x)$ in the local region of the fireball. The second one is that the distribution functions for the various partonic species $f_i(p)$ $(i = g, q)$ appearing for example in Eq. (3.37) (3.38) (3.39) are not at once equivalent to the equilibrium Fermi or Bose expressions, rather they have to be considered as time dependent functions of the non-equilibrium expanding system. In order to do that in a rigorous way we should derive the equation of motions starting from an effective lagrangian which describes the system in terms of the quasi-particle fields and then trace back the same calculation we have done for the case of the linear sigma model with the final result to get the exact equation of motions for the QPM distribution functions. A similar procedure has been applied for example in the case of the NJL model [155] [156], which we described in Chapter 1. However, for our case we may place in a so-called *Mean Field Approximation* and view the QPM masses as arising from the contribution of a scalar field which has the well known effect to generate effective space-time dependent masses. Then, what we have to do is simply write the Boltzmann equation starting from a free Lagrangian coupled to a scalar field, that is exactly the result obtained for the linear sigma model case just including the collision integral to the Vlasov equation Eq. (3.35). Hence, we have

$$\left(p_\mu \partial_x^\mu + m^*(x)\partial_x^\mu m^*(x)\partial_{p,\mu}\right) f_{g,q,\bar{q}}(x,p) = C[f_g, f_q, f_{\bar{q}}](x,p) \tag{3.42}$$

In the QPM $m^*(x)$ is linked to the bag pressure $B(x)$ through the constraint Eq. (3.38) which account for thermodynamic consistency, but in the more general case of non-equilibrium this relation can be derived by constructing the energy-momentum tensor for the quasi-particle system [157]

$$T^{\mu\nu}(x) = \sum_{i=g,q,\bar{q}} \nu_i \int \frac{d^3\vec{p}}{(2\pi)^3 2E_i(p,x)} p^\mu p^\nu f_i(x,p) + \eta^{\mu\nu} B(m^*(x)) \tag{3.43}$$

where $E_i(p,x) = \sqrt{p^2 + m^*(x)}$ and the sum is carried over the gluons and all the quark (antiquark) flavors. Then, imposing the conservation law $\partial_\mu T^{\mu\nu}(x) = 0$, one gets an expression which links the effective mass $m^*(x)$ to the distribution functions of the bulk partons

$$\frac{\partial B}{\partial m^*} = -\nu_i \int \frac{d^2\vec{p}}{(2\pi)^3} \frac{m^*(x)}{E_i(p,x)} f_i(x,p) \tag{3.44}$$

which we have to solve self-consistently with eq. (3.42) and for the validity of the approach we have to assure the this space-time dependent mass is equivalent to the QPM mass Eq. (3.36) calculated at the equilibrium temperature, i.e. $m^*(x) = m_i(T)$. A detail description of this check with the consequent result to get a self-consistent non-equilibrium generalization of the stationary QPM thermodynamics followed by the correct meaning of the distribution functions in Eq. (3.42) is described in [158].

3.3.3 Transport theory at fixed η/s

Long last we have built our kinetic transport theory to describe from a microscopic point of view the dynamical evolution of the QGP and we could compare it to the hydrodynamics prescriptions which are based instead on macroscopic conservation laws as we discussed in the paragraphs of Sec. (2.3). However, it is not our aim to pull out differences among these approaches, because the only thing we need is to setup a realistic picture of the *bulk* properties to layout the dynamics of Heavy-Quarks (HQs) on it. The analysis of the main QGP properties, among which the evidence a large elliptic flow $v_2(p_T)$, through the use of both hydrodynamical and transport calculations to study the dynamics of HICs have shown that theoretical predictions are in agreement on the evaluation of a very small shear-viscosity to entropy-density ratio η/s, very close to the conjectured lower-bound limit $\eta/s = 1/4\pi$ calculated in the infinite strongly interacting regime AdS/CFT. Moreover, it appears that the T-dependence of the viscosity coefficient is a key ingredient to which collective properties of the system are very sensitive and to reproduce the experimental observations at RHIC and LHC energies (REF.) Hence, within our Boltzmann approach we need to account very carefully for these dissipative effects and the only way to do that is handling with the collision term on the right hand side of Eq. (3.42). Rather than making an expansion of the $C[f_g, f_q, f_{\bar{q}}](x, p)$ kernel over the microscopic processes, we explore the possibility to gauge the collision integral to viscous hydrodynamics by means of the Chapman-Enskog approximation [50] which allows to construct a relativistic Boltzmann transport approach at fixed η/s [159]. Once the transport theory is directly linked to hydrodynamics, it still maintains its powerful applicability to investigate the non-equilibrium features of the system. As proved in Ref. [160] [161] by means on an analytic calculation with Green-Kubo formulas of transport coefficients, such as electric conductivity [39] or bulk and shear viscosity from correlators of the corresponding fluxes or tensors at thermal equilibrium, the choice of the Chapma-Enskog method ensures an accurate estimate of the shear viscosity compared to the Relaxation Time Approximation (RTA) or other methods which develops non controlled ansatz on the collision integral to cast directly in the kinetic equations [155] [162] [163]. In Ref. [164] the shear viscosity at first order of Chapman-Enskog theory is evaluated for the general case of a relativistic gas of massive particles colliding with a non-isotropic and energy dependent cross section. Main formulas can be manipulated to get the following expression taken from Ref. [161]

$$\eta_{CE}^{I} = \frac{0.8}{g(z,a)} \frac{T}{\sigma_{tot}} \tag{3.45}$$

where $z = m/T$ and the function $g(z,a)$ is given by the following expression

$$\begin{aligned} g(z,a) &= \frac{32}{25} \frac{z}{K_3^2(z)} \int_1^{\infty} dy \left(y^2 - 1\right)^3 h(2zya) \\ &\times \left[(z^2y^2 + 1/3)K_3(2zy) - zyK_2(2zy)\right] \\ h(a) &= 4a(1+a)\left[(2a+1)\log(1+1/a) - 2\right] \end{aligned} \tag{3.46}$$

with the microscopic parameter $a = T/m_D$ controlling the grade of anisotropy of the cross section. Indeed by introducing the Debye screening mass $m_D = \sqrt{4\pi\alpha_s}T$ and employing a standard pQCD differential two-body elastic cross section

$$\frac{d\sigma}{dt} \propto \frac{\pi\alpha_s^2}{\left(t - m_D^2\right)^2}\left(1 + \frac{m_D^2}{s}\right) \tag{3.47}$$

normalized to the proper color factors regarding the interacting partonic species of the bulk, we see that a larger value of $a \gg 1$, i.e. $m_D \gg T$, corresponds to a more isotropic cross section. The idea is to invert the Chapman-Enskog relation Eq. (3.45) as done in [165] and to compute the total cross section for bulk interaction as function of the shear viscosity and the local temperature $T(x)$ and density of the system. Referring to Eq. [48] we write the inverted formula in the following way

$$\sigma_{tot}\left(n(x), T(x)\right) = \frac{1}{15} \frac{<p>}{g(z,a)n(x)} \frac{1}{\eta/s} \tag{3.48}$$

where $< p > \sim 3T$ is the average momentum of the bulk partons. In our approach the temperature is not provided as in the hydrodynamics case, rather it is estimated from the particle density $n(x)$ and the energy density $\epsilon(x)$ which are calculated through the distribution functions. By assuming local thermal equilibrium statement for massive particles, we have [166]

$$n(x) = \lambda \frac{\nu_{QGP}}{2\pi^2} T^3 z^2 K_2(z) \quad , \quad \epsilon(x) = \lambda \frac{\nu_{QGP}}{2\pi^2} m^2 \left[3\frac{K_2(z)}{z^2} + \frac{K_1(z)}{z} \right] \tag{3.49}$$

where the introduced fugacity λ addresses the remaining non-equilibrium effects and $\nu_{QGP} = \sum_{i=q,q,\bar{q}} \nu_i$ represent the QGP internal degrees of freedom. As in Eq. (3.46) the modified Bessel functions of the second kind [167] appears as function of the mass parameter $z = m/T$. Finally, the local temperature $T(x)$ is derived by inverting the expression we obtain through Eq. (3.49) for the energy per particle

$$e \equiv \frac{\epsilon}{m \cdot n} = 3T + m \frac{K_1(m/T)}{K_2(m/T)} \tag{3.50}$$

We see that in the massless limit Eq. (3.50) reduces to the simplified relation $T = m \cdot e/3$. Collecting the results we infer from eq. (3.48) that the local cross section for bulk interaction behaves like $\sigma_t ot \sim T^{-2}/(\eta/s)$ as function of temperature at fixed η/s.

3.4 Transport Theory for Heavy Quarks

3.4.1 Derivation of Fokker-Planck Equation

In Chapter 2 we presented the main properties of Heavy-Quarks (HQs) in the QGP. Among these the condition stated on charm and bottom masses, i.e. $M_{HQ} \gg \Lambda_{QCD}, T$, have been considered useful for simplify the transport framework with which describing HQ dynamics in the plasma. The starting point for the description of dynamical evolution of HQs in the QCD medium is the Boltzmann equation Eq. (3.5) for the HQ phase-space distribution f_{HQ} where we consider no mean field interaction and considering a two-body collision kernel.

$$p_\mu \partial_x^\mu f_{HQ}(x,p) = C[f_{HQ}, f_g, f_q, f_{\bar{q}}](x,p) \tag{3.51}$$

With simple manipulation this equation may be also written as [127]

$$\left[\frac{\partial}{\partial t} + \frac{\vec{p}}{E_p} \cdot \frac{\partial}{\partial \vec{x}}\right] f_{HQ}(t, \vec{x}, p, t) = C[f_{HQ}] \tag{3.52}$$

where the dividing $E_p = \sqrt{p^2 + M_{HQ}^2}$ has been reabsorbed into the definition of the collision integral $C[f_{HQ}]$. If HQs are distributed uniformly in the plasma, we can integrate f_{HQ} over the space volume V

$$f_{HQ}(p, t) = \frac{1}{V} \int d^3\vec{x}\, f_{HQ}(t, \vec{x}, \vec{p}) \tag{3.53}$$

and thus obtain an evolution equation for the HQ distribution as function only of the momentum

$$\frac{\partial}{\partial t} f_{HQ}(p, t) = \frac{1}{V} \int d^3\vec{x}\, C[f_{HQ}] \tag{3.54}$$

Let us concentrate now on the dissipative term appearing on the right hand side of Eq. (3.54). We consider HQs interacting by two-body elastic scattering with light quarks (antiquarks) and gluons of a thermal *bulk* at temperature T. We label the equilibrium distribution of the heat bath partons with a $\hat{f}_i$ for $(i = g, q, \bar{q})$ and assume it does not depend on time and position. Then, the collision integral takes the following form [168]

$$\begin{aligned} C[f_{HQ}] =& \frac{1}{2E_p} \frac{1}{\gamma_{HQ}} \sum_{i=g,q,\bar{q}} \int \frac{d^3\vec{k}}{(2\pi)^3 2E_k} \int \frac{d^3\vec{p}'}{(2\pi)^3 2E_{p'}} \int \frac{d^3\vec{k}'}{(2\pi)^3 2E_{k'}} \overline{|\mathcal{M}_{HQ,i}|^2} \\ &\times (2\pi)^4\, \delta(p + k - p' - k') \left(f_{HQ}(p, t)\hat{f}_i(k) - f_{HQ}(p', t)\hat{f}_i(k')\right) \end{aligned} \tag{3.55}$$

In Eq. (3.55) $\overline{|\mathcal{M}_{HQ,i}|^2}$ is the spin-color summed matrix element for a scattering process of type $HQ(p) + g, q(k) \rightarrow HQ(p') + g, q(k')$ which we can express in terms of the total cross section

$$\begin{aligned} \sigma_{HQ+i}(p, k) =& \frac{1}{\gamma_{HQ} \cdot \gamma_i} \frac{1}{4F} \int \frac{d^3\vec{p}'}{(2\pi)^3 2E_{p'}} \int \frac{d^3\vec{k}'}{(2\pi)^3 2E_{k'}} \\ &\times (2\pi)^4\, \delta(p + k - p' - k')\, \overline{|\mathcal{M}_{HQ,i}|^2} \end{aligned} \tag{3.56}$$

where $\gamma_{HQ} \cdot \gamma_i$ are the spin -color statistical factors of the initial state and the flux factor and its relation to the relative velocity is given by

$$F_i = \sqrt{(p \cdot k)^2 - (M_{HQ} \cdot m_i)^2} = E_p E_k \cdot v_{rel} \tag{3.57}$$

Then, we can manipulate Eq. (3.55) using Eq. (3.56) and Eq. (3.56) in order to express the collision integral

$$C[f_{HQ}] = \sum_{i=g,q,\bar{q}} \int \frac{d^3\vec{q}}{(2\pi)^3} \left[\omega_i(p+q,q) f_{HQ}(p+q) - \omega_i(p,q) f_{HQ}(p)\right] \tag{3.58}$$

in terms of the transition rate for collisions between a HQ and a i-flavor parton of the heat bath occurring with some momentum transfer $\boldsymbol{q}$

$$\omega_i(p,q) = \gamma_i \int \frac{d^3\vec{k}}{(2\pi)^3} \hat{f}_i(k) v_{rel} \sigma_{HQ+i}(p,k) \tag{3.59}$$

where $\gamma_g = 16$ and $\gamma_q = 6$, the sum in Eq. (3.58) carried out for all possible quark (antiquark) flavors. Accordingly to this definition [127] the first term of the collision integral in Eq. (3.58) corresponds to a gain contribution, because it describes the transition rate of a HQ scattering from a state of momentum $p + q$ to a momentum state p, while the second term is a loss contribution describing the scattering out of a HQ with initial momentum p.

The derivation of the Fokker-Planck Equation starts from the evolution equation for $f_{HQ}(p,t)$ with collision term in Eq. (3.58) and it is based on the so called *Landau approximation* by one assumes that the relevant momentum transfer of the elastic scattering obeys the condition $\boldsymbol{q} \ll |\vec{p}|$. Then, the gain term of the collision integral in Eq. (3.58) can be expanded with respect to $\boldsymbol{q}$

up to the second order[1]

$$
\begin{aligned}
\omega(p+q,q)f_{HQ}(t,p+q) \simeq \omega(p,q)f_{HQ}(t,p) &+ q_i\frac{\partial}{\partial p_i}\left[\omega(p,q)f_{HQ}(t,p)\right] \\
&+ \frac{1}{2}q_j q_h \frac{\partial^2}{\partial p_j \partial p_h}\left[\omega(p,q)f_{HQ}(t,p)\right]
\end{aligned}
\tag{3.60}
$$

Plugging this expansion in Eq. (3.58), the collision integral simplifies to

$$
C[f_{HQ}] \simeq \sum \int \frac{d^3\vec{q}}{(2\pi)^3}\left[q_i\frac{\partial}{\partial p_i} + \frac{1}{2}q_j q_h \frac{\partial^2}{\partial p_j p_h}\right]\left[\omega(p,q)f_{HQ}(t,p)\right] \tag{3.61}
$$

where the sum accounts for all possible elastic scattering channels. In the end, we have reduced the integro-differential Boltzmann equation Eq. (3.51) into a diffusion equation for $f_{HQ}(p,t)$ which contains only differential operators and it is known as *Fokker-Planck Equation*

$$
\frac{\partial}{\partial t}f_{HQ}(p,t) = \frac{\partial}{\partial p_j}\left[A_j(p)f_{HQ}(p,t) + \frac{\partial}{\partial p_h}\left[B_{jh}(p)f_{HQ}(p,t)\right]\right] \tag{3.62}
$$

In Eq. (3.62) the dissipative interaction of HQs with the heat bath is encoded in the *drag* and *diffusion* coefficients which are given according to Eq. (3.61) in terms of the transition rate as

$$
\begin{aligned}
A_j(p) &= \sum \int \frac{d^3\vec{q}}{2\pi^3} q_j \omega(p,q) \\
B_{jh}(p) &= \sum \frac{1}{2}\int \frac{d^3\vec{q}}{2\pi^3} q_j q_h \omega(p,q)
\end{aligned}
\tag{3.63}
$$

Using Eq. (3.59) these HQ transport coefficient can be written as function of the total cross section for elastic scattering of HQ with any parton species

---

[1] From what follows we drop the index i which labels the flavor of the *bulk* parton scattering with the HQ.

$i = g, q, \bar{q}$ in the *bulk* system

$$\begin{aligned} A_j(p,T) &= \sum_{i=g,q,\bar{q}} \gamma_i \int \frac{d^3\vec{k}}{2\pi^3} \hat{f}_i(k) v_{rel} \sigma_{HQ+i}(p,k)\ (p-p')_j \\ B_{jh}(p,T) &= \sum_{i=g,q,\bar{q}} \gamma_i \int \frac{d^3\vec{k}}{2\pi^3} \hat{f}_i(k) v_{rel} \sigma_{HQ+i}(p,k)\ (p-p')_j\, (p-p')_h \end{aligned} \tag{3.64}$$

In particular, we have explicitly expressed the dependence on the heat bath temperature coming from the equilibrium distribution functions $\hat{f}_i$ and used a delta function to fix the transfer momentum $\boldsymbol{q}$ knowing the initial and final momentum of the HQ. Then, if we consider the heat bath to be isotropic, with such condition together with local equilibrium implying that transport coefficient are defined in the rest frame of the background medium, rotational symmetry allows for the following simplification of Eq. (3.64)

$$\begin{aligned} A_j(p,T) &= A(p,T) p_j \\ B_{jh}(p,T) &= B_1(p,T) P^{\parallel}_{jh}(p) + B_0(p,T) P^{\perp}_{jh}(p) \end{aligned} \tag{3.65}$$

where the projection operators on the longitudinal and transverse HQ momentum component are given by

$$P^{\parallel}_{jh}(p) = \frac{p_j p_k}{|\vec{p}|^2} \quad , \quad P^{\perp}_{jh}(p) = \delta_{jk} - \frac{p_j p_k}{|\vec{p}|^2} \tag{3.66}$$

and the corresponding scalar *drag* and *diffusion* (longitudinal and transverse) coefficients read

$$\begin{aligned} A(p,T) &= \left\langle 1 - \frac{\vec{p} \cdot \vec{p}'}{|\vec{p}|^2} \right\rangle \\ B_0(p,T) &= \frac{1}{4} \left\langle |\vec{p}'|^2 - \frac{(\vec{p} \cdot \vec{p}')^2}{|\vec{p}|^2} \right\rangle \\ B_1(p,T) &= \left\langle \frac{(\vec{p} \cdot \vec{p}')^2}{|\vec{p}|^2} - 2\vec{p} \cdot \vec{p}' + |\vec{p}|^2 \right\rangle \end{aligned} \tag{3.67}$$

By means of the notation $\langle X(p) \rangle$ we indicate for a general function $X(p)$ the following integration

$$
\begin{aligned}
\langle X(p,T)\rangle &\equiv \sum_{i=g,q,\bar{q}} \gamma_i \int \frac{d^3\vec{k}}{(2\pi)^3} \hat{f}_i(k) v_{rel} \sigma_{HQ+i}(p,k)\, X(p) \\
&= \frac{1}{2E_p}\frac{1}{\gamma_{HQ}} \sum_{i=g,q,\bar{q}} \int \frac{d^3\vec{k}}{(2\pi)^3 2E_k} \int \frac{d^3\vec{p}'}{(2\pi)^3 2E_{p'}} \int \frac{d^3\vec{k}'}{(2\pi)^3 2E_{k'}} \qquad (3.68) \\
&\times (2\pi)^4\, \delta(p+k-p'-k')\, \overline{|\mathcal{M}_{HQ,i}|^2}\, X(p)
\end{aligned}
$$

where the second line is obtained plugging the definition of the total cross section according to Eq. (3.56). Moreover, one can associate to the transport coefficients in Eq. (3.67) the other two quantities defined as

$$
\langle 1\rangle = \Gamma(p,T) \quad , \quad \left\langle E_p - E_p' \right\rangle = \hat{e}(p,T) \qquad (3.69)
$$

which correspond respectively to the rate and HQ energy loss associated to the *elastic* scattering processes. Eq. (3.67) (Eq. (3.68)) is suitable to be solved by multi-dimensional MonteCarlo integration [168] as we will show in the next Chapter. This provides us with a tool to investigate both the temperature and the momentum dependence of HQ transport coefficients related to the interaction kernel ($\mathcal{M}$) implemented in our transport model. Indeed one of the goal of this work is to show that regarded the effects encoded within the transport coefficients, they can have a strong effect on the measured observables, hence enlightening on the properties of the QCD medium [169] [170].

3.4.2 The role of HQ Transport Coefficients

The aim of this thesis is to describe the HQ dynamics in the QGP by means of a Boltzmann approach where the non-perturbative effects are evaluated by means of the Quasi-Particle Model (QPM) whose interaction strength is tuned to reproduce lQCD thermodynamics and *bulk* observables. In comparison to Fokker-Planck approach we can extract from our Boltzmann collision kernel an effective definition of *drag* and *diffusion* coefficients according to Eq. (3.67) and compare their momentum and temperature dependence to pQCD expectations and other models. Before doing this, we find important to understand the physical meaning of such coefficient. In order to do that we still keep the diffusion approximation and in particular, we consider the limit of small HQ momentum $p \to 0$. In such non-relativistic regime both *drag* and *diffusion* coefficients Eq. (3.67) become constant values at a fixed temperature T of the heat bath, usually indicated respectively as $A(p \to 0, T) \equiv \gamma(T)$ and $B_0(p \to 0, T) = B_1(p \to 0, T) \equiv D(T)$. Then, the Fokker-Planck Eq. (3.62) simplifies to

$$\begin{aligned} \frac{\partial}{\partial t} f_{HQ}(p,t) &= \frac{\partial}{\partial p_j}\left[p_j \gamma f_{HQ}(p,t) + \frac{\partial}{\partial p_h}\left[\delta_{jh} D f_{HQ}(p,t)\right]\right] \\ &= \gamma \frac{\partial}{\partial p_j}\left[p_j f_{HQ}(p,t)\right] + D \frac{\partial^2 f_{HQ}(p,t)}{\partial p^2} \end{aligned} \tag{3.70}$$

whose solution starting from an initial condition $f_{HQ}(\vec{p}, 0) = \delta(\vec{p} - \vec{p}_0)$ takes the following Gaussian profile

$$f_{HQ}(p,t) \propto \exp\left[-\frac{\gamma}{2D}\frac{[\vec{p} - \vec{p}_0 \exp(-\gamma t)]^2}{1 - \exp(-2\gamma t)}\right] \tag{3.71}$$

Eq. (3.70) describes the evolution of the HQ momentum distribution function $f_{HQ}(p,t)$ undergoing 3-dimensional Brownian motion which involves the combined effect of a drift force coupled to random scatterings at small angles. From the equation of average HQ momentum

$$\langle \vec{p} \rangle = \vec{p}_0 \exp(-\gamma t) \tag{3.72}$$

we can see that the coefficient γ relates exactly to the friction or *drag* force which determines the relaxation rate of the HQ three-momentum to its equilibrium value $\vec{p}$. We notice that in Eq. (3.72) $\vec{p}$ tends asymptotically to zero as a vector, resulting in the isotropization of the HQ momentum distribution while converging to equilibrium. Instead for the variance equation and using Eq. (3.72) we obtain

$$\left\langle (\vec{p} - \vec{p}_0)^2 \right\rangle = \left\langle \vec{p}^2 \right\rangle - \langle \vec{p} \rangle^2 = \frac{3D}{\gamma}\left[1 - \exp(-2\gamma t)\right] \tag{3.73}$$

from which we observe that the coefficient D represents precisely the diffusion part governing the HQ momentum fluctuations around the equilibrium value. In the limit $t \to \infty$ HQs must reach thermal equilibrium with the heat bath, meaning that the solution Eq. (3.71) should asymptotically approach to the non-relativistic Maxwell-Boltzmann distribution with temperature T. Such condition implies that *drag* and *diffusion* coefficients should satisfy the well known *Einstein fluctuation-dissipation relation*

$$D = \gamma M_{HQ} T \tag{3.74}$$

At sufficient large time compared to the relaxation time of HQ momentum that from the mean Eq. (3.72) we can identify with the inverse of the drag $\tau_{eq} = \gamma^{-1}$, the diffusion in momentum space has converted into a 3-dimensional broadening in the position distribution at time $t \gg \tau_{eq}$

$$\left\langle \vec{x}^2(t) \right\rangle - \langle \vec{x}(t) \rangle^2 = 3\frac{T^2}{D} = 6 D_s(T) t \tag{3.75}$$

governed by the so defined *spatial diffusion coefficient* $D_s(T)$ which in the validity of the Einstein relation is related to the *drag*, i.e. to the HQ thermalization time, through the following expression

$$2\pi T D_s = \frac{2\pi T^2}{M_{HQ}\gamma} = \frac{2\pi T^2}{M_{HQ}} \tau_{eq} \tag{3.76}$$

In natural unit $[\gamma] \sim fm^{-1}$, $[D] \sim GeV^2 fm^{-1}$, so in Eq. (3.76) it results that the introduced $2\pi T D_s$ coefficient on the left hand side is dimensionless. Moreover, since in kinetic theory the HQ relaxation time is expected to be proportional to M_{HQ}, from Eq. (3.76) we can infer that D_s is instead mass independent. This leads to the possibility to measure HQ interaction within the QCD medium without any mass scale constraint and to construct phenomenological models which by extracting the spatial diffusion coefficient and comparing to *quenched* lQCD expectations can directly probe the QGP properties.

3.5 Numerical solution of Boltzmann equation

In this last section we discuss about the numerical implementation of the transport equations Eq. (3.45) and Eq. (3.51) which we use for describing the dynamics of respectively bulk partons $i = g, q, \bar{q}$ and Heavy Quarks (HQs). In order to solve the Relativistic Boltzmann Equation (RBE), we divide the coordinate space V into a 3D lattice constituted by N_{cells} of volume $\Delta^3\vec{x}$ and we employ *test-particle method* to sample the bulk parton or the HQ phase-space distribution function $f(x, p)$ within a sufficient small time-step Δt as done firstly by Wong [171] and performed in many transport appraoches .Usually test particles are chosen to be fictitious point-like objects, hence $f(x, p)$ can be written as a sum over N_{test} coordinates and momenta on-shell δ functions (see Eq. (3.3))

$$f(\vec{x}, \vec{p}, t) = \omega \sum_{i=1}^{N_{test}} \delta^{(3)}(\vec{x} - \vec{r}_i(t))\delta^{(3)}(\vec{p} - \vec{p}_i(t)) \tag{3.77}$$

where $\vec{r}_i(t)$ and $\vec{p}_i(t)$ indicate respectively the position and the momentum of the i- particle, whileω is a normalization factor which relates the integral of phase distribution to the real particle density.

$$\frac{1}{V}\int d^3\vec{x}\int \frac{d^3\vec{p}}{(2\pi)^3} f(\vec{x}, \vec{p}, t) = \frac{\omega}{(2\pi)^3}\frac{N_{test}}{V} = n(x) \tag{3.78}$$

Then, plugging Eq. (3.77) into the corresponding RBE for the bulk partons or the HQs, the solution of the transport system reduces to solve the classical Hamilton equation of motion for each test particle which are written below

$$\frac{d\vec{r}_i(t)}{dt} = \frac{\vec{p}_i}{m_i} \quad , \quad \frac{d\vec{p}_i}{dt} = -\nabla_{\vec{r}} E_i(\vec{r}, t) + \left(\frac{\partial \vec{p}_i}{\partial t}\right)_{coll} \tag{3.79}$$

where in the first equation m_i corresponds to the QPM mass Eq. (3.36) for the case of bulk partons, or it is equivalent to the value $m_i = M_{HQ} = M_c, M_b$ (see Chapter 2) for the case of charm and bottom quarks. In the second equation, on the right hand side the second term accounts for the momentum variation due to the dissipative effects encoded in the collision integral, while the first term is the mean field contribution coming from the spatial dependence of the generalized non-equilibrium QPM dispersion relation $E_i(\vec{r},t) = \sqrt{p_i^2(t) + m_i(\vec{r},t)^2}$. Applying the spatial gradient on this last expression, we can express the equation of motions in the following form

$$\frac{d\vec{r}_i(t)}{dt} = \frac{\vec{p}_i}{m_i} \quad , \quad \frac{d\vec{p}_i}{dt} = -\frac{m_i(\vec{r},t)}{E_i(\vec{r},t)} \nabla_{\vec{r}} m_i(\vec{r},t) + \left(\frac{\partial \vec{p}_i}{\partial t}\right)_{coll} \tag{3.80}$$

The mean field contribution is originated from the space-time dependence of the bulk masses which are related to the QPM expressions Eq.(3.36) through the condition $m_i(\vec{r},t) = m_{QPM,i}(T(\vec{r},t))$ for $i = g, q$ where $T(\vec{r},t)$ is the temperature of the local cell centered at position $\vec{r}$ and calculated at time t from the energy and particle densities Eq. (3.50). On the other hand HQs propagate with constant mass M_{HQ}, meaning that we do not consider any mean field interaction, rather the variation of HQ momentum occurs due to the scattering collision term. In order to perform the complete simulation algorithm, from the initial conditions setup to the subsequent test propagation and collision of test particles, we use a partonic cascade code which is written in the FORTRAN programming language and it is mainly composed of four routines:

1) The **cascade** head routine where initial parameters and tables are read and the volume environment is built up, whether there is the intention to create a uniform static box for test performances or to set up a realistic event simulation for RHIC and LHC Heavy-Ion Collisions (HICs).

2) The **init** routine where all initial particle's spectra in coordinate and momentum space are initialized respectively according to the Glauber profile (see Sec.Eq. (2.2)) or uniformly and by means of parametrized distributions. Test particles of each flavor, whether they are partons of the *bulk* or HQs, are randomly sampled in each volume cell, thus we can follow their trajectory along the entire simulation period.

3) The **prop** routine where test particle positions and momenta coordinates with respect to some fixed environment frame are updated after each mesh time Δt by solving the equation of motion Eq. (3.80) which are numerically implemented in the following way

$$\begin{cases} \vec{p}_i(t+\Delta t) = \vec{p}_i(t-\Delta t) - 2\Delta t \left[\frac{m_i(\vec{r}_i(t))}{E_i(t)}\right] D_{\vec{r}} m_i(\vec{r}_i(t)) + 2\Delta t \cdot \left(\frac{\partial \vec{p}_i}{\partial t}\right)_{coll} \\ \vec{r}_i(t+\Delta t) = \vec{r}_i(t-\Delta t) - 2\delta t \cdot \left[\frac{\vec{p}_i(t)}{E_i(t)}\right] \end{cases} \tag{3.81}$$

where $D_{\vec{r}}$ corresponds to some proper discretized form of the gradient operator $\nabla_{\vec{r}}$. These equations must be solved for each test particle i of a given flavor, either it is a heavy quark or a gluon or a light quark (antiquark) of the *HQ*. For the latter case Eq. (3.81) must be solved self-consistently with the gap equation Eq. (3.44) which plugging the expression Eq. (3.77) becomes

$$\frac{\partial B}{\partial m_i} + \nu_i \frac{\omega}{(2\pi)^3} \frac{m_i}{V} \sum_{j=1}^{N_c ell} E_j \tag{3.82}$$

In order to study HQs dynamics within our Boltzmann approach we simplify the transport setup of the *bulk* system by choosing a constant mass value $m_g = m_q = 0.5\, GeV$ which in the end gives us an EoS still in agreement with lQCD thermodynamics.However, we do not account for this approximation for what concerns HQ interaction which is built up consistently with the QPM prescriptions. Of course, we have the possibility to choose between a QPM collision kernel to a pQCD one which is done conjointly with a switch from a massive to a massless *bulk*. The jump to the new trajectory's point of each test particle is evaluated by knowing at first the momentum and energy at time t and the variation of their values after Δt. All particles must satisfy on-shell condition $E_i(t) = \sqrt{p_i(t)^2 + m_i^2}$ which is checked at every time step. We choose a sufficient small $\Delta^3\vec{r}$ and Δt and secure that the solution obtained by test-particle method tends asimptotically to the exact solution of the RBE.

4) The **coll** routine where the numerical implementation of the Boltzmann collision integral $C[f]$ is pursued. In order to solve numerically the collision integral we make use of the *stochastic method* introduced for the first time by Greiner and Xu [172] and nowadays employed by many transport codes.In contrast to more widespread geometrical algorithms which do not preserve explicitly Lorentz covariance and consequently violate causality in relativistic frames leading to a sort of artifacts in particle's spectra, facing particle collisions with a probabilistic approach appears to be the right method and thus overcomes such numerical problem. We give a brief description of the stochastic algorithm for implementing two-body elastic collisions between gluons and light quarks of the medium or HQs and *bulk* partons in the following paragraph.

3.5.1 Stochatic algorithm for the collision integral

Let us consider the two-body collision integral given by [172]

$$\begin{aligned} C_{22} = & \frac{1}{2E_1}\int \frac{d^3p_2}{(2\pi)^3 2E_2}\,\frac{1}{\nu}\int \frac{d^3p_1'}{(2\pi)^3 2E_1'}\frac{d^3p_2'}{(2\pi)^3 2E_2'}\, f_1' f_2' \\ & |\mathcal{M}_{1'2'\to 12}|^2 (2\pi)^4 \delta^{(4)}(p_1' + p_2' - p_1 - p_2) \\ & - \frac{1}{2E_1}\int \frac{d^3p_2}{(2\pi)^3 2E_2}\,\frac{1}{\nu}\int \frac{d^3p_1'}{(2\pi)^3 2E_1'}\frac{d^3p_2'}{(2\pi)^3 2E_2'}\, f_1 f_2 \\ & |\mathcal{M}_{12\to 1'2'}|^2 (2\pi)^4 \delta^{(4)}(p_1 + p_2 - p_1' - p_2') \end{aligned} \tag{3.83}$$

This represent the dissipative kernel of the RBE for the distribution function $f_1 \equiv f(\vec{r}_1, \vec{p}_1, t)$ and analogous notation we use for the integrated functions $f_2, f_{1'}, f_{2'}$. In Eq. (3.83) the statistical factor ν is set to 2 when considering double counting in case particles 1' and 2' are identical, otherwise ν is set to 1. The two terms in C_{22} expression are respectively the gain term which enriches the number of particles in the state 1 because it accounts for collisions of type $1'2' \to 1\,2$, while the loss term describes the inverse scattering $1\,2 \to 1'\,2'$ which brings particles out of the considered volume of phase spaces. The four-delta function accounts for total energy and momentum conservation. The main microscopic ingredient in Eq. (3.83) is represented by the scattering amplitude of the two-body process, which is usually symmetric for time reversal, i.e. $\mathcal{M}_{1'2'\to12} = \mathcal{M}_{12\to1'2'}$. Then, the total cross section of the two-body scattering process is given by [1]

$$\sigma_{22} = \frac{1}{2F}\frac{1}{\nu}\int \frac{d^3p_1^{'}}{(2\pi)^3 2E_1^{'}}\frac{d^3p_2^{'}}{(2\pi)^3 2E_2^{'}}|\mathcal{M}_{12\to1'2'}|^2(2\pi)^4\delta^{(4)}(p_1+p_2-p_1^{'}-p_2^{'}) \tag{3.84}$$

where we defined the invariant flux factor of the initial particle state

$$F = \sqrt{(p_1\cdot p_2)^2 - m_1^2 m_2^2} \tag{3.85}$$

and also the relative particle velocity which is obtained in the following way

$$v_{rel} = \frac{F}{E_1E_2} = \frac{\sqrt{[s-(m_1+m_2)^2][s-(m_1-m_2)^2]}}{2E_1E_2} \tag{3.86}$$

being the Mandelstam variable $s = (p_1+p_2)^2$ equivalent to the square of the collision energy in the center-of-mass frame of the scattering particles. The basic idea of the algorithm is to sample stocastically the scattering processes of the two particles according to a collision probability P_{22} by comparing the value of this probability with a random number which is uniformly chosen between 0 and 1. For evaluating the P_{22} we refer directly to the collision integral term Eq. (3.83). Indeed if we assume that two test particles 1 and 2 at time t are in the same unit cell of volume Δ^3x and have respectively momenta lying in the range $(\vec{p}_1, \vec{p}_1 + \Delta^3p_1)$ and $(\vec{p}_2, \vec{p}_2 + \Delta^3p_2)$ we can express the collision rate per unit of phase space of such pair as

$$\begin{aligned}\frac{\Delta N_{coll}^{2\to2}}{\Delta t\frac{1}{(2\pi)^3}\Delta^3x\Delta^3p_1} &= \frac{1}{2E_1}\frac{\Delta^3p_2}{(2\pi)^3 2E_2}f_1f_2 \times \frac{1}{\nu}\int\frac{d^3p_1^{'}}{(2\pi)^3 2E_1^{'}}\frac{d^3p_2^{'}}{(2\pi)^3 2E_2^{'}} \\ &\times|\mathcal{M}_{12\to1'2'}|^2(2\pi)^4\delta^{(4)}(p_1+p_2-p_1^{'}-p_2^{'})\end{aligned} \tag{3.87}$$

By definition (see Eq. (3.1)) the distribution function f_i is the number of particles of the same species located in the i cell with unit phase space volume

$\Delta\vec{x}\Delta\vec{p}_i/(2\pi)^3$, so we can write it as

$$f_i(\vec{x},\vec{p},t) = \frac{\Delta N_i}{\Delta^3 x \frac{\Delta^3 p_i}{(2\pi)^3}} \tag{3.88}$$

Inserting Eq. (3.88) for $i = 1,2$ in Eq. (3.87) and using the definition of the two-body cross section Eq. (3.46), the formula for the collision rate becomes

$$\Delta N_{coll}^{2\to 2} = \left(f_1 \frac{\Delta^3 p_1}{(2\pi)^3}\right)\left(f_2 \frac{\Delta^3 p_2}{(2\pi)^3}\right) v_{rel}\sigma_{22}\, \Delta^3 x\, \Delta t \tag{3.89}$$

Finally the absolute collision probability P_{22} is obtained by considering such interaction rate among all particles in the state 1 and 2. Hence, we have

$$P_{22} = \frac{\Delta N_{coll}^{2\to 2}}{\Delta N_1 \Delta N_2} = v_{rel}\sigma_{22}\frac{\Delta t}{\Delta^3 x} \tag{3.90}$$

where for calculating $\Delta N_{1,2}$ we used the inverted expression of Eq. (3.50). The probability has to be divided by N_{test} if test particle method for sampling the phase space distribution is used ($P_{22} \to P_{22}/N_{test}$). Since in Eq. (3.90) the probability is proportional to σ_{22} the latter condition is equivalent to scale the total scattering cross section by N_{test} ($\sigma_{22} \to \sigma_{22}/N_{test}$) [171] [173]. We point out that from Eq. (3.84) the definition of σ_{22} is provided as function of generic scattering amplitudes. Specifically, for the case of an elastic collision involving only gluons and light quarks (antiquarks) of the medium we consider the Chapman-Enskog formula Eq. (3.48) where $T(x) = T(cell,t)$ and $n(x) = \sum_{i=g,q,\bar{q}} N_i/\Delta^3\vec{x}$ are respectively the temperature and the *bulk* density calculated in the cell where the collision occurs at time t. On the other hand, if we sample a scattering process between a *bulk* parton and a heavy quark, the total cross section is derived according to the QCD scattering matrices, the same we use to calculate HQ transport coefficient (see Eq. (3.64)), thus resulting in the correct description of *drag* and *diffusion* forces we expect either in the pQCD or in the QPM framework (see Chapter 4). In the limit $\Delta t \to 0$ and $\Delta^3 p \to 0$ the numerical solution with the stochastic method converges to the exact solutions of the Boltzmann equation. A reasonable convergent result is obtained when Δt and $\Delta^3 x$ are taken smaller than the typical time and spatial inhomogeneity of the particle densities. The stochastic procedure has to be carried out among all pair of particles which belong to the same cell and for the entire space grid. It means that for a single cell the number of random extractions equals the possible pairs $N_{pair} = N(N-1)/2$, where N corresponds to the total particle's number in the cell. In order to reduce the computational time we use the scheme in Ref. [174] [175] and used also in Ref. [172]. We randomly choose $\mathcal{N} < N_{pair}$ among all possible pairs in each cell and, in order to perform the stochastic method only for the $\mathcal{N}$ sample, we correct the collision probability in the following manner

$$P_{22} \to P_{22}^{eff} = P_{22} \frac{N_{pair}}{\mathcal{N}} = P_{22} \frac{N(N-1)/2}{\mathcal{N}} \tag{3.91}$$

where in Eq. (3.91) P_{22} has been already scaled by N_{test} according to the test-particle prescriptions [171] [173]. Further improvement of the method, that avoids in particular the possibility of P_{22}^{eff} to exceed one and thus break the stochastic implementation, is done by choosing $\mathcal{N}$ differently for each cell ($\mathcal{N}(cell)$) in the following way. Initially we calculate the maximum effective probability achievable in the cell under consideration. This value can be derived from the previous definition

$$max\left(P_{22}^{eff}\right) = P_{22}^{max} \frac{N(N-1)/2}{\mathcal{N}(cell)} \tag{3.92}$$

where $P_{22}^{max} = v_{rel}^{max} \frac{\sigma_{22}^{max}}{N_{test}} \frac{\Delta t}{\Delta^3 x}$ is the maximum real probability in the cell (scaled by test particle number). Subsequently the maximum of collision probability in Eq. (3.92) is normalized to 1 and from this condition we obtain the following unique condition to calculate $\mathcal{N}(cell)$

$$\mathcal{N}(cell) = Integer\left[P_{22}^{max} N(N-1)/2\right] \tag{3.93}$$

Using the value of $N(cell)$ provided by Eq. (3.93) we ensure that our effective probability Eq. (3.91) will not exceed 1 in any case and in the meanwhile we achieve to minimize the calculation time of the collision algorithm up to the maximum limit allowed by the method itself.

CHAPTER 4

HQS' TRANSPORT COEFFICIENTS

4.1 Boltzmann approach for HQ dynamics

The propagation of Heavy Quarks (HQs) in the QGP is described by means of the Relativistic Boltzmann Eq. (3.51) for the on-shell single HQ phase-space distribution function f_{HQ} that we write again here

$$p_\mu \partial^\mu_x f_{HQ}(x,p) = C[f_{HQ}, f_g, f_q, f_{\bar{q}}](x,p) \tag{4.1}$$

and which we solve numerically through test-particle method in the same manner we have done for the *bulk* partons. In Eq. (4.1) the collision integral $C[f_{HQ}, f_g, f_q, f_{\bar{q}}](x,p)$ encodes the dissipative part governing the evolution of HQs inside the hot QCD medium. In this work we consider only elastic two-body scattering processes between a HQ and either a gluon or a light quark (antiquark) of the *bulk*, i.e. $HQ(p_1) + i(g,q)(p_2) \rightarrow HQ(p'_1) + i(g,q)(p'_2)$.

Therefore our collision integral takes the expression

$$
\begin{aligned}
C[f_{HQ}, f_q, f_{\bar{q}}] =& \frac{1}{2E_1} \sum_{i=g,q,\bar{q}} \int \frac{d^3 p_2}{2E_2(2\pi)^3} \frac{1}{\nu} \int \frac{d^3 p_1'}{2E_1'(2\pi)^3} \int \frac{d^3 p_2'}{2E_2'(2\pi)^3} \\
& \times \overline{|\mathcal{M}_{HQ,i}|^2} (2\pi)^4 \delta^4(p_1 + p_2 - p_1' - p_2') \\
& \times [f_{HQ}(p_1') f_i(p_2') - f_{HQ}(p_1) f_i(p_2)]
\end{aligned} \tag{4.2}
$$

which in each unit cell of volume $\Delta\vec{x}$ and in each time step Δt we map by means of the stochastic algorithm described in Chapter 3 into a probability of collision Eq. (3.90) which is proportional to the total cross section

$$
\begin{aligned}
\sigma_{22} =& \frac{1}{4 v_{rel} E_1 E_2} \int \frac{d^3 p_1'}{2E_1'(2\pi)^3} \int \frac{d^3 p_2'}{2E_2'(2\pi)^3} \\
& \times \overline{|\mathcal{M}_{HQ,i}|^2} (2\pi)^4 \delta^4(p_1 + p_2 - p_1' - p_2')
\end{aligned} \tag{4.3}
$$

Within the Boltzmann dynamics we choose to implement two different models for describing HQ interaction inside the QGP

[pQCD] In the first one we calculate the scattering cross section through Leading-Order (LO) pQCD Feynman diagrams depicted in Appendix B employing the scattering matrices from Ref. [80] in which we consider massless partons of the *bulk* and the value of the coupling constant α_s either as a constant or running in accordance to Eq. (1.14) with $Q^2 = (2\pi T)^2$. As a praxis of this approach we introduce also a Debye screening mass $m_D \sim \sqrt{4\pi\alpha_s} T$ to regularize the IR divergence in the massless gluon propagator.

[QPM] In our second scheme we account for QCD non-perturbative contribute to HQ interaction by means of the Quasi-Particle Model (QPM). Hence, light quarks and gluons are dressed with T-dependent effective masses $m_{g,q} \simeq g(T)T$ whose exact expressions are written in Eq. (3.36), while the strength coupling $g(T)$ follows the QPM logarithmic formula in Eq. (3.41) with parameter values fitted to the results of Wuppertal-Budapest lQCD collaboration [154]. in agreement also with other mod-

> els [176] [177]. To calculate the total cross section of HQ interaction Eq. (4.3) we start from the same Feynman diagrams of the pQCD scheme with slight modifications in order to include the QPM masses with the T-dependent coupling constant $\alpha_s(T) = g^2(T)/4\pi$ from QPM interaction.

The complete expressions of the scattering matrices for the various channels are collected in the Appendix B where it is possible to check that in the massless limit $m_{g,q} \to 0$ and at high temperature $T \geq 3T_c$ the QPM interaction matches with the pQCD paradigma.

4.1.1 Monte-Carlo calculation for *drag* and *diffusion*

In Sec. (3.4) we derived the Fokker-Planck equation which describes the propagation of HQs in a thermal medium within the approximation of Brownian motion. In particular, we saw that the interaction kernel is encoded inside some transport coefficients which in general depend on the HQ momentum p and on the temperature T of the heat bath and whose expression can be expressed by means of the following expectation value (see eq. (3.68))

$$\begin{aligned}\langle X(p,T)\rangle &\equiv \sum_{i=g,q,\bar{q}} \gamma_i \int \frac{d^3\vec{k}}{(2\pi)^3} \hat{f}_i(k) v_{rel} \sigma_{HQ+i}(p,k)\, X(p) \\ &= \frac{1}{2E_p}\frac{1}{\gamma_{HQ}} \sum_{i=g,q,\bar{q}} \int \frac{d^3\vec{k}}{(2\pi)^3 2E_k} \int \frac{d^3\vec{p}'}{(2\pi)^3 2E_{p'}} \int \frac{d^3\vec{k}'}{(2\pi)^3 2E_{k'}} \\ &\times (2\pi)^4\, \delta(p+k-p'-k')\, \overline{|\mathcal{M}_{HQ,i}|^2}\, X(p)\end{aligned} \tag{4.4}$$

where $\hat{f}_i(k)$ indicates the thermal equilibrium distribution function of the *bulk* partons $i = g, q, \bar{q}$. Then, depending on the function $X(p)$ one derives the definition for the collision rate or the energy loss Eq. (3.69) and above all the formula for the *drag* and *diffusion* coefficients Eq. (3.68) that we write again here

$$
\begin{aligned}
A(p,T) &= \left\langle 1 - \frac{\vec{p}\cdot\vec{p}'}{|\vec{p}|^2} \right\rangle \\
B_0(p,T) &= \frac{1}{4}\left\langle |\vec{p}'|^2 - \frac{(\vec{p}\cdot\vec{p}')^2}{|\vec{p}|^2} \right\rangle \\
B_1(p,T) &= \left\langle \frac{(\vec{p}\cdot\vec{p}')^2}{|\vec{p}|^2} - 2\vec{p}\cdot\vec{p}' + |\vec{p}|^2 \right\rangle
\end{aligned}
\tag{4.5}
$$

These coefficients are usually provided as external input to the Fokker-Planck equation which is numerically solved through differential stochastic Langevin equation where HQs propagate under the effect of a *drag* force and a random force which is directly linked to the *diffusion* part [169, 178, 179, 180]. Then, this framework is coupled to some description of the QGP evolution that can be obtained either by a hydrodynamical model or by relativistic Boltzmann approach to build up a full package and carry out realistic simulations of HICs provided also some initial conditions and a hadronization mechanism. As discussed in Chapter 3 our transport model is set in the domain of a full Boltzmann description for what concerns the *bulk* part and also the propagation of charm and bottom. However, for the aim of this work we need to have knowledge about the expected behavior of the *drag* and *diffusion* coefficients for our QPM and pQCD model.

For this reason inspired by Ref. [168] we have developed a Monte-Carlo code written in FORTRAN language for calculating HQ transport coefficient within different interaction schemes that is based on the numerical solution of the multiple-integrals appearing in Eq. (4.4). In order to implement such expression in a computer program, we have to perform some simple steps that in the end brings to the following result

$$
\begin{aligned}
\langle X(p,T)\rangle = \sum_{i=g,q,\bar{q}} \frac{1}{(2\pi)^3} \int dk\, k^2\, \hat{f}_i(k) \int d\cos\chi \\
\times \int dt\, v_{rel} \left(\frac{d\sigma}{dt}\right)_{HQ+i} \int d\phi_{cm}\, X(\ldots)
\end{aligned}
\tag{4.6}
$$

In Eq. (4.6) the first two integrations refer to the *bulk* parton $i = g, q, \bar{q}$ kinematics, while the last two belong to the final HQ state evaluated in the center-of-mass (*cm*) frame of the colliding particles. In particular, ϕ_{cm} is the azimuthal angle, while the Mandelstam variable t is defined from the diffusion angle θ_{cm} through the following relation

$$t = -2\hat{p}^2 \left(1 - \cos(\theta_{cm})\right) \ , \ \hat{p}^2 = \frac{1}{4s}\left[(s - M_{HQ}^2 - m_i^2)^2 - 4m_i^2 M_{HQ}^2\right] \tag{4.7}$$

where we have indicated as $\hat{p}$ the absolute HQ momentum in the *cm* frame and derived its expression in terms of the Mandelstam variable $s = (p + k)^2$, i.e. the total collision energy in the *cm* frame. In Eq. (4.6) the differential cross section for HQ interaction and the relative velocity are

$$\left(\frac{d\sigma}{dt}\right)_{HQ+i} = \frac{1}{64\pi\hat{p}^2 s}\overline{|\mathcal{M}_{HQ,i}|^2} \tag{4.8}$$

$$v_{rel} = \frac{2s\left[(s - M_{HQ}^2 - m_i^2)^2 - 4M_{HQ}^2 m_i^2\right]^{1/2}}{(s + M_{HQ}^2)(s - M_{HQ}^2 + m_i^2)} \tag{4.9}$$

This are quite generalized expression to consider also a massive *bulk* made of quasi-particles with thermal QPM masses taken from Eq. (3.36) and scattering matrices entering in Eq. (4.8) that can be read in Appendix B. It is easy to check that in the limit of a massless *bulk* ($m_i \to 0$) valid for our pQCD scheme all these relations reduce to the original work [168].

Transport coefficients for charm and bottom quarks resulting from the calculations within the Monte-Carlo code both for the pQCD running coupling scheme and the QPM are collected in the plots below. We notice that as T increases the *drag* coefficient from QPM tend to the pQCD results and also that at all temperature we recover the non-relativistic condition for the *diffusion*, i.e. $B_0 = B_1$ at $p \to 0$.

4.1.2 Test transport coefficients in a box

In the stochastic method the Boltzmann-like collision integral is mapped into a scattering probability P_{coll} which in the end is proportional to the total cross section σ_{22}. For the HQ interaction σ_{22} is equivalent to σ_{HQ+i} regarding

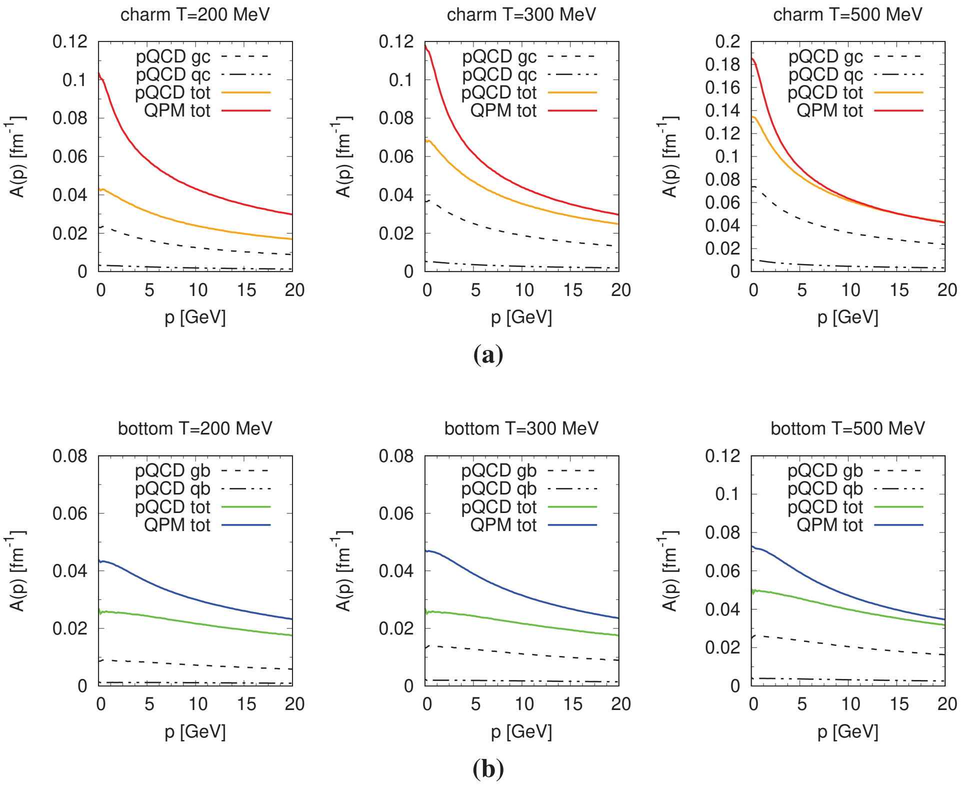

(a)

(b)

Figure 4.1: Drag coefficient within pQCD and QPM interaction for charm **(a)** and bottom **(b)** as function of HQ momentum p calculated for three different temperatures of the heat bath. In each plot dashed black curves are the contribution from pQCD gluon-HQ scattering, while dash-double dotted curves are the one from light quark-HQ scattering. Colored lines indicate the sum $gc(b) + 2N_f * qc(b)$ where $N_f = 3$ is the number of flavor and the factor 2 stands for the doubling from antiquarks.

the flavor of the particle which scatters with the HQ, i.e. $i = g, q, \bar{q}$. In addition, when a collision between a HQ and a *bulk* parton occurs, the final momentum space of the process is sampled through a random extraction of the diffusion angle in the center-of-mass frame of the pair, namely θ_{cm}, according to the differential cross section $d\sigma_{HQ+i}/dt$. We remind that the Mandelstam variable t is directly linked to the variable θ_{cm} through the relation

$$t = -2\hat{p}^2\,(1 - \cos(\theta_{cm})) \;\; , \;\; \hat{p}^2 = \frac{1}{4s}\left[(s - M_{HQ}^2 - m_i^2)^2 - 4m_i^2 M_{HQ}^2\right] \quad (4.10)$$

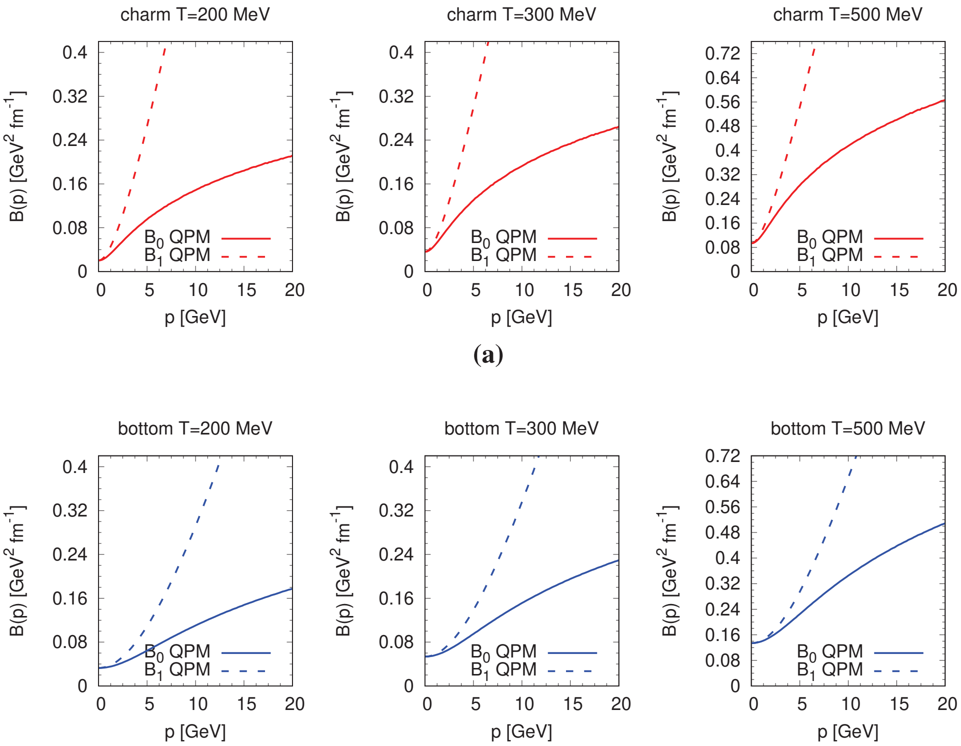

(a)

(b)

Figure 4.2: Diffusion coefficient within QPM interaction for charm **(a)** and bottom **(b)** as function of HQ momentum p calculated for three different temperatures of a heat bath constituted of gluons and quarks plus antiquarks with $N_f = 3$. Curves refer to the total contributions from all these species; transverse diffusion $B_0(p)$ is represented as solid line, while longitudinal diffusion $B_1(p)$ is in dashed font.

where again $\hat{p}$ is the absolute HQ momentum in the *cm* expressed in terms of the Mandelstam variable $s = (p + k)^2$ on the right hand side. Instead the azimuthal angle ϕ_{cm} is sampled uniformly. Since this procedure is exactly equivalent to perform the integration in Eq. (4.6), it certainty must happen that the distributions for *drag* and *diffusion* coefficients extracted from the Boltzmann code agree with the functional behavior obtained by MC integration. In order to perform this check, we carried out simulations for a static QCD medium at fixed temperature T. We chose a volume of the box of $V = 125\, fm$ and we distributed homogeneously a number of *bulk* quarks and gluons according to their values at equilibrium

$$N_{g,q} = V\frac{\nu_{g,q}}{2\pi^2}m_{g,q}^2 T^2 K_2\left(\frac{m_{g,q}}{T}\right) \to V\frac{\nu_{g,q}T^3}{\pi^2}\ (m_{g,q}=0) \tag{4.11}$$

After doing this, we initialize $N_{HQ} = 1000$ HQs inside the box by distributing them homogeneously in space and with some general power law spectrum and let them propagate inside the medium at fixed T for a sufficient amount of number of time steps of range $\Delta t = 0.02\, fm$ each. In the end we finalize the extraction of *drag* and *diffusion* coefficients through proper distributions that we derive with the few steps below. Indeed substituting the test-particle expansion Eq. (3.77) to the phase-space function appearing in the transport coefficients definition Eq. (3.68) we get

$$\langle X(p,T)\rangle = \frac{1}{2\pi}\sum_{test} v_{rel}\sigma_{tot}(s)\left[\frac{1}{\sigma_{tot}(s)}\int dt\frac{d\sigma}{dt}\int d\phi X(\ldots)\right] \tag{4.12}$$

where $(\ldots)$ indicate both the p and T parameters, as well as other integrated kinematic variables. In Eq. (4.12) we explicitly inserted the total cross section for HQ scattering $\sigma_{22} \equiv \sigma_{tot}(s)$ which plays the role of collision probability in the stochastic algorithm. Therefore, we recognize inside the square brackets a sort of expectation value that we can write by means of a Monte-Carlo importance sampling as

$$\langle X(p,T)\rangle = \sum_{test} v_{rel}\sigma_{tot}(s)\sum_{h(\sigma),k} X^{\sigma}\left(s,u_h,\phi_k\right) \tag{4.13}$$

where we indicated as $X^{\sigma}\left(s,t_h,u_h,\phi_k\right)$ the random variable associated to the observable $X(\ldots)$ and whose values are determined by extracting the Mandelstam variable t, meaning the diffusion angle θ_{cm}, according to the differential cross section (that explains the extra σ label), while the angle ϕ is an uniform random variable. Thus, the $1/2\pi$ coefficient can be absorbed within the integration over the angle ϕ. The formula in Eq. (4.13) can be recast into a sum series over the number occurring in the all box cells and for the total simulation events. Finally, since transport coefficients $X(p,T)$ are defined for a single HQ given its momentum p we have to divide the resulting formula by the momentum distribution of HQs at each time-step, namely $N_{HQ}(p)$, and average by the density of *bulk* partons $\rho_i(T)$ in each cell. Hence, the mean expression is given by

$$\langle X(p,T)\rangle_{BOX} = \sum_{events}\sum_{cell}\sum_{i=g,q,\bar{q}}\left(\frac{v_{rel}\sigma_{tot}X^{\sigma}(\ldots)\rho_i(T)}{N_{HQ}(p)\rho_i(T)}\right) \tag{4.14}$$

In the following plots we show all our extracted transport coefficients for our two different models, pQCD and QPM, obtained performing simulations for charm and bottom propagation within a static medium at equilibrium for two different temperatures. In this check, there was no need to tune the HQ interaction to some precise suppression amount, hence we did not consider any enhancement of the interaction through a constant K factor.

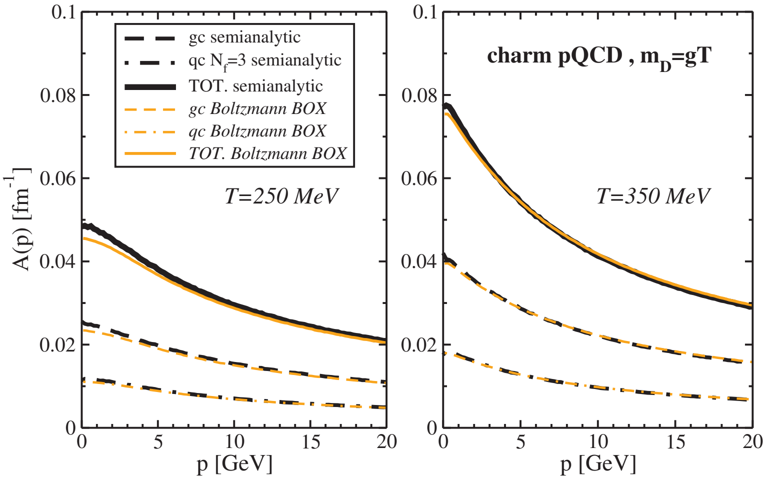

Figure 4.3: Drag coefficient $A(p)$ from pQCD model of charm quarks in a static box at $T = 250\,MeV$ (left) and $T = 350\,MeV$ (right) compared to semi-analytic calculations from MC integration. Semi-analytic results are represented with black lines: dashed is the contribution from only *gc* scattering, dash-dotted is the one from *qc* interaction with number of flavor $N_f = 3$, while solid curve is the sum over the two ones, assuming double contribution for the case of quarks (antiquarks). Extracted Boltzmann distributions follow the same font but with colored curves.

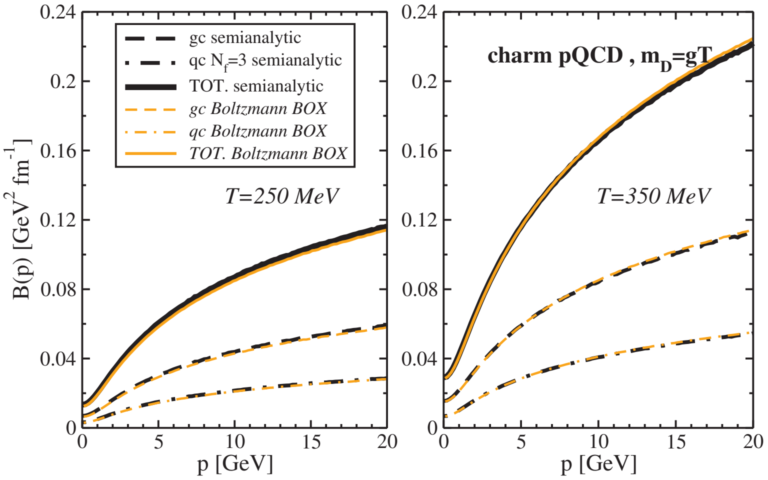

Figure 4.4: Extracted transverse diffusion coefficient $B_0(p)$ from pQCD model of charm quarks in a static box at $T = 250\,MeV$ (left) and $T = 350\,MeV$ (right) compared to semi-analytic calculations from MC integration. Fonts and colors are the same used for the corresponding drag.

4.2 Model comparison for HQ transport coefficients

The dynamical evolution of HQs in QGP has be described by means of many transport models based either on relativistic Botlzmann equation [181] [182] [183] [184] or on Fokker-Planck/Langevin paradigma [185][186] [187], some of them also including radiative energy loss along with a collisional kernel. However, in the original setup to describe the final HQ observables which are measured in high-energy HICs with the use of proper parameters, the extracted HQ transport coefficients from these models have a large discrepancy that can vary by a factor of over 5. In order to investigate the origin of this large uncertainty, we join a working group [188] for the systematic comparison of HQ transport coefficients by with various transport models. On behalf this collaboration we carried out calculations for our pQCD and QPM models, the former within a Langevin approach, while the latter implemented in the full Boltzmann code as discussed at the beginning of this Chapter.

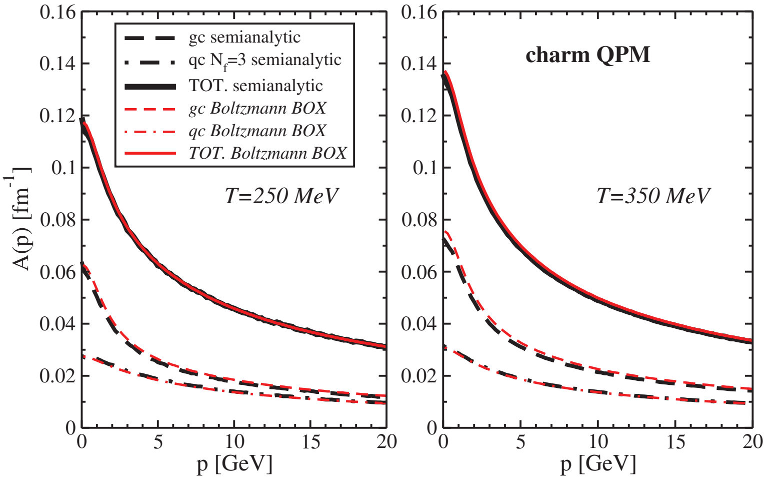

Figure 4.5: Extracted drag coefficient $A(p)$ from QPM interaction of charm quarks in a static box at $T = 250\,MeV$ (left) and $T = 350\,MeV$ (right) compared to semi-analytic calculations. The font and color notation is the same as the pQCD case in the previous plot.

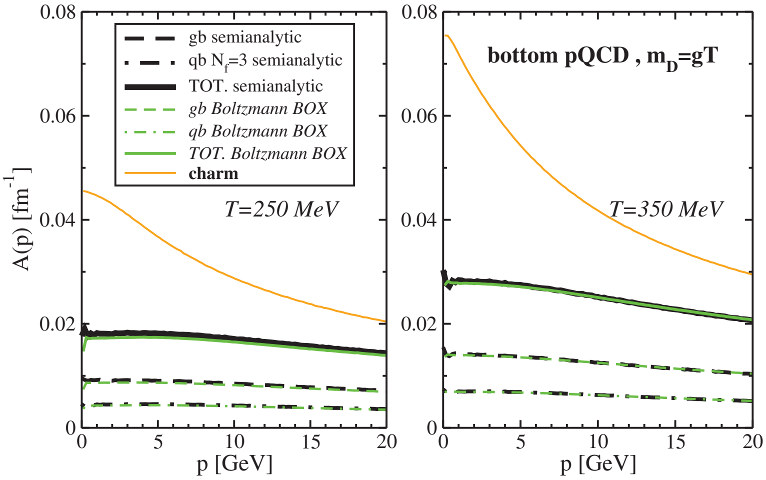

Figure 4.6: Extracted drag coefficient $A(p)$ from pQCD model of bottom quarks in a static box at $T = 250\,MeV$ (left) and $T = 350\,MeV$ (right) compared to semi-analytic calculations. The font and color notation is the same as the previous check for charm. The total contribution of drag coefficient for bottom quarks (solid green line) is also compared to the one of charm quarks (solid orange line).

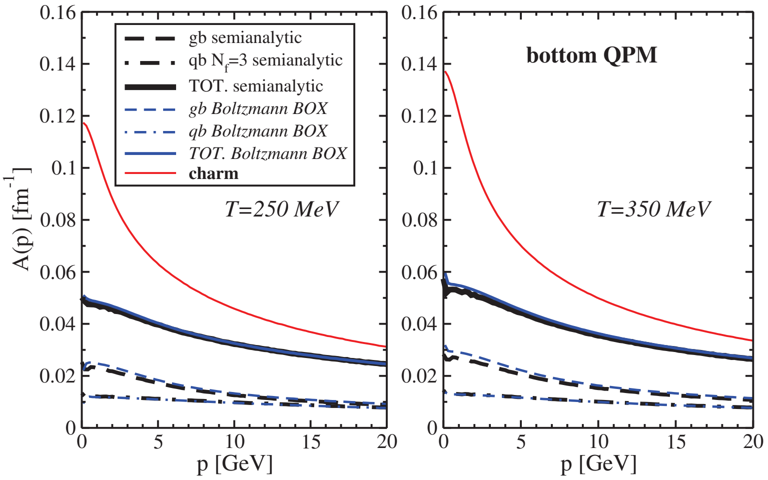

Figure 4.7: Drag coefficient $A(p)$ from QPM interaction of bottom quarks in a static medium (box) at fixed temperature $T = 250\,MeV$ (left) and $T = 350\,MeV$ (right) compared to semi-analytic calculations. The font and color notation is the same as the pQCD case in the previous plot. Similarly the total contribution of drag coefficient for bottom quarks (solid blue line) is also compared to the one of charm quarks (solid red line).

4.2.1 Suppression of HQs in a "brick" problem

At the beginning of this procedure we setup our box framework devised for the analysis of the nuclear modification in a so-called "brick" medium of QGP. In this scheme charm quarks are distributed inside a homogeneous and thermal equilibrated plasma at defined temperature T consisting gluons and light quarks with $N_f = 3$ flavor with total number given by Eq. (4.11). In particular, we initialize charm quarks with a simplified power-law parametrization for the transverse momentum p_T spectrum that is inspired by LO pQCD calculations [189] (see also [127])

$$\frac{d^2N}{d^2p_T} \propto \frac{1}{\left(p_T^2 + \Lambda^2\right)^{\alpha}} \tag{4.15}$$

with parameters $\alpha = 3.52$, $\Lambda = 1.85\,GeV$, while we set their starting longitudinal momentum $p_z = 0$. Then we let charm quarks evolve through the "brick" medium at fixed $T = 250\,MeV$ and we calculate the suppression factor $R_{AA}(t)$ defined as the ratio between the momentum spectra at certain time t with the initial momentum spectrum at $t = 0$. Indeed the distributions are analyzed at the partonic level in order to exclude contributions to the final observables coming from the hadronization mechanism. Within this “brick” setup we follow the common baseline established for all transport models by tuning the charm interaction as to obtain a $R_{AA} = 0.3$ at $p_T = 15\,GeV$ and at $t = 3\,fm$. In our Boltzmann QPM framework, we do this by multiplying the charm cross section by a constant factor $K = 3.4$ and then extracting the *drag* and *diffusion* coefficients in the way discussed in the previous paragraph. Instead for the Langevin pQCD approach the parameter K is included directly within the input *drag*, while the *diffusion* is derived by means of the FDT scheme which here is implemented as the inverse of the generalized relativistic Einstein relation Eq. (3.74).

In Fig. (4.8) the $R_{AA}(p_T)$ of charm quarks obtained in our calculations, labeled as “Catania QPM” and “pQCD”, is presented along with the results from the other transport models. The single plot on the left reports the common baseline for the suppression at time $t = 3\,fm$, while the three plots on the right describe the time evolution of the charm R_{AA} in the“brick” setup. In the complete work Ref. [188] the choice of this common baseline derives from a second phase of tuning of the parameters, that is why it is indicated in the figures with a “tune 2” label, and it is settled on the following considerations. First that a box temperature of $T = 250\,MeV$ should be reasonable approximation of the average temperature over an average distance of $3\,fm$ for he QGP created in realistic $Pb - Pb$ collisions. On the other hand the value of $R_{AA} = 0.3$ is close to the experimentally measured suppression of D mesons in central collisions at LHC energy [190]. In this way it was possible to reduce all the theoretical uncertainties arising from initial conditions and dynamical *bulk* which are treated differently within the original transport frameworks and hence along with the hadronization mechanism can have a strong impact on the estimate of HQ transport coefficients as it was observed in a “tune 1” phase of this work and later investigated detailly in Ref. [191].

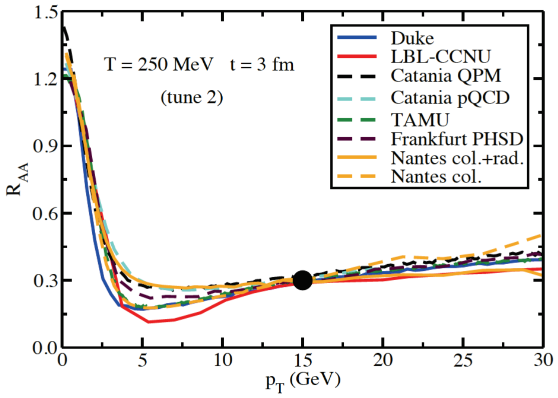

(a)

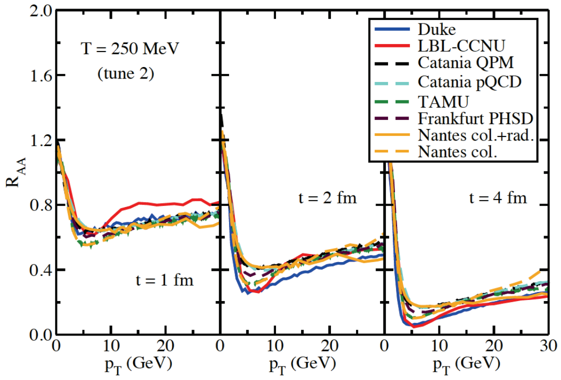

(b)

Figure 4.8: **(a)** The common baseline of charm quark nuclear modification factor $R_{AA}(p_T)$ in the "brick" medium. **(b)** The evolution profile of charm R_{AA} in the "brick" at three different times: from left to right $t = 1, 2, 3\, fm$. Pictures are taken respectively from Fig. 7 and Fig. 8 of Ref. [188] where it is given a brief description of the various transport models with references therein.

4.2.2 Analysis of HQ transport coefficients in the "brick"

In this study the extracted *drag* and *diffusion* coefficients are defined as follows

$$A(p) = \frac{\Delta\langle p_L \rangle}{\Delta t} \quad , \quad \hat{q}(p) = \frac{\Delta\langle p_T^2 \rangle}{\Delta t} \tag{4.16}$$

In eq. (4.16) $A(p)$ is the mean charm momentum loss along the longitudinal direction of propagation, hence it can be derived by multiplying the expectation value Eq. (4.14) of the original *drag* definition [168] (see first relation of Eq. (3.67)) by the charm momentum itself. Instead the parameter $\hat{q}$ quantifies the broadening of the p distribution per unit of time in the direction orthogonal to the charm momentum, thus it is equivalent to the *diffusion* coefficient and in particular, $\hat{q} = 4B_0(p)$. Despite the presence of transport approaches which include both elastic and inelastic processes, among this work those that in Fig. (4.8) are marked by solid lines, the transport coefficient $\hat{q}$ is conventionally defined through the elastic part only, since the momentum broadening which is related to the HQ energy loss kernel [192] for in medium gluon radiation at LO pQCD is regulated by collisions. The $\hat{q}$ coefficient is also viewed as a "jet" parameter, because it can be formally related to the coupling between a energetic parton or HQ and the medium density at the energy scale typical scattering processes that lead the high p_T jet parton or HQ to split into a spray of emitted gluons [193]. Then, it is possible to prove that in the limit of jet parton approaching to thermal momentum $p \rightarrow T$, the $\hat{q}$ is directly linked to the *bulk* properties and specifically to *shear* viscosity as $\eta/s \approx 1.25T^3/\hat{q}$ [194].

In Fig. (4.9) we present the results for the $A(p)$ coefficient extracted by the various transport models involved in the common "brick".

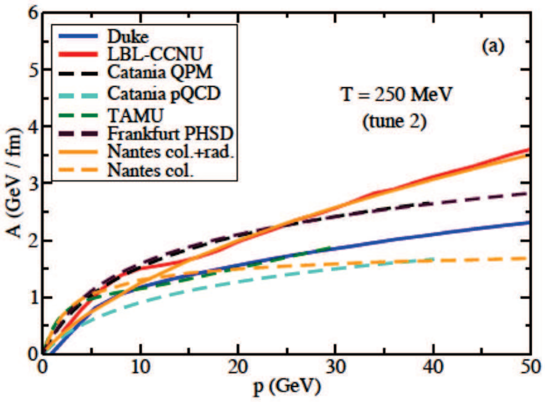

Figure 4.9: Extracted total *drag* coefficient $A(p)$ from the common baseline setup for charm suppression in "brick" medium at $T = 250\,MeV$. Picture is taken from Fig.98(a) of Ref. [188].

We observe that through this systematic study we achieve to reduce the uncertainty band of the extracted *drag* within a factor of about 2, which is the smallest intrinsic error available for such quantity at present time. Meanwhile we get an idea about the remaining differences among the models that may arise because the HQ R_{AA} is determined not only by the average energy loss, i.e. the *drag*, but especially at high p_T it is also an inference of the fluctuations in the momentum distribution, i.e. of the broadening of the spectrum. This means that a small variation for the extracted *drag* by constraining the total charm suppression does not lead to a small difference in the resulting *diffusion* and also that a larger discrepancy in the *drag* may arise between the models which are purely elastic compared to those which account also for inelastic processes. This is visible in Fig. (4.10) where we report the values for both $A(p)$ and $\hat{q}/T^3$ coefficients from the separated contribution of pure elastic energy loss, meaning that for $A(p)$ the results are the same except for the solid cases which belong to models where inelastic processes are taken into account, while for $\hat{q}/T^3$ they represent the whole estimated transverse momentum broadening.

In this issue also the analysis of more differential distributions can reveal other sources of uncertainty between the transport models. Hence, as last plan of this work we modify the initial spectrum of charm quarks inside the “brick” medium by distributing them according to a delta function with $p_z = 0$ and carrying out simulations for two different initial energy, $E_{init} = 5\,,\,30\,GeV$. Then we let charm quark evolve in the thermal heat bath and we calculate the average energy loss $\langle E\rangle$, the transverse momentum broadening $\langle k_T^2\rangle$ and the longitudinal fluctuations $\langle k_L^2\rangle - \langle k_L\rangle^2$ as function of time t. All these results are depicted in Fig. (4.11) taken from Ref. [188]. We notice that while all models agree quite well for what concerns the total amount of quenching in the “brick”, quantitatively estimated by $\langle E\rangle$, they show significant a difference in the transverse and longitudinal fluctuations which increase from a factor 2 to about a factor 5 when the charm initial energy passes from $E_{init} = 5\,GeV$ to $E_{init} = 30\,GeV$. Moreover, we observe that such discrepancy is maintained also within a pure elastic energy loss scenario and may arise in the case of charm quark due to the divergence of Langevin dynamics from the full Boltz-

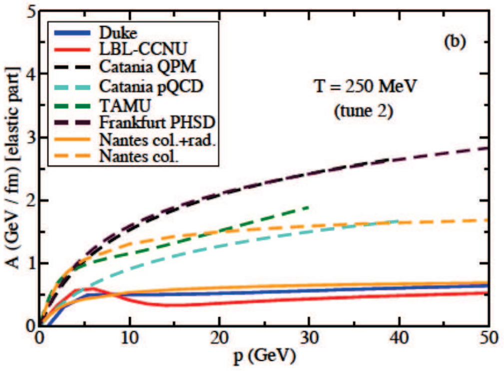

(a)

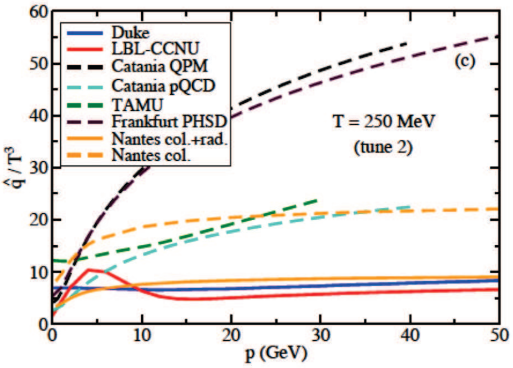

(b)

Figure 4.10: Extracted *drag* coefficient $A(p)$ **(a)** and transverse momentum broadening $\hat{q}/T^3 = 4B_0(p)/T^3$ **(b)** for the pure elastic energy loss kernel of the various transport models tuned to the common baseline for charm R_{AA} in "brick" medium at $T = 250\,MeV$. Picture are taken respectively from Fig.98 (b) and (c) of Ref. [188]

mann. For a detail discussion about this topic we refer to [195].

As stated in Ref. [188] we conclude that the analysis of the HQ dynamics within a "brick" QGP medium with a common baseline for the suppression factor R_{AA} can have an impact on constraining the total amount of energy loss, i.e. the *drag* coefficient, since it reduces uncertainties coming from initial conditions, *bulk* evolution and hadronization scheme. On the other hand, the intrinsic fluctuations coupled to the HQ propagation shatter the final agreement among the different transport approaches which seem to converge into the following three groups.

(1) Models which incorporates both elastic and inelastic energy loss (like Duke, LBL-CCNU) at high momentum estimate the largest *drag* coefficient $A(p)$ correlated with the smallest value of the *diffusion* parameter $\hat{q}(p)$ which is roughly constant as function of momentum.

(2) Models which contain only pQCD-driven collisions (like TAMU, Nantes coll.+rad. and "Catania pQCD") follow in the middle, since they to the extraction intermediate $A(p)$ and $\hat{q}$.

(3) Models which account for elastic non-perturbative interaction through quasi-particle formalism (PHSD and "Catania QPM") are characterized by a large $A(p)$ along the entire momentum range correlated by the largest transverse broadening $\hat{q}$.

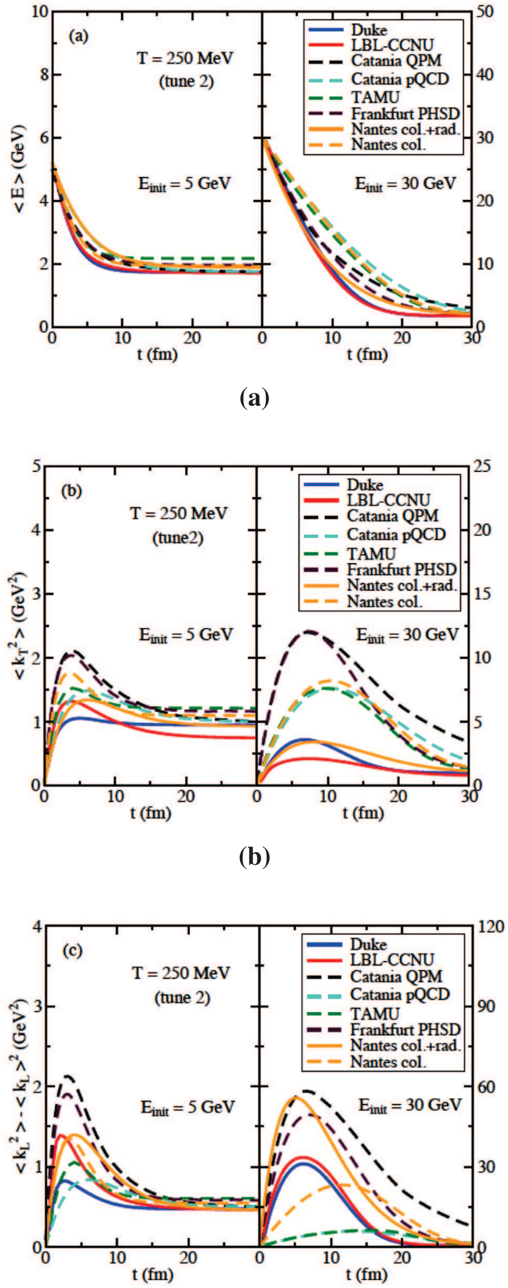

(a)

(b)

(c)

Figure 4.11: Time evolution of **(a)** average energy **(b)** transverse momentum broadening (c) longitudinal fluctuation of charm quark in the "brick" setup with initial energy $E_{init} = 5\,GeV$ (left) , $E = 30\,GeV$ (right). Picture is taken from Fig. 10 of Ref. [188]

CHAPTER 5

HQS' SUPPRESSION AND ELLIPTIC FLOW

In this chapter we collect the whole results obtained by performing simulations for realistic HICs both at RHIC and LHC scenarios within our Boltzmann Quasi-Particle Model (QPM). In particular, we will first discuss briefly about the setup of initial conditions for HICs and QGP evolution tuned to reproduce final multiplicity distributions and collective flow. Then, we will focus on the initialization of Heavy Quarks (HQs) both in pp and in AA collisions by looking at the Heavy-Flavor (HF) mesons and baryons spectra in comparison with experimental measurements. In the main section of the chapter we will collect our results for charmed meson nuclear modificiation factor $R_{AA}(p_T)$ and elliptic flow $v_2(p_T)$ for RHIC and LHC simulations within the dynamical Boltzmann evolution with QPM interaction described in detail in Chapter 3 and 4. We will analyze the obtained suppression and elliptic flow of D mesons by means of our hybrid fragmentation plus coalescence hadronization model introduced in Chapter 2 and in the wake of the following works [75] [196]. Meanwhile, we will provide our first predictions of B meson production in HICs and present interesting results of bottom observables compared to experimental measurements (if available). Starting from the cited papers, our final study will be concentrated on two specific topics. In the first one we will address some questions regarding the description of D suppression along with the evidence of an enhanced production of

Λ_c baryons both at RHIC and LHC energies and we will concentrate on the formulation of a new method for constructing the R_{AA} of D mesons at small p_T through a constrain on the hadronization of charm quarks, specifically to the ratio Λ_c/D^0 measured at RHIC and LHC. Through this procedure we can also infer on the suppression of Λ_c baryon itself and have a robust theoretical apparatus to study B and Λ_b production in HICs. In the second one we will focus on the investigation of charm and bottom thermalization in the QGP by estimating the HQ spatial diffusion coefficient $D_s(T)$ which can compare to lQCD expectations and other phenomenological models. In particular, we will emphasize on the fact the analysis of HQ transport coefficients at the bottom mass scale will lead to benefits that can be summarize in a reduction of the uncertainties coming from the adopted transport model (Langevin vs Boltzmann) and in a better agreement with lQCD quenched approximation.

5.1 Initial conditions for HICs

We performed simulations for RHIC *AuAu* collisions at center-of-mass energy $\sqrt{s} = 200\,AGeV$ and for LHC *PbPb* collisions at $\sqrt{s} = 2.76 - 5.02\,ATeV$ with the possibility to choose among different centrality classes by fixing of the initial impact parameter b and employing standard Glauber model to calculate $N_{coll}(b)$ and $N_{part}(b)$. However, our transport code is already settable for starting with initial conditions from MC Glauber model which includes event-by-event fluctuations [197]. In our calculations we start with total number of massive *bulk* partons $dN/dy_0 = 1400$ at RHIC and $dN/dy_0 = 2870 - 3480$ at LHC @$2.76 - 5.02\,ATeV$ fixed for the centrality range $0 - 5\%$ corresponding to $b \simeq 2.5\,fm$. Then, assuming longitudinal boost invariance we distribute with uniform pseudo-rapidity $\eta = y = 1/2\ln((t+z)/(t-z))$ within a range of $\eta \in [-2.5, 2.5]$ for RHIC and $\eta \in [-3.5, 3.5]$ for LHC binned with $\Delta\eta = 0.1$. At more peripheral centralities, i.e. $b > 2.5\,fm$, the number of partons is scaled according to a two component model [198]

$$\frac{dN}{dy}(b) = \alpha \left[(1-x)\,\frac{N_{part}(b)}{2} + xN_{coll}(b) \right] \tag{5.1}$$

where $\alpha = (dN/dy_0)/[0.5 \cdot (1-x) \cdot N_{part}(b) + x \cdot N_{part}(b)]$ is the normalization factor in such a way that at $b = 2.5\,fm$ we get back to the values $dN/dy_0 = 1400$ at RHIC and $dN/dy_0 = 2870 - 3480$ at LHC. For $N_{part}(b)$ and $N_{coll}(b)$ we employ parametrized expressions as function of b which reproduce the expectations from standard Glauber model (see Eq. (2.11), Eq. (2.12) and the average lines in Fig. (2.8)). The parameter x is chosen according to some constraints of the initial spatial eccentricity of the *fireball*. In particular, we set $x = 0.15$ for RHIC and $x = 1.0$ at LHC, meaning that for the former case the *bulk* is distributed mostly in accordance to N_{part}, while for the latter case it follows essentially the N_{coll} distribution. The change of initial eccentricity through the variation of the x parameter has quite strong impact on the final elliptic flow of the light partons, however we have not analyzed such behavior in detail since we are mostly interested in the HQ observables which need a reasonable but not so precise description of the *bulk* observables.

5.1.1 Transverse distributions for soft and hard partons

The number of initial partons obtained from Eq. (5.1) is distributed between gluons and light quarks (antiquarks) according to equilibrium condition, i.e. through the ratio of internal degrees of freedom ν_g/ν_q with $\nu_g = 16$ and $\nu_q = 6N_f$ with number of quark flavors $N_f = 3$. Then, partons of the various species are divided into a *soft* and a *hard* component by randomly sampling their initial transverse momentum p_T and comparing it with a parameter cut which is fixed in order to ensure the continuity of the partonic p_T spectra. In particular, we fix $p_0 = 2.0\,GeV$ at RHIC and $p_0 = 3.5\,GeV$ in agreement with some pQCD approaches [199] [200]. Soft partons of the *bulk* have $p_T \leq p_0$ and are distributed in the transverse plane according to the participant distribution at given impact parameter b

$$\begin{aligned}\frac{dN_{part}(b)}{ds} &= T_A(s,b)\left[1-\exp\left(-\sigma_{NN}^{in}T_B(s,b)\right)\right]\\ &- T_A(s,b)\left[1-\exp\left(-\sigma_{NN}^{in}T_A(s,b)\right)\right]\end{aligned} \quad (5.2)$$

where σ_{NN}^{in} is the inelastic nucleon-nucleon cross section which we choose to be equivalent to the inelastic contribution of proton-proton collisions with values of $40\,mb$ at RHIC and $70\,mb$ at LHC energy. For Eq. (5.2) we calculate also the nuclear thickness functions

$$T_A(s,b) = \int dz\,\rho_A\left(s-\frac{b}{2},z\right) \quad , \quad T_B(s,b) = \int dz\,\rho_B\left(s+\frac{b}{2},z\right) \quad (5.3)$$

employing the Wood-Saxon expression of nuclear density profile given in Eq. (2.1) (see Fig. (2.4)) with parameter values taken from Ref. [32]. Instead the distribution of hard partons in the transverse plane is obtained from binary nucleon-nucleon collisions in the Glauber model at the same impact parameter b

$$\frac{dN_{coll}(b)}{ds} = T_A(s,b)\,T_B(s,b)\,\sigma_{NN}^{in} \quad (5.4)$$

5.1.2 p_T spectra for soft and minijet partons

Soft and hard partons of the *bulk* differ also for the initial distribution in transverse momentum p_T, the former consisting of a plasma of quarks and gluons at local thermal equilibrium, the latter being equivalent to the products of initial binary pQCD collisions, named as *minijets*. Soft partons are so distributed according to the exponential formula

$$\frac{dN_j}{d^2p_T} = \frac{\nu_j m_T}{(2\pi)^3}\exp\left(-\frac{m_T}{T}\right) \quad (5.5)$$

where ν_j is the color-spin degenerancy factor for $j = g, q, \bar{q}$ and the transverse mass $m_T = \sqrt{m^2 + p_T^2}$ is calculated using constant quasi-particle mass both for light quarks and gluons fixed at the value $m = 0.5\,GeV$ [201], since already at this stage we are able to reproduce with quite good approximation the EoS of lQCD [154]. In Eq. (5.5) T refers to the initial temperature of the local cell (r_T, η) in coordinate space where soft partons are localized. Knowing the density of soft partons inside each cell we can calculate $T(r_T, \eta)$ by making use of the following expression

$$T(r_T, \eta) = T_0 \left(\frac{\rho(r_T, \eta)}{\rho(r_T, \eta)} \right)^{1/3} \tag{5.6}$$

Then, the temperature profile is scaled with respect to the value in the central cell which is fixed to the value $T_0 = 0.365\, GeV$ and $T_0 = 0.55\, GeV$ respectively at RHIC and LHC as is usually done in hydrodynamical simulations [54, 202, 203, 204]. From the condition $T_0 \tau_0 \sim 1$ we also fix the starting time of the QGP phase. In particular, with $\tau_0 = 0.6\, fm$ at RHIC and $\tau_0 = 0.3\, fm$ at LHC we try to follow the recent estimates based on models of initial stages of HICs implemented both in hydrodynamics and in transport frameworks. Corrections to Eq. (5.6) arise from the fact that soft partons are massive particles, hence temperature should be derived from proper inversion of density formula with Bessel functions included. In order to do that we start by calculating $T(r_T, \eta)$ from the massless relation Eq. (5.6) and perform Newton-Rhapson algorithm until we match with the massive behavior.

Transverse momentum distributions of *minijets* at mid-rapidity can be derived from pQCD calculations within the factorization theorem, meaning that these partonic p_T spectra should be multiplied with tabled PDFs and the result convoluted with proper FFs for fragmentation of light partons to get semi-inclusive hadron spectra at mid-rapidity in agreement with the measured ones in pp collisions (see Eq. (2.59)).

In our calculations we employ the following power-law expression for parton species $j = g,\ q,\ \bar{q}$

$$\frac{dN_j}{d^2 p_T} = \left(\frac{A}{1 + \frac{p_T}{B}} \right)^n \tag{5.7}$$

with parameter values $A = 4.0157(g) - 2.6724(q)$, $B = 1$, $n = 8.4$ at RHIC as used in Ref. [66] and $A = 2.43059$, $B = 4.07368$, $n = 6.72689$ at LHC from ALICE report [205]. The total number of minijets for quarks and gluons is given by the integral of Eq. (5.7) properly scaled by $N_{coll}(b)$ for the fixed impact parameter b. We checked that actually this parametrization of minijets are in agreement with recent pQCD updates used for example in Ref. [200] and that convoluted with NLO Kniehl-Kramer-Potter (KKP) FFs [63] lead to an acceptable description of measured charged particle spectra at LHC as shown in Fig. (5.1).

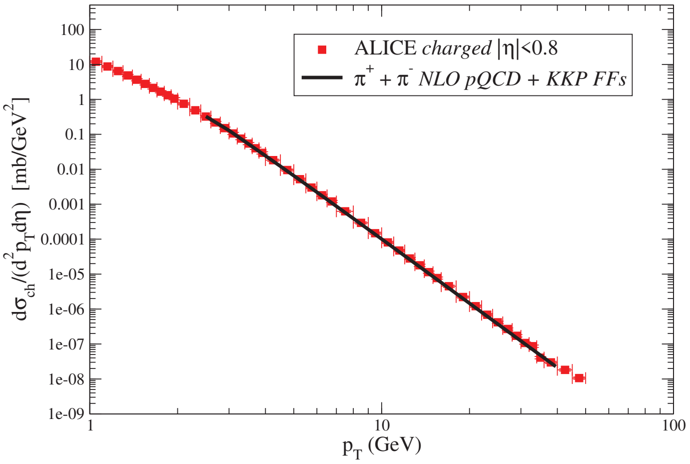

Figure 5.1: Charged pion p_T spectrum at high p_T obtained from initial minijet distribution Eq. (5.7) with parameter values of LHC and convoluted to FFs parametrized with NLO KKP [63] compared to charged particle p_T spectra measured by ALICE at pp collisions and center-of-mass energy $\sqrt{s} = 7\,TeV$. Minijet distribution is properly scaled in order to match with the experimental total cross section of production of charged particles which at so high p_T are mostly dominated by pions.

5.2 QGP evolution and *bulk* observables

The dynamical evolution of the fireball is described by means of the Relativistic Boltzmann Equation (RBE) Eq. (3.42) that we write again here

$$\left(p_\mu \partial_x^\mu + m^*(x)\partial_x^\mu m^*(x)\partial_{p,\mu}\right) f_{g,q,\bar{q}}(x,p) = C[f_g, f_q, f_{\bar{q}}](x,p) \qquad (5.8)$$

Since we consider a massive bulk of light quarks and gluons with constant $m^*(x) = m = 0.5\,GeV$ the mean field term on the left hand side of the RBE is actually zero and also the gap equation for the bag pressure $B(x)$ Eq. (3.43) is automatically solved. The collision integral $C[f_g, f_q, f_{\bar{q}}]$ encoding the interaction between the *bulk* partons is tuned to a fixed value of $\eta/s(T)$ that is realized by computing the local cross section according to the Chapmann-Enskog (CE) formula Eq. (3.48) as discussed in detail in Chapter 3 and referring to [161] [48]. In this way we gauge the whole dissipative effect to the desired $\eta/s(T)$ and simulate the evolution of the fluid in analogy to what is performed in hydodynamics [54, 202, 203, 204]. For the partonic phase we choose the constant value $\eta/s = 1/4\pi$ and model the increasing of η/s at the freezout transiton towards the hadronic phase by means of a Maxwell construction. We solve numerically Eq. (5.8) by sampling $N_{test} = 300$ test-particles for each real parton as described in Sec. (3.5) and map the collision integral $C[f_g, f_q, f_{\bar{q}}]$ by means of the improved stochastic method (see Chapter 3). Time evolution of the QGP is followed till a proper of $\tau_{max} \sim 9\,fm$ at RHIC and $\tau_{max} \sim 14\,fm$ at LHC which is much larger than the QGP lifetime, but in this way we ensure that elliptic flow v_2 of the *bulk* system is saturated and freezout condition is established in the whole fireball. To conclude this section we present our results for two main *bulk* observables, mainly the final (pesudo-)rapidity distribution $dN_{ch}/dy(\eta)$ for specific centrality classes (where *ch* indicates the contribution from only charged particles) and the elliptic flow $v_2(p_T)$ of light quarks and gluons averaged with respect to their initial number. In Fig. (5.2) we present the results for the *bulk* at RHIC *AuAu* collisions at $\sqrt{s_{NN}} = 200\,GeV$, showing on the left the final $dN_{ch}/d\eta$ obtained in simulations with increasing impact parameter b, while on the right the $v_2(p_T)$ at specific $b = 7.5\,fm$. In the same manner in Fig. (5.3) we show results for LHC *PbPb* collisions at $\sqrt{s_{NN}} = 5.02\,TeV$ with the final $dN_{ch}/d\eta$ for various centrality classes and $v_2(p_T)$ at impact parameter corresponding to semi-peripheral collisions. All these partonic results are compared with the relative experimental data which are of course at hadronic level. In order to make this comparison reasonable we are implicitly assuming quark-hadron duality and even though we should consider the contribution coming from the hadronization in the light sector. In particular, we should take care of the fact that an enhancement of about a factor 20% on the final particle multiplicity comes when going from partons to hadrons as well as the $v_2(p_T)$ increases at low p_T due to coalescence [68]. However, for the aim of this work we are more interested in HQ observables providing a rough description of QGP evolution which in the meantime is in agreement with hydrodynamics for what concerns for example the dissipative effects (η/s) and also the entropy density.

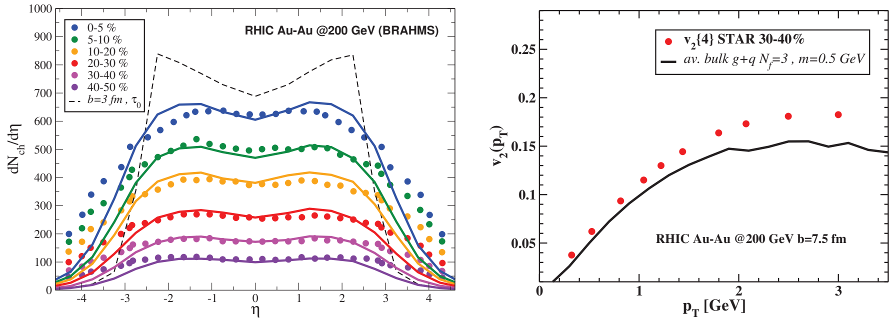

(a) **(b)**

Figure 5.2: **(a)** Final time pseudo-rapidity distributions of *bulk* partons obtained at RHIC simulations and compared to experimental data for $dN_{ch}/d\eta$ at various centralities from BRAHMS [131]. Initial time $\tau_0 = 0.6\,fm$ pseudo-rapidity distribution at most central collisions ($b = 3\,fm$) is indicated with dashed black line. **(b)** Elliptic flow $v_2(p_T)$ for averaged massive bulk $m = 0.5\,GeV$ of gluons and quarks with $N_f = 3$ obtained at RHIC minimum bias $b = 7.5\,fm$ collisions compared to charged $v_2\{4\}$ measured at STAR [133]. Uncertainty bars correlated to the experimental data are too small to be visible in the plots.

5.3 Initial conditions for HQs in pp and in AA collisions

At given impact parameter b of the simulation charm and bottom quarks are initially distributed in transverse coordinate space according to the binary nucleon-nucleon collisions Eq. (5.4) from Glauber model, while in the mo-

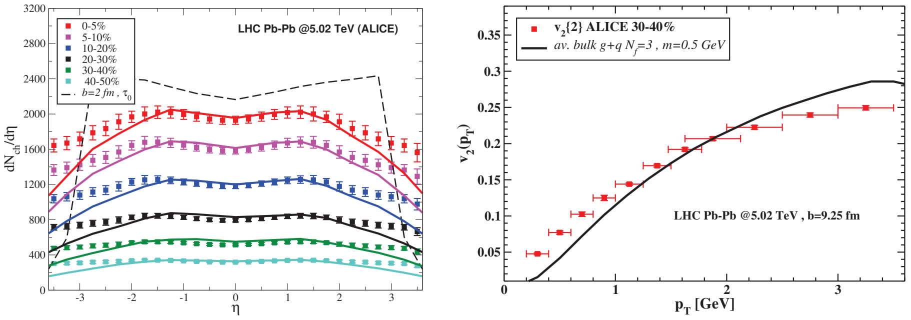

(a) **(b)**

Figure 5.3: **(a)** Final time pseudo-rapidity distributions of *bulk* partons obtained at at LHC *PbPb* @5.02 TeV collisions and compared to $dN_{ch}/d\eta$ experimental data from Ref. [206]. Initial time $\tau_0 = 0.3\,fm$ pseudo-rapidity distribution at most central collisions ($b = 2\,fm$) is indicated with dashed black line. **(b)** Elliptic flow $v_2(p_T)$ for mixed bulk $m = 0.5\,GeV$ of gluons and quarks with $N_f = 3$ obtained at LHC simulations at $b = 9.25\,fm$ and compared to charged $v_2\{2\}$ from ALICE [207].

mentum space we employ the following power-law spectrum

$$\left(\frac{dN_{HQ}}{d^2\vec{p}_T}\right)_0 = \frac{x_0}{\left(1 + x_3 \cdot p_T^{x_1}\right)^{x_2}} \tag{5.9}$$

fitting the parameter to reproduce Fixed Order + Next-to-Leading Logarithm (FONLL) p_T distributions in pp collisions at mid-rapidity for RHIC [85] [86] and LHC [87] (highest) [208] energies. The value of these parameters are collected in the two tables below and in Fig. (5.4) we show the corresponding behavior of the fit with respect to the central value of FONLL predictions. In this case we normalize our distributions Eq. (5.9) to the FONLL cross section of $c\bar{c}$ and $b\bar{b}$ production in pp collisions at mid-rapidity and for the various energies. In particular, we have $\sigma_{c\bar{c}} = 256\,\mu b$ and $\sigma_{b\bar{b}} = 1.86\,\mu b$ at RHIC $\sqrt{s} = 200\,GeV$ from Ref. [85], while we have $\sigma_{c\bar{c}} \simeq 5\,mb$ and $\sigma_{b\bar{b}} \simeq 75\,\mu b$ at LHC $\sqrt{s} = 7\,TeV$ from Ref. [87]. A useful parametrization of $\sigma_{c\bar{c}}(\sqrt{s})$ cross section fitted to the experimental data for charm production in pp collisions can be found in Ref. [209].

Charm FONLL

$pp\ \sqrt{s}\,[GeV]$	x_0	x_1	x_2	x_3
200	0.011	1.524	6.119	0.162
2760	18.887	1.785	3.654	0.096
5500	20.284	1.951	3.137	0.075
7000	21.284	2.039	2.916	0.065

(a)

Bottom FONLL

$pp\ \sqrt{s}\,[GeV]$	x_0	x_1	x_2	x_3
200	0.018	1.875	4.772	0.030
2760	0.302	1.709	3.605	0.035
5500	0.468	1.838	3.076	0.030
7000	0.592	1.651	3.607	0.035

(b)

Table 5.1: Parameter values of p_T spectrum for bare charm (a) and bottom (b) obtained from power-law fit Eq. (5.9) of FONLL calculations for pp collisions at various center-of-mass energies $\sqrt{s}$.

D and B meson production in pp collisions

Measurements in pp reactions represents our baseline for analyze HQ production and suppression in AA collisions. We convolute charm and bottom p_T distribution given in Eq. (5.9) to Peterson [108] functions (see Eq. (2.83)) to obtain respectively the D and B mesons spectra

$$\frac{dN_h}{d^2p_T} = \int dz \left(\frac{dN}{d^2p_T} \right)_0 \frac{D_{HQ\to h}(z)}{z^2}\ , \ D_{HQ\to h}(z) = \left[z \left(1 - \frac{1}{z} - \frac{\epsilon_c}{1-z} \right)^2 \right]^{-1} \tag{5.10}$$

where as done also in Ref. [196] for charmed mesons we fix the parameter $\epsilon_c = 0.06$ in the fragmentation functions in the right Eq. (5.10) in comparison to the measured D^0 and D^* yield in pp collisions at RHIC energy measured by STAR [210] and to reproduce also the production of D^0, D^+, D^* or their average spectrum at LHC energy for the available experimental data [211]. The resulting D mesons spectra are shown in Fig. (5.5) and in Fig. (5.6) respectively for RHIC and LHC where our results are scaled with the proper fragmentation fractions $c \to D^0$, D^+, D^* taken from Ref. [212] (see also [213])

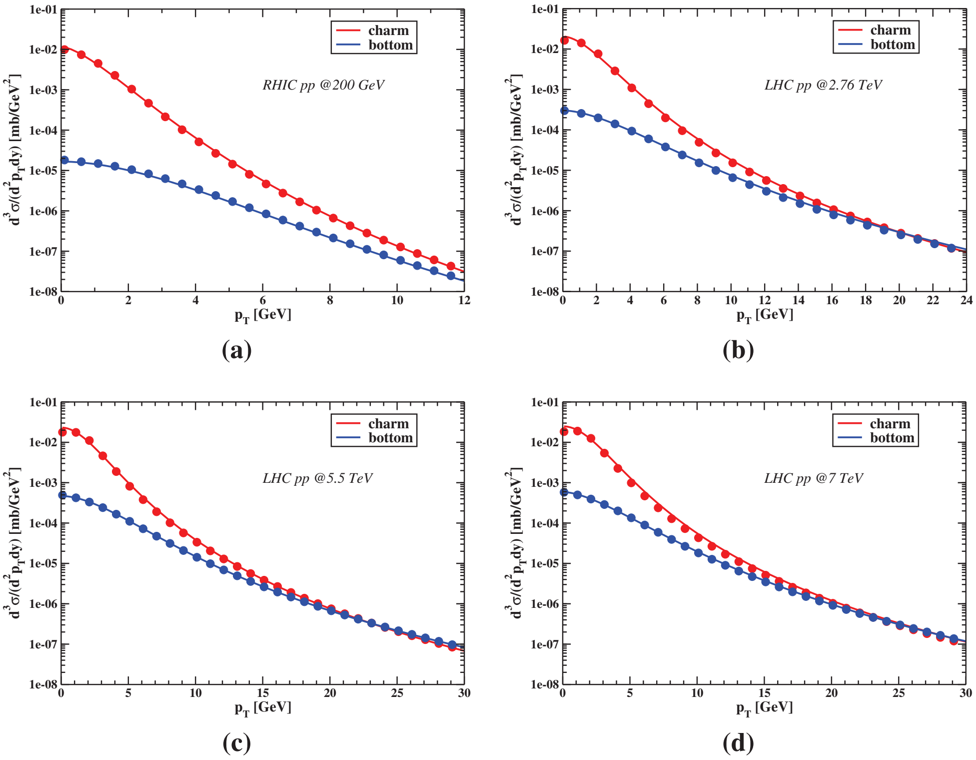

Figure 5.4: Transverse momentum distributions of charm (blue) and bottom (red) from the fit of FONLL calculations in *pp* collisions at RHIC energy $\sqrt{s} = 200\,GeV$ and LHC energies $\sqrt{s} = 2.76\,,\,5.5\,,\,7\,TeV$. Dots refer to FONLL central predictions at mid-rapidity $|y| < 0.5$, while solid lines correspond to power-law expression Eq. (5.9) for initializing HQs within the transport code.

in order to get the approximate conversion from the total $\sigma_{c\bar{c}}$ to the value of the cross section for the various hadronic channels and take into account also different rapidity intervals.

Since the bottom production cross section at RHIC energy is very small, the only way to constraint the p_T distributions should pass from a study of the single electrons from the decay of B and D mesons trying to unfold the contribution coming from the former to the one originated from the latter. That would require the implementation of the semi-leptonic decay process after the hadronization of HQs in *pp* collisions [215], while in HICs that should be followed by a hadronic re-scattering phase which it is currently not realized in our transport approach. However, for the purpose of this thesis

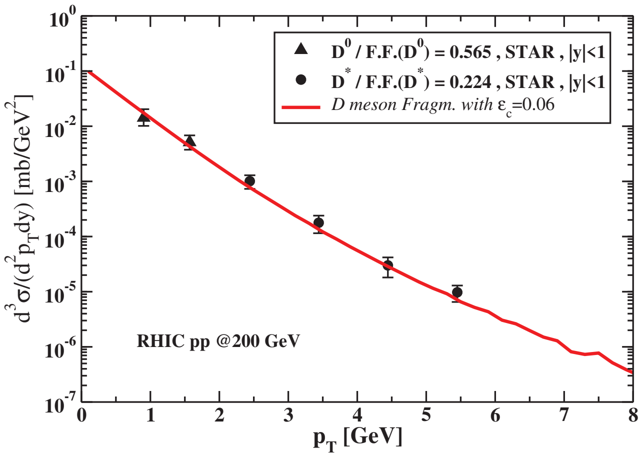

Figure 5.5: Transverse momentum distribution of D mesons obtained from the fragmentation of charm quarks in pp collisions at $\sqrt{s} = 200\,GeV$ and compared with the experimental data from STAR collaboration [210].

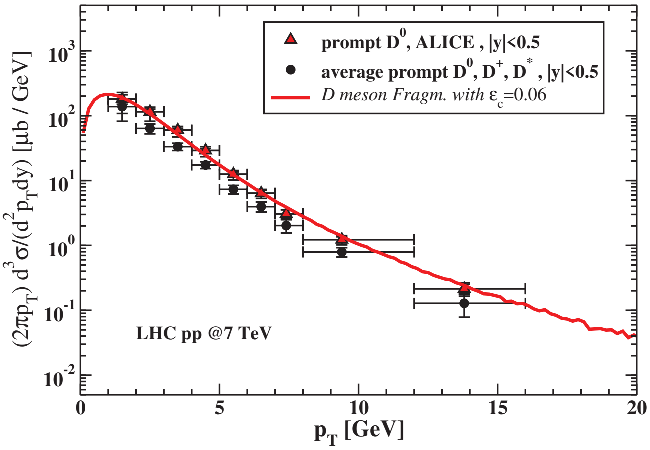

Figure 5.6: p_T distribution of D mesons at mid-rapidity obtained from the fragmentation of charm quarks in pp collisions at $\sqrt{s} = 7\,TeV$. This result is compared with experimental points for prompt D^0 (red filled circles) and average $D^0 + D^+ + D^*$ (red filled triangles) measured at ALICE [214].

we still work fine when we focus directly on the production of bottom at LHC energies. Indeed when convoluting the bottom FONLL spectrum to the Peterson function we fix the fragmentation parameter $\epsilon_c = 0.01$ to reproduce the p_T spectrum of B^0 and $B^{\pm}$ mesons measured in pp collisions at $\sqrt{s}$ =

$7\,TeV$ by CMS collaboration [216]. In Fig. (5.7) we show the obtained result in comparison with the experimental data. We notice that with respect to the case of D mesons by normalizing our spectrum to the total FONLL cross section we underestimate the measured yield.

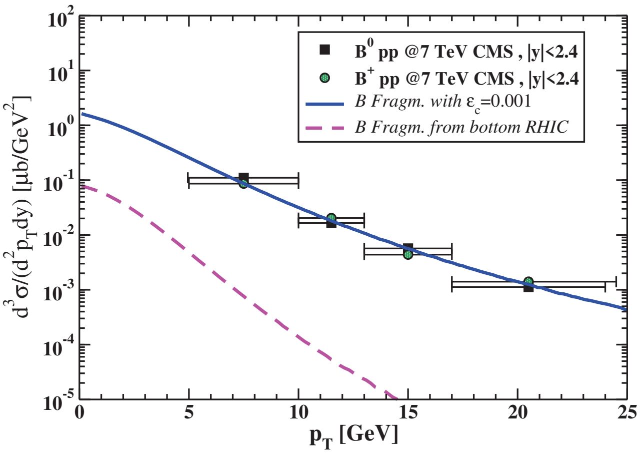

Figure 5.7: p_T distribution of B mesons obtained from the fragmentation of bottom quarks in pp collisions at $\sqrt{s} = 7\,TeV$ (red line) and compared with experimental data from CMS collaboration [216]. The dashed orange curve is the expected p_T spectrum of B mesons at RHIC energy.

Λ_c yield in pp collisions

The production of prompt Λ_c^+ baryon has been recently measured at LHC in pp collisions at $\sqrt{s} = 7\,TeV$ [217] and in $PbPb$ collisions at $\sqrt{s_{NN}} = 5.02\,TeV$ [218] with corresponding ratios

$$\left(\frac{\Lambda_c^+}{D^0}\right)_{pp} \simeq 0.6 \quad , \quad \left(\frac{\Lambda_c^+}{D^0}\right)_{PbPb} \simeq 1 \tag{5.11}$$

The former is almost constant in the analyzed range of p_T and has a value which is much higher than previous measurements carried out in $e^- + e^+$ and ep collisions. This issue has not been addressed yet, even if some explanations can be drawn within the general idea about the possible existence of a QGP phase in small system as indicated for example by the large collective flow which is studied within hydrodynamics [219] [220]. Then, if a medium is formed also in high multiplicity pp events, a coalescence mechanism for charm quarks like the one we use in HICs can be applied to address the observed enhancement of the ratio at low p_T which cannot be described within a only fragmentation scenario [71]. For the latter, instead, a solution relative to its order of magnitude $(\Lambda_c/D^0) \sim 1$, actually observed both at RHIC and LHC energies, as well as its p_T dependence can be found with quite certainty by looking at the strong impact of coalescence. Basing on the hybrid hadronization approach for HQs which we described in Chapter 2 and referring especially to our paper [75], we will present some quantitative estimates for D and Λ_c suppression factor in HICs later in this Chapter. In this paragraph we make use of the available Λ_c data to tune once more the fragmentation function Eq. (5.10) of charm quarks in pp collisions in order to fix our baseline for the later study of Λ_c suppression. In Fig. (5.8) we show that with a value of $\epsilon_c = 0.12$ we are able to fit the shape of the p_T distribution measured by ALICE [217] and also we find an agreement with the statement done in Ref. [221], meaning that fragmentation function becomes softer going from meson to baryon, because more energy is needed to pop-up two quarks from the vacuum. That results into a value of the parameter ϵ_c for Λ_c which is roughly two times larger than the one for D mesons.

5.4 Suppression and Elliptic flow of HQs

After initializing the HQs with the proper p_T distributions we follow their propagation and let them interact inside the expanding medium by sampling stochastically their collisions with the QPM partons as described at beginning of Chapter 4 and at each small time step Δt we update their coordinate and momentum values. Finally, when freezout condition for energy and particle density is established, we collect the final spectra and anysotropic distributions of both HQs and *bulk* partons and couple them within our hybrid hadronization framework for HQs described in Chapter 2 to construct in the end the $R_{AA}(p_T)$ and the $v_2(p_T)$ of the corresponding Heavy-Flavor (HF) hadrons. In the following paragraphs we present our results for these two observables and compare them with the experimental data at RHIC and LHC.

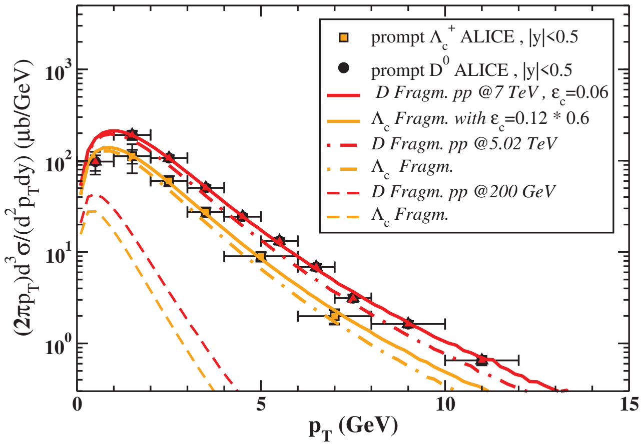

Figure 5.8: p_T distribution of Λ_c baryon (orange lines) in pp collisions at $\sqrt{s} = 200\,GeV$ (dash-dotted), $\sqrt{s} = 5.02\,TeV$ (dashed) and $\sqrt{s} = 7\,TeV$ (solid) obtained from the fragmentation of charm quarks and compared with previous results form p_T spectrum of D meson (black lines) as well as with the experimental data from ALICE collaboration [217] for the highest energy case (orange squares). We choose normalization factor to match with the measured ratio $(\Lambda_c/D^0)_{pp} \simeq 0.6$.

5.4.1 Results at RHIC

The nuclear modification factor of D mesons at RHIC $AuAu@200\,AGeV$ most central collisions corresponding to an impact parameter $b = 3.25\,fm$ are represented in Fig. (5.9) and compared to the updated experimental data of D^0 production from STAR [124].

The dashed orange line is the R_{AA} obtained by considering only fragmentation into D mesons of all charm quarks evolved within the Boltzmann approach. Instead the solid line is the result for the scenario of fragmentation plus coalescence hadronization mechanism. In this case the R_{AA} is constructed by imposing the total number of charm quarks N_{AA}^{charm} plugged into the hadronization code, that we calculate by integrating their p_T distribution, to be equivalent to the expected number of D mesons produced by charm fragmentation in pp collisions, namely N_{pp}^{D}, scaled by the proper $N_{coll}(b)$ factor.

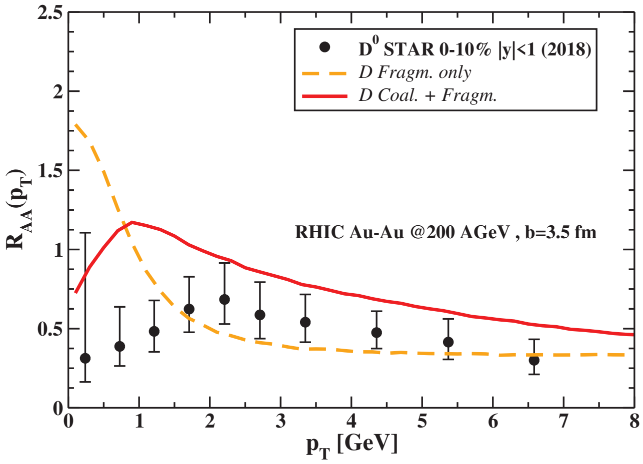

Figure 5.9: Nuclear modification factor R_{AA} of D mesons in RHIC $AuAu$ collisions at $\sqrt{s_{NN}} = 200\,GeV$ and centrality $0-10\%$ compared to STAR old data [123] and new data from update analysis [124].

Hence, we can formally write the R_{AA} definition as

$$R_{AA}^{D^0}(p_T) = \frac{\left(dN/d^2p_T\right)^{D^0}_{AA\;coal+fragm}}{\frac{N_{AA}^{charm}}{N_{pp}^{D}}\left(dN/d^2p_T\right)^{D^0}_{pp\;fragm}} \tag{5.12}$$

where the following relations are considered

$$N_{AA}^{charm} = \int d^2p_T\left(\frac{dN}{d^2p_T}\right)^{charm}_{AA},\; N_{pp}^{D} = \int d^2p_T\left(\frac{dN}{d^2p_T}\right)^{charm}_{pp} \otimes D_{c\to D} \tag{5.13}$$

where $D_{c\to D}$ corresponds to the parmetrized Peterson expression [108] (see Eq. (2.83)) with tuned parameter $\epsilon_c = 0.06$ [196] [75] and the p_T spectrum at denominator of Eq. (5.12) includes also the proper fragmentation fraction FF into D^0 among all the other possible D states. In particular, we use $FF(D^0) = 0.6$ taken from the combined analysis in Ref [212]. Through the results at RHIC in this paragraph as well as thos for LHC in the next one we will use the definition of R_{AA} as stated in Eq. (5.12). In agreement with the results of Ref. [196] the effect of coalescence implies an increasing of the R_{AA} at $p_T > 1\,GeV$, hence a decreasing of the suppression because D mesons formed from recombination get the charm momentum gained with the light quark one, whereas D mesons coming from fragmentation have always smaller momentum with respect to the original charm quark. This explains also the decreasing of R_{AA} at $p_T < 1\,GeV$ as a consequence of the depletion of the final spectrum of D mesons at low p_T where coalescence is the dominant mechanism and also the fact that such spectrum does not scale linearly with the final p_T distribution of charms. We obtain similar result also for the R_{AA} at RHIC peripheral collisions $b = 7.5\,fm$ where after we achieve a good description of D meson suppression we can look also at the produced elliptic flow $v_2(p_T)$ both for charm and D mesons. The results for the two observables are depicted respectively in Fig. (5.10) and in Fig. (5.11) along with the experimental measurements from STAR available at same centrality.

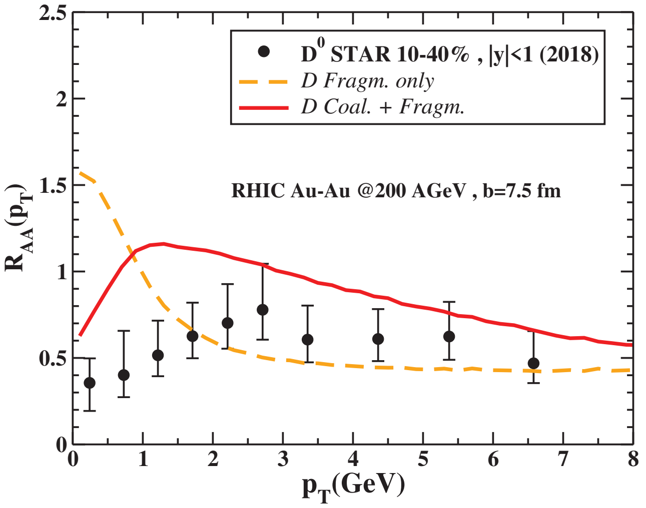

Figure 5.10: Nuclear modification factor R_{AA} of D mesons in RHIC $AuAu$ collisions at $\sqrt{s_{NN}} = 200\,GeV$ and centrality $10-40\%$ compared to STAR old data [123] and new data from update analysis [124].

We observe in Fig. (5.11) that the v_2 of D obtained within a only fragmentation scenario (dashed orange line) is equal to that of charm quarks (dotted black line), except for a little shift at low p_T arising from the fact that the anysotropy in the distribution of D mesons at given p_T comes directly from the anysotropy in the distribution of bare charms at slight larger transverse momentum. Instead an enhancement of the produced v_2 of D mesons is provided by coalescence, since charm quarks by recombination with the

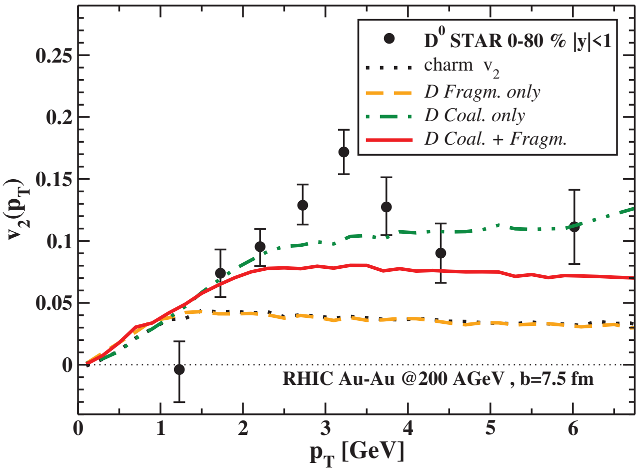

Figure 5.11: Elliptic flow v_2 of D mesons obtained within various hadronization mechanisms and compared to the measured v_2 of D^0 at minimum bias from STAR [137].

light partons acquire also their collective flow. As we can see in Fig. (5.11) when charm anysotropies from Boltzmann evolution are coupled to the fragmentation plus coalescence mechanism, the resulting v_2 (solid red line) is about 20% larger than the charm v_2 at freezout, the latter being substantially equivalent to the v_2 from fragmentation. Similarly to what has been done in Ref. [196] the impact of coalescence on the formation of elliptic flow can be estimated by considering also a scenario where D mesons are produced only via recombination, meaning that in our hadronization model we switch off the fragmentation probability. We observe that the developed v_2 for D mesons (dash double-dotted green curve) can increase by a factor 2 with respect to the v_2 from fragmentation, since in this case all charm quarks couple with the anysotropies of the *bulk* partons and thus gain much more in collective flow.

Within our Boltzmann QPM transport approach coupled to the hybrid hadronization model we are able to perform simulations for studying the dynamical evolution of bottom quarks and the consequent suppression and elliptic flow of B mesons. In Fig. (5.12) we show also our predictions for the B meson R_{AA} at RHIC central collisions with $b = 3.25\, fm$. Our results for the R_{AA} are derived with analogous expression of Eq. (5.12), but in this case we do not account for the various possible final states, rather we assume that all bottom quarks evolve in a single B species. We observe that with a final p_T spectrum of B mesons originated by only fragmentation (dashed teal line) we already describes quite well the estimated shape of the suppression factor which by the effect of a larger mass has a smooth decreasing at low p_T with respect to the charm behavior (see Fig. (5.9)). On the other hand the R_{AA} of$B$ tends asymptotically to the value for D mesons at high p_T where the dependence on the HQ mass in the collisional energy loss kernel becomes negligible. In the same we show also the R_{AA} of B mesons resulting from both fragmentation plus recombination mechanism. We notice that at the level of suppression the effect of coalescence is much less significant compared to what we have seen for the charm case. An explanation on this fact can be related to the different stiffness of the final p_T distribution. Bottom quarks are expected to finish their dynamical evolution in the QGP with a harder spectrum compared to charms and since $\epsilon_c(b) < \epsilon_c(c)$ fragmentation tends to preserve this hierarchy. Coalescence instead will lead to a gain in momentum which in percentage is smaller when the starting HQ spectrum is harder, like the one of bottom.

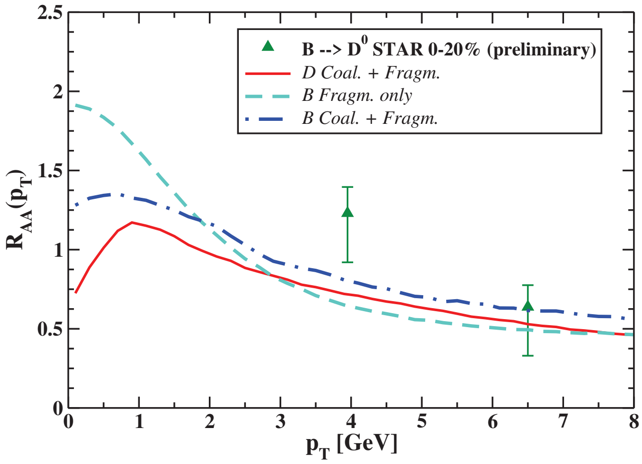

Figure 5.12: Predictions for B meson R_{AA} at RHIC most central collisions compared to previous results for D meson R_{AA}. Green triangles refer to preliminary measurements from non-prompt D^0 suppression at STAR with points taken from Fig. 36 in Ref. [77].

5.4.2 Results at LHC

Within the same Boltzmann QPM framework we carried simulations for LHC $PbPb$ collisions at $\sqrt{s} = 2.76\,ATeV$ and also $\sqrt{s} = 5.02\,ATeV$. In most central reactions at such high energies we have to take into account for CNMEs which we include in terms of shadowing function $S(p_T)$ multiplying the initial pp distributions of charm and bottom quarks

$$\left(\frac{dN_{HQ}}{d^2\vec{p}_T}\right)_0^{shadowing} = \left(\frac{dN_{HQ}}{d^2\vec{p}_T}\right)_0 * S(p_T) \tag{5.14}$$

while for more peripheral collisions $b \geq 5\,fm$ we brutally switch off this effect by imposing $S(p_T) = 1$. The behavior of $S(p_T)$ at $b < 5\,fm$ is extracted from a fit to EPS09 package [90]. Theoretical and experimental groups which adopt the EPS09 parametrization to include initial conditions usually assume in addition some functional dependence of the (anti)shadowing effect both on the impact parameter b and also on the transverse position r_T at which the HQ pair is produced such that it is strong in central collisions and in the central region of the fireball, while decreasing in peripheral collisions and on the fireball surface. This results essentially in a smooth variation of the initial HQ p_T spectrum which at small b and r_T it is affected by the maximum (anti)shadowing (enhancement)depletion like in Eq. (5.14), while at larger values of these parameters it reduces to the p_T distribution in pp collisions (5.9). We have not included such effect in this work yet, but in future we plan to do by coupling the EPS09 package to some b and r_T functional expression which is self-consistently derived from the initial Glauber profile, rather than being implemented as external source.

In this section we present our results for HF R_{AA} and v_2 obtained performing simulations within our Boltzmann approach set up for LHC $PbPb$ collisions at the center-of-mass energy of $\sqrt{s} = 5.02\,ATeV$. In Fig. (5.13) the suppression of D mesons at impact parameter $b = 3.25\,fm$ is compared to experimental measurements and related uncertainties from ALICE [125] and CMS collaborations [126] that in the plot are indicated respectively with black squares ad red circles. We carried out calculations without CNMEs and preliminary ones including the same parametrization of the shadowing function $S(p_T)$ we used at lower energy *PbPb* collisions at LHC. The former are depicted with dashed font, while the latter are represented with solid lines. Black lines correspond to the case where D mesons are produced only by fragmentation, while colored lines are the results where full hadronization by coalescence plus fragmentation is included.

By switching to a coalescence plus fragmentation hadronization, the effect of recombination on the D suppression is less significant at LHC compared to the previous RHIC result. This is due to the fact that the impact of coalescence strongly depends on the slope of the final charm p_T distribution which is given as an input to the hadronization [196] [75]. Indeed HQs which, after being quenched by medium interaction end up still with a harder distribution, do not gain so much in percentage from the momentum of *bulk* partons as if they have started with a softer one. This reflects into a smaller increase of the slope of the LHC spectrum of D mesons from recombination with respect to the RHIC one which comes a faster decreasing of the charm p_T distribution.

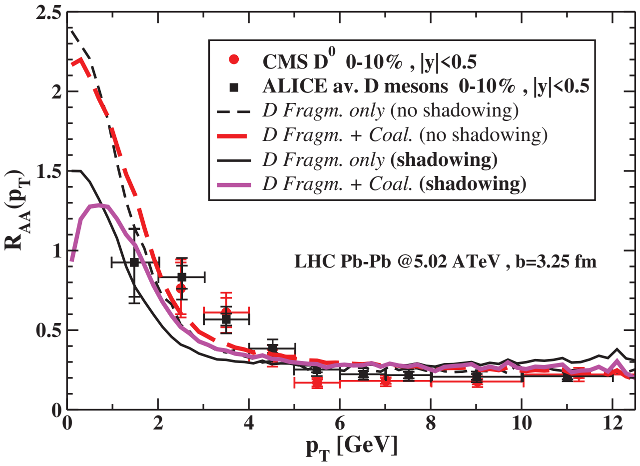

Figure 5.13: D meson R_{AA} in LHC *PbPb* collisions at $\sqrt{s_{NN}} = 5.02\,TeV$ for centrality $0-10\%$ compared to experimental meassiurements for averaged $D^0 + D^+ + D^*$ from ALICE [125] and prompt D^0 suppression from CMS [126].

The suppression of D mesons at higher centrality range ($b = 9.25\,fm$) is depicted in Fig. (5.14) along with the resulting elliptic flow obtained within our Boltzmann framework coupled with the hybrid fragmentation plus coalescence model [75]. In this calculation we have not included (anti)shadowing.

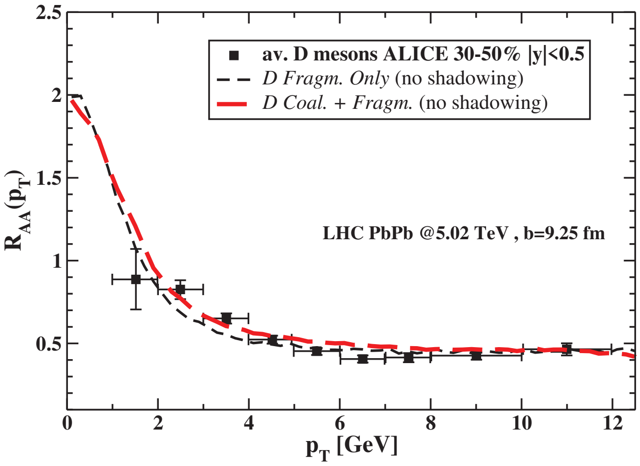

Figure 5.14: $R_{AA}(p_T)$ of D mesons at LHC $PbPb$ $\sqrt{s_{NN}} = 5.02\,TeV$ peripheral collisions ($b = 9.25\,fm$) compared to ALICE experimental data [125].

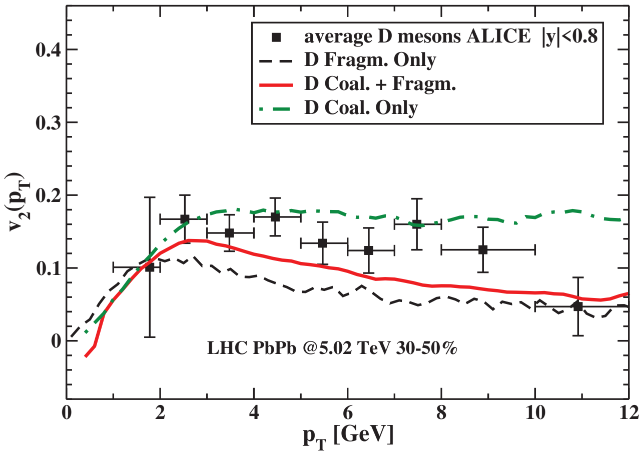

Figure 5.15: $v_2(p_T)$ of D mesons at LHC collisions for centrality 30−50% compared to ALICE measurements [138].

Since we are able to describe quite well the R_{AA} of D mesons measured at ALICE [125], we can move to a comparison at level of produced elliptic flow $v_2(p_T)$. Our results are shown in Fig. (5.15) along with the experimental data [138]. We notice that charm quarks appear to build up large collective flow also at LHC energies, as we can infer by looking at the v_2 of D mesons produced by fragmentation (dashed black line) which is equivalent to the v_2 of original charms (dotted black line), expect for the slight shift at small p_T. Again adding coalescence within the hadronization mechanism enhances the final elliptic flow of D (solid red line) of a factor about 20% compared to the v_2 from fragmentation. Hence, despite the small effect on suppression, coalescence is still effective when coupling the anysotropies of the *bulk* to the HQ distributions. As a proof we show in Fig. (5.15) the elliptic flow of D mesons produced within hadronization by only recombination (dash-double dotted green line) that is about a factor 1.8 larger than the v_2 from fragmentation.

Finally, we collect also our preliminary predictions for bottom suppression and elliptic flow at LHC energy. In particular, the R_{AA} of B mesons for $PbPb$ collisions at $\sqrt{s_{NN}} = 5.02\, ATeV$ and impact parameter $b = 9.25\, fm$ is presented in Fig.(5.16) along with the suppression of D mesons taken from Fig. (5.13). Our results indicate that within the explored p_T range a mass hierarchy effect within the amount of dissipated energy $\Delta E_c > \Delta E_b$ is visible through the R_{AA} of B mesons that results higher than the R_{AA} of D mesons. Moreover, at high p_T the former tends to become equivalent to the latter, indicating that at $p_T \geq 10\, eV$ this mass dependent effect should vanish. We could compare this results to available experimental data from CMS collaboration, where the production of HQs at bottom level is being under investigation through the analysis of non prompt J/ψ [222] and non prompt D^0, but also by means of measurement of $B^{\pm}$ suppression [223]. However, data points are located in a high p_T region where it is supposed that energy loss by medium-induced radiation is the dominant effect, so a direct comparison among the quantities is not feasible. The dashed teal line refers to the R_{AA} of B meson produced within only hadronization by fragmentation, where the parameter $\epsilon_b = 0.01$ is tuned to the B spectrum in pp collisions (see Fig. (5.7)). Instead the full hadronization by fragmentation and recombination is depicted with dash-dotted blue line. We observe the same small impact of coalescence on the R_{AA} formation, except at values of $p_T \leq 2\, GeV$, for the reason discussed before. For what concerns the elliptic flow, we show our predictions in Fig. (5.17) from which we infer that the bottom quarks couple with *bulk* anysotropies with a mass effect that seems to vanish at $p_T \geq 5\,GeV$ where we obtain $v_2(B) \approx v_2(D)$ for the fragmentation case, as we can see comparing the dashed curves, black for D mesons and teal for B mesons. The scenario should be maintained within a fragmentation plus coalescence scenario, because the former hadronization mechanism overcomes the latter at such high energies.

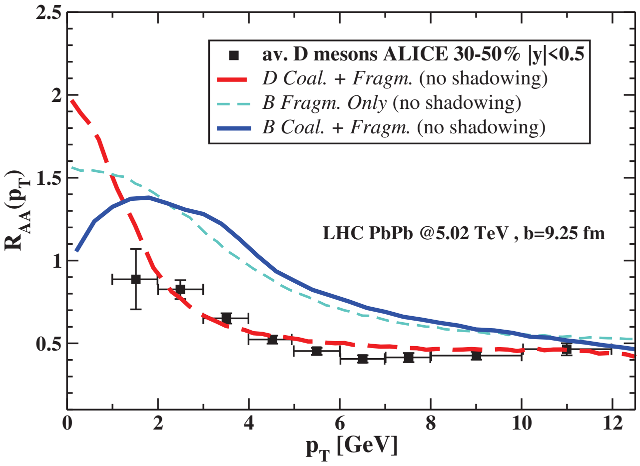

Figure 5.16: B meson $R_{AA}(p_T)$ in LHC collisions at $\sqrt{s_{NN}} = 5.02\,GeV$ for centrality $30-50\%$ compared to D meson R_{AA} taken from Fig. (5.13).

5.4.3 Effect of Λ_c production in the nuclear modification factor

In our recent work [75] we used our hybrid fragmentation plus coalescence hadronization model for HQs described in Chapter 2 to calculate the charmed baryon-to-meson ratio both at RHIC and LHC energies. In this case the coalescence model is tuned in such a way that the sum of the probabilities over all possible hadronic species becomes 1 in the limit $p_T \to 0$, as it is possible to see in Fig. (2.15). What we found is that within a fragmentation plus

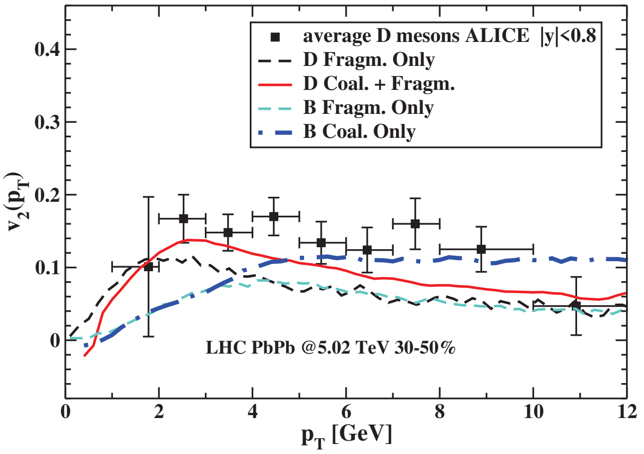

Figure 5.17: *B* meson $v_2(p_T)$ from either only fragmentation (dashed orange line) or only coalescence mechanism (solid red line) compared to previous results for *D* meson elliptic flow with various hadronization scenarios and together with the measured ALICE data for the average $D^0 + D^+ + D^*$ taken from Ref. [138].

coalescence model we were able to reproduce the enhancement of Λ_c production in HICs and quantitatively estimate a value of Λ_c/D^0 ratio which was in agreement with the single experimental point available from STAR at that time [224]. In Ref. [75] we also noticed that in our hadronization scenario the p_T dependence of the baryon-to-meson ratios is sensitive to the masses of the coalescing quarks in a rather different way compared to other models. Motivated by these results we carried out simulations also at LHC *PbPb* collisions at $\sqrt{s_{NN}} = 5.02\,TeV$ and came up with predictions which indicate the enhancement of Λ_c production with the same order of magnitude of the one observed at RHIC. To summarize this work we present our estimated Λ_c/D^0 as function of transverse momentum in Fig. (5.18) both for RHIC (left) and LHC (right) collisions where solid lines refer to a scenario where charm quarks hadronize by only coalescence mechanism (dashed-dotted black curve), while dashed lines are the case where we account for coalescence plus fragmentation. In the same figure we show also a comparison with the updated data from STAR and the measurements made by ALICE [218].

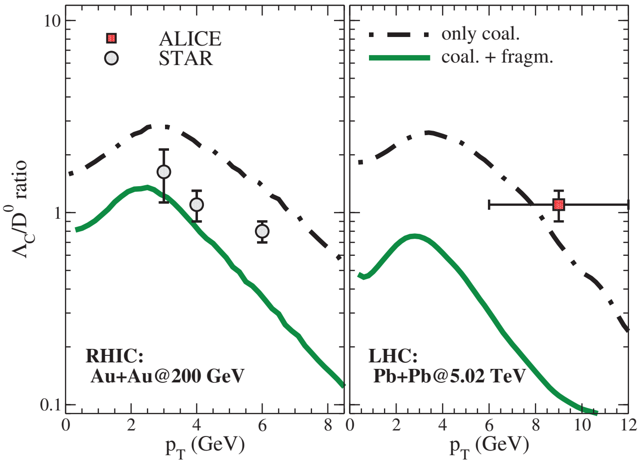

Figure 5.18: The baryon-to-meson ratio form charmed hadrons as function of p_T predicted from the hybrid fragmentation plus coalescence model [75] and compared to experimental measurements at RHIC (left plot) and LHC (right plot). STAR and ALICE data are respectively from Ref. [225] and Ref. [218].

We believe that one of the possible observables that can be affected by the enhancement of Λ_c production in AA collisions is the nuclear modification factor. In pp collisions charm quarks still hadronize preferably into D mesons, because the probability to fragment into a baryon state is very low. On the other hand in a hadronization scenario where the production of Λ_c is comparable to the one of D^0 mesons and considering the conservation of the total charm quarks, the suppression factor of D^0 at low momenta decreases significantly. In Fig. (5.19) we present our predictions for R_{AA} of D^0 mesons obtained from charm evolution in the QGP within a Boltzmann QPM transport framework coupled to hadronization by fragmentation plus coalescence model where the effect of the enhancement charmed baryon production is treated in such a way to reproduce the measured $\Lambda_c/D^0 \sim 1$ (see left plot Fig. (5.18)). In particular, our new results (thick green lines) are compared with our previous results for the R_{AA} of D^0 mesons (thin red line). The effect of Λ_c production follows a p_T trend which is governed by the coalescence model, having the strongest impact for $p_T \leq 2\,GeV$, while reducing at higher momenta where both results converge to the fragmentation value.

,

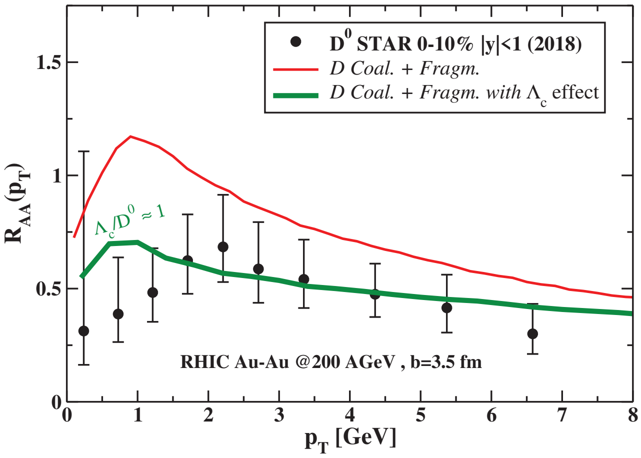

(a)

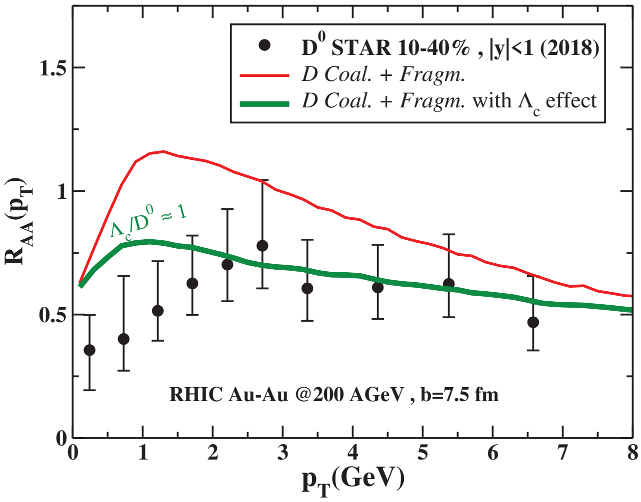

(b)

Figure 5.19: The nuclear modification factor $R_{AA}(p_T)$ of D^0 mesons at RHIC central (a) and peripheral (b) collisions obtained within a fragmentation plus coalescence scenario with enhancement of Λ_c/D^0 ratio and compared to experimental measurements from STAR collaboration [124].

5.5 HQ's thermalization in the QGP

5.5.1 Spatial diffusion coefficient for charm

After we constraint the total HQ interaction with the *bulk* by reproducing the experimentally observed nuclear modification factor R_{AA} and the elliptic flow v_2 both at RHIC and LHC energies, our Boltzmann approach is suitable for extracting the charm spatial diffusion coefficient $D_s(T)$. We remind that in kinetic theory we related the D_s to thermalization time of HQs through Eq. (3.76) that we write again

$$2\pi T D_s(T) = \frac{2\pi T^2}{M_{HQ} A(T, p \to 0)} = \frac{2\pi T^2}{M_{HQ}} \tau_{th} \tag{5.15}$$

where in Chapter 3 we used the notation $A(T, p \to 0) \equiv \gamma = \tau_{th}^{-1}$ to indicate the *drag* coefficient in the non-relativistic limit $p \to 0$. Then, since we are looking at HQ interaction at low p_T, we can be sure that our result will not be affected by the absence of a radiative energy loss mechanism within our interaction kernel. The goal of this work is provide a phenomenological estimate of $2\pi T D_s$ similarly to other transport models for HQs and in particular, to compare our result to the expectations from lQCD where the D_s is calculated from the spectral functions (see (2.85)). We start with the charm D_s by presenting results obtained within our QPM approach implemented within the Boltzmann transport framework that can be compared to those obtained in the case the same QPM interaction kernel is setup within a Fokker-Planck/Langevin model [196]. For our estimate we employ Eq. (5.15) with $M_c = 1.3\, GeV$ and T-dependent *drag* coefficient $A(T, p = 0.1\, GeV)$ from QPM interaction multiplied by the proper constant K factor used to reproduce the measured R_{AA} and v_2 at RHIC and LHC. Our final value is set to $K = 2.4$. We observe that the extracted $2\pi T D_s(T)$ from our phenomenological approach matches with lQCD expectations. This is an important result, meaning that by means of HQ dynamics we are probing properties a strong interacting system which has the properties of the expected QGP phase. In particular, from Eq. (5.15) the spatial diffusion coefficient D_s is directly linked

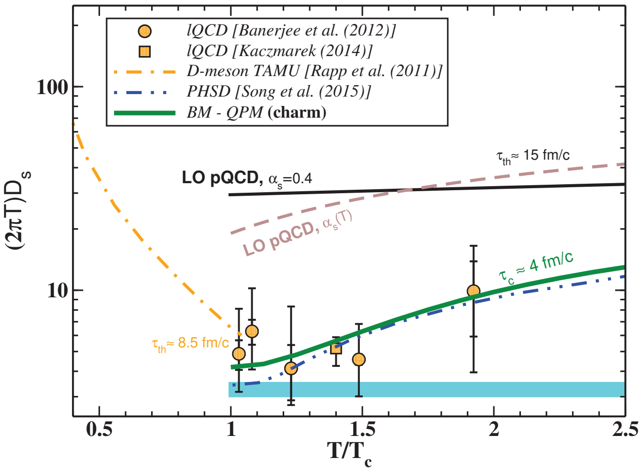

Figure 5.20: Spatial diffusion coefficient as function of temperature obtained within the QPM Boltzmann (green solid) transport approach tuned to reproduce experimental R_{AA} and v_2 of D mesons at RHIC and LHC energies. Both results are compared with quenched lQCD expectations from Ref. [112] (circles) and Ref. [113] (squares), along with estimates from other phenomenological models both for the D_s of charm [209] (dashed double dotted blue) and also for the D_s coefficient of D meson hadronic matters [226] (dash dotted red). In the picture calculations based on LO pQCD with constant α_s (solid black line) and running $\alpha_s(T)$ (dashed brown line) are shown as well as AdS/CFT value scaled to match the energy density of QCD plasma [227] (light blue blank).

to the HQ relaxation time τ_{th}, hence it is a measure of the QCD interaction. Quantitatively τ_{th} can be estimated by inverting Eq. (5.15) and writing in the following way

$$\tau_{th} = \frac{M_{HQ}}{2\pi T^2}\,(2\pi T D_s) \simeq 1.3 \cdot M_{HQ}\frac{2\pi T D_s}{(T/T_c)^2} \quad [fm] \tag{5.16}$$

At the temperature of QGP created at RHIC collisions $T \simeq 2T_c$ with our Botlzmann result for D_s is close to the lQCD point a $2\pi T D_s \approx 10$ at $T \simeq 2T_c$ and if we apply Eq. (5.15) to get charm thermalization time we obtain $\tau_{th} \approx 4\, fm$ with $M_c = 1.3\, GeV$.

5.5.2 Spatial diffusion coefficient for bottom

In the previous section we presented our results for R_{AA} and v_2 of HQs obtained within our Boltzmann approach and showed up that, after reproducing both observables for charmed hadrons, with the same parameter $K = 2.4$ we are able to reproduce with quite good approximation the measure suppression factor for bottom quarks as well as predicting a reasonable elliptic flow in agreement with the few data available. Then, our transport framework is setup already to extract the $2\pi T D_s$ coefficient at the bottom scale leading us to the possibility to investigate the HQ thermalization at larger mass scale. If we base only on the assumption coming from kinetic theory, then what we expect is that τ_{th} should depend linearly on M_{HQ} and this would lead to a comparison between charm and bottom relaxation time of the form $\tau_{th}(b) = M_b/M_c \sim 3.2\tau_{th}(c)$, with respectively $M_b = 4.2\,GeV$, $M_c = 1.3\,GeV$. Using the $\tau_{th}(c) \approx 3.5\,fm$ value obtained from the Boltzmann estimate of charm D_s at $T \simeq 2T_c$, our first estimate would be $\tau_{th}(b) \approx 11.3\,fm$, which means correctly that thermalization of bottom is quite excluded at RHIC. Since our estimate of HQ τ_{th} comes from a phenomenological prediction of the $2\pi T D_s$, we could accept this result only in the case the latter coefficient is truly mass independent, allowing us to directly compare our predictions to lQCD expectations which we remind are evaluated in quenched approximation. We provide a quantitative estimate of this issue for the QPM interaction in the following way. In Fig. (5.21) the ratio between the spatial diffusion coefficient D_s as function of temperature is derived from the *drag* coefficient of the QPM interaction at $p = 0.1\,GeV$ where we use the HQ mass M_{HQ} as a free parameter and fix it at the values $M_{HQ} = 1.3\,,\ 4.2\,,\ 12\,GeV$, being respectively the first M_c, the second M_b, while the third one we label as M^* and it corresponds to the mass of a fictitious super-heavy partner with increased mass of the same order of the charm to bottom step. The constant mass ratios M_b/M_c and M^*/M_b are sketched in Fig. (5.21) respectively with blue and red dashed lines. Similarly the ratios for spatial diffusion coefficients among charm and bottom ($D_s(c)/D_s(b)$) and bottom super-heavy quark ($D_s(b)/D_s(M^*)$) are represented respectively by blue solid and dash-dotted red line. As we can see

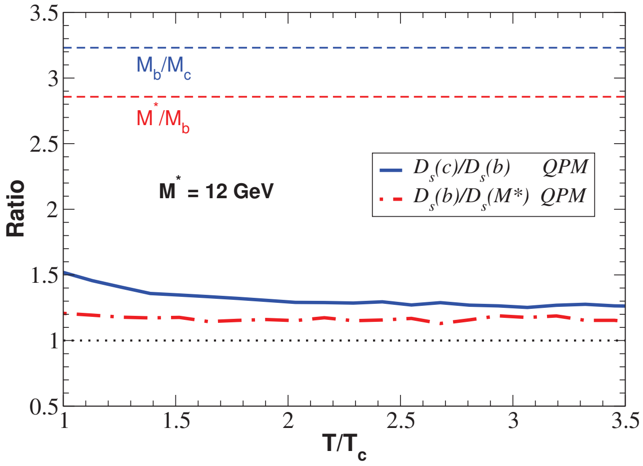

Figure 5.21: Ratio among spatial diffusion coefficient D_s calculated within a QPM interaction for three different M_{HQ} values.

within a mass difference of $M_b/M_c \approx 3.2$ the resulting discrepancy between $D_s(b)$ and $D_s(c)$ within the QPM interaction is about 50% at $T \approx T_c$ and not smaller than 30% at higher temperatures. On the other hand, the ratio between $D_s(b)$ and the D_s calculated with $M^* \approx 3M_b$ stays almost constant at a value of about 1.2 as function of temperature. Then, we conclude that at the bottom mass scale we are closer to the quenched limit with a discrepancy of the order of 20% which it is quite reasonable approximation if we takes into account the uncertainties on the lQCD points. At this benefit we must add the condition $M_{HQ} \gg gT$ which at the level of M_b is still valid, hence ensuring a small difference between Langevin and Boltzmann dynamics and resulting in a almost negligible uncertainty coming from the adopted transport model to estimate the bottom D_s. [195] The extracted bottom $2\pi T D_s(T)$ from Boltzmann QPM approach is represented in Fig. (5.22) and compared to lQCD and AdS/CFT expectations as well our results for the charm case.

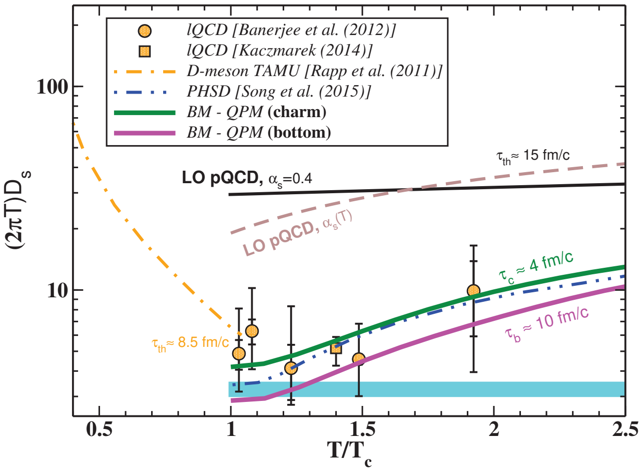

Figure 5.22: Predictions of spatial diffusion coefficient for bottom quark obtained within the Boltzmann QPM approach (magenta solid line) and compared with the D_s of charm obtained with the same theoretical framework (solid green line) as well as with lQCD quenched points from Ref. [112] (circles) and Ref. [113] (squares), LO-QCD with constant or running $\alpha_s(T)$ and AdS/CFT expectation [227].

CONCLUSIONS

In this thesis we have studied the dynamical expansion of the Quark-Gluon Plasma (QGP) created in ultra-relativistic Heavy-Ion Collisions (HICs) by means of a microscopic transport model. In particular, we have focused on the propagation of Heavy Quarks (HQs), mainly charm and bottom, which due to their large masses are produced by hard binary collisions at early stages $\tau_f \leq 0.1\, fm$, so they can probe the entire phase-space evolution of the QGP *fireball*. Moreover, since the thermalization time of HQs is larger than the one of light partons and eventually comparable with the lifetime of the QGP, they can preserve key information of their dynamical evolution. The study of HQ propagation through the QGP is subject of many theoretical and phenomenological models which aim to provide a simultaneous description of the nuclear modification factor $R_{AA}(p_T)$ and the elliptic flow $v_2(p_T)$ which have been widely measured in the experiments conducted at RHIC and LHC facilities. The goal of our work is to develop a consistent approach for HQ dynamics and hadronization that leads towards an understanding of the $R_{AA} - v_2$ "puzzle" and is suitable to tackle new challenges in this interesting sector. With this purpose we have implemented a 3+1 dimensional transport framework based on the numerical solution of the Relativistic Boltzmann Equation (RBE) both for HQs and *bulk* matter partons (gluons and light quarks) where the phase-space distribution functions are sampled by test-particle method, while the collision integral is mapped stochastically through the scattering cross section. In particular, we have focused on the low transverse momentum region by including only elastic processes between HQs and light partons, while neglecting the possible radiative energy loss mechanisms which become effective at $pt \geq 10\,GeV$. In the low p_T region the interaction of HQs, parametrized in terms of the *drag* coefficient γ, appears to differ from the expected pQCD behavior. In transport models this translates in the use of a momentum dependent K parameter multiplying the pQCD scattering cross section. We have accounted for non-perturbative effects by prescription of a Quasi-Particle Model (QPM) where light quarks and gluons of the QCD medium are dressed with effective thermal masses $m_{g,q} \sim g(T)T$ and the T-dependence of the coupling $g(T)$ is tuned to fit the Equation of State (EoS) of lattice QCD (lQCD). This results into an enhancement of the strength interaction towards the critical temperature T_c which gives rise to an approximately constant *drag* coefficient $\gamma(T)$ near T_c, reflecting a behavior typical of a liquid rather than a gas system. We believe that such temperature dependence of the HQ interaction is a key ingredient to achieve a simultaneous description of both R_{AA} and v_2, since it traces the different time evolution of these observables.

In the first part of this thesis we have focused on the analysis of HQ transport parameters, namely *drag* and *diffusion* coefficients, that we studied thoroughly by performing numerical simulations in static QCD medium at fixed temperature and by comparing the results for charm quark dynamics among various transport models in order to reduce the systematical uncertainty of the extracted *drag* force.

In the second part we have carried out simulations of realistic HICs at RHIC and LHC energies employing a formulation of relativistic kinetic theory with fixed value of η/s rather than concentrating on specific microscopic processes. In this way, we can gauge our transport approach for the QGP evolution to the language of hydrodynamics, but in addition we can extend our study including non-equilibrium features such as *minijet* distributions at intermediate p_T. For HQs instead we have used our QPM interaction kernel and absorbed other non-perturbative effects within a constant K factor. In order to compare our results with the experimental Heavy-Flavor (HF) R_{AA} and v_2

measurements, we have coupled the final charm and bottom Boltzmann evolution to a hybrid fragmentation plus coalescence hadronization model. This framework has been used in related works where it was found that it is possible to obtain the correct p_T dependence of the measured D meson spectra both at RHIC and LHC and describe also the absolute yield of the charmed baryon-to-meson ratio in agreement with the observed value of $\Lambda_c/D^0 \sim 1$. For what concerns our analysis, we have computed the D meson nuclear modification factor $R_{AA}(p_T)$ and elliptic flow $v_2(p_T)$ and provided our results within two possible scenarios: one considering only hadronization by fragmentation and another including also coalescence. It arises that the latter mechanism inverts the relation between the two observables established during the dynamical evolution in the QGP and maintained by the former, implying an increasing of the R_{AA} conjointly with the rising of the v_2. We have seen that at RHIC energy the coalescence mechanism plays a fundamental role in order to reproduce the observed D suppression and above all it strongly couples charm anysotropies to the collective motion of the *bulk* to get a final D meson elliptic flow in agreement with the experimental measurements. Instead at LHC the coalescence is still effective for the formation of v_2, while its effect on the R_{AA} is reduced because hadronization by fragmentation is more dominant.

A novelty of our work is represented by the possibility to study the impact of strong Λ_c production on the the nuclear modification factor of D mesons. We have presented for the first time a quantitative estimate of the evolution of the $R_{AA}(p_T)$ constraining the charm hadronization within a scenario where baryon enhancement is addressed in agreement with the measured $\Lambda_c/D^0 \simeq 1$. We have shown that at RHIC energy such effect is everything-but-marginal. Indeed it reduces the characteristic peak of R_{AA} at $p_T \sim 1\,GeV$ by a factor 1.5 and it leads our results to a better agreement with the experimental data in the explored p_T range.

Within the same Boltzmann framework we have studied also the production of B mesons in HICs and we have presented our results for R_{AA} compared with the available experimental data. We notice that we have achieved to obtain a reasonable description of bottom suppression without changing the K factor which we fixed for charm interaction. From the point of view of hadronization, we have seen that coalescence does not change significantly the R_{AA}, because bottom quarks have harder p_T spectrum compared to charm, implying a smaller gain in transverse momentum when they recombine with the light quarks of the medium. On the other hand, we have found that a fast conversion of the initial *bulk* eccentricity to momentum anysotropy leads to the formation of v_2 which is comparable between charm and bottom and later it is risen up by coalescence showing a mass dependent effect. We point out also that our results for B meson v_2 and R_{AA} are more properly predictions, due to the lacking of experimental data for the former and the large statistical uncertainties related to the latter observable. Such predictions will be useful for the future measurements in the B sector which it could be explored in the planned high luminosity LHC facility.

Finally, we have investigated the thermalization of charm quarks in the QGP by calculating the spatial diffusion coefficient $2\pi T D_s(T)$ which we extract from our Boltzmann QPM approach after reproducing the observed R_{AA} and v_2 of D mesons. In particular, we have found that our estimate of $D_s(T)$ is in agreement with expectations from lQCD and other phenomenological models and from the relation $\tau_{th} = M_{HQ} D_s(T)/T$ it leads to a charm thermalization time $\tau_{th} \approx 4\, fm$ at $T \simeq 2T_c$ to be compared with the overastimated pQCD value of $\tau_{th} \approx 15\, fm$. Our predictions of R_{AA} and v_2 of D mesons indicate the possibility to discriminate among the different T dependence of the *drag* coefficient $\gamma(T) = \tau_{th}^{-1}$ and to probe the strong non-perturbative QGP properties within the present lQCD uncertainties. Moreover, in accordance with kinetic theory the thermalization time should scale linearly with M_{HQ}, thus resulting in D_s parameter which is a mass independent measure of the QCD interaction. As final goal of this work we have checked this issue by carrying out predictions for spatial diffusion coefficient of bottom quark within the same Boltzmann approach. Within the QPM interaction the mass difference among charm and bottom leads to a discrepancy in the ratio $D_s(c)/D_s(b)$ of about 50% at $T \simeq T_c$ and decreasing slightly to 30% at higher temperatures. This means that at the mass scale of charm quark the quenched limit used in lQCD is not reasonable. Moreover, it has been pointed out that in the strong interacting QGP ($g \sim 2$) the condition $M_{HQ} > gT$ is challenging at least for charm quark, implying a difference within the Fokker-Planck/Langevin and the Boltzmann dynamics. For this reason we conclude that our estimate of the spatial coefficient $2\pi T D_s(T)$ at the bottom mass scale can reduce the discrepancy arising from the adopted transport model and it is also closer to the lQCD quenched paradigma.

In conclusion, the results presented in this thesis represent a starting point for future developments and investigations. In an upcoming work we will include initial state fluctuations to study the impact of T-dependence of the charm *drag* coefficient on higher anysotropic flows v_3, v_4, v_5 and looking at the correlations between heavy and light harmonics $v_n(heavy) - v_n(light)$ which are planned to be measured at RHIC and LHC experiments. The improvement of our Boltzmann approach by implementing an in-medium gluon radiation mechanism consistent with our QPM interaction will allow to push our analysis of D meson R_{AA} and v_2 at higher transverse momentum and it will be important for the study of more differential observables, like azimuthal $D - \bar{D}$ correlations. These are eventually measurable more in pA than in AA collisions, hence a comprehension of the initial stage phenomena affecting the dynamical evolution of HQs will be a fundamental task. In this direction we are working also to couple our Boltzmann transport model with a realistic description of initial vorticity and strong Electro-Magnetic fields created in HICs with the aim to study the formation of the directed flow v_1 and the possible splitting between matter and anti-matter $D^0 - \bar{D}^0$ which if measured would represent a clear signature of the deconfined partonic phase.

CHAPTER 6

APPENDIX

6.1 Appendix A

We report the scattering cross section for Heavy Quark (HQ) pair production which at hadron colliders such as RHIC and LHC happens through two main processes, namely the quark-antiquark annihilation and the gluon fusion. For the calculation we employ scattering pQCD matrices at Leading-Order (LO) which are represented by the Feynman diagrams in Fig.(2.13) and we neglect the masses of light partons as done also in Ref. [80]. Hence, the Lorentz invariant cross section can be written as following

$$\frac{d\sigma}{dt} = \frac{\overline{\mathcal{M}^2}}{16\pi s^2} \tag{6.1}$$

where we introduced the Mandelstam variables s, t and $u = M_{HQ}^2 - s - t$ for the partonic kinematics (usually indicated with a "hat" notation). The quark-antiquark annihilation corresponds to the single Feynman diagram in Fig. (2.13) on the upper left and its related scattering amplitude is given by

$$\overline{|\mathcal{M}_{q\bar{q}}|^2} = \frac{1}{\gamma_{q\bar{q}}} * \frac{256\pi^2\alpha_s^2}{s^2}\left[(t - M_{HQ}^2)^2 + (u - M_{HQ}^2)^2 + 2sM_{HQ}^2\right]$$

where α_s is the QCD coupling constant and $\gamma_{q\bar{q}} = 36$ are the spin-color degrees of freedom of the initial quark-antiquark pair. Instead the gluon fusion process involves three possible channels (t, u, s) related to three different Feynman diagrams at tree level. Starting from the upper right plot depicted in Fig.(2.13) and going to the diagrams below, the corresponding scattering amplitudes are

$$\overline{|\mathcal{M}_t|^2} = \frac{1}{\gamma_{gg}} * \frac{256 * (8/3)\pi^2\alpha_s^2}{(t - M_{HQ}^2)^2} \left[(M_{HQ}^2 - t)(M_{HQ}^2 - u) - 2M_{HQ}^2(M_{HQ}^2 + t)\right]$$

$$\overline{|\mathcal{M}_u|^2} = \frac{1}{\gamma_{gg}} * \frac{256 * (8/3)\pi^2\alpha_s^2}{(u - M_{HQ}^2)^2} \left[(M_{HQ}^2 - t)(M_{HQ}^2 - u) - 2M_{HQ}^2(M_{HQ}^2 + u)\right]$$

$$\overline{|M_s|^2} = \frac{1}{\gamma_{gg}} * \frac{256 * (12)\pi^2\alpha_s^2}{s^2} \left[(M_{HQ}^2 - t)(M_{HQ}^2 - u)\right]$$

where $\gamma_{gg} = 256$ are the color-polarization degrees of freedom of the initial gluon pair. Together with these contributions one has to include the mixed interference terms. Hence, we get

$$2\,\overline{\mathcal{M}_t\,\mathcal{M}_u^*} = \frac{1}{\gamma_{gg}} * \frac{256 * (2/3)\pi^2\alpha_s^2}{(t - M_{HQ}^2)(u - M_{HQ}^2)} \left[M_{HQ}^2(4M_{HQ}^2 - s)\right]$$

$$2\,\overline{\mathcal{M}_s\,\mathcal{M}_t^*} = \frac{1}{\gamma_{gg}} * \frac{256 * (6)\pi^2\alpha_s^2}{s(t - M_{HQ}^2)} \left[(M_{HQ}^2 - t)(M_{HQ}^2 - u) + M_{HQ}^2(u - t)\right]$$

$$2\,\overline{\mathcal{M}_s\,\mathcal{M}_u^*} = \frac{1}{\gamma_{gg}} * \frac{256 * (6)\pi^2\alpha_s^2}{s(u - M_{HQ}^2)} \left[(M_{HQ}^2 - t)(M_{HQ}^2 - u) + M_{HQ}^2(t - u)\right]$$

6.2 Appendix B

We summarize the scattering matrices for $HQ + g(q) \to HQ + g(q)$ process calculated at Leading-Order (LO) pQCD and compared with the results reported in Ref. [80] where *bulk* partons are considered as massless particles, while HQ mass is indicated as M. We also include the full extension considering non-zero masses for gluon or light quarks that we employ in the case non-perturbative interaction is treated within a Quasi-Particle Model (QPM) prescription. These scattering matrices are related to the Feynman diagrams

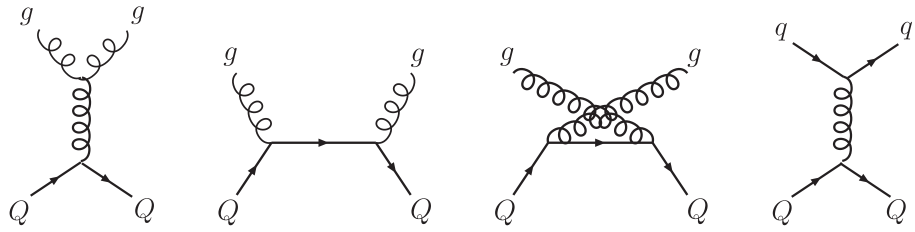

(a) **(b)** **(c)** **(d)**

Figure 6.1: Feynman diagrams for heavy quark (Q) scattering off gluons (g) and light quarks (q) at tree level [127].

at tree level depicted in Fig. (6.1) and indicated with corresponding subscript letters. Firstly we report the three contributions t,s and u-channel coming from HQ scattering off gluons along with the interference terms. Secondary we evaluate the single t-diagram for the scattering between HQ and light quarks. We point out that the dominant contribution arises from the t-channel exchange due to the divergent behavior of the gluon propagator towards the forward scattering $t \to 0$. In the pQCD case we treat such infrared singularity by introducing a regulator μ which we identify with the Debye in medium screening mass $m_D = gT$ where $g = \sqrt{4\pi\alpha_s(Q^2)}$ denotes the pQCD coupling constant running with the momentum transfer $Q^2 = (\pi T)^2$ in according with Eq. (1.14). Instead in the QPM case the gluon propagator is consistently regularized by means of the in medium self-energy arising from the resummation of higher order corrections that is approximately equivalent to its effective mass $m_g \sim gT$ where $g(T)$ follows the QPM parametrization in Eq. (3.41). The gluon t-channel exchange diagram in Fig. (6.1)(a) has square amplitude

$$
\begin{aligned}
\overline{|\mathcal{M}_a|^2} &= \frac{1}{\gamma_a} * \left(\sum \mathcal{M}_a \mathcal{M}_a^*\right) \\
&= \frac{1}{\gamma_a} * \frac{3072\pi^2\alpha_s^2}{(t-\mu^2)^2}\left[(s-M^2)(M^2-u) + m_g^2\left(5m_g^2 + 2(4M^2 - s - u)\right)\right] \\
&\underbrace{\rightarrow}_{m_g \to 0} \frac{1}{\gamma_a} * \frac{3072\pi^2\alpha_s^2}{(t-\mu^2)^2}\left[(s-M^2)(M^2-u)\right]
\end{aligned}
$$

where the initial state average constant γ_a is the product over the initial gluon and HQ spin-color degrees of freedom, i.e. $= \gamma_g^i \cdot \gamma_Q^i = 16 \cdot 6 = 96$. Similarly the s-channel in Fig. (6.1)(b) is given by

$$\begin{aligned}
\overline{|\mathcal{M}_b|^2} &= \frac{1}{\gamma_b} * \left(\sum \mathcal{M}_b \mathcal{M}_b^*\right) \\
&= \frac{1}{\gamma_b} * \frac{2048\pi^2\alpha_s^2}{3(s-M^2)^2} \left[(s-M^2)(M^2-u) + 2M^2(s+M^2) + m_g^2(4M^2+m_g^2)\right] \\
&\underbrace{\rightarrow}_{m_g\to 0} \frac{1}{\gamma_b} * \frac{2048\pi^2\alpha_s^2}{3(s-M^2)^2} \left[(s-M^2)(M^2-u) + 2M^2(M^2+s)\right]
\end{aligned}$$

while the scattering amplitude $\mathcal{M}_c$ for the u-channel in Fig.. (6.1)(c) is obtained by replacing the initial gluon momentum with minus the final gluon momentum in the matrix $\mathcal{M}_b$ (crossing symmetry). In terms of Mandelstam variables this corresponds to the $s \leftrightarrow u$ exchange when evaluating $\overline{|\mathcal{M}_b|^2}$ from $\overline{|\mathcal{M}_c|^2}$ or viceversa. Hence, one gets

$$\begin{aligned}
\overline{|\mathcal{M}_c|^2} &= \frac{1}{\gamma_c} * \left(\sum \mathcal{M}_c \mathcal{M}_c^*\right) \\
&= \frac{1}{\gamma_c} * \frac{2048\pi^2\alpha_s^2}{3(u-M^2)^2} \left[(s-M^2)(M^2-u) + 2M^2(u+M^2) + m_g^2(4M^2+m_g^2)\right] \\
&\underbrace{\rightarrow}_{m_g\to 0} \frac{1}{\gamma_c} * \frac{2048\pi^2\alpha_s^2}{3(u-M^2)^2} \left[(s-M^2)(M^2-u) + 2M^2(M^2+u)\right]
\end{aligned}$$

where $\gamma_c = \gamma_b = \gamma_a = 96$. Then, one has to derive the interference terms over the three possible channels. Starting from the b-c mixing, one has

$$\begin{aligned}
\frac{1}{\gamma_{b,c}} * \left(\sum \mathcal{M}_b \mathcal{M}_c^*\right) &= \frac{1}{\gamma_{b,c}} * \left(\sum \mathcal{M}_b^* \mathcal{M}_c\right) \\
&= \frac{1}{\gamma_{b,c}} \frac{256\pi^2\alpha_s^2}{3(s-M^2)(M^2-u)} \left[M^2(4M^2-t) + 2m_g^2(M^2-t)\right] \\
&\underbrace{\rightarrow}_{m_g\to 0} \frac{1}{\gamma_{b,c}} \frac{256\pi^2\alpha_s^2}{3(s-M^2)(M^2-u)} \left[M^2(4M^2-t)\right]
\end{aligned}$$

and in a similar way one can calculate the *a*-*b* interference channel

$$\begin{aligned}\frac{1}{\gamma_{a,b}} * \left(\sum \mathcal{M}_a\mathcal{M}_b^*\right) = \frac{1}{\gamma_{a,b}} &* \left(\sum \mathcal{M}_a^*\mathcal{M}_b\right)\\ &= \frac{1}{\gamma_{a,b}}\frac{768\pi^2\alpha_s^2}{(s-M^2)(t-\mu^2)}\left[(2M^2s-su-M^4)+m_g^2\left(5m_g^2+2(4M^2-s-u)\right)\right]\\ &\underbrace{\rightarrow}_{m_g\to0}\frac{1}{\gamma_{a,b}}\frac{768\pi^2\alpha_s^2}{(s-M^2)(t-\mu^2)}\left[(s-M^2)(M^2-u)+M^2(s-u)\right]\end{aligned}$$

as well as the *a*-*c* one which is obtained from the last one by applying the $s \leftrightarrow u$ symmetry with extra -1 factor since a fermionic pair is crossed

$$\begin{aligned}\frac{1}{\gamma_{a,c}} * \left(\sum \mathcal{M}_a\mathcal{M}_c^*\right) = \frac{1}{\gamma_{a,c}} &* \left(\sum \mathcal{M}_a^*\mathcal{M}_c\right)\\ &= \frac{-1}{\gamma_{a,c}}\frac{768\pi^2\alpha_s^2}{(M^2-u)(t-\mu^2)}\left[(2M^2u-su-M^4)+m_g^2\left(5m_g^2+2(4M^2-s-u)\right)\right]\\ &\underbrace{\rightarrow}_{m_g\to0}\frac{-1}{\gamma_{a,c}}\frac{768\pi^2\alpha_s^2}{(M^2-u)(t-\mu^2)}\left[(s-M^2)(M^2-u)+M^2(u-s)\right]\end{aligned}$$

where $\gamma_{b,c}$,$\gamma_{a,b}$,$\gamma_{a,c}$ are all equal to $\gamma_a = 96$. Instead the HQ scattering off light quarks occurs through the *t*-channel diagram represented in Fig. (6.1)(d) which leads to the following square amplitude[1]

$$\begin{aligned}\overline{|\mathcal{M}_d|^2} &= \frac{1}{\gamma_d}N_f * \left(\sum \mathcal{M}_d\mathcal{M}_d^*\right)\\ &= \frac{1}{\gamma_d}N_f * \frac{256\pi^2\alpha_s^2}{(t-\mu^2)^2}\left[(s-M^2-m_q^2)^2+(M^2+m_q^2-u)^2+2t(M^2+m_q^2)\right]\\ &\underbrace{\rightarrow}_{m_q\to0}\frac{1}{\gamma_d}N_f * \frac{256\pi^2\alpha_s^2}{(t-\mu^2)^2}\left[(s-M^2)^2+(M^2-u)^2+2tM^2\right]\end{aligned}$$

where N_f is the number of light quark flavors and μ denotes the IR regulator of the gluon propagator singularity which is treated analogously to the *t*-exchange diagram in Fig. (6.1). The corresponding total cross sections derived from Eq.(3.56) within the QPM and pQCD model are depicted below.

---

[1] The same calculation happens for the elastic scattering between HQs and light antiquarks $\bar{q}$, that can be addressed by multiplying by a factor 2.

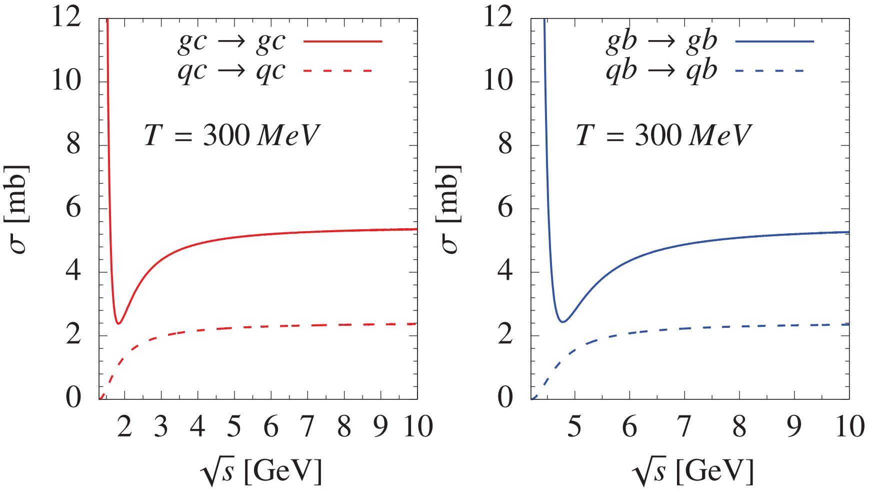

Figure 6.2: Scattering cross section for pQCD interaction between charm (left) or beauty (right) with massless gluons and light quarks at $T = 300\,MeV$, corresponding to coupling constant $\alpha_s = 0.4$ and Debye screening mass $m_D = 0.67\,GeV$.

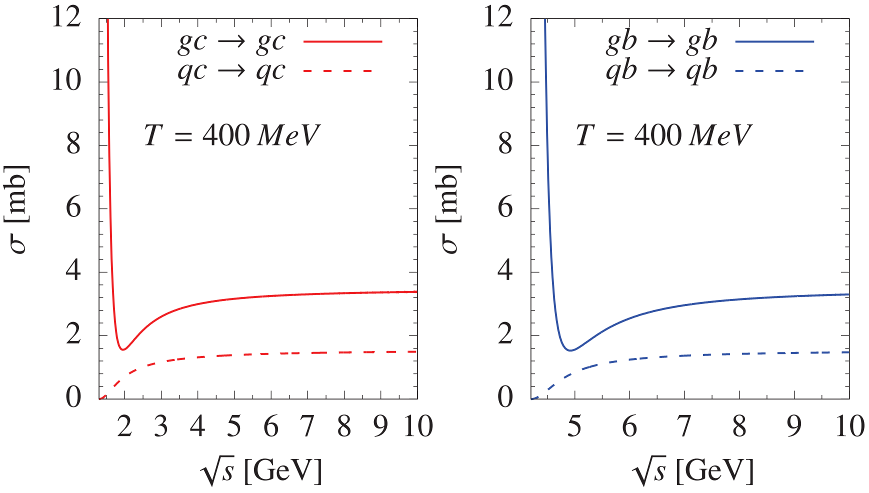

Figure 6.3: Scattering cross section for pQCD interaction between charm (left) or beauty (right) with massless gluons and light quarks at $T = 400\,MeV$, corresponding to coupling constant $\alpha_s = 0.35$ and Debye screening mass $m_D = 0.84\,GeV$.

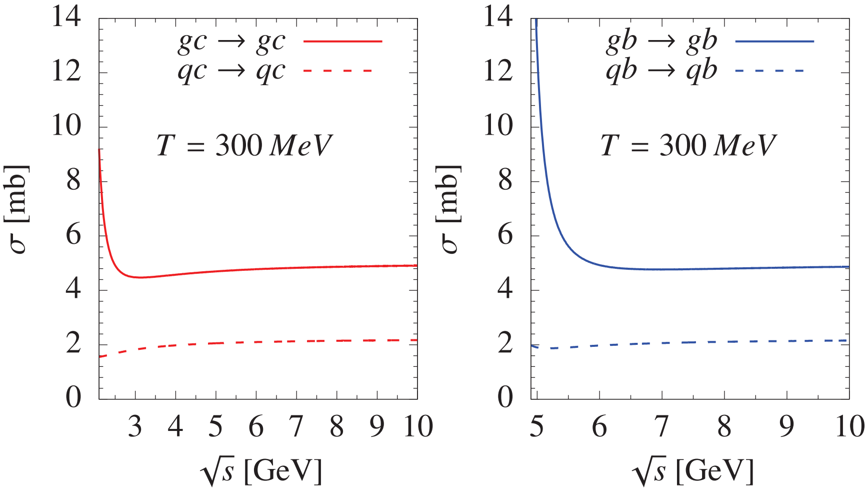

Figure 6.4: Scattering cross section for QPM interaction between charm (left) or beauty (right) with massive gluons and light quarks at $T = 300\,MeV$, corresponding to QPM coupling constant $\alpha_s = 0.81$ and thermal masses $m_g = 0.70\,GeV$, $m_q = 0.47\,GeV$.

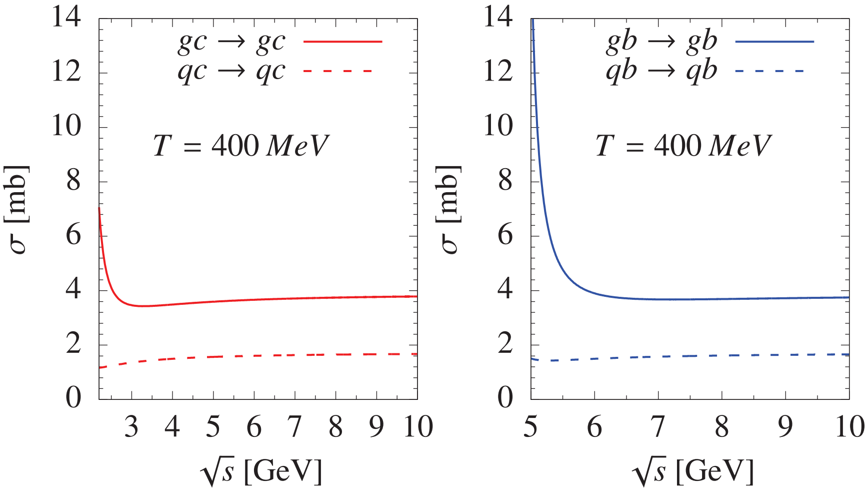

Figure 6.5: Scattering cross section for QPM interaction between charm (left) or beauty (right) with massive gluons and light quarks at $T = 400\,MeV$, corresponding to QPM coupling constant $\alpha_s = 0.42$ and thermal masses $m_g = 0.79\,GeV$, $m_q = 0.53\,GeV$.

BIBLIOGRAPHY

[1] Michele Maggiore. *A Modern introduction to quantum field theory*. Oxford University Press, 2005.

[2] W. Greiner, S. Schramm, and E. Stein. *Quantum chromodynamics*. 2002.

[3] Michael E. Peskin and Daniel V. Schroeder. *An Introduction to quantum field theory*. Addison-Wesley, Reading, USA, 1995.

[4] Steven Weinberg. *The Quantum theory of fields. Vol. 1: Foundations*. Cambridge University Press, 2005.

[5] Steven Weinberg. *The quantum theory of fields. Vol. 2: Modern applications*. Cambridge University Press, 2013.

[6] Taizo Muta. *Foundations of Quantum Chromodynamics: An Introduction to Perturbative Methods in Gauge Theories, (3rd ed.)*, volume 78 of *World scientific Lecture Notes in Physics*. World Scientific, Hackensack, N.J., 2010.

[7] W. Greiner and J. Reinhardt. *Quantum electrodynamics*. 1992.

[8] Richard D. Field. *Applications of Perturbative QCD*, volume 77. Addison-Wesley Publishing Company (Frontiers in Physics), 1989.

[9] H. David Politzer. Reliable Perturbative Results for Strong Interactions. *Phys. Rev. Lett.*, 30:1346–1349, 1973.

[10] David J. Gross and Frank Wilczek. Ultraviolet Behavior of Non-Abelian Gauge Theories. *Phys. Rev. Lett.*, 30:1343–1346, 1973.

[11] Sidney R. Coleman and David J. Gross. Price of asymptotic freedom. *Phys. Rev. Lett.*, 31:851–854, 1973.

[12] Siegfried Bethke. The 2009 World Average of alpha(s). *Eur. Phys. J.*, C64:689–703, 2009.

[13] Szabocls Borsanyi, Zoltan Fodor, Christian Hoelbling, Sandor D. Katz, Stefan Krieg, and Kalman K. Szabo. Full result for the QCD equation of state with 2+1 flavors. *Phys. Lett.*, B730:99–104, 2014.

[14] J. Beringer et al. Review of Particle Physics (RPP). *Phys. Rev.*, D86:010001, 2012.

[15] Kenneth G. Wilson. Confinement of Quarks. *Phys. Rev.*, D10:2445–2459, 1974.

[16] O. Kaczmarek, F. Karsch, P. Petreczky, and F. Zantow. Heavy quark anti-quark free energy and the renormalized Polyakov loop. *Phys. Lett.*, B543:41–47, 2002.

[17] Olaf Kaczmarek and Felix Zantow. Static quark anti-quark free and internal energy in 2-flavor QCD and bound states in the QGP. *PoS*, LAT2005:192, 2006.

[18] Nambu, Yoichiro and Jona-Lasinio, G. Dynamical Model of Elementary Particles Based on an Analogy with Superconductivity 1. *Phys. Rev.*, 122:345–358, 1961.

[19] Nambu, Yoichiro and Jona-Lasinio, G. Dynamical Model of Elementary Particles Based on an Analogy with Superconductivity 2. *Phys. Rev.*, 124:246–254, 1961.

[20] S. P. Klevansky. The Nambu-Jona-Lasinio model of quantum chromodynamics. *Rev. Mod. Phys.*, 64:649–708, 1992.

[21] U. Vogl and W. Weise. The Nambu and Jona Lasinio model: Its implications for hadrons and nuclei. *Prog. Part. Nucl. Phys.*, 27:195–272, 1991.

[22] S. Eidelman et al. Review of particle physics. Particle Data Group. *Phys. Lett.*, B592(1-4):1–5, 2004.

[23] Claudia Ratti. Lattice QCD and heavy ion collisions: a review of recent progress. *Rept. Prog. Phys.*, 81(8):084301, 2018.

[24] Tillmann Boeckel and Jurgen Schaffner-Bielich. A little inflation at the cosmological QCD phase transition. *Phys. Rev.*, D85:103506, 2012.

[25] Michael J. Fromerth and Johann Rafelski. Hadronization of the quark Universe. 2002.

[26] Claudia Ratti, Szabolcs Borsanyi, Zoltan Fodor, Christian Hoelbling, Sandor D. Katz, Stefan Krieg, and Kalman K. Szabo. Recent results on QCD thermodynamics: lattice QCD versus Hadron Resonance Gas model. *Nucl. Phys.*, A855:253–256, 2011.

[27] M. Cheng et al. The QCD equation of state with almost physical quark masses. *Phys. Rev.*, D77:014511, 2008.

[28] New State of Matter Created at CERN. *The CERN Courier.*, 6, 2000.

[29] Georges Aad et al. Observation of a new particle in the search for the Standard Model Higgs boson with the ATLAS detector at the LHC. *Phys. Lett.*, B716:1–29, 2012.

[30] Serguei Chatrchyan et al. Observation of a new boson at a mass of 125 GeV with the CMS experiment at the LHC. *Phys. Lett.*, B716:30–61, 2012.

[31] Michael L. Miller, Klaus Reygers, Stephen J. Sanders, and Peter Steinberg. Glauber modeling in high energy nuclear collisions. *Ann. Rev. Nucl. Part. Sci.*, 57:205–243, 2007.

[32] H. De Vries, C. W. De Jager, and C. De Vries. Nuclear charge and magnetization density distribution parameters from elastic electron scattering. *Atom. Data Nucl. Data Tabl.*, 36:495–536, 1987.

[33] Tetsuo Hatsuda Kohusuke Yagi and Yasuo Miake. *Quark Gluon Plasma: From Big Bang to Little Bang*, volume 23. Cambridge Monographs on Particle Physics, Nuclear Physics and Cosmology, 2008.

[34] C. Y. Wong. *Introduction to high-energy heavy ion collisions*. 1995.

[35] R. J. Glauber and G. Matthiae. High-energy scattering of protons by nuclei. *Nucl. Phys.*, B21:135–157, 1970.

[36] Santosh K. Das, Salvatore Plumari, Sandeep Chatterjee, Jane Alam, Francesco Scardina, and Vincenzo Greco. Directed Flow of Charm Quarks as a Witness of the Initial Strong Magnetic Field in Ultra-Relativistic Heavy Ion Collisions. *Phys. Lett.*, B768:260–264, 2017.

[37] Umut Gursoy, Dmitri Kharzeev, and Krishna Rajagopal. Magnetohydrodynamics, charged currents and directed flow in heavy ion collisions. *Phys. Rev.*, C89(5):054905, 2014.

[38] H. T. Ding, A. Francis, O. Kaczmarek, F. Karsch, E. Laermann, and W. Soeldner. Thermal dilepton rate and electrical conductivity: An analysis of vector current correlation functions in quenched lattice QCD. *Phys. Rev.*, D83:034504, 2011.

[39] A. Puglisi, S. Plumari, and V. Greco. Electric Conductivity from the solution of the Relativistic Boltzmann Equation. *Phys. Rev.*, D90:114009, 2014.

[40] John David Jackson. *Classical Electrodynamics*. Wiley, 1998.

[41] Kirill Tuchin. Time and space dependence of the electromagnetic field in relativistic heavy-ion collisions. *Phys. Rev.*, C88(2):024911, 2013.

[42] J. D. Bjorken. Highly Relativistic Nucleus-Nucleus Collisions: The Central Rapidity Region. *Phys. Rev.*, D27:140–151, 1983.

[43] Larry D. McLerran and Raju Venugopalan. Computing quark and gluon distribution functions for very large nuclei. *Phys. Rev.*, D49:2233–2241, 1994.

[44] Larry D. McLerran and Raju Venugopalan. Gluon distribution functions for very large nuclei at small transverse momentum. *Phys. Rev.*, D49:3352–3355, 1994.

[45] Larry D. McLerran and Raju Venugopalan. Green's functions in the color field of a large nucleus. *Phys. Rev.*, D50:2225–2233, 1994.

[46] Francois Gelis, Edmond Iancu, Jamal Jalilian-Marian, and Raju Venugopalan. The Color Glass Condensate. *Ann. Rev. Nucl. Part. Sci.*, 60:463–489, 2010.

[47] Dmitri Kharzeev, Eugene Levin, and Marzia Nardi. Color glass condensate at the LHC: Hadron multiplicities in pp, pA and AA collisions. *Nucl. Phys.*, A747:609–629, 2005.

[48] Marco Ruggieri, Francesco Scardina, Salvatore Plumari, and Vincenzo Greco. Thermalization, Isotropization and Elliptic Flow from Nonequilibrium Initial Conditions with a Saturation Scale. *Phys. Rev.*, C89(5):054914, 2014.

[49] A. Bazavov et al. The chiral and deconfinement aspects of the QCD transition. *Phys. Rev.*, D85:054503, 2012.

[50] S. R. De Groot. *Relativistic Kinetic Theory. Principles and Applications*. 1980.

[51] E.M. Lifshitz, L.P. Pitaevskii, J.B. Sykes, and R.N. Franklin. *Physical Kinetics*. Course of theoretical physics. Elsevier Science, 1995.

[52] W. Israel and J. M. Stewart. Transient relativistic thermodynamics and kinetic theory. *Annals Phys.*, 118:341–372, 1979.

[53] G. S. Denicol, E. Molnár, H. Niemi, and D. H. Rischke. Derivation of fluid dynamics from kinetic theory with the 14-moment approximation. *Eur. Phys. J.*, A48:170, 2012.

[54] Paul Romatschke and Ulrike Romatschke. Viscosity Information from Relativistic Nuclear Collisions: How Perfect is the Fluid Observed at RHIC? *Phys. Rev. Lett.*, 99:172301, 2007.

[55] Fred Cooper and Graham Frye. Comment on the Single Particle Distribution in the Hydrodynamic and Statistical Thermodynamic Models of Multiparticle Production. *Phys. Rev.*, D10:186, 1974.

[56] Fred Cooper, Graham Frye, and Edmond Schonberg. Landau's Hydrodynamic Model of Particle Production and electron Positron Annihilation Into Hadrons. *Phys. Rev.*, D11:192, 1975.

[57] Albino, Simon. The Hadronization of partons. *Rev. Mod. Phys.*, 82:2489–2556, 2010.

[58] R. D. Field and R. P. Feynman. Quark Elastic Scattering as a Source of High Transverse Momentum Mesons. *Phys. Rev.*, D15:2590–2616, 1977.

[59] Field, R. D. and Feynman, R. P. A Parametrization of the Properties of Quark Jets. *Nucl. Phys.*, B136:1, 1978.

[60] Gribov, V. N. and Lipatov, L. N. Deep inelastic e p scattering in perturbation theory. *Sov. J. Nucl. Phys.*, 15:438–450, 1972. [Yad. Fiz.15,781(1972)].

[61] Dokshitzer, Yuri L. Calculation of the Structure Functions for Deep Inelastic Scattering and e^+e^- Annihilation by Perturbation Theory in Quantum Chromodynamics. *Sov. Phys. JETP*, 46:641–653, 1977. [Zh. Eksp. Teor. Fiz.73,1216(1977)].

[62] Altarelli, Guido and Parisi, G. Asymptotic Freedom in Parton Language. *Nucl. Phys.*, B126:298, 1977.

[63] Bernd A. Kniehl, G. Kramer, and B. Potter. Testing the universality of fragmentation functions. *Nucl. Phys.*, B597:337–369, 2001.

[64] Albino, S. and Kniehl, B. A. and Kramer, G. AKK Update: Improvements from New Theoretical Input and Experimental Data. *Nucl. Phys.*, B803:42–104, 2008.

[65] Carl B. Dover, Ulrich W. Heinz, Ekkard Schnedermann, and Joszef Zimanyi. Relativistic coalescence model for high-energy nuclear collisions. *Phys. Rev.*, C44:1636–1654, 1991.

[66] Greco, V. and Ko, C. M. and Levai, P. Parton coalescence and antiproton / pion anomaly at RHIC. *Phys. Rev. Lett.*, 90:202302, 2003.

[67] R. J. Fries, Berndt Muller, C. Nonaka, and S. A. Bass. Hadron production in heavy ion collisions: Fragmentation and recombination from a dense parton phase. *Phys. Rev.*, C68:044902, 2003.

[68] V. Greco, C. M. Ko, and P. Levai. Parton coalescence at RHIC. *Phys. Rev.*, C68:034904, 2003.

[69] R. J. Fries, Berndt Muller, C. Nonaka, and S. A. Bass. Hadronization in heavy ion collisions: Recombination and fragmentation of partons. *Phys. Rev. Lett.*, 90:202303, 2003.

[70] R. J. Fries, Berndt Muller, C. Nonaka, and S. A. Bass. Hadronization in heavy ion collisions: Recombination or fragmentation? *J. Phys.*, G30:S223–S228, 2004.

[71] V. Minissale, S. Plumari, G. Coci, S. K. Das, and V. Greco. Heavy Hadrons Production by Coalescence Plus Fragmentation in AA Collisions at RHIC and LHC. *MDPI Proc.*, 10(1):9, 2019.

[72] Vincenzo Minissale, Francesco Scardina, and Vincenzo Greco. Hadrons from coalescence plus fragmentation in AA collisions at energies available at the BNL Relativistic Heavy Ion Collider to the CERN Large Hadron Collider. *Phys. Rev.*, C92(5):054904, 2015.

[73] V. Greco and C. M. Ko. Quark coalescence and the scaling of hadron elliptic flow. 2005.

[74] Greco, V. and Ko, C. M. and Rapp, R. Quark coalescence for charmed mesons in ultrarelativistic heavy ion collisions. *Phys. Lett.*, B595:202–208, 2004.

[75] Salvatore Plumari, Vincenzo Minissale, Santosh K. Das, G. Coci, and V. Greco. Charmed Hadrons from Coalescence plus Fragmentation in relativistic nucleus-nucleus collisions at RHIC and LHC. *Eur. Phys. J.*, C78(4):348, 2018.

[76] T. Matsui and H. Satz. J/ψ Suppression by Quark-Gluon Plasma Formation. *Phys. Lett.*, B178:416–422, 1986.

[77] Xin Dong and Vincenzo Greco. Heavy quark production and properties of Quark?Gluon Plasma. *Prog. Part. Nucl. Phys.*, 104:97–141, 2019.

[78] Francesco Prino and Ralf Rapp. Open Heavy Flavor in QCD Matter and in Nuclear Collisions. *J. Phys.*, G43(9):093002, 2016.

[79] Liliana Apolinário, José Guilherme Milhano, Gavin P. Salam, and Carlos A. Salgado. Probing the time structure of the quark-gluon plasma with top quarks. *Phys. Rev. Lett.*, 120(23):232301, 2018.

[80] B. L. Combridge. Associated Production of Heavy Flavor States in p p and anti-p p Interactions: Some QCD Estimates. *Nucl. Phys.*, B151:429–456, 1979.

[81] Eric Laenen, S. Riemersma, J. Smith, and W. L. van Neerven. Complete O (alpha-s) corrections to heavy flavor structure functions in electroproduction. *Nucl. Phys.*, B392:162–228, 1993.

[82] S. Alekhin, J. Blumlein, and S. Moch. PDF fit in the fixed-flavor-number scheme. *Nucl. Phys. Proc. Suppl.*, 222-224:41–51, 2012.

[83] B. A. Kniehl, G. Kramer, I. Schienbein, and H. Spiesberger. Hadroproduction of D and B mesons in a massive VFNS. *AIP Conf. Proc.*, 792(1):867–870, 2005.

[84] B. A. Kniehl, G. Kramer, I. Schienbein, and H. Spiesberger. Inclusive D*+- production in p anti-p collisions with massive charm quarks. *Phys. Rev.*, D71:014018, 2005.

[85] Matteo Cacciari, Paolo Nason, and Ramona Vogt. QCD predictions for charm and bottom production at RHIC. *Phys. Rev. Lett.*, 95:122001, 2005.

[86] R. Vogt, M. Cacciari, and P. Nason. QCD predictions of heavy quark production at RHIC. *Nucl. Phys.*, A774:661–664, 2006.

[87] Matteo Cacciari, Stefano Frixione, Nicolas Houdeau, Michelangelo L. Mangano, Paolo Nason, and Giovanni Ridolfi. Theoretical predictions for charm and bottom production at the LHC. *JHEP*, 10:137, 2012.

[88] A. Andronic et al. Heavy-flavour and quarkonium production in the LHC era: from proton?proton to heavy-ion collisions. *Eur. Phys. J.*, C76(3):107, 2016.

[89] Jaroslav Adam et al. D-meson production in p-Pb collisions at $\sqrt{s_{\rm NN}}$ =5.02 TeV and in pp collisions at $\sqrt{s}$ =7 TeV. *Phys. Rev.*, C94(5):054908, 2016.

[90] K. J. Eskola, H. Paukkunen, and C. A. Salgado. EPS09: A New Generation of NLO and LO Nuclear Parton Distribution Functions. *JHEP*, 04:065, 2009.

[91] T. Lappi. The Glasma initial state at the LHC. *J. Phys.*, G35:104052, 2008.

[92] F. Gelis, T. Lappi, and L. McLerran. Glittering Glasmas. *Nucl. Phys.*, A828:149–160, 2009.

[93] T. Lappi and L. McLerran. Some features of the glasma. *Nucl. Phys.*, A772:200–212, 2006.

[94] Stanislaw Mrowczynski. Heavy Quarks in Turbulent QCD Plasmas. *Eur. Phys. J.*, A54(3):43, 2018.

[95] Stanislaw Mrowczynski. Transport of Heavy Quarks Across Glasma. *PoS*, HardProbes2018:128, 2018.

[96] Yifeng Sun, Gabriele Coci, Santosh Kumar Das, Salvatore Plumari, Marco Ruggieri, and Vincenzo Greco. Impact of Glasma on heavy quark observables in nucleus-nucleus collisions at LHC. 2019.

[97] S. K. Wong. Field and particle equations for the classical Yang-Mills field and particles with isotopic spin. *Nuovo Cim.*, A65:689–694, 1970.

[98] Marco Ruggieri and Santosh K. Das. Cathode tube effect: Heavy quarks probing the glasma in p -Pb collisions. *Phys. Rev.*, D98(9):094024, 2018.

[99] M. Ruggieri, L. Oliva, G. X. Peng, and V. Greco. Evolution of pressures and correlations in the Glasma produced in high energy nuclear collisions. *Phys. Rev.*, D97(7):076004, 2018.

[100] Marco Ruggieri and Santosh Kumar Das. Diffusion of charm and beauty in the Glasma. *EPJ Web Conf.*, 192:00017, 2018.

[101] Betty Bezverkhny Abelev et al. Measurement of prompt D-meson production in $p - Pb$ collisions at $\sqrt{s_{NN}} = 5.02$ TeV. *Phys. Rev. Lett.*, 113(23):232301, 2014.

[102] Roel Aaij et al. Study of prompt D^0 meson production in pPb collisions at $\sqrt{s_{\mathrm{NN}}} = 5$ TeV. *JHEP*, 10:090, 2017.

[103] Liang He. Measurement of directed flow of D^0 and $\bar{D}^0$ mesons in 200 GeV Au+Au collisions at RHIC using the STAR detector. *PoS*, HardProbes2018:148, 2019.

[104] Fabrizio Grosa. Measurement of D-meson nuclear modification factor and flow in Pb–Pb collisions with ALICE at the LHC. *PoS*, HardProbes2018:138, 2018.

[105] C. Albertus, Jose Enrique Amaro, E. Hernandez, and J. Nieves. Charmed and bottom baryons: A Variational approach based on heavy quark symmetry. *Nucl. Phys.*, A740:333–361, 2004.

[106] Xin-Nian Wang. Effect of jet quenching on high p_T hadron spectra in high-energy nuclear collisions. *Phys. Rev.*, C58:2321, 1998.

[107] Chien-Wen Hwang. Charge radii of light and heavy mesons. *Eur. Phys. J.*, C23:585–590, 2002.

[108] C. Peterson, D. Schlatter, I. Schmitt, and Peter M. Zerwas. Scaling Violations in Inclusive e+ e- Annihilation Spectra. *Phys. Rev.*, D27:105, 1983.

[109] Mikko Laine and Aleksi Vuorinen. Basics of Thermal Field Theory. *Lect. Notes Phys.*, 925:pp.1–281, 2016.

[110] Heng-Tong Ding, Frithjof Karsch, and Swagato Mukherjee. Thermodynamics of Strong-Interaction Matter from Lattice QCD. In Xin-Nian Wang, editor, *Quark-Gluon Plasma 5*, pages 1–65. 2016.

[111] Sz. Borsanyi, G. Endrodi, Z. Fodor, S. D. Katz, S. Krieg, C. Ratti, and K. K. Szabo. QCD equation of state at nonzero chemical potential: continuum results with physical quark masses at order mu^2. *JHEP*, 08:053, 2012.

[112] Debasish Banerjee, Saumen Datta, Rajiv Gavai, and Pushan Majumdar. Heavy Quark Momentum Diffusion Coefficient from Lattice QCD. *Phys. Rev.*, D85:014510, 2012.

[113] Olaf Kaczmarek. Continuum estimate of the heavy quark momentum diffusion coefficient κ. *Nucl. Phys.*, A931:633–637, 2014.

[114] A. Francis, O. Kaczmarek, M. Laine, T. Neuhaus, and H. Ohno. Nonperturbative estimate of the heavy quark momentum diffusion coefficient. *Phys. Rev.*, D92(11):116003, 2015.

[115] Miklos Gyulassy, Ivan Vitev, Xin-Nian Wang, and Ben-Wei Zhang. Jet quenching and radiative energy loss in dense nuclear matter. 2003.

[116] M. Gyulassy, P. Levai, and I. Vitev. Reaction operator approach to nonAbelian energy loss. *Nucl. Phys.*, B594:371–419, 2001.

[117] Carlos A. Salgado and Urs Achim Wiedemann. Calculating quenching weights. *Phys. Rev.*, D68:014008, 2003.

[118] Magdalena Djordjevic and Ulrich W. Heinz. Radiative energy loss in a finite dynamical QCD medium. *Phys. Rev. Lett.*, 101:022302, 2008.

[119] Magdalena Djordjevic. Theoretical formalism of radiative jet energy loss in a finite size dynamical QCD medium. *Phys. Rev.*, C80:064909, 2009.

[120] A. Majumder and M. Van Leeuwen. The Theory and Phenomenology of Perturbative QCD Based Jet Quenching. *Prog. Part. Nucl. Phys.*, 66:41–92, 2011.

[121] Y. Akiba. Probing the properties of dense partonic matter at RHIC. *Nucl. Phys.*, A774:403–408, 2006.

[122] A. Adare et al. Production of ω mesons in $p + p$, d+Au, Cu+Cu, and Au+Au collisions at $\sqrt{s_N N} = 200$ GeV. *Phys. Rev.*, C84:044902, 2011.

[123] Guannan Xie. Nuclear Modification Factor of D^0 Meson in Au + Au Collisions at $\sqrt{s_{NN}}$=200 GeV. *Nucl. Phys.*, A956:473–476, 2016.

[124] Jaroslav Adam et al. Centrality and transverse momentum dependence of D^0-meson production at mid-rapidity in Au+Au collisions at $\sqrt{s_{\mathrm{NN}}} = 200\,\mathrm{GeV}$. *Phys. Rev.*, C99(3):034908, 2019.

[125] S. Acharya et al. Measurement of D^0, D^+, D^{*+} and D_s^+ production in Pb-Pb collisions at $\sqrt{s_{\mathrm{NN}}} = 5.02$ TeV. *JHEP*, 10:174, 2018.

[126] Albert M Sirunyan et al. Nuclear modification factor of D^0 mesons in PbPb collisions at $\sqrt{s_{\mathrm{NN}}} = 5.02$ TeV. *Phys. Lett.*, B782:474–496, 2018.

[127] Ralf Rapp and Hendrik van Hees. Heavy Quarks in the Quark-Gluon Plasma. In *Quark-gluon plasma 4*, pages 111–206, 2010.

[128] Yuri L. Dokshitzer and D. E. Kharzeev. Heavy quark colorimetry of QCD matter. *Phys. Lett.*, B519:199–206, 2001.

[129] Tetsufumi Hirano, Ulrich W. Heinz, Dmitri Kharzeev, Roy Lacey, and Yasushi Nara. Elliptic Flow from a Hybrid CGC, Full 3D Hydro and Hadronic Cascade Model. *J. Phys.*, G34:S879–882, 2007.

[130] John Adams et al. Experimental and theoretical challenges in the search for the quark gluon plasma: The STAR Collaboration's critical assessment of the evidence from RHIC collisions. *Nucl. Phys.*, A757:102–183, 2005.

[131] I. Arsene et al. Quark gluon plasma and color glass condensate at RHIC? The Perspective from the BRAHMS experiment. *Nucl. Phys.*, A757:1–27, 2005.

[132] Raimond Snellings. Elliptic Flow: A Brief Review. *New J. Phys.*, 13:055008, 2011.

[133] J. Adams et al. Azimuthal anisotropy at RHIC: The First and fourth harmonics. *Phys. Rev. Lett.*, 92:062301, 2004.

[134] Matthew Luzum and Paul Romatschke. Conformal Relativistic Viscous Hydrodynamics: Applications to RHIC results at s(NN)**(1/2)

= 200-GeV. *Phys. Rev.*, C78:034915, 2008. [Erratum: Phys. Rev.C79,039903(2009)].

[135] G. Policastro, Dan T. Son, and Andrei O. Starinets. The Shear viscosity of strongly coupled N=4 supersymmetric Yang-Mills plasma. *Phys. Rev. Lett.*, 87:081601, 2001.

[136] A. Adare et al. Scaling properties of azimuthal anisotropy in Au+Au and Cu+Cu collisions at s(NN) = 200-GeV. *Phys. Rev. Lett.*, 98:162301, 2007.

[137] L. Adamczyk et al. Measurement of D^0 Azimuthal Anisotropy at Midrapidity in Au+Au Collisions at $\sqrt{s_{NN}}$=200 GeV. *Phys. Rev. Lett.*, 118(21):212301, 2017.

[138] Shreyasi Acharya et al. *D*-meson azimuthal anisotropy in mid-central Pb-Pb collisions at $\sqrt{s_{\rm NN}} = \mathbf{5.02}$ TeV. *Phys. Rev. Lett.*, 120(10):102301, 2018.

[139] Albert M Sirunyan et al. Measurement of prompt D^0 meson azimuthal anisotropy in Pb-Pb collisions at $\sqrt{s_{NN}}$ = 5.02 TeV. *Phys. Rev. Lett.*, 120(20):202301, 2018.

[140] Shreyasi Acharya et al. Event-shape engineering for the D-meson elliptic flow in mid-central Pb-Pb collisions at $\sqrt{s_{\rm NN}}$ = 5.02 TeV. *JHEP*, 02:150, 2019.

[141] Hans-Thomas Elze. Relativistic quantum transport theory. *AIP Conf. Proc.*, 631:229–252, 2002.

[142] K. Huang. *Statistical mechanics*. 1987.

[143] H. Weyl. Quantum mechanics and group theory. *Z. Phys.*, 46:1, 1927.

[144] Krishna Rajagopal and Frank Wilczek. Static and dynamic critical phenomena at a second order QCD phase transition. *Nucl. Phys.*, B399:395–425, 1993.

[145] Mark G. Alford, Krishna Rajagopal, and Frank Wilczek. Color flavor locking and chiral symmetry breaking in high density QCD. *Nucl. Phys.*, B537:443–458, 1999.

[146] H. T. Elze, Johann Rafelski, and L. Turko. Entropy production in relativistic hydrodynamics. *Phys. Lett.*, B506:123–130, 2001.

[147] Jean-Paul Blaizot and Edmond Iancu. The Quark gluon plasma: Collective dynamics and hard thermal loops. *Phys. Rept.*, 359:355–528, 2002.

[148] Salvatore Plumari, Wanda M. Alberico, Vincenzo Greco, and Claudia Ratti. Recent thermodynamic results from lattice QCD analyzed within a quasi-particle model. *Phys. Rev.*, D84:094004, 2011.

[149] A. Peshier and W. Cassing. The Hot non-perturbative gluon plasma is an almost ideal colored liquid. *Phys. Rev. Lett.*, 94:172301, 2005.

[150] A. Peshier, Burkhard Kampfer, and G. Soff. From QCD lattice calculations to the equation of state of quark matter. *Phys. Rev.*, D66:094003, 2002.

[151] Peter Levai and Ulrich W. Heinz. Massive gluons and quarks and the equation of state obtained from SU(3) lattice QCD. *Phys. Rev.*, C57:1879–1890, 1998.

[152] M. Ruggieri, P. Alba, P. Castorina, S. Plumari, C. Ratti, and V. Greco. Polyakov Loop and Gluon Quasiparticles in Yang-Mills Thermodynamics. *Phys. Rev.*, D86:054007, 2012.

[153] Hamza Berrehrah, Pol-Bernard Gossiaux, Jörg Aichelin, Wolfgang Cassing, and Elena Bratkovskaya. Dynamical collisional energy loss and transport properties of on- and off-shell heavy quarks in vacuum and in the Quark Gluon Plasma. *Phys. Rev.*, C90(6):064906, 2014.

[154] Szabolcs Borsanyi, Gergely Endrodi, Zoltan Fodor, Antal Jakovac, Sandor D. Katz, Stefan Krieg, Claudia Ratti, and Kalman K. Szabo.

The QCD equation of state with dynamical quarks. *JHEP*, 11:077, 2010.

[155] S. Plumari, V. Baran, M. Di Toro, G. Ferini, and V. Greco. Does the NJL chiral phase transition affect the elliptic flow of a fluid at fixed η/s? *Phys. Lett.*, B689:18–22, 2010.

[156] V. Baran, M. Colonna, V. Greco, M. Di Toro, S. Plumari, and R. Zus. Kinetic approaches to phase transitions in strongly interacting matter. *J. Phys. Conf. Ser.*, 338:012020, 2012.

[157] M. Bluhm, B. Kampfer, and K. Redlich. Ratio of bulk to shear viscosity in a quasigluon plasma: from weak to strong coupling. *Phys. Lett.*, B709:77–81, 2012.

[158] F. Scardina, M. Colonna, S. Plumari, and V. Greco. Quark-to-gluon composition of the quark-gluon plasma in relativistic heavy-ion collisions. *Phys. Lett.*, B724:296–300, 2013.

[159] Salvatore Plumari, Armando Puglisi, Maria Colonna, Francesco Scardina, and Vincenzo Greco. Shear viscosity and chemical equilibration of the QGP. 2012. [J. Phys. Conf. Ser.420,012029(2013)].

[160] Armando Puglisi, Salvatore Plumari, and Vincenzo Greco. Shear viscosity ? to electric conductivity $?_{el}$ ratio for the quark?gluon plasma. *Phys. Lett.*, B751:326–330, 2015.

[161] S. Plumari, A. Puglisi, F. Scardina, and V. Greco. Shear Viscosity of a strongly interacting system: Green-Kubo vs. Chapman-Enskog and Relaxation Time Approximation. *Phys. Rev.*, C86:054902, 2012.

[162] G. Ferini, M. Colonna, M. Di Toro, and V. Greco. Scalings of Elliptic Flow for a Fluid at Finite Shear Viscosity. *Phys. Lett.*, B670:325–329, 2009.

[163] V. Greco, M. Colonna, M. Di Toro, and G. Ferini. Anisotropies in momentum space at finite Shear Viscosity in ultrarelativistic heavy-ion collisions. 2008. [Prog. Part. Nucl. Phys.62,562(2009)].

[164] Anton Wiranata and Madappa Prakash. Shear Viscosities from the Chapman-Enskog and the Relaxation Time Approaches. *Phys. Rev.*, C85:054908, 2012.

[165] A. Puglisi, S. Plumari, F. Scardina, and V. Greco. Transport coefficients of Quark-Gluon Plasma in a Kinetic Theory approach. *J. Phys. Conf. Ser.*, 527:012016, 2014.

[166] L. P. Csernai. *Introduction to relativistic heavy ion collisions*. 1994.

[167] M. Abramowitz and I. A. Stegun. *Handbook of Mathematical Functions with Formulas, Graphs, and Mathematical Tables*. 1972.

[168] B. Svetitsky. Diffusion of charmed quarks in the quark-gluon plasma. *Phys. Rev.*, D37:2484–2491, 1988.

[169] Santosh K. Das, Francesco Scardina, Salvatore Plumari, and Vincenzo Greco. Toward a solution to the R_{AA} and v_2 puzzle for heavy quarks. *Phys. Lett.*, B747:260–264, 2015.

[170] Vincenzo Greco. Heavy Flavor Production, Flow and Energy Loss. *Nucl. Phys.*, A967:200–207, 2017.

[171] Cheuk-Yin Wong. Dynamics of nuclear fluid. VIII. Time-dependent Hartree-Fock approximation from a classical point of view. *Phys. Rev.*, C25:1460–1475, 1982.

[172] Zhe Xu and Carsten Greiner. Thermalization of gluons in ultrarelativistic heavy ion collisions by including three-body interactions in a parton cascade. *Phys. Rev.*, C71:064901, 2005.

[173] G. Welke, R. Malfliet, C. Gregoire, M. Prakash, and E. Suraud. Collisional relaxation in simulations of heavy-ion collisions using Boltzmann-type equations. *Phys. Rev.*, C40:2611–2620, 1989.

[174] P. Danielewicz and G. F. Bertsch. Production of deuterons and pions in a transport model of energetic heavy ion reactions. *Nucl. Phys.*, A533:712–748, 1991.

[175] K. Weber, B. Blaettel, W. Cassing, H. C. Doenges, A. Lang, T. Maruyama, and U. Mosel. Relativistic potentials for a counter-streaming nuclear matter scenario with a covariant momentum dependent interaction. *Nucl. Phys.*, A552:571–590, 1993.

[176] H. Berrehrah, E. Bratkovskaya, W. Cassing, P. B. Gossiaux, J. Aichelin, and M. Bleicher. Collisional processes of on-shell and off-shell heavy quarks in vacuum and in the Quark-Gluon-Plasma. *Phys. Rev.*, C89(5):054901, 2014.

[177] A. Peshier, Burkhard Kampfer, O. P. Pavlenko, and G. Soff. A Massive quasiparticle model of the SU(3) gluon plasma. *Phys. Rev.*, D54:2399–2402, 1996.

[178] Shanshan Cao, Guang-You Qin, and Steffen A. Bass. Energy loss, hadronization and hadronic interactions of heavy flavors in relativistic heavy-ion collisions. *Phys. Rev.*, C92(2):024907, 2015.

[179] Min He, Rainer J. Fries, and Ralf Rapp. $\mathbf{D_s}$-Meson as Quantitative Probe of Diffusion and Hadronization in Nuclear Collisions. *Phys. Rev. Lett.*, 110(11):112301, 2013.

[180] Munshi Golam Mustafa, Dipali Pal, Dinesh Kumar Srivastava, and Markus Thoma. Radiative energy loss of heavy quarks in a quark gluon plasma. *Phys. Lett.*, B428:234–240, 1998.

[181] Shanshan Cao, Tan Luo, Guang-You Qin, and Xin-Nian Wang. Linearized Boltzmann transport model for jet propagation in the quark-gluon plasma: Heavy quark evolution. *Phys. Rev.*, C94(1):014909, 2016.

[182] Jan Uphoff, Oliver Fochler, Zhe Xu, and Carsten Greiner. Elastic and radiative heavy quark interactions in ultra-relativistic heavy-ion collisions. *J. Phys.*, G42(11):115106, 2015.

[183] Taesoo Song, Wolfgang Cassing, Pierre Moreau, and Elena Bratkovskaya. Open charm and dileptons from relativistic heavy-ion collisions. *Phys. Rev. C*, 97:064907, Jun 2018.

[184] Pol Bernard Gossiaux, Vincent Guiho, and Jorg Aichelin. Charmonia enhancement in quark-gluon plasma with improved description of c-quarks phase-distribution. *J. Phys.*, G31:S1079–S1082, 2005.

[185] A. Beraudo, A. De Pace, M. Monteno, M. Nardi, and F. Prino. Heavy flavors in heavy-ion collisions: quenching, flow and correlations. *Eur. Phys. J.*, C75(3):121, 2015.

[186] Min He, Rainer J. Fries, and Ralf Rapp. Heavy Flavor at the Large Hadron Collider in a Strong Coupling Approach. *Phys. Lett.*, B735:445–450, 2014.

[187] Yingru Xu, Jonah E. Bernhard, Steffen A. Bass, Marlene Nahrgang, and Shanshan Cao. Data-driven analysis for the temperature and momentum dependence of the heavy-quark diffusion coefficient in relativistic heavy-ion collisions. *Phys. Rev.*, C97(1):014907, 2018.

[188] Shanshan Cao et al. Towards the extraction of heavy-quark transport coefficients in quark-gluon plasma. 2018.

[189] Guy D. Moore and Derek Teaney. How much do heavy quarks thermalize in a heavy ion collision? *Phys. Rev.*, C71:064904, 2005.

[190] Betty Abelev et al. Suppression of high transverse momentum D mesons in central Pb-Pb collisions at $\sqrt{s_{NN}} = 2.76$ TeV. *JHEP*, 09:112, 2012.

[191] Yingru Xu et al. Resolving discrepancies in the estimation of heavy quark transport coefficients in relativistic heavy-ion collisions. *Phys. Rev.*, C99(1):014902, 2019.

[192] Ben-Wei Zhang, En-ke Wang, and Xin-Nian Wang. Multiple parton scattering in nuclei: Heavy quark energy loss and modified fragmentation functions. *Nucl. Phys.*, A757:493–524, 2005.

[193] Karen M. Burke et al. Extracting the jet transport coefficient from jet quenching in high-energy heavy-ion collisions. *Phys. Rev.*, C90(1):014909, 2014.

[194] Abhijit Majumder, Berndt Muller, and Xin-Nian Wang. Small shear viscosity of a quark-gluon plasma implies strong jet quenching. *Phys. Rev. Lett.*, 99:192301, 2007.

[195] Santosh K. Das, Francesco Scardina, Salvatore Plumari, and Vincenzo Greco. Heavy-flavor in-medium momentum evolution: Langevin versus Boltzmann approach. *Phys. Rev.*, C90:044901, 2014.

[196] Francesco Scardina, Santosh K. Das, Vincenzo Minissale, Salvatore Plumari, and Vincenzo Greco. Estimating the charm quark diffusion coefficient and thermalization time from D meson spectra at energies available at the BNL Relativistic Heavy Ion Collider and the CERN Large Hadron Collider. *Phys. Rev.*, C96(4):044905, 2017.

[197] Salvatore Plumari, Giovanni Luca Guardo, Francesco Scardina, and Vincenzo Greco. Initial state fluctuations from mid-peripheral to ultra-central collisions in a event-by-event transport approach. *Phys. Rev.*, C92(5):054902, 2015.

[198] Dmitri Kharzeev and Marzia Nardi. Hadron production in nuclear collisions at RHIC and high density QCD. *Phys. Lett.*, B507:121–128, 2001.

[199] Xin-Nian Wang. Systematic study of high p_T hadron spectra in pp, p A and A A collisions from SPS to RHIC energies. *Phys. Rev.*, C61:064910, 2000.

[200] Jiechen Xu, Jinfeng Liao, and Miklos Gyulassy. Bridging Soft-Hard Transport Properties of Quark-Gluon Plasmas with CUJET3.0. *JHEP*, 02:169, 2016.

[201] Salvatore Plumari, Francesco Scardina, Vincenzo Minissale, Lucia Oliva, and Vincenzo Greco. Initial State fluctuations from midperiph-

eral to ultracentral collisions in a transport approach. *J. Phys. Conf. Ser.*, 981(1):012017, 2018.

[202] Huichao Song, Steffen A. Bass, and Ulrich Heinz. Elliptic flow in 200 A GeV Au+Au collisions and 2.76 A TeV Pb+Pb collisions: insights from viscous hydrodynamics + hadron cascade hybrid model. *Phys. Rev.*, C83:054912, 2011. [Erratum: Phys. Rev.C87,no.1,019902(2013)].

[203] Bjoern Schenke, Sangyong Jeon, and Charles Gale. (3+1)D hydrodynamic simulation of relativistic heavy-ion collisions. *Phys. Rev.*, C82:014903, 2010.

[204] Harri Niemi, Gabriel S. Denicol, Pasi Huovinen, Etele Molnar, and Dirk H. Rischke. Influence of the shear viscosity of the quark-gluon plasma on elliptic flow in ultrarelativistic heavy-ion collisions. *Phys. Rev. Lett.*, 106:212302, 2011.

[205] Christian Wolfgang Fabjan et al. ALICE: Physics performance report, volume II. *J. Phys.*, G32:1295–2040, 2006.

[206] Jaroslav Adam et al. Centrality dependence of the pseudorapidity density distribution for charged particles in Pb-Pb collisions at $\sqrt{s_{\rm NN}}$ = 5.02 TeV. *Phys. Lett.*, B772:567–577, 2017.

[207] Jaroslav Adam et al. Anisotropic flow of charged particles in Pb-Pb collisions at $\sqrt{s_{\rm NN}} = 5.02$ TeV. *Phys. Rev. Lett.*, 116(13):132302, 2016.

[208] Matteo Cacciari, Michelangelo L. Mangano, and Paolo Nason. Gluon PDF constraints from the ratio of forward heavy-quark production at the LHC at $\sqrt{S} = 7$ and 13 TeV. *Eur. Phys. J.*, C75(12):610, 2015.

[209] Taesoo Song, Hamza Berrehrah, Daniel Cabrera, Juan M. Torres-Rincon, Laura Tolos, Wolfgang Cassing, and Elena Bratkovskaya. Tomography of the Quark-Gluon-Plasma by Charm Quarks. *Phys. Rev.*, C92(1):014910, 2015.

[210] L. Adamczyk et al. Measurements of D^0 and D^* Production in $p + p$ Collisions at $\sqrt{s} = 200$ GeV. *Phys. Rev.*, D86:072013, 2012.

[211] Betty Abelev et al. Measurement of charm production at central rapidity in proton-proton collisions at $\sqrt{s} = 2.76$ TeV. *JHEP*, 07:191, 2012.

[212] Mykhailo Lisovyi, Andrii Verbytskyi, and Oleksandr Zenaiev. Combined analysis of charm-quark fragmentation-fraction measurements. *Eur. Phys. J.*, C76(7):397, 2016.

[213] Claude Amsler et al. Review of Particle Physics. *Phys. Lett.*, B667:1–1340, 2008.

[214] B. Abelev et al. Measurement of charm production at central rapidity in proton-proton collisions at $\sqrt{s} = 7$ TeV. *JHEP*, 01:128, 2012.

[215] Taesoo Song, Hamza Berrehrah, Juan M. Torres-Rincon, Laura Tolos, Daniel Cabrera, Wolfgang Cassing, and Elena Bratkovskaya. Single electrons from heavy-flavor mesons in relativistic heavy-ion collisions. *Phys. Rev. C*, 96:014905, Jul 2017.

[216] Vardan Khachatryan et al. Measurement of the total and differential inclusive B^+ hadron cross sections in pp collisions at $\sqrt{s} = 13$ TeV. *Phys. Lett.*, B771:435–456, 2017.

[217] Shreyasi Acharya et al. Λ_c^+ production in pp collisions at $\sqrt{s} = 7$ TeV and in p-Pb collisions at $\sqrt{s_{\rm NN}} = 5.02$ TeV. *JHEP*, 04:108, 2018.

[218] Shreyasi Acharya et al. Λ_c^+ production in Pb-Pb collisions at $\sqrt{s_{\rm NN}} = 5.02$ TeV. *Submitted to: Phys. Lett.*, 2018.

[219] Ryan D. Weller and Paul Romatschke. One fluid to rule them all: viscous hydrodynamic description of event-by-event central p+p, p+Pb and Pb+Pb collisions at $\sqrt{s} = 5.02$ TeV. *Phys. Lett.*, B774:351–356, 2017.

[220] Piotr Bo?ek. Small systems ? hydrodynamics. *Nucl. Phys.*, A956:208–215, 2016.

[221] Santosh K. Das, Juan M. Torres-Rincon, Laura Tolos, Vincenzo Minissale, Francesco Scardina, and Vincenzo Greco. Propagation of heavy baryons in heavy-ion collisions. *Phys. Rev.*, D94(11):114039, 2016.

[222] CMS Collaboration. Measurement of prompt and nonprompt charmonium suppression in PbPb collisions at 5.02 TeV. 2017.

[223] Albert M Sirunyan et al. Measurement of the $B^{\pm}$ Meson Nuclear Modification Factor in Pb-Pb Collisions at $\sqrt{s_{NN}} = 5.02$ TeV. *Phys. Rev. Lett.*, 119(15):152301, 2017.

[224] Long Zhou. Measurements of Λ_c^+ and D_s^+ productions in Au+Au collisions at $\sqrt{s_{NN}} = 200$ GeV from STAR. *Nucl. Phys.*, A967:620–623, 2017.

[225] Sooraj Radhakrishnan. Measurements of open charm production in Au+Au collisions at $\sqrt{s}_{NN} = 200$GeV with the STAR experiment at RHIC. *Nucl. Phys.*, A982:659–662, 2019.

[226] J. Aichelin, V. Ozvenchuck, T. Gousset, and P. B. Gossiaux. Analysis of the Quark-Gluon Plasma by Heavy Quarks. *J. Phys. Conf. Ser.*, 623(1):012002, 2015.

[227] Steven S. Gubser. Comparing the drag force on heavy quarks in N=4 super-Yang-Mills theory and QCD. *Phys. Rev.*, D76:126003, 2007.